An Analytical and Experimental Investigation of the Response of Elliptical Composite Cylinders

by

Carol Ann Meyers

Dissertation submitted to the Faculty of the
Virginia Polytechnic Institute and State University
in partial fulfillment of the requirements for the degree of
DOCTOR OF PHILOSOPHY
in
Engineering Mechanics

APPROVED:

M. W. Hyer, Chairman

M. S. Cramer

O. H. Griffin, Jr.

E. R. Johnson

R. H. Plaut

April 19, 1996

Blacksburg, Virginia

Keywords: Elliptical, Noncircular, Cylinder, Composite, Axial Compression, Pressure

AN ANALYTICAL AND EXPERIMENTAL INVESTIGATION OF THE RESPONSE OF ELLIPTICAL COMPOSITE CYLINDERS

by

Carol Ann Meyers

Committee Chair: Michael W. Hyer
Engineering Mechanics

(ABSTRACT)

An analytical and experimental investigation of the response of composite cylinders of elliptical cross-section to axial compression and internal pressure loadings is discussed. Nine eight-ply graphite-epoxy elliptical cylinders, three lay-ups for each of three cross sectional aspect ratios, are specifically examined. The lay-ups studied are a quasi-isotropic $(\pm 45/0/90)_s$, an axially-stiff $(\pm 45/0_2)_s$, and a circumferentially-stiff $(\pm 45/90_2)_s$. The elliptical cross sections studied are characterized by semi-minor axis (b) to semi-major axis (a) ratios of b/a = 0.70, 0.85, and 1.00 (circular). The cross sections are obtained by holding the semi-major axis constant for all cross sections, and only varying the semi-minor axis. The nominal semi-major axis for all specimens was 5.00 in. (127 mm), and all specimens were cut to the same length, which provided a length-to-radius ratio of 2.9 for the circular cylinders. For the elliptical cross section cylinders, the length-to-radius ratios, L/R(s), ranged from two to slightly greater than six, where R(s) is the function describing the circumferential variation of the radius. A geometrically nonlinear special-purpose analysis, based on Donnell's nonlinear shell equations, is developed to study the prebuckling responses of geometrically perfect cylinders. In this analysis the circumferentially-varying radius of curvature of the cylinder is expanded in a cosine series. While elliptical sections are studied here, it should be noted that such an expansion will accommodate any cross section with at least two axes of symmetry. The displacements are likewise expanded in a harmonic series using the Kantorovich method. The total potential energy, written in terms of the displacements, is then integrated over the circumferential coordinate. The variational process then yields the governing Euler-Lagrange equations and boundary conditions. This process has been automated using the symbolic manipulation package *Mathematica*©. The resulting nonlinear ordinary differential equations are then integrated via the finite difference method. A geometrically nonlinear finite element analysis is also utilized to compare with the prebuckling solutions of the special-purpose analysis and to study the prebuckling and buckling responses of geometrically imperfect cylinders. The imperfect cylinder geometries are represented by an analytical approximation of the measured shape imperfections.

An accompanying experimental program is carried out to provide a means for comparison between the real and theoretical systems using a test fixture specifically designed for the present investigation to allow for both axial compression and internal pressurization. A description of the test fixture is included. Three types of tests were run on each specimen: (1) low internal pressure with no axial end displacement, (2) low internal pressure with a low level compressive axial displacement and, (3) compressive axial displacement to failure, with no internal pressure. The experimental data from these tests are compared to predictions for both perfect and imperfect cylinder geometries. Prebuckling results are presented in the form of displacement and strain profiles for each of the three sets of load conditions. Buckling loads are also compared to predicted values based upon classical estimates as well as linear and nonlinear finite element results which include initial shape imperfections. Lastly, the postbuckling and failure characteristics observed during the tests are described.

Acknowledgments

The financial support of this work by the Charles E. Minor Fellowship and the Structural Mechanics Branch of the NASA Langley Research Center through the NASA-Virginia Tech Composites Program, Grant NAG-1-343, is gratefully acknowledged.

I would like to thank my advisor, Professor M. W. Hyer, for his technical and professional guidance and encouragement during the past five years of study and research. Special thanks are also given to Professors M. S. Cramer, O. H. Griffin, E. R. Johnson, and R. H. Plaut for serving on the Ph.D. dissertation and advisory committee and for providing technical guidance during the course of the research.

I am very grateful to my grant monitor, Dr. J. H. Starnes, Jr. for his continuous support and technical guidance throughout my doctoral program. I am also thankful for the use of the excellent laboratory and computational facilities made available to me by the Structural Mechanics Branch of the NASA-Langley Research Center. I would like to thank all of my friends and colleagues at the NASA-Langley Research Center for their valuable discussions, technical assistance, advice, and encouragement. Special thanks are also given to Juan Cruz for his invaluable technical advice and for the friendship and hospitality which he extended to me during my internship at the NASA-Langley Research Center.

Many individuals working for, or under contract to, the NASA-Langley Research Center contributed to success of this effort and I would like to acknowledge their support. In particular, I would like to recognize the following individuals for their outstanding technical efforts: W. A. Waters, Jr. (general technical support), W. Huling (computational support), J. J. Kiss and M. A. Cole (testing and data acquisition), F. Walters and B. Stockum (specimen machining and potting), K. Bloxom (specimen strain-gaging), and D. Croom and T. Burns (specimen surface shape measurement).

I am grateful to my friends in the NASA-Virginia Tech Composites Program, especially to my longtime friends Lynda Oleksuk and Danniella Muheim. I am most grateful to my closest friend, my husband, Larry London. I will always be indebted to my family and friends for their help, support, and patience.

Finally, I would like to dedicate this dissertation to my grandmother, Elizabeth Minn Meyers, who passed away too soon to see this degree completed. Her love, her courage, and her deep respect for education provided a constant inspiration.

Table of Contents

List of Figures

List of Tables

Chapter 1.0 Introduction

Due to their high structural efficiency, thin-walled cylinders are used extensively as primary structural elements in many important applications. Because fiber-reinforced composites provide high specific strength and specific stiffness, as well as the ability to tailor strength and stiffness parameters, composite cylinders are of particular interest in the design of lightweight, efficient structures. This is especially true in the aerospace industry. While circular cylinders are perhaps the most common, and hence the most widely studied form of composite cylinder, future transport fuselages may involve noncircular cross sections. Such a construction may be required due to aerodynamic, internal storage, or other considerations. In order to use composites in the design of a fuselage with a noncircular cross section, several issues will need to be addressed, including not only the effects of the noncircular geometry, but also material orthotropy, interlaminar stresses, and the addition of stiffeners, rings, and cutouts. It is also likely that it will be desirable to vary the structural properties according to circumferential position, so that each circumferential section is tailored to best meet its loading requirements. However, before addressing such complex structures, a good understanding must first be developed of the simpler structural elements, such as thin, unstiffened composite cylinders of noncircular cross section with a uniform lamination. The aim of the investigation described in this dissertation is to understand how the degree of out-of-roundness of the cross section, described in terms of ellipticity, in combination with material orthotropy affects the response of composite cylinders to the simple load conditions of axial compression and internal pressure.

The present study is both analytical and experimental in nature, involving the investigation of nine composite cylinders of elliptical cross section with three lay-ups and three cross sectional aspect ratios. These nine cylinders were tested using a fixture constructed for this project to allow for both axial compression and internal pressurization. The geometrically nonlinear response of the cylinders was analyzed using both a special purpose code and a finite element program. The special purpose code is used to efficiently study and gain physical insight into the character of the cylinders' prebuckling response. The finite element code is utilized to study the buckling and postbuckling responses, as well as to study the response to geometric imperfections, accurately modelled according to measurements made on the actual cylinders.

This dissertation begins in the next chapter with a review of some of the relevant literature related to the study of noncircular cylinders. In ch. 3, a description is given of the particular problem studied here, including a brief discussion of the theory of surfaces as it relates to the derivation of the shell equations for

cylinders with a continuously varying radius of curvature. The specific geometries studied, definitions, and nomenclature are introduced. The formulation of the equations and the solution approach developed for the special purpose code are also described. Lastly, the finite element code used and it's application are discussed in general terms.

Chapter 4 discusses the behavior of elliptical cross section cylinders in response to internal pressure and to axial compression in the prebuckling range based on the numerical results obtained with the special purpose code. The convergence of this solution is first discussed. Numerical examples are then shown to illustrate the specific issues involved with each type of loading. These results are also compared with those that can be obtained from simplified methods, such as using membrane theory adapted to noncircular cylinders, or using nonmembrane results from circular cylinders to predict the behavior at particular circumferential locations on an elliptical cylinder.

The experimental program is described in ch. 5, including the details of the specimens, the test fixtures, instrumentation, and test procedures.

Measured and observed experimental responses are discussed and compared with the predicted responses in ch. 6. The experimental data are first used to discuss and evaluate the symmetry and uniformity of the test setup. The test results are then compared to numerical predictions based on both perfect and geometrically imperfect cylinders. Prebuckling deflections and strain distributions are discussed and compared in detail. Buckling loads are also compared to predicted values based upon classical estimates as well as linear and nonlinear finite element results which include initial shape imperfections. Lastly, the postbuckling and failure characteristics observed during the tests are also described.

Finally, a discussion of the study, conclusions, and recommendations for future work are presented in ch. 7.

The method of measuring the initial shape imperfections of these specimens and a description of the application of these measurements in the STAGS finite element models are described in Appendix A. The fabrication, preparation, and nondestructive evaluation of the test specimens are discussed in Appendix B. For completeness, results for cases not detailed in ch. 6 are given in Appendix C.

Chapter 2.0 Literature Review

Although over the last 30-40 years considerable attention has been given to both theoretical and experimental evaluation of the responses of circular cylinders to simple loadings [1, 2, 3], relatively little theoretical work has been done for noncircular cylinders, and even fewer related experimental results have been reported. Nevertheless, attention can be drawn to the work of several investigators. A brief discussion of this work is given below.

Analysis

While the membrane response of cylinders with varying curvature is only slightly more difficult to obtain than that for circular cylinders [4, 5, 6], the nonmembrane response of cylinders with varying curvature is significantly more difficult to analyze than for their circular counterparts. It should be noted that because it is possible to construct many noncircular shells from circular shell segments, this method has often been employed to simplify such analyses, e. g., [6, 7, 8]. In the following, the discussion will be limited to shells with continuously varying curvature and the term 'noncircular' will always refer to shells with continuously varying curvature.

The earliest nonmembrane analysis of a shell of continuously varying curvature was performed by Marguerre [9], who expanded the curvature in a Fourier series with respect to the circumferential arc-length in order to more accurately study the stability of so-called long wing noses (the terminology used for wing leading edges). This basic approach has since been used in the majority of all subsequent analyses of shells of constantly varying curvature, including the present study.

Pressure

Very little work is available for pressurized noncircular cylinders. For the case of internal pressure, while nonmembrane results can be found for cylinders constructed of circular shell segments, e. g. [7], only membrane solutions for isotropic noncircular cylinders can be found [4, 5, 6]. A small body of work exists for isotropic oval cylinders subjected to external pressure. These studies are based primarily on the work of Romano and Kempner [10, 11], who first investigated the effects of lateral pressure on short, simply-supported, noncircular cylinders in 1958. In [10, 11] a Donnell-type linear shell theory was used and a double Fourier series solution was assumed for the displacements in order to obtain results for a simply-

supported mildly oval cylinder. Vafakos, Romano, and Kempner [12] extended this work to clamped oval cylinders with more severely oval cross sections. In order to have greater flexibility in defining boundary conditions, rather than using a double Fourier series expansion, displacements were expanded only in the circumferential direction, and the principle of minimum total potential energy was used to obtain ordinary differential equations in the axial coordinate. These were solved using an assumed series of complex functions. Vafakos, Nissel, and Kempner [13, 14] then applied this energy solution to the previous problem of simply-supported oval shells, finding excellent agreement between the two solutions. In all of these papers, the radius of curvature was described as a function of the circumferential length using a one-term Marguerre-type expansion of the form

$$\frac{1}{R(s)} = \frac{1}{R_o}\left(1 + \xi\cos\left(\frac{4\pi s}{C}\right)\right), \tag{2.1}$$

where ξ was a parameter describing the eccentricity of the oval, C was the circumferential length of the cylinder, and R_o was the radius of a circular cylinder having the same circumferential length as the oval. (Such an oval was sometimes referred to in the subsequent literature as a 'Kempner oval'.) The cylinders compared had varying cross-sectional aspect ratios, but the same circumferential length. It was shown that the maximum stresses and displacements, as well as the variation in these quantities, increased significantly with increasing semi-major to semi-minor aspect ratio. Unlike circular cylinders, there was a clear variation of stresses and displacements in the circumferential as well as the axial direction. The bending stresses, especially the axial bending stress, comprised a significant portion of the total stress. This was especially true for the cylinders with clamped boundary conditions.

Axial Compression

A membrane solution for isotropic elliptical cylinders under axial compression due to uniform end-shortening can be found in Novozhilov [7]. The earliest nonmembrane work available on the response of noncircular cylinders was performed by Kempner and Chen [15, 16, 17]. In these studies, the buckling and initial postbuckling responses of oval cylinders of the type described in [10] were examined using equations analogous to the Donnell shell equations. The approximate solution used in these studies was obtained by an extension of an energy solution applied to circular cylinders [18], modified by taking into consideration that the total potential energy would no longer be a continuous function of a circumferential wavelength parameter. Several important results from these studies can be cited. In considering families of ovals having the same circumferential length, it was observed that the classical buckling load, σ_{cr}, decreased with increasing out-of-roundness. It was reasoned that this was because the least rigid regions at the ends of minor axis of the oval shell, where $R = R_{max}$, are responsible for the onset of instability in the classical sense.

Using an asymptotic buckling solution, it was further shown that for infinitely thin shells the buckling stress of an oval cylinder corresponds to the classical buckling stress of an axially compressed circular cylinder whose radius of curvature is equal to the maximum radius of curvature of the oval cylinder, i. e.,

$$\sigma_{cr}^{ellipse} \equiv \sigma_{cr}^{circle}\Big|_{R = R_{max}} \tag{2.2}$$

For oval cylinders having finite thickness, eqn. 2.2 represented a lower bound on the buckling stress and provided a very good approximation for moderately thin cylinders, $R_{avg}/H > 100$.

While the buckling load decreased with increasing out-of-roundness, it was noted that the postbuckling load vs. end-shortening relation for oval cylinders always lay above that for the corresponding circular cylinder, and the minimum load in the postbuckling range increased with increasing out-of-roundness. Further, for the more severe ovals, stresses in the postbuckling region were obtained which exceeded the buckling stress. This indicated that sufficiently eccentric oval cylinders might be less imperfection sensitive than circular cylinders. These results were explained physically by considering that after buckling occurs, the stiffer, larger curvature regions of the shell would carry the main portion of the applied load. It was shown that as the curvature of the ends of the major axis approached infinity, the postbuckling load vs. end-shortening relation for the cylinder behaved more and more like the relation for a flat plate.

In response to this finding, Hutchinson [19] applied Koiter's method to investigate the sensitivity of oval cylinders to initial imperfections, showing that oval cylinders with minor to major axes ratios of $b/a > 0.2$ were very imperfection sensitive. Hutchinson also studied elliptical cylinders and found similar results to those obtained for oval cylinders. Subsequently, Kempner and Chen [20] modified their previous analysis and confirmed Hutchinson's results for the initial postbuckling region, but indicated that the snap-through behavior for an oval cylinder with moderate to large eccentricity would be much less drastic than for a circular cylinder. Because buckling of a circular cylinder occurs instantaneously over the entire circumference of the cylinder, it is accompanied by a catastrophic drop in load-bearing capacity so that the initial buckling load and the collapse load for a circular cylinder are identical. However, after initial buckling and a short drop in load, it was found that for some oval cylinders a higher load could be attained after which collapse would occur. This analysis indicated that these load points were less sensitive to imperfections and they suggested that this second maximum load would be a more meaningful stability parameter for oval cylinders than the initial buckling load.

These results were supported by the work of Almroth, Brogan, and Marlowe [21], on the collapse of elliptical cylinders and cones. This study was performed using a two-dimensional finite difference analysis (the precursor to the STAGS finite element program used in the current study). It was argued that for shells with noncircular cross sections, bifurcation buckling need not be considered, as the deformation pattern prior to collapse already would contain a component of the buckling mode which would develop at collapse.

Hence only a nonlinear analysis was performed. It was found that elliptical cylinders (and cones) exhibit more than one maximum load. This analysis also allowed the inclusion of a simple initial shape imperfection. For sufficiently large imperfection amplitudes it was found that the first sharp maximum disappeared. While this primary buckling load was sensitive to imperfections, the second maximum did not appear to be imperfection sensitive. Tennyson, Booton, and Caswell [22] also investigated the effects of imperfections on the buckling of elliptical cylinders. Taking the approximation given in eqn. 2.2 to predict the buckling load for a perfect elliptical cylinder, they reasoned that the buckling load reduction due to an axial imperfection distribution could be estimated using Koiter's axisymmetric imperfection theory for a circular cylinder having a radius equal to the maximum radius of curvature of the elliptical cylinder. These results were shown to agree reasonably well with those of Hutchinson.

Feinstein, Erikson, and Kempner [23] considered the effects of clamped end conditions on the buckling of axially compressed oval cylinders. This study represents one of the few to make any attempt to take into account a nonmembrane prebuckling state. To accomplish this, linear prebuckling equilibrium equations, written in terms of displacements, were further simplified using assumptions referred to as "pseudo-symmetry," wherein all derivatives with respect to the circumferential coordinate were neglected, but the dependence of the radius of curvature upon the circumferential coordinate was retained. The stability equations were then solved using a Fourier method in conjunction with a higher-order difference method. For clamped circular or nearly circular cylinders only a small reduction in the buckling load by comparison to an infinite cylinder was found. For moderately oval cylinders little or no difference was found. However, for more eccentric oval cylinders, the cylinders with clamped ends exhibited a buckling load above that of infinite cylinders. The effects of stiffeners on short oval cylinders were investigated by Volpe, Chen, and Kempner [24]. For unstiffened clamped cylinders, their results agreed well with those of [23]. Unstiffened simply-supported oval cylinders were also considered, and were shown to have, in all cases, buckling loads below those for cylinders with clamped end conditions. Similar trends were observed for oval cylinders with external stiffeners.

Very few investigators have considered composite cylinders with noncircular cross-sections. Sun [25] applied Hutchinson's [19] analysis to oval and elliptical composite cylinders. It was found that symmetric cross-ply cylinders were relatively imperfection insensitive, even for moderate minor to major axis aspect ratios. Cylinders with quasi-isotropic and unidirectional lay-ups were insensitive to imperfections only for extremely eccentric cross-sections. In the range of moderate eccentricity, elliptical cylinders were found to have much higher predicted buckling loads than the oval cylinder having the same eccentricity and the same circumferential length. Soldatos [26, 27] developed a fully nonlinear transversely shear deformable shell theory applicable to noncircular cylinders. A linearized version of this theory was applied to the problem of buckling of thick anti-symmetric cross-ply oval cylinders. Galerkin's method was used to solve the buckling

problem and the solutions were compared with those obtained using a classical Love-type shell theory. It was concluded that with increasing eccentricity of the cross-section, the effects of transverse shear deformations on the buckling load decreased.

Most recently, Sheinman and Firer [28, 29] investigated the buckling and postbuckling of angle-ply and unsymmetrically laminated oval and elliptical cylinders. In this study, Donnell-type shell equations were written in terms of the Hu-Washizu mixed formulation and the radius of curvature expanded in a Marguerre-type series. The normal displacement and Airy's stress function were then expanded in the circumferential direction and Galerkin's method used to obtain ordinary differential equations. Linear prebuckling equations were solved and the result substituted into the buckling equations, and a second set of ordinary differential equations was then obtained. These were reduced further using the finite difference method in order to obtain an eigenvalue problem. Unlike circular cylinders, the coupling of the wave number was found to be very significant for the noncircular cylinders, especially as the eccentricity of the cross-section increased. The inclusion of at least 10 wave numbers was necessary to obtain convergence of the buckling loads. Similar to Sun [25], the buckling loads for the moderate elliptical cylinders were found to be much higher than those for the corresponding oval cylinders, especially for the unsymmetric laminate. This was due in part to the fact that the smallest curvature of an elliptical cross-section was significantly less than that of an oval cross-section with the same minor to major axis aspect ratio. Solutions beyond the limit point for initially imperfect oval and elliptical cylinders were obtained using the Rik's constant arc-length algorithm. It was found that the noncircular cylinders were less imperfection sensitive than circular ones, and that, for largely eccentric cross sections, the noncircular shells are insensitive to initial geometric imperfections.

Vibration

Lastly, several analyses of the vibration of noncircular cylinders can also be found in the literature. Although the results of these studies do not directly relate to the subject of this investigation, because the formulations for vibration of noncircular shells are related to those for buckling, and because a somewhat wider variety of cases has been investigated for vibration than for pressurization or axial compression, some of the more recent vibration studies are also mentioned here. In particular, Soldatos [30] has studied cross-ply oval cylinders using a Flügge-type theory, finding that Flügge-type and Donnell-type equations give nearly identical results for short cylinders with moderate oval eccentricity, the comparison becoming worse as the eccentricity and/or the length of the cylinder increases. Antisymmetric cross-ply oval shells were also investigated by Hui and Du [31], who included the effects of axial imperfections in a Donnell-type analysis. They concluded that imperfections on the order of the shell thickness may significantly raise or lower the fundamental frequency, depending upon the type of imperfection and the shell lay-up. Most recently, a study

of the free vibration of thick noncircular shells with a circumferentially varying thickness was performed by Suzuki and Leissa [32], showing that the inclusion of transverse shear deformations tends to lower the frequency of thick shells, while a parabolic thickness variation tends to raise them. For further discussion of vibration of noncircular shells, an excellent review of earlier work can be found in [33].

Experimental Work

Very few experimental results have been reported in the literature for noncircular cylinders for any type of loading, and no experimental results appear to be available for composite cylinders with noncircular cross-sections. Sewall and Pusey [34] have studied the vibrations of clamped-free thin aluminum cylinders of elliptical cross section. Yao and Jenkins [35], following the work of Slepov [36], made an extensive analytical and experimental investigation of buckling due to external pressure of simply-supported elliptical cylinders fashioned from PVC sheets. They found fairly good agreement between their Galerkin's method solution for the buckling load and the experimental results, providing that the cylinders were neither too short nor too thick. The analytically-predicted buckling modes, however, were not observed in most experiments. Kempner, et al. [37] compared the analysis of [13, 14], discussed above, with experimental results from David Taylor Model Basin on hydrostatically pressurized ring-reinforced oval cylindrical shells. Although the test specimens were pieced ovals with two different skin thicknesses, simple approximations in the analysis resulted in a favorable comparison of experimental and theoretical results. No experimental results appear to have been reported for internally pressurized noncircular cylinders.

Of greatest interest for this study are three experimental investigations of the buckling and postbuckling responses of oval and elliptical cylinders to axial compression. Each of these studies was prompted by the analytical results of Kempner and Chen [15, 16, 17], discussed above, which indicated that some noncircular cylinders might be relatively imperfection insensitive and might even support loads in excess of their classical buckling load. To accompany the analysis, discussed above, Hutchinson [19] also reported experimental results for axially compressed elliptical cylinders constructed of Mylar sheet formed around elliptical wooden end pieces. These results showed buckling occurred at loads as little as one-half of the classical buckling load (eqn. 2.2), presumably due to the imperfection sensitivity of the cylinders. However, the more severely elliptical cylinders (minor to major axis ratio of less than one-third) carried load in excess of the load at which buckles initially appeared and one cylinder reached a maximum postbuckling load which exceeded the classical buckling load by about 25%. Tennyson, Booton, and Caswell [22] investigated the buckling of elliptical cylinders using test cylinders manufactured from a liquid epoxy using a spin-casting process. These cylinders were spun-cast in circular form and then deformed to an elliptical shape by bonding each shell to machined aluminum end plates having the desired cross-sectional shape. For some of these cylinders, specific axial imperfections were introduced by cutting the axial imperfection into the inner

surface of the cylinder with a hydraulic tracer tool. Of course, this resulted in a thickness variation as well as a shape imperfection. For both the "perfect" and imperfect test specimens, buckling was characterized by a buckle pattern localized near the area of minimum curvature. The "perfect" cylinders buckled at loads within 10% of the "reduced classical load," obtained by taking into account an assumed 10% reduction in the classical buckling load due to the clamped boundary conditions. Significant imperfection sensitivity was observed, confirming Hutchinson's results. The agreement between the analysis, discussed above, and the test results was quite good. It was also observed that for the more severely elliptical cylinders, maximum compressive loads exceeded the initial buckling loads, but not by the large degree predicted by Kempner and Chen [20].

Lastly, a very careful study was performed by Feinstein, Erikson, and Kempner [38], who fabricated a series of oval cylinders by wrapping and heat treating sheets of Mylar over mandrels of the desired geometry. The cylinders produced in this manner retained their shape when removed from the mandrels and thus lacked the large initial stresses which would be expected in the test specimens of the previously cited studies. The cylinders were fitted to end fixtures which had grooves machined to be very close fitting to the inside of the cylinders. The outside was anchored to the fixture using a low-melting-point metal alloy. These fixtures were attached to the testing machine in such a way that minute adjustments in alignment could be made to obtain a state as close as possible to perfectly symmetric loading. They found that as the eccentricity of the oval cross-section became more extreme, the increase in the maximum postbuckling load greatly increased. For the cylinder with minor to major aspect ratio of 0.5, this maximum postbuckling load was as large as 5 times the initial buckling load. Even moderate ovals (aspect ratio of 0.7) could, after an initial drop in load after buckling, carry loads appreciably in excess of the initial buckling load. For all of the oval cylinders, the initial buckles occurred in the region of the minimum curvature, resulting in a relatively small drop in load, after which the load again increased until the maximum load was reached, at which point the buckles propagated completely through the regions of maximum curvature and a large drop in load occurred, resulting in a collapse as catastrophic as that for a circular cylinder. These results showed excellent agreement with the analysis given in [20].

None of the studies cited above have examined the nonlinear prebuckling response of composite cylinders with noncircular cross-sections, nor do there appear to be any investigations of the effects of internal pressure or combined pressure and axial compression on such cylinders. No experimental results exist for the response of composite elliptical cylinders for any load case. These facts represent the genesis for the current work, which is described beginning in the next chapter.

Chapter 3.0 Description of Problem and Solution Approach

In this chapter a description of the problem, including a basic description of surface theory, and a general discussion of the approaches to the various solutions is given. The nomenclature to be used in the following chapters is also introduced.

Description of Problem

Consider a cylinder of constant thickness H and axial length L. The cross sectional shape of the reference surface, which will be taken here to be the middle surface of the cylinder, is an ellipse lying in the y-z plane and described by

$$\frac{y^2}{a^2} + \frac{z^2}{b^2} = 1, \tag{3.1}$$

where a and b are the semi-major and semi-minor axes of the ellipse, respectively. The degree of a given cylinder's ellipticity will be described in terms of the ratio of these axes, b/a. The cylinders under consideration here, illustrated in Figure 3-1, are symmetrically laminated and have semi-minor to semi-

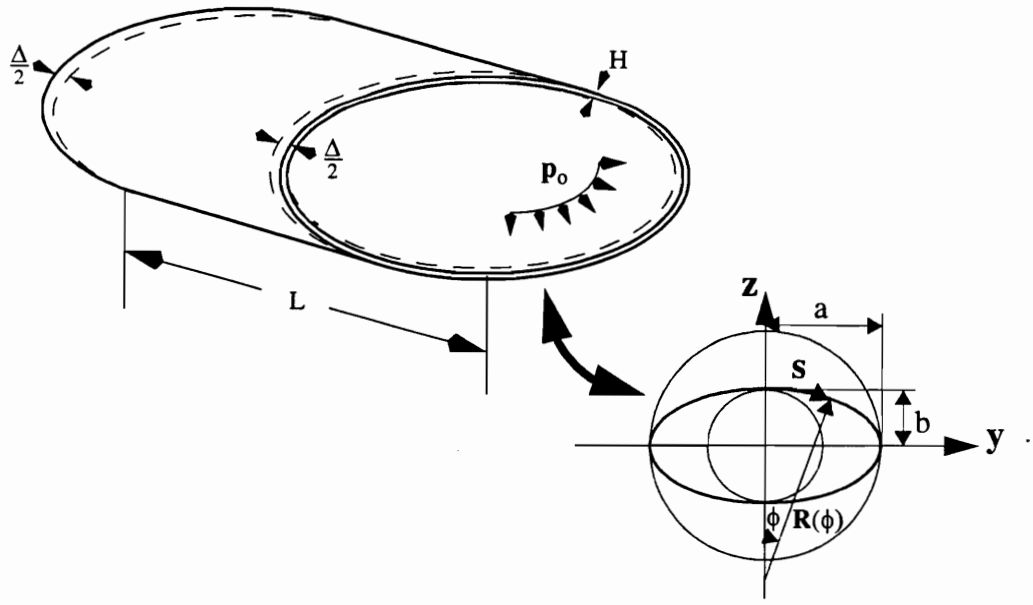

Figure 3-1 Description of Problem.

major axis ratios of $0.70 \leq b/a \leq 1.00$. Only thin cylinders are studied. In the laminate nomenclature the orientation of the layers is defined relative to the +x axis. These cylinders are subject to clamped-clamped boundary conditions. Explicitly stated, these boundary conditions are:

$$\text{at } x = \pm L/2:$$

$$\begin{aligned} &\text{i)} \quad u^o = \mp\frac{\Delta}{2} \\ &\text{ii)} \quad v^o = 0 \\ &\text{iii)} \quad w^o = 0 \\ &\text{iv)} \quad \beta_x^o = 0 \end{aligned} \tag{3.2}$$

The topics of specific interest are:

1. Response due to low internal pressure.
2. Response due to low levels of combined internal pressure and axial compression.
3. Geometrically nonlinear prebuckling response due to axial compression.
4. Buckling and postbuckling response due to axial compression.

Also of interest in this study is the degree of influence that initial shape imperfections have upon elliptical cylinders, as compared to circular cylinders, for the types of loading listed above.

Surface Theory

A thin shell can be described in terms of its reference surface, thus some basic information relating to theory of surfaces is necessary in order to further describe the problem at hand. What is presented here is by no means a detailed discussion of this topic. More useful information can be found in numerous texts dealing with differential geometry, theory of surfaces, and shell theory [6, 39, 40].

As stated above, the type of cylinder to be studied here can be described in terms of its reference surface. A cylindrical shell can be generated by a straight line, called a generator, moving parallel to itself along a curve called a profile. The cylinder is named by the shape of the profile, e. g., a circular or elliptical cylinder. The generators and profiles provide a natural set of coordinate lines. The generators lie parallel to the axis of the cylinder. The circumferential coordinate is measured along the profiles, and may be defined by either ϕ or s, where s is the arc length, such that

$$ds = R(\phi)\, d\phi, \tag{3.3}$$

where $R(\phi)$ is the radius of curvature and ϕ is the angle which the radius of curvature makes with the vertical plane, as illustrated in Figure 3-1. Based upon this definition of ϕ and eqn. 3.1, the parametric equations of the reference surface of an elliptical cylinder can be written in terms of x and ϕ as

$$
\begin{aligned}
x &= x \\
y &= \frac{a^2 \sin\phi}{\sqrt{a^2 \sin^2\phi + b^2 \cos^2\phi}} \\
z &= \frac{b^2 \cos\phi}{\sqrt{a^2 \sin^2\phi + b^2 \cos^2\phi}}
\end{aligned}
\tag{3.4}
$$

Clearly these equations provide a mapping between the two-dimensional surface described in terms of surface coordinates $\{x, \phi\}$ and three-dimensional Cartesian space $\{x, y, z\}$. Because every surface described by a rectangular coordinate system, $\{x_1, x_2, x_3\}$, may be defined in terms of two parameters, ξ_1 and ξ_2, assign:

$$
\begin{aligned}
x_1 &= x \\
x_2 &= y \qquad \text{and} \qquad \xi_1 = x \\
x_3 &= z \qquad\qquad\quad \xi_2 = \phi
\end{aligned}
\tag{3.5}
$$

For convenience of notation, in what follows, the convention will be used that English subscripts run from 1 through 3 and Greek subscripts run 1 to 2.

Using the relations given above, let the equation of the undeformed surface be written in terms of the radius vector

$$
\hat{r} = \hat{r}(\xi_\alpha) = x_i(\xi_\alpha)\,\hat{e}_i, \tag{3.6}
$$

where $\hat{e}_i$ are the unit vectors of the Cartesian coordinate system. This vector represents the distance between the origin and a given point on the surface. Given two points $\{\xi_1, \xi_2\}$ and $\{\xi_1+d\xi_1, \xi_2+d\xi_2\}$, arbitrarily near to each other on the reference surface, the increment of the radius vector moving from the first point to the second point is

$$
d\hat{r} = \hat{r}_{,\alpha}\, d\xi_\alpha, \tag{3.7}
$$

where $,_{(\,)}$ denotes differentiation with respect to the variable ( ). Thus the differential arc length on the surface is

$$
d\hat{r} \cdot d\hat{r} = ds^2 = \hat{r}_{,\alpha}\, \hat{r}_{,\beta}\, d\xi_\alpha d\xi_\beta \,. \tag{3.8}
$$

Now the $\hat{r}_{,\alpha}$ represent tangents to the coordinate lines of the surface and the magnitudes of these vectors are denoted by

$$\left\| \vec{r}_{,\alpha} \right\| = A_\alpha . \tag{3.9}$$

Equation 3.8 can therefore be written as

$$ds^2 = A_1^2 d\xi_1^2 + 2A_1 A_2 \cos\chi d\xi_1 d\xi_2 + A_2^2 d\xi_2^2 \tag{3.10}$$

where χ is the angle between the coordinate lines. This is the "first fundamental form" of the surface and the A_α are known as the Lamé coefficients. The system described by eqn. 3.4 is orthogonal so that $\cos\chi = 0$ and eqn. 3.10 reduces to

$$ds^2 = A_\alpha^2 d\xi_\alpha^2 . \tag{3.11}$$

Further, using eqn. 3.4, for this elliptical cylindrical surface

$$A_1 = 1$$

$$A_2 = \frac{a^2 b^2}{\left(a^2 \sin^2\phi + b^2 \cos^2\phi\right)^{3/2}} . \tag{3.12}$$

Define also from eqn. 3.9 the unit vectors tangent to the coordinate lines:

$$\hat{t}_\alpha = \frac{\vec{r}_{,\alpha}}{A_\alpha} \tag{3.13}$$

and the unit vector normal to the surface by

$$\hat{t}_1 \times \hat{t}_2 = \hat{n} . \tag{3.14}$$

These equations, however, do not completely define the surface by themselves. The problem remains to find the curvature of a curve lying in the surface. Let $\vec{r} = \vec{r}(s)$, where s is the arc length from a certain origin, be the vectorial equation of a curve on the surface. Denoting by τ the unit vector along the tangent to $\vec{r}(s)$, then

$$\bar{\tau} = \frac{d\vec{r}}{ds} = \vec{r}_{,\alpha} \frac{d\xi_\alpha}{ds} . \tag{3.15}$$

According to Frenet's formula (see ref. 6), the derivative of this vector is

$$\frac{d\bar{\tau}}{ds} = \frac{d^2\vec{r}}{ds^2} = \frac{\hat{N}}{\rho} . \tag{3.16}$$

where $1/\rho$ is the curvature of the curve and $\hat{N}$ is the unit vector of the principal normal to the curve. Substituting eqn. 3.15 into eqn. 3.16 results in the expression

$$\frac{\hat{N}}{\rho} = \dot{r}_{,\alpha\beta}\frac{d\xi_\alpha}{ds}\frac{d\xi_\beta}{ds} + \hat{r}_{,\alpha}\frac{d^2\xi_\alpha}{ds^2}. \tag{3.17}$$

Multiplying through by the unit normal to the surface, one obtains:

$$\frac{\cos\varphi}{\rho} = (\hat{n}\cdot\dot{r}_{,\alpha\beta})\frac{d\xi_\alpha}{ds}\frac{d\xi_\beta}{ds} = L_{\alpha\beta}d\xi_\alpha d\xi_\beta, \tag{3.18}$$

where φ is the angle between the normal to the surface, $\hat{n}$, and the principal normal to the curve, $\hat{N}$. Now the expression $L_{\alpha\beta}d\xi_\alpha d\xi_\beta$ is called the "second fundamental form" of the surface and is related to the curvature of a curve on the surface. From eqn. 3.18 it is possible to obtain the normal curvatures of the surface. In this case, $\hat{n}$ and $\hat{N}$ are either parallel, $\varphi = 0$, or have opposite directions, $\varphi = \pi$. If one takes the outer normal of the curve as the positive normal to the surface, $\varphi = \pi$ results and the normal curvature is, using eqn. 3.10,

$$-\frac{1}{R} = \frac{L_{\alpha\beta}d\xi_\alpha d\xi_\beta}{A_\gamma^2 d\xi_\gamma^2}. \tag{3.19}$$

Considering first $d\xi_1$ = constant and then $d\xi_2$ = constant in eqn. 3.19, one obtains normal curvatures of the surfaces in the ξ_1 and ξ_2 directions, respectively, as

$$\frac{1}{R_1} = \frac{-L_{11}}{A_1^2}; \qquad \frac{1}{R_2} = \frac{-L_{22}}{A_2^2} \tag{3.20}$$

and

$$\frac{1}{R_{12}} = \frac{L_{12}}{A_1 A_2} \tag{3.21}$$

defines the twist of the surface. For the case considered here, defined by eqn. 3.4, $L_{12} = 0$ and hence there is no twist curvature. Further, for this particular case

$$\frac{1}{R_1} = 0; \qquad \frac{1}{R_2} = \frac{a^2 b^2}{\left(a^2\sin^2\phi + b^2\cos^2\phi\right)^{3/2}} = \frac{1}{R(\phi)}. \tag{3.22}$$

Based on this definition of $1/R(\phi)$, it is possible to find the maximum and minimum radius of an elliptical cylinder as:

$$R_{max} = R(0) = \frac{a^2}{b}$$
$$R_{min} = R\left(\frac{\pi}{2}\right) = \frac{b^2}{a} \tag{3.23}$$

At this point, note that a necessary and sufficient condition for ξ_α to be the principal coordinates is that

$$\cos\chi = 0$$
$$L_{12} = 0 \tag{3.24}$$

Therefore $\{x,\phi\}$ of eqn. 3.4 are the principal coordinates and eqn. 3.22 represents the principal curvatures of the surface. Note also that $A_2 = 1/R_2 = 1/R(\phi)$, which, as will become apparent in the next section, is a convenient result of the form of the elliptical coordinates chosen here.

Nonlinear Kinematic Shell Equations for Elliptical Cylinders

The nonlinear strain-displacement relations used in this study to describe the deformation of an elliptical cylinder are the relations of Mushtari-Donnell-Vlasov classical thin shell theory. These equations represent the greatest simplification of nonmembrane shell theory. A discussion of the appropriateness of this theory for the problem of a cylinder of continuously varying curvature can be found in [19, 41].

In moving from the reference surface coordinates, define the position vector to an arbitrary point within the shell as

$$\vec{R} = \vec{r} + \xi_3 \hat{n}, \tag{3.25}$$

where $\vec{r}$ is the position vector to a point on the reference surface and ξ_3 is the coordinate measured from the reference surface through the thickness along the normal, $\hat{n}$. This relation can be used to calculate the Lamé coefficients for the shell itself. It is assumed, however, that the shell wall is thin by comparison to the minimum radius of curvature, so that $\xi_3/R(\phi)$ terms can be neglected in comparison to unity. By employing this assumption, the shell Lamé coefficients reduce to those for the reference surface.

It should be noted that the form of eqn. 3.24 implies that for an elliptical cylinder composed of constant thickness layers, only the reference surface will actually describe an ellipse as defined by eqn. 3.1. All other locations within the shell described by ξ_3 = constant other than 0 deviate from being true ellipses by an error on the order of the value of ξ_3.

Define now a displacement vector between the deformed and undeformed shell by

$$\vec{\Delta} = u_\alpha \hat{t}_\alpha + w\hat{n}. \tag{3.26}$$

Using Love's assumptions for first-order shell theories, the displacements at any point on the shell wall can be approximated by

$$\begin{aligned} u_\alpha(\xi_\gamma, \xi_3) &= u_\alpha^o(\xi_\gamma) + \xi_3 \beta_\alpha^o(\xi_\gamma) \\ w(\xi_\gamma, \xi_3) &= w^o(\xi_\gamma), \end{aligned} \tag{3.27}$$

where the $u_\alpha{}^o$ are the displacements of the shell reference surface in the ξ_α direction, w is the displacement along the normal to reference surface, and the $\beta_\alpha{}^o$ are the midsurface rotations. Using these quantities, the well-known kinematic relations for Mushtari-Donnell-Vlasov shell theory (see ref. 41) are given by

$$\begin{aligned} \varepsilon_\alpha(\xi_\beta, \xi_3) &= \varepsilon_\alpha^o(\xi_\beta) + \xi_3 \kappa_\alpha^o(\xi_\beta) \\ \gamma_{12}(\xi_\beta, \xi_3) &= \gamma_{12}^o(\xi_\beta) + \xi_3 \kappa_{12}^o(\xi_\beta) \end{aligned} \tag{3.28}$$

where

$$\begin{aligned} \varepsilon_1^o(\xi_1, \xi_2) &= \frac{1}{A_1}\left(\frac{\partial u_1^o}{\partial \xi_1}\right) + \frac{u_2^o}{A_1 A_2}\frac{\partial A_1}{\partial \xi_2} + \frac{w^o}{R_1} + \frac{1}{2}\left(\beta_1^o\right)^2 \\ \varepsilon_2^o(\xi_1, \xi_2) &= \frac{1}{A_2}\left(\frac{\partial u_2^o}{\partial \xi_2}\right) + \frac{u_1^o}{A_1 A_2}\frac{\partial A_2}{\partial \xi_1} + \frac{w^o}{R_2} + \frac{1}{2}\left(\beta_2^o\right)^2 \\ \gamma_{12}^o(\xi_1, \xi_2) &= \frac{A_1}{A_2}\frac{\partial}{\partial \xi_2}\left(\frac{u_1^o}{A_1}\right) + \frac{A_2}{A_1}\frac{\partial}{\partial \xi_1}\left(\frac{u_2^o}{A_2}\right) + \beta_1^o \beta_2^o \\ \kappa_1^o(\xi_1, \xi_2) &= \frac{1}{A_1}\left(\frac{\partial \beta_1^o}{\partial \xi_1}\right) + \frac{\beta_2^o}{A_1 A_2}\frac{\partial A_1}{\partial \xi_2} \\ \kappa_2^o(\xi_1, \xi_2) &= \frac{1}{A_2}\left(\frac{\partial \beta_2^o}{\partial \xi_2}\right) + \frac{\beta_1^o}{A_1 A_2}\frac{\partial A_2}{\partial \xi_1} \\ \kappa_{12}^o(\xi_1, \xi_2) &= \frac{A_1}{A_2}\frac{\partial}{\partial \xi_2}\left(\frac{\beta_1^o}{A_1}\right) + \frac{A_2}{A_1}\frac{\partial}{\partial \xi_1}\left(\frac{\beta_2^o}{A_2}\right) \end{aligned} \tag{3.29}$$

and

$$\beta_1^o = -\frac{1}{A_1}\left(\frac{\partial w^o}{\partial \xi_1}\right) \qquad \text{and} \qquad \beta_2^o = -\frac{1}{A_2}\left(\frac{\partial w^o}{\partial \xi_2}\right). \tag{3.30}$$

Substituting eqns. 3.12 and 3.22 into the above equations, and using relations 3.5, results in a set of kinematic equations resembling those for a circular cylinder in all respects, except that the radius of curvature is everywhere a function of the circumferential coordinate rather than a constant. These equations can be further simplified by employing eqn. 3.3 so that

$$\frac{1}{R(\phi)}\frac{\partial}{\partial\phi} \rightarrow \frac{\partial}{\partial s}. \tag{3.31}$$

Then, using also $u_1^o = u^o$ and $u_2^o = v^o$, eqns. 3.29 and 3.30 for an elliptical cylinder can be written in the convenient form

$$\begin{aligned}
\varepsilon_x^o &= \frac{\partial u^o}{\partial x} + \frac{1}{2}\left(\beta_x^o\right)^2 \\
\varepsilon_s^o &= \frac{\partial v^o}{\partial s} + \frac{w^o}{R(s)} + \frac{1}{2}\left(\beta_s^o\right)^2 \\
\gamma_{xs}^o &= \frac{\partial u^o}{\partial s} + \frac{\partial v^o}{\partial x} + \beta_x^o\beta_s^o \\
\kappa_x^o &= \frac{\partial \beta_x^o}{\partial x} \\
\kappa_s^o &= \frac{\partial \beta_s^o}{\partial s} \\
\kappa_{xs}^o &= \frac{\partial \beta_s^o}{\partial x} + \frac{\partial \beta_x^o}{\partial s}
\end{aligned} \tag{3.32}$$

and

$$\beta_x^o = -\frac{\partial w^o}{\partial x} \qquad \text{and} \qquad \beta_s^o = -\frac{\partial w^o}{\partial s}. \tag{3.33}$$

Solution Approach

Two approaches are used here to study the response of elliptical cylinders to internal pressure and axial compression loading. The first is based on a semi-analytical approach and is used to study in detail the prebuckling response of perfect cylinders. The formulation and method of solution developed for this approach are given in detail in the following discussion. In order to also study the effects of imperfections on prebuckling response, the STAGS [43] finite element program was used to accurately model imperfections measured from the experimental specimens. This finite element analysis was also used to study the buckling

and postbuckling responses of the cylinders. The STAGS finite element code and its application are discussed below in general terms. A detailed description of the initial shape imperfection measurements and their use in the finite element code are given in Appendix A.

Prebuckling Response of Perfect Cylinders with Elliptical Cross Section

The fact that the radius of curvature of the cylinder varies circumferentially presents a problem in finding closed-form solutions to the problem. This necessitates use of an approximate solution, the key to which is finding good approximate representations for the variation of the radius and the primary variables. In this study the primary variables are the components of displacement. The displacement approach is chosen to allow for a more realistic representation of the clamped boundary conditions used in the experiments. This is opposed to using the stress formulation approach wherein boundary information regarding displacements are more complicated to enforce.

Here the radius is expanded in a cosine series using the method suggested by Marguerre [9]:

$$\frac{1}{R(s)} = \sum_{i=0}^{I} a_{4i} \cos(4i\pi s/C); \tag{3.34}$$

where s is the circumferential coordinate, C is the circumferential length, and I is the number of terms in the series. The a_{4i} are known constants. While elliptical cross sections are studied here, it should be noted that such an expansion will accommodate any cross section with at least two axes of symmetry, for example, many oval cross sections. The displacements are likewise expanded in a harmonic series using the Kantorovich method. Based on the expansion for the radius of curvature, the forms of these series are taken to be

$$\begin{aligned}
u^0(x,s) &= u_0^0(x) + \sum_{n=1}^{N} u_n^0(x) \cos(4n\pi s/C) + \sum_{m=1}^{M} u_m^0(x) \sin(4m\pi s/C); \\
v^0(x,s) &= v_0^0(x) + \sum_{m=1}^{M} v_m^0(x) \cos(4m\pi s/C) + \sum_{n=1}^{N} v_n^0(x) \sin(4n\pi s/C); \\
w^0(x,s) &= w_0^0(x) + \sum_{n=1}^{N} w_n^0(x) \cos(4n\pi s/C) + \sum_{m=1}^{M} w_m^0(x) \sin(4m\pi s/C),
\end{aligned} \tag{3.35}$$

where M and N are the maximum number of terms in the given series.

Now the total potential energy, including the work done by internal pressure, p_o, is given by

$$\pi = \frac{1}{2}\int\int\int [\sigma_x \varepsilon_x + \sigma_s \varepsilon_s + \tau_{xs}\gamma_{xs}]\, dx ds d\xi_3 - \int\int p_o w^o dx ds. \tag{3.36}$$

For a laminated cylinder, each ply of the laminate is assumed to be in a state of plane stress, so that the stresses in the k'th ply of the laminate can be described by Hooke's Law as

$$\begin{bmatrix} \sigma_x \\ \sigma_s \\ \tau_{xs} \end{bmatrix}^{(k)} = \begin{bmatrix} \bar{Q}_{11} & \bar{Q}_{12} & \bar{Q}_{16} \\ \bar{Q}_{12} & \bar{Q}_{22} & \bar{Q}_{26} \\ \bar{Q}_{16} & \bar{Q}_{26} & \bar{Q}_{66} \end{bmatrix}^{(k)} \begin{bmatrix} \varepsilon_x \\ \varepsilon_s \\ \gamma_{xs} \end{bmatrix} \tag{3.37}$$

where the $\overline{Q}_{ij}$'s are the transformed reduced ply stiffnesses of the k'th ply [42, 44].

After integrating eqn. 3.36 through the thickness, the expression for the total potential energy becomes

$$\begin{aligned} \pi &= \frac{1}{2}\int\int\left[N_x \varepsilon_x^o + N_s \varepsilon_s^o + N_{xs}\gamma_{xs}^o + M_x \kappa_x^o + M_s \kappa_s^o + M_{xs}\kappa_{xs}^o - p_o w^o\right] dx ds \\ &= \int\int [U(x, s)]\, dx ds, \end{aligned} \tag{3.38}$$

where the stress resultants for a symmetrically-laminated shell, using the kinematic relations given by eqn. 3.32 and the Hooke's Law equations in eqn. 3.37, are given by:

$$\begin{aligned} N_x &= \int \sigma_x d\xi_3 = A_{11}\varepsilon_x^o + A_{12}\varepsilon_s^o + A_{16}\gamma_{xs}^o \\ N_s &= \int \sigma_s d\xi_3 = A_{12}\varepsilon_x^o + A_{22}\varepsilon_s^o + A_{26}\gamma_{xs}^o \\ N_{xs} &= \int \sigma_{xs} d\xi_3 = A_{16}\varepsilon_x^o + A_{26}\varepsilon_s^o + A_{66}\gamma_{xs}^o \\ M_x &= \int \sigma_x \xi_3 d\xi_3 = D_{11}\kappa_x^o + D_{12}\kappa_s^o + D_{16}\kappa_{xs}^o \\ M_s &= \int \sigma_s \xi_3 d\xi_3 = D_{12}\kappa_x^o + D_{22}\kappa_s^o + D_{26}\kappa_{xs}^o \\ M_{xs} &= \int \sigma_{xs} \xi_3 d\xi_3 = D_{16}\kappa_x^o + D_{26}\kappa_s^o + D_{66}\kappa_{xs}^o, \end{aligned} \tag{3.39}$$

and the strains and curvatures in the above expressions are defined in terms of the displacements by eqns. 3.32-3.33. By substituting eqns. 3.32-3.33 into eqns. 3.38 and 3.39, the total potential energy can be written entirely in terms of the reference surface displacements. This is then integrated explicitly over the circumferential coordinate after substituting in the assumed forms of displacements, given in eqn. 3.35, resulting in an energy expression dependent only on the axial coordinate. Symbolically, these steps can be written as:

$$\pi = \int_{-\frac{L}{2}}^{\frac{L}{2}} \left[\int_0^C \{U(x,s)\}\, ds \right] dx$$
$$= \int_{-\frac{L}{2}}^{\frac{L}{2}} F(x, y_i, y'_i, y''_i) dx; \qquad i = 1, 3(N+M+1), \tag{3.40}$$

where the y_i represent the functional coefficients of the expressions in eqn. 3.35, and ( )' represents differentiation with respect to the axial coordinate.

The variational process then yields the governing Euler-Lagrange equations for the $y_i(x)$ and associated boundary conditions in the axial, x, direction. The form of these equations is given by [45]:

$$\frac{d^2}{dx^2}\left(\frac{\partial F}{\partial y_i''}\right) - \frac{d}{dx}\left(\frac{\partial F}{\partial y_i'}\right) + \frac{\partial F}{\partial y_i} = 0 \tag{3.41}$$

with boundary conditions:

$$\begin{aligned} &y_i' \text{ specified} \quad \text{or} \quad \frac{\partial F}{\partial y_i''} = 0 \\ &y_i \text{ specified} \quad \text{or} \quad \frac{d}{dx}\left(\frac{\partial F}{\partial y_i''}\right) - \frac{\partial F}{\partial y_i'} = 0 \end{aligned} \tag{3.42}$$

Defining intermediate variables in order to obtain first-order form, it is possible to obtain a set of nonlinear, coupled, first-order ordinary differential equations of the form

$$\bar{y}_i'(x) = f_i(\bar{y}_j(x)); \qquad i, j = 1, 8(N+M+1), \tag{3.43}$$

where

$$\bar{y}_i(x) = \{u_k^o, v_k^o, w_k^o, q_k, r_k, t_k, g_k, h_k\}; \qquad k = 1, (N+M+1), \tag{3.44}$$

and

$$q_k = \frac{dw_k^o}{dx}; \quad r_k = \frac{dq_k}{dx}; \quad t_k = \frac{dr_k}{dx}; \quad g_k = \frac{du_k^o}{dx}; \quad h_k = \frac{dv_k^o}{dx}. \tag{3.45}$$

This process has been automated using the symbolic manipulation package *Mathematica*© [46]. The resulting coupled nonlinear ordinary differential equations in x of the first-order form are written into FORTRAN code using the FORTRANASSIGN package within *Mathematica*©. These equations are integrated

via the finite-difference method using the IMSL subroutine DBVPFD [47] which is based on a variable order, variable step, finite difference algorithm using Newton's method.

STAGS Finite Element Analysis

The STAGS finite element program was used to predict the nonlinear prebuckling responses, as well as the buckling end-displacements and loads of cylinders with initial geometric imperfections. Among its features are extensive nonlinear and bifurcation buckling capabilities and the option of providing user-written subroutines which can be used to define the geometry of a shell and to accurately include initial geometric imperfections from measured data.

The finite element models for each of the cylinders consisted of a uniform mesh of 51 axial by 97 circumferential grid points. The element used in these models is the STAGS 410 element, a four-node quadrilateral element. It employs the nonlinear Lagrangian strain tensor and can accommodate large rotations by the use of a corotational algorithm. While other, newer and more computationally expensive elements are available, the 410 element provides an effective and efficient building block for the description of nonlinear thin-shell response and its behavior is well understood. The finite element model for the cylinder with b/a = 0.70 cross sectional aspect ratio is shown in Figure 3-2.

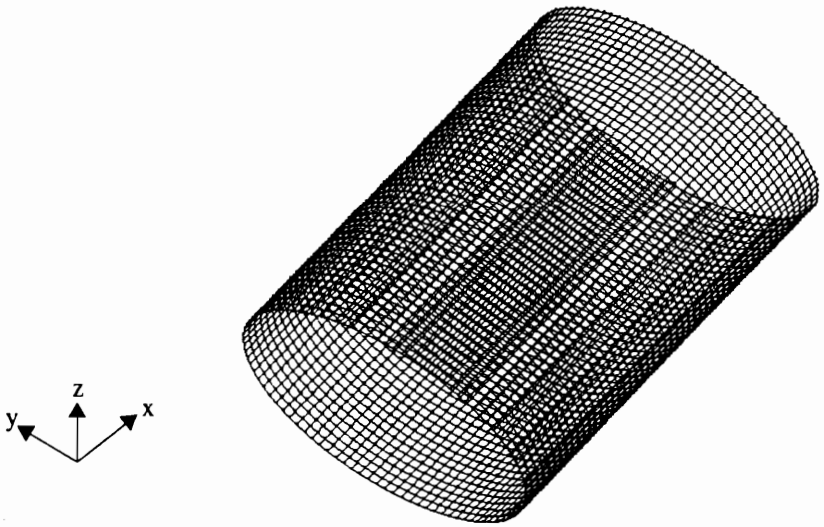

Figure 3-2 STAGS Finite Element Model for Cylinder withb/a = 0.70.

For internal pressure loads, STAGS provides a "live" pressure load option for which pressure remains normal to the shell surface throughout deformation. For combined loading, it is possible to define two load systems at the same time which can be controlled separately throughout the solution process. For the axial

compression problem, STAGS can provide solutions to the generalized eigenvalue for buckling relative to either a linear or nonlinear prebuckling state. However, the best approach is to conduct a nonlinear collapse analysis [48]. Prebuckling solutions are obtained for incrementally increasing values of the load parameter using the nonlinear option which is based on Newton's Method. The presence of a limit point or a bifurcation point is indicated by one or more negative roots in the tangent stiffness matrix.

Geometric imperfections are defined in the finite element model by specifying discrete nodal displacements representing perturbations relative to the ideal geometry. The ideal shape is obtained from a best fit of the surface measurements of the test specimens, and imperfections are calculated from deviations in the data from this ideal shape. The imperfection measurement data are then reduced to obtain coefficients of a double Fourier series representation of these data and this series used directly in the STAGS analysis. This procedure is discussed in more detail in Appendix A.

Chapter 4.0 Numerical Results

Numerical results are given in this chapter to illustrate the behavior of elliptical composite cylinders to internal pressure and to axial compression in the prebuckling range of loading. These results are presented for a cylinder with the most severely elliptical cross-section, b/a = 0.70, considered in this study and a lay-up of $(+45_2/-45_2)_s$. Although this laminate was not produced for the experimental phase of the study, it is used here in order to demonstrate the ability of the analysis to capture the effects of large D_{16} and D_{26}. Material properties for Hercules AS4/3501-6 are used as input for these results. These properties are [49]:

$$\begin{aligned} E_1 &= 18.85 \text{ Msi } (130 \text{ GPa}); \qquad E_2 = 1.407 \text{ Msi } (9.7 \text{ GPa}); \\ G_{12} &= 0.725 \text{ Msi } (5.0 \text{ GPa}); \qquad \nu_{12} = 0.30; \qquad h = 0.0055 \text{ in } (0.140 \text{ mm}) \end{aligned} \tag{4.1}$$

In the following, axial loads will be given as a percentage of the classical buckling load. The method for obtaining the classical buckling load for an elliptical cylinder was given in eqn. 2.2. Specializing this result for laminated cylinders, the classical buckling load and associated end-shortening are given by

$$\begin{aligned} P_{cr}^{ellipse} &= \sigma_{cr}^{ellipse} \times C \times H = \frac{2}{R_{max}} \sqrt{E_s H D_{11}} \\ \Delta_{cr}^{ellipse} &= \frac{P_{cr}^{ellipse} L}{E_x C H}, \end{aligned} \tag{4.2}$$

where

$$\begin{aligned} E_x &= \frac{A_{11}A_{22} - A_{12}^2}{A_{22} H} \\ E_s &= \frac{A_{11}A_{22} - A_{12}^2}{A_{11} H}. \end{aligned} \tag{4.3}$$

Convergence of Solution

The convergence of the Fourier series given in eqn. 3.34 for 1/R(s) is shown in Figure 4-1 for an ellipse with major axis, a = 5 in. (127 mm) and minor axis, b = 0.70a, the most severe ellipticity considered in the present study. In this figure, the difference between the exact solution for 1/R(s) and the approximate solution, normalized by the exact solution, is plotted as a function of the circumferential coordinate s,

normalized by the circumferential length, C (see Figure 3-1). As can be seen from this figure, 4 terms (I=3) in this series provides convergence within ±2.5% of the exact solution, and 7 terms (I=6) results in less than ±.05% error.

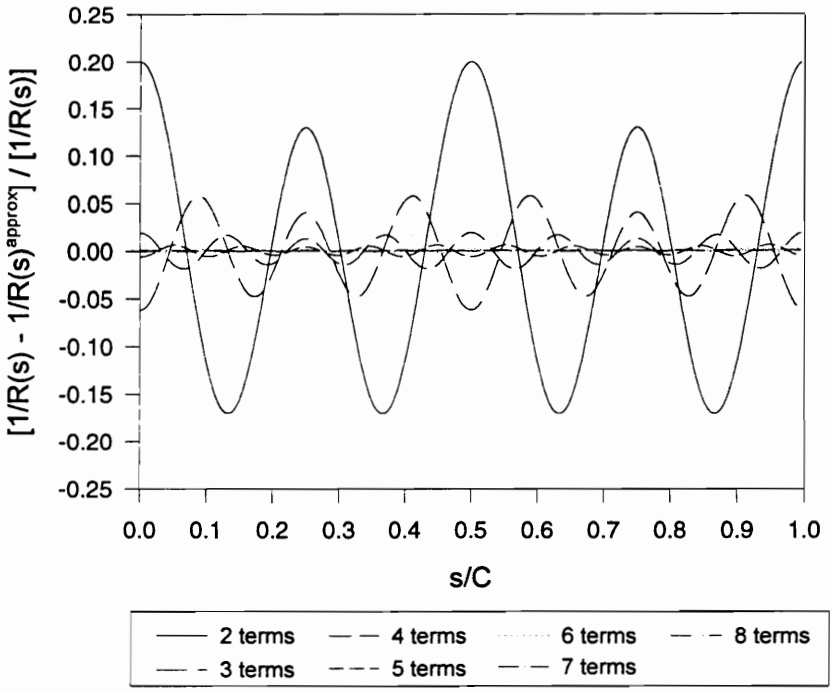

Figure 4-1 Convergence of the Series for Radius of Curvature.

Recognizing that the cosine terms will dominate the response for the axial and radial displacement, and the sine terms for circumferential displacement, if N=7 and M=4 are used for the series expansions of the displacements, then based on eqn. 3.35, these functions will be:

$$\begin{aligned} u(x,s) &= u_0(x) + u_1(x)\cos(4\pi s/C) + u_2(x)\cos(8\pi s/C) + u_3(x)\cos(12\pi s/C) + u_4(x)\cos(16\pi s/C) + \\ &\quad u_5(x)\cos(20\pi s/C) + u_6(x)\cos(24\pi s/C) + u_7(x)\cos(28\pi s/C) + \\ &\quad u_8(x)\sin(4\pi s/C) + u_9(x)\sin(8\pi s/C) + u_{10}(x)\sin(12\pi s/C) + u_{11}(x)\sin(16\pi s/C), \end{aligned}$$

$$\begin{aligned} v(x,s) &= v_0(x) + v_1(x)\cos(4\pi s/C) + v_2(x)\cos(8\pi s/C) + v_3(x)\cos(12\pi s/C) + v_4(x)\cos(16\pi s/C) + \\ &\quad v_5(x)\sin(4\pi s/C) + v_6(x)\sin(8\pi s/C) + v_7(x)\sin(12\pi s/C) + \\ &\quad v_8(x)\sin(16\pi s/C) + v_9(x)\sin(20\pi s/C) + v_{10}(x)\sin(24\pi s/C) + v_{11}(x)\sin(28\pi s/C), \end{aligned} \tag{4.4}$$

$$\begin{aligned} w(x,s) &= w_0(x) + w_1(x)\cos(4\pi s/C) + w_2(x)\cos(8\pi s/C) + w_3(x)\cos(12\pi s/C) + w_4(x)\cos(16\pi s/C) + \\ &\quad w_5(x)\cos(20\pi s/C) + w_6(x)\cos(24\pi s/C) + w_7(x)\cos(28\pi s/C) + \\ &\quad w_8(x)\sin(4\pi s/C) + w_9(x)\sin(8\pi s/C) + w_{10}(x)\sin(12\pi s/C) + w_{11}(x)\sin(16\pi s/C). \end{aligned}$$

In Figure 4-2 and Figure 4-3 the coefficient functions $w_0(x)$, $w_1(x)$,...$w_{11}(x)$, normalized by the laminate thickness, are plotted versus the normalized axial coordinate for a $(+45_2/-45_2)_s$ clamped cylinder with elliptical cross section characterized by b/a = 0.70. These results are given in Figure 4-2 for the cylinder loaded by one atmosphere internal pressure with the ends restrained against axial displacement, and in Figure 4-3 for uniform axial end displacement to 90% of the classical buckling value, eqn. 4.2. The cylinder is of length L, where $L/R_{max} = 1.75$, and the origin of the axial coordinate is at midspan. The maximum radius of curvature of the cross section, R_{max}, occurs at the end of the semi-minor axis, i.e., at s/C = 0. The first term, $w_0(x)$, represents the response of an 'equivalent circular cylinder', that is, a circular cylinder with radius such that the cylinder has the same circumferential length as the elliptical cylinder, i. e., $R_0 = C/2\pi$. The addition of the other terms can then be thought of as corrections to this circular cylinder response. That the series given in eqn. 4.4 is reasonably well converged can be seen in that $w_7(x)$ and $w_{11}(x)$ show negligible variation from zero. It can also be seen that the coefficient functions of cosine terms dominate the response, while the coefficient functions of sine terms add only small corrections. Note, however, that the coefficients of sine terms are anti-symmetric about the centerline of the cylinder. This is more readily apparent in Figure 4-3 for the case of axial end-shortening, but also exists in a small degree for the case of internal pressure. It is these terms which allow the analysis to account for any skewing in the deformed

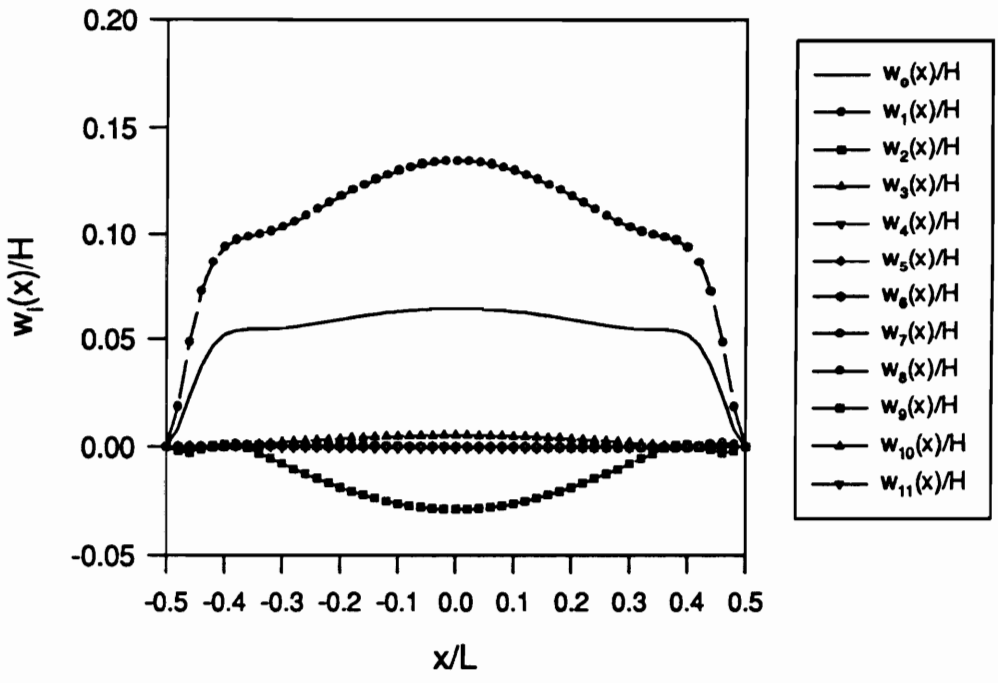

Figure 4-2 Convergence of Normalized Radial Displacement, Internal Pressure Loading of 1 Atm.

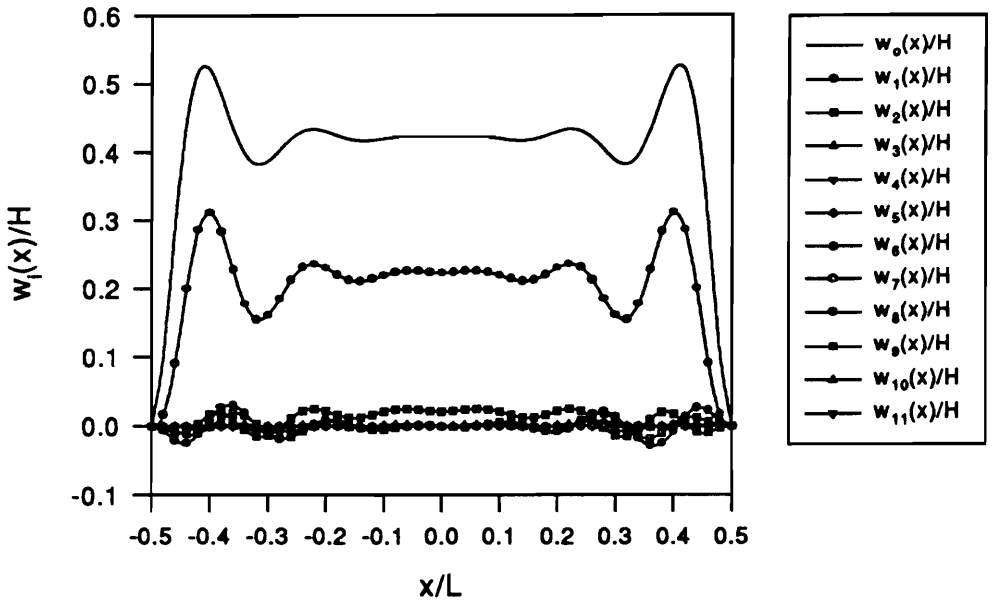

Figure 4-3 Convergence of Normalized Radial Displacement, Axial End-Shortening at 90% of Buckling Value.

shape due D_{16} and D_{26}. It is important to note that for the axial end-shortening case, the "equivalent circular cylinder" response, $w_0(x)$, provides the largest contribution, while for the internal pressure case, the second term in the series, $w_1(x)$, dominates the response. This is the case because, as will be seen, the primary response of the internally pressurized elliptical cylinder is the tendency to become more circular. This means points at the ends at the semi-minor axis move outward radially, while points at the ends of the semi-major axis move inward radially. This effect is best represented by the $\cos(4\pi s/C)$ term in the series, i.e., the term for which $w_1(x)$ is the coefficient.

To further illustrate the convergence of this solution, the convergence of the normalized coefficient functions for the series representing $v(x,s)$ is shown in Figure 4-4 for the case of one atmosphere internal pressure, and in Figure 4-5 for the case of axial end-shortening to 90% of buckling. For both cases, the series is reasonably well converged in that $v_4(x)$ and $v_{11}(x)$ show negligible variation from zero. Again, the first term, $v_0(x)$, represents the response for an equivalent circular cylinder, which in both cases is equal to zero. In this case, the coefficient functions of sine terms dominate the response, while the coefficient functions of cosine terms add only small corrections. For the case of internal pressure, the largest component of the circumferential displacement reaches a magnitude roughly one-half of the maximum of the largest component of the radial displacement. For the case of axial end-shortening, while the values of these terms are at least an order of magnitude less than the related terms for the $w(x,s)$ series, they are not negligible. The presence of significant circumferential displacements represents a fundamental difference between circular and elliptical cylinders.

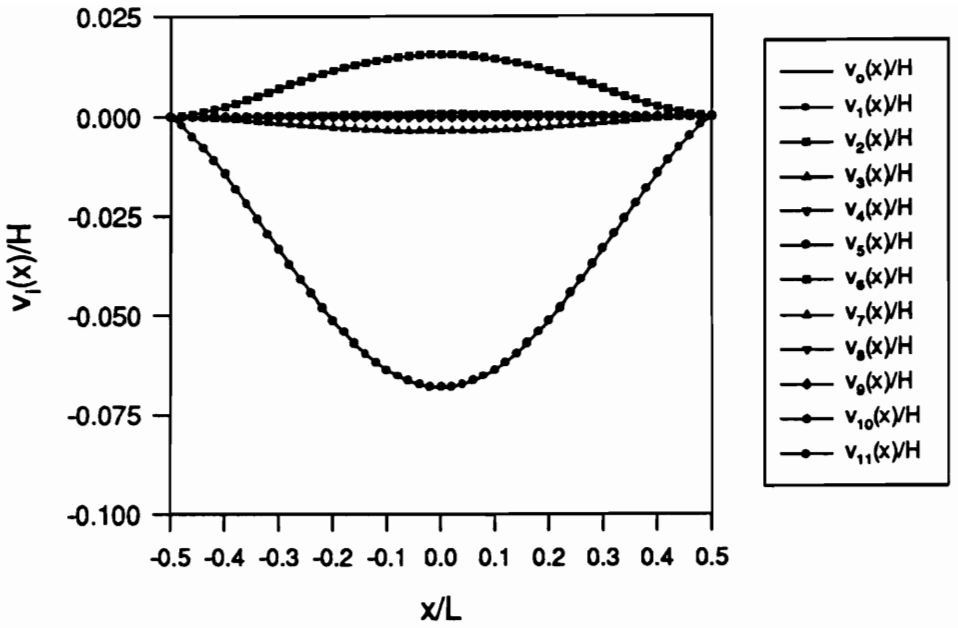

Figure 4-4 Convergence of Normalized Circumferential Displacement, Internal Pressure Loading of 1 Atm.

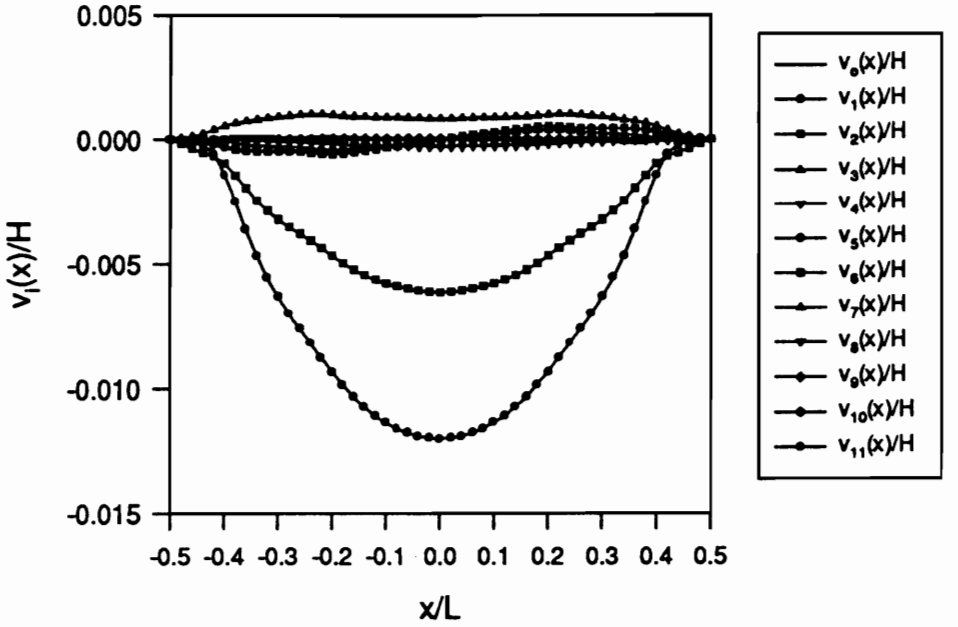

Figure 4-5 Convergence of Normalized Circumferential Displacement, Axial End-Shortening at 90% of Buckling Value.

To further establish confidence in the solution, results were checked against the solutions obtained from a STAGS finite model for the perfect elliptical cylinder. This was done for the more difficult case of end-shortening to 90% of the classical buckling load. A comparison of these results is shown here for both the normalized radial displacement in Figure 4-6, and for the stress resultant M_x in Figure 4-7. These results are plotted in both cases as a function of the normalized axial coordinate at two circumferential locations, s/C = 0 (the maximum radius of curvature) and s/C = 1/4 (the minimum radius of curvature). Excellent agreement is shown for both cases, with differences between the present analysis and STAGS in both cases being within ±3%.

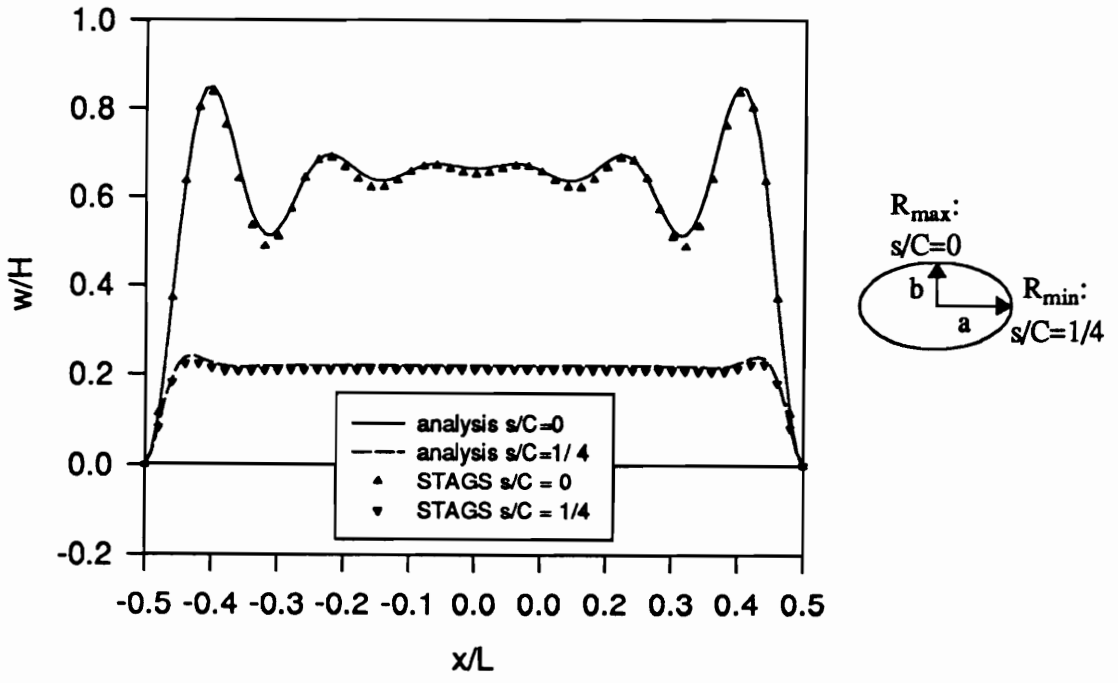

Figure 4-6 Comparison Between STAGS and Analysis for Normalized Radial Displacements, Axial End-Shortening at 90% of Buckling Value.

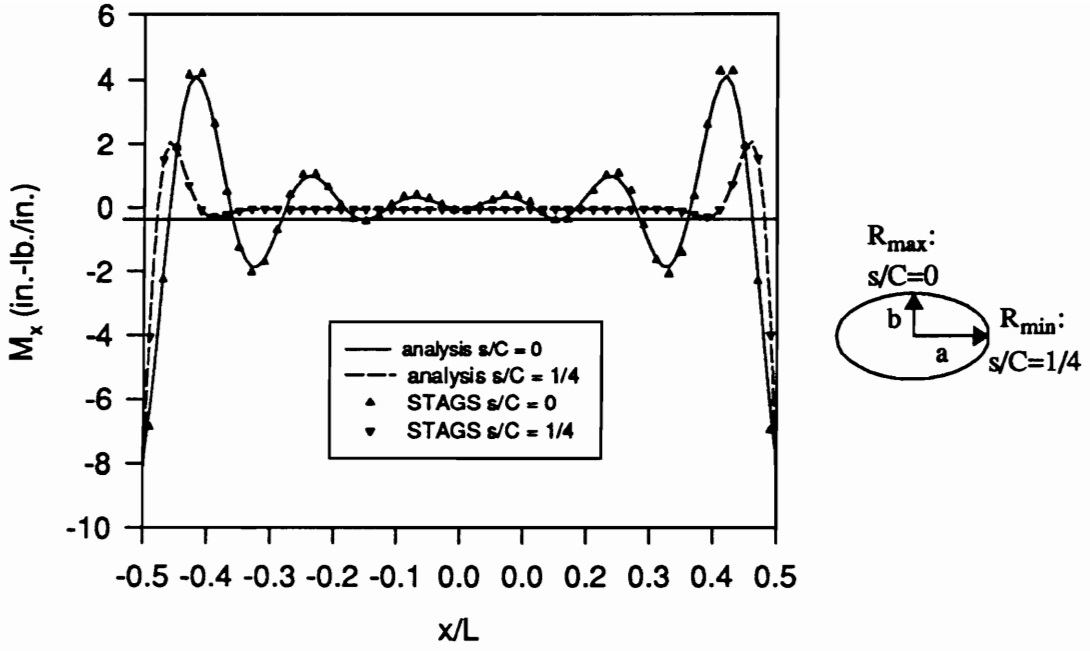

Figure 4-7 Comparison Between STAGS and Analysis for M_x, Axial End-Shortening at 90% of Buckling Value.

Internal Pressure

Unlike circular cylinders, the responses of elliptical cylinders to even simple loadings like internal pressure vary with both the axial and circumferential coordinates. Using the results shown in Figure 4-2, the normalized radial displacements for the cylinder loaded by one atmosphere internal pressure are shown as a function of the normalized axial coordinate at s/C = 0 and s/C = 1/4 in Figure 4-8. Notice that the response at s/C = 1/4, the minimum radius of curvature, is negative due to the tendency of the elliptical cross-section to become more circular when loaded by internal pressure. Also some boundary layer effects are evident due to clamped end conditions and the requirement that the cylinder be fixed against axial displacement. Unlike a circular cylinder, the value of the radial displacement is strongly dependent on the circumferential coordinate. Another interesting feature can be seen by examining the responses at s/C = ±1/8, which are shown in Figure 4-9 for the normalized radial displacement. Note that the results for s/C = 1/8 and s/C = -1/8 are not symmetric about the midspan of the cylinder. For a symmetric, balanced laminate this skewing of the deformed shape can only be due to the influence of bending twisting stiffnesses, D_{16} and D_{26}. Thus the differences between the radial displacements at s/C = 1/8 and s/C = -1/8 can be viewed as a crude measure of the influence of nonmembrane quantities. This is particularly evident for this laminate due to its large values of D_{16} and D_{26}. It can be seen that a deviation exists between the two solutions over nearly 60% of the cylinder length even for a cylinder loaded by very low levels of internal pressure.

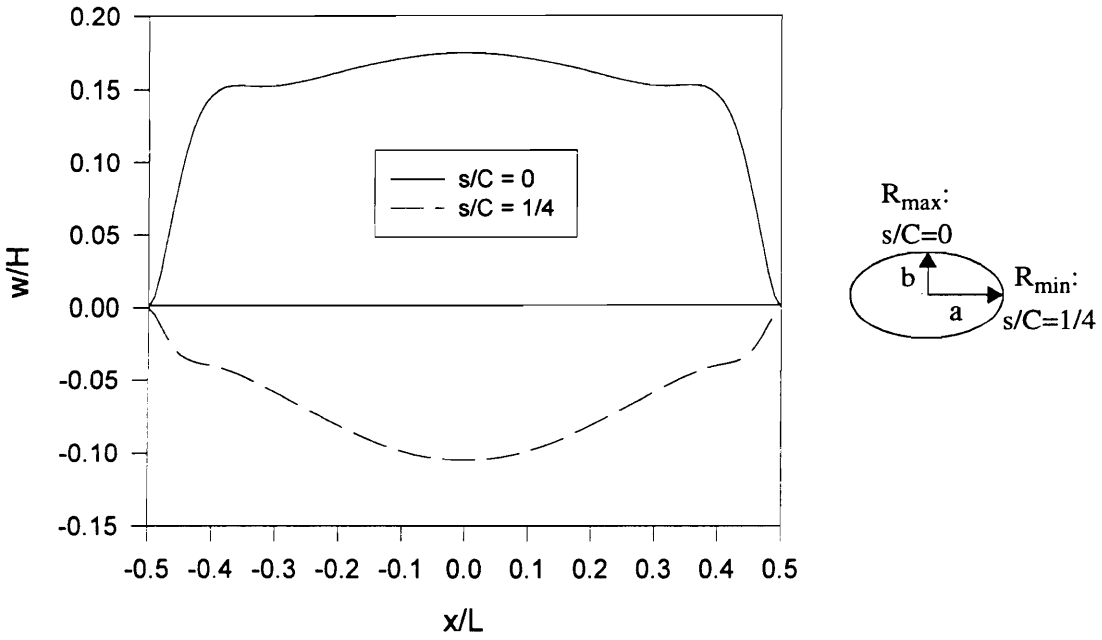

Figure 4-8 Normalized Radial Displacements at s/C = 0 and s/C = 1/4, Internal Pressure Loading.

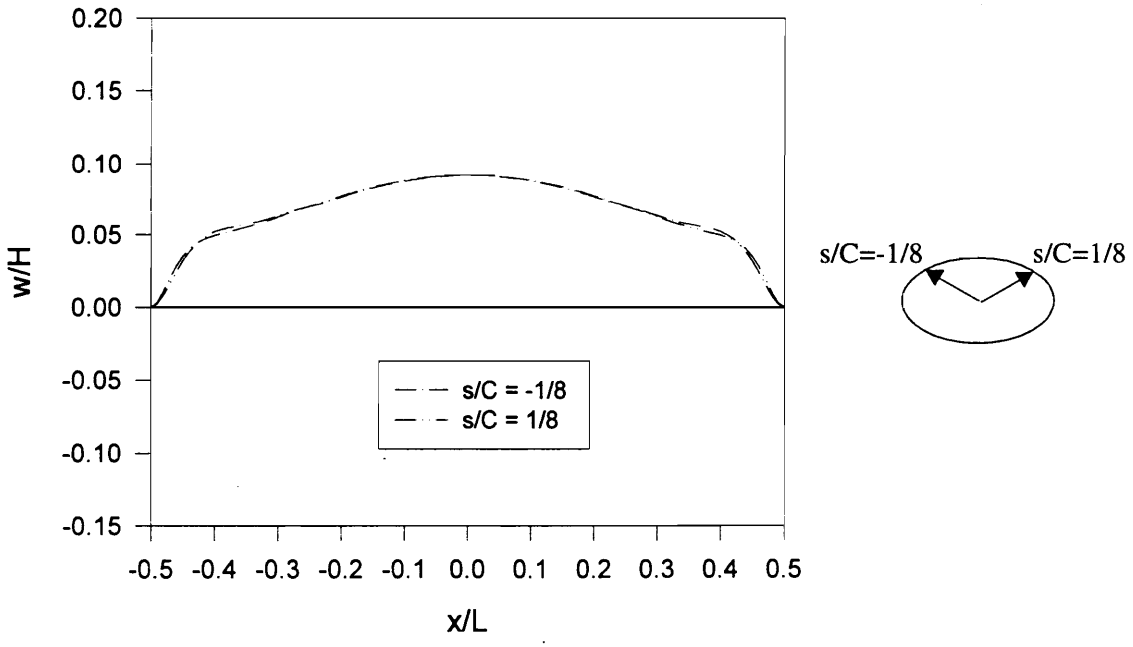

Figure 4-9 Normalized Radial Displacements at s/C = -1/8 and s/C = 1/8, Internal Pressure Loading.

The variation of circumferential and axial midplane strain as a function of both the normalized axial and normalized circumferential coordinate are given in Figures 4-10 and 4-11, respectively. The strains are plotted over one-quarter of the cylinder, $0.0 \leq x/L \leq 0.5$ and $0.0 \leq s/C \leq 0.25$. It should be noted that in order to provide the best point of view for examining these quantities, Figures 4-10 and 4-11 are rotated 180^{o} with respect to each other. This is also true of all the other surface plots of axial and circumferential quantities in this chapter. The circumferential midplane strain distribution clearly varies with both the axial and

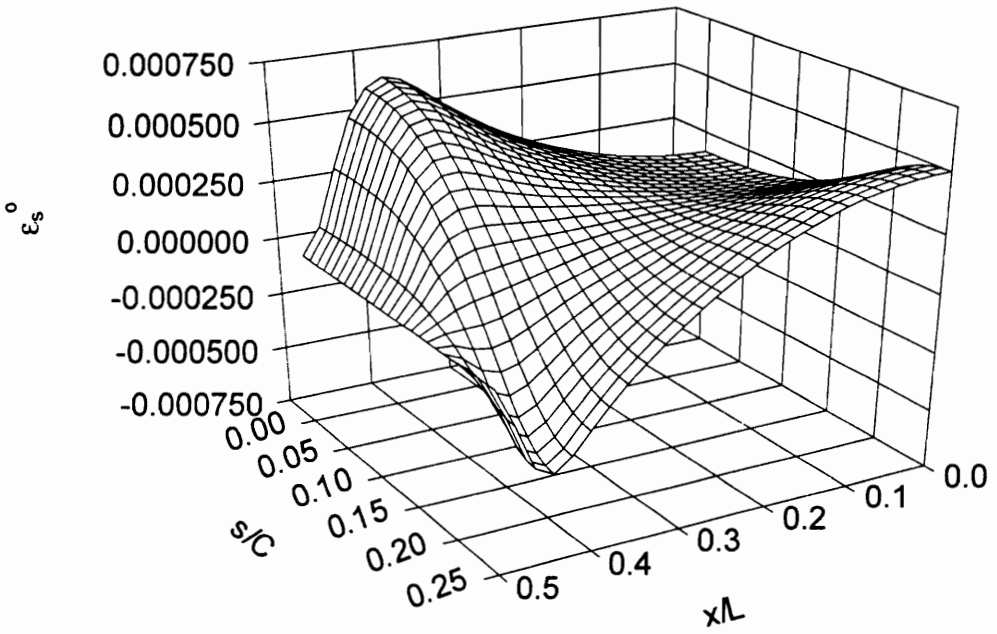

Figure 4-10 Circumferential Midplane Strain Over One-Quarter of the Cylinder, Internal Pressure Loading.

circumferential coordinates, exhibiting as great a variation in the axial direction as in the circumferential direction. Recall that due to the presence of non-zero circumferential displacements, the circumferential midplane strain does not vary simply as w/R(s). The axial midplane strain also varies to a large degree with both axial and circumferential coordinates. Even at low pressure, with the ends of the cylinder restrained against axial movement, axial strains are produced in an elliptical cylinder. Further, even at midspan, these strains are as great as the circumferential strains. Indeed, at the midspan of the cylinder, the axial midplane strain shows a larger gradient in the circumferential direction, changing from compressive strain at the minimum radius of curvature to tensile strain at the maximum radius of curvature.

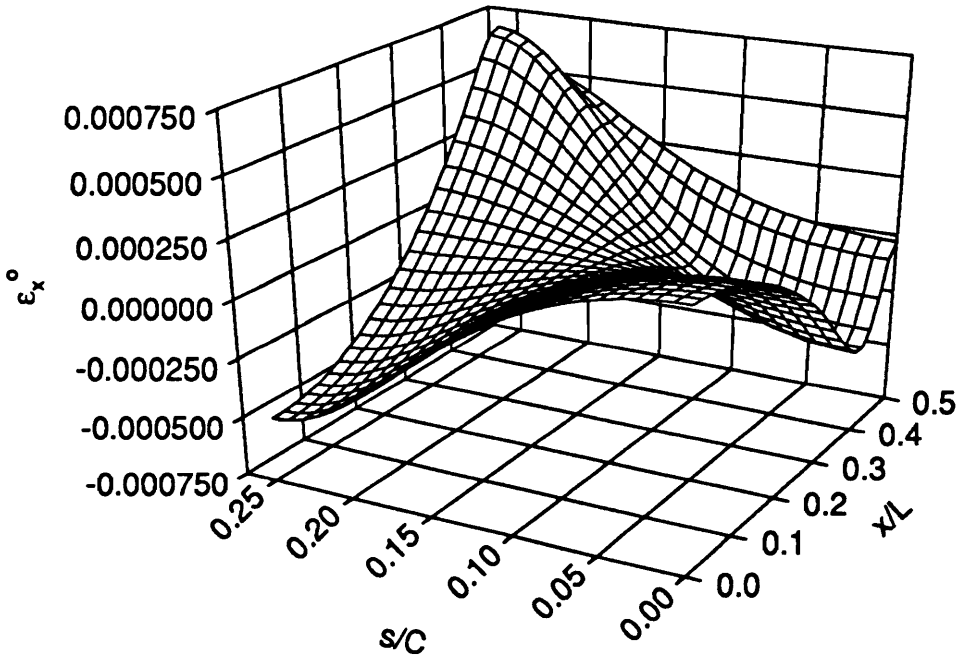

Figure 4-11 Axial Midplane Strain Over One Quarter of the Cylinder, Internal Pressure Loading.

The peaks and valleys of the circumferential strain distribution, however, are at opposite locations from those in the axial strain distribution, so that the stress resultants calculated from their combination show a smoother and less dramatic variation with the axial and circumferential coordinates near midspan. The distribution of N_x over $0.0 \le x/L \le 0.5$ and $0.0 \le s/C \le 0.25$ is shown in Figure 4-12. The axial stress resultant varies between tensile and compressive values along both the x and s directions. The largest magnitude of N_x is tensile and occurs at the clamped end near the minimum radius of curvature. The shape of this function is similar to that for the axial strain, but with much smoother transitions between positive and negative values. Little resemblance can be seen, however, between the strain distributions and the distribution of the stress resultant N_s, which is shown over the quarter cylinder in Figure 4-13. Although there is an obvious gradient in the circumferential direction, the distribution is remarkably uniform in the axial direction for a given value of s/C throughout most of the cylinder's length. The formula for N_s from membrane theory is

$$N_s = p_0 * R(s). \tag{4.5}$$

The degree to which eqn. 4.5 is accurate is illustrated in Figure 4-14, which shows N_s from the geometrically nonlinear analysis normalized by the membrane approximation given in eqn. 4.5 over one quarter of the cylinder. For $x/L < 0.35$, N_s varies from the value of eqn. 4.5 by less than 1%. However such good

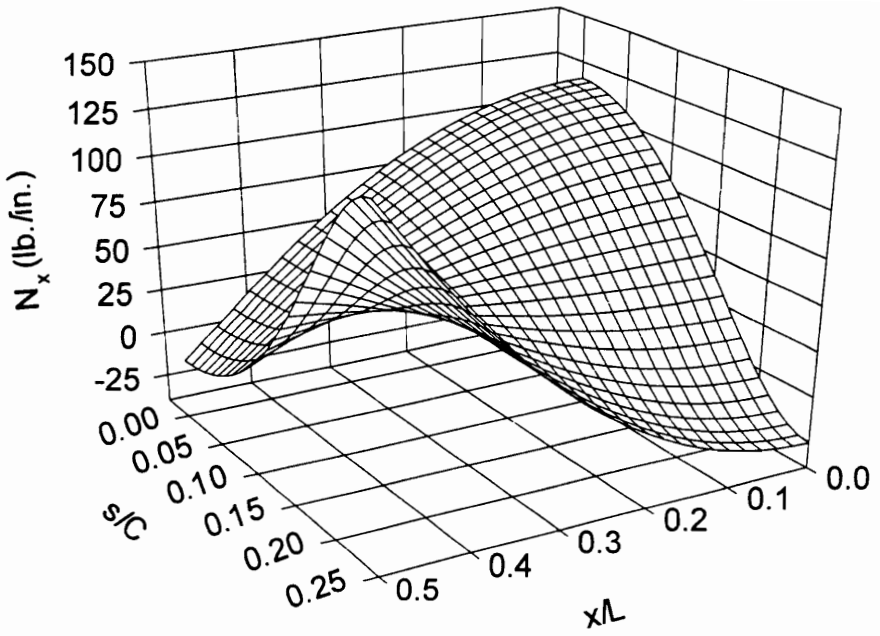

Figure 4-12 N_x Over One Quarter of the Cylinder, Internal Pressure Loading.

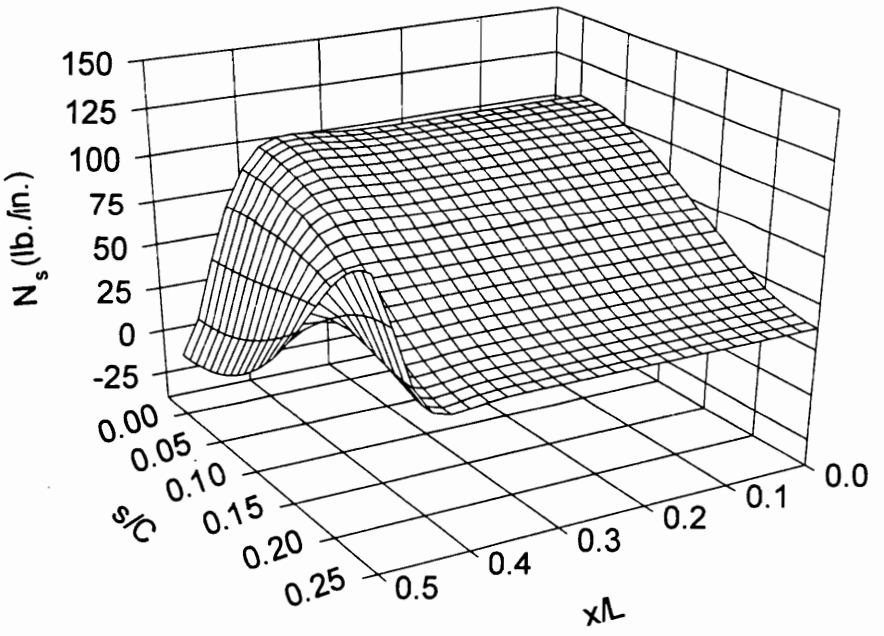

Figure 4-13 N_s Over One Quarter of the Cylinder, Internal Pressure Loading.

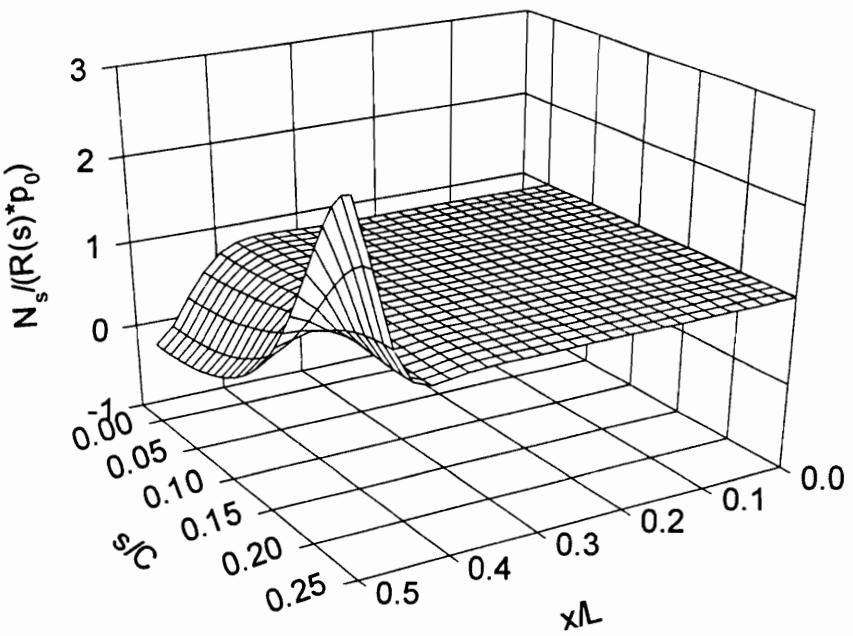

Figure 4-14 $N_s/(R(s)*p_0)$ Over One Quarter of the Cylinder, Internal Pressure Loading.

approximations cannot be found in all cases. Examples of this can be seen in Figures 4-15 and 4-16. In Figure 4-15, a comparison is made between calculations of the circumferential midplane strain at midspan using membrane theory, linear analysis, and nonlinear analysis. The membrane results are based upon the membrane formulation for noncircular cylinders given by Novozhilov [4]. Circumferential midplane strain results are plotted against the normalized circumferential coordinate over one quarter of the cross-section, from s/C = 0 to s/C = 1/4. A similar comparison between these methods of calculation is made for the normalized radial displacement at midspan in Figure 4-16. These figures also provide a clearer view of the way in which these quantities can vary with the circumferential coordinate. The circumferential strain more than doubles between the points near the maximum radius of curvature and the highly curved regions around the minimum radius of curvature. The radial displacement decreases from a maximum positive value at the maximum radius of curvature to a negative value of nearly equal magnitude at the minimum radius of curvature. This further illustrates the influence of the non-zero circumferential displacement component on the circumferential strain. Membrane results in both cases show the poor correlation with the nonmembrane results, even at midspan where the agreement should be best. Perhaps even more surprising is that even for such a low load level there is a small but noticeable difference between the linear and nonlinear analyses. This difference is everywhere within ± 5.5% for the radial displacements, but for circumferential strains becomes more pronounced near the semi-major axis, varying from the nonlinear analysis by 7.2%.

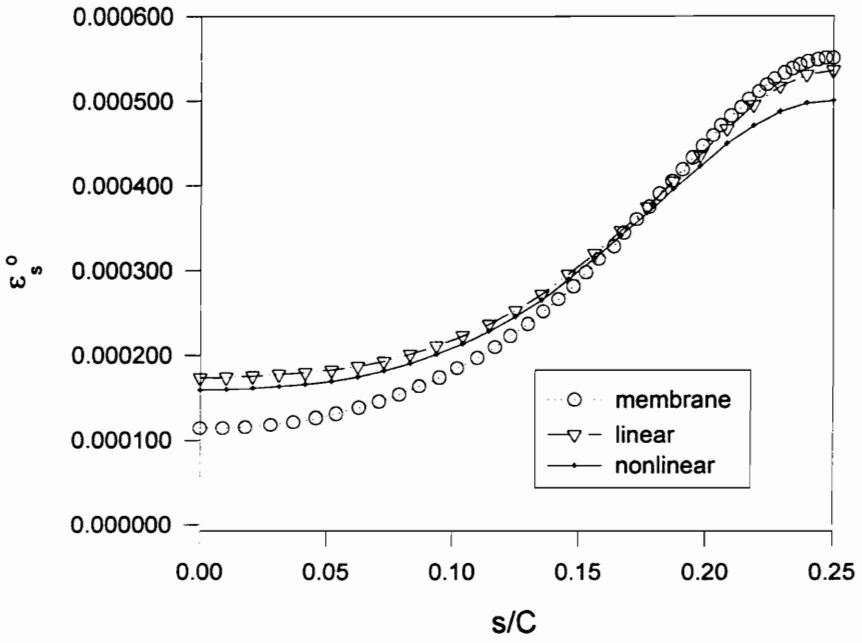

Figure 4-15 Comparison of Circumferential Midplane Strain at Midspan Using Membrane, Linear, and Nonlinear Analyses, Internal Pressure Loading.

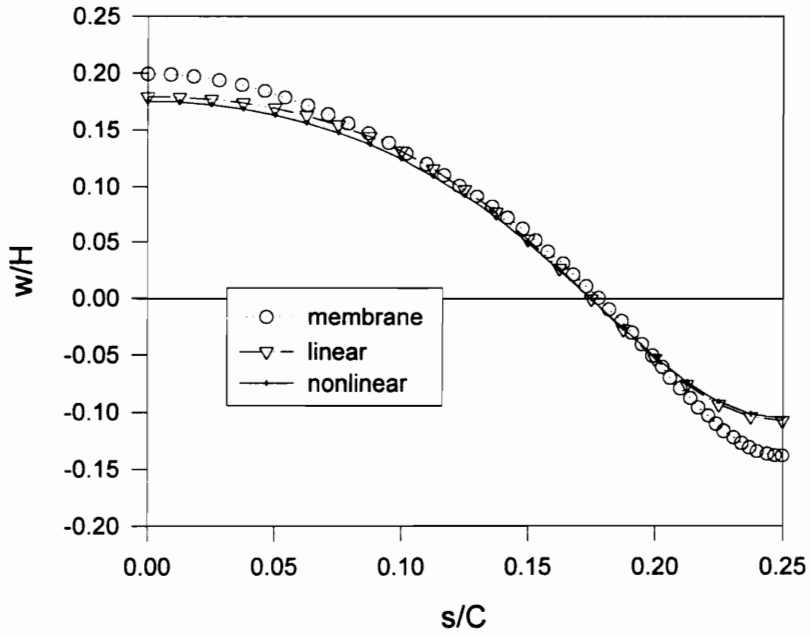

Figure 4-16 Comparison of Normalized Radial Displacement at Midspan Using Membrane, Linear and Nonlinear Analyses, Internal Pressure Loading.

Axial Compression

Figure 4-17 illustrates the way in which the coefficient functions for radial displacement given in Figure 4-3 sum for two values of circumferential location, s/C = 0 and s/C = 1/4. The cylinder is loaded to 90% of the classical buckling load. In this figure the normalized radial displacement is plotted against the normalized axial coordinate at the maximum and minimum radii of curvature of the elliptical cross-section. Notice that the length of the displacement boundary layer associated with the end conditions varies with the circumferential coordinate. Both the response and the length of the boundary layer are greatest at the maximum radius of curvature, where the boundary layer extends through nearly the entire cylinder, and least at the minimum radius of curvature, where the boundary layer quickly dies out. Intermediate results are shown in Figure 4-18 for the normalized radial displacement at s/C = -1/8 and s/C =1/8. Note also that,

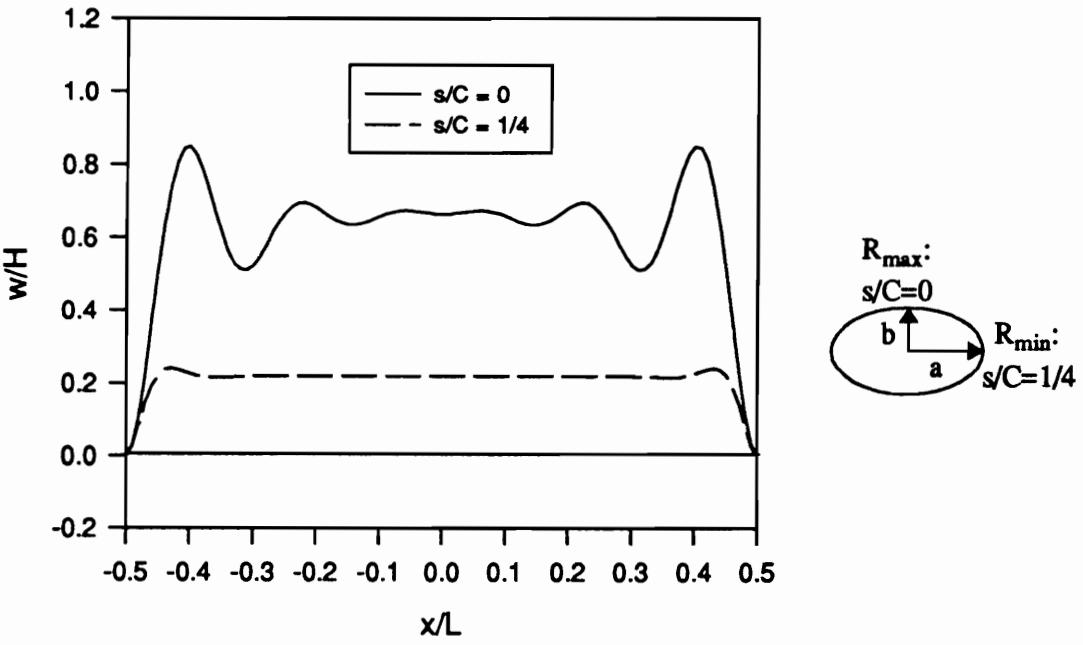

Figure 4-17 Normalized Radial Displacement at s/C = 0 and s/C = 1/4, Axial End-Shortening.

as in Figure 4-9, the response at s/C = 1/8 exhibits a lack of symmetry relative to the response at s/C = -1/8. This effect is more prominent for axial compression than it was for internal pressurization, but is again due to the skewing of the deformed shape which arises due to the relatively large D_{16} and D_{26} for this laminate.

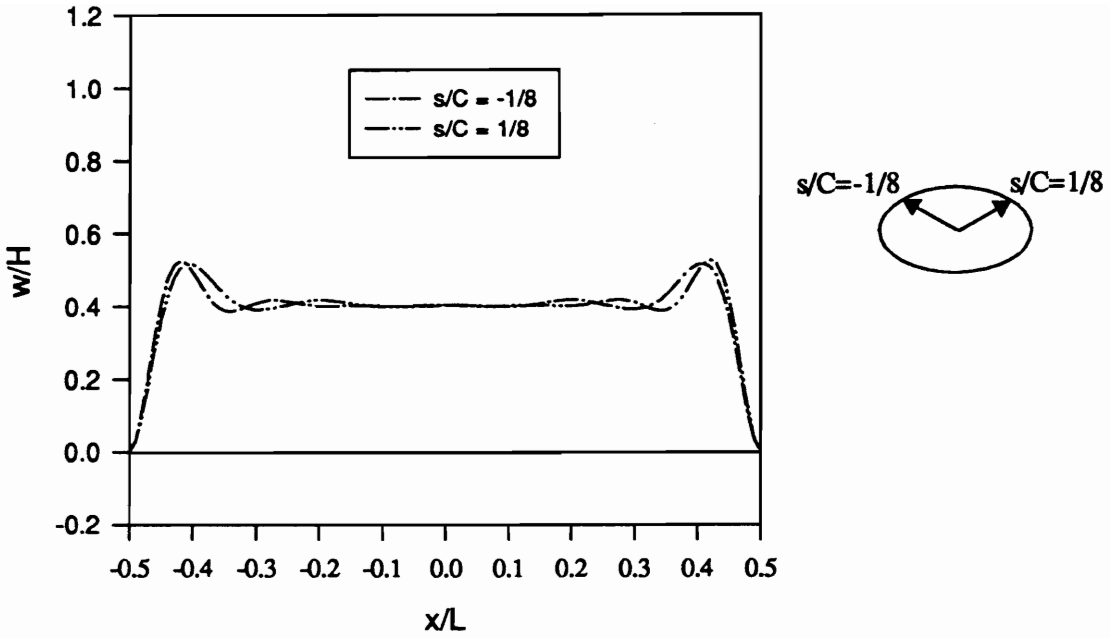

Figure 4-18 Normalized Radial Displacement at s/C = -1/8 and s/C = 1/8, Axial End-Shortening.

In order to further illustrate the response of an elliptical cylinder to axial end-shortening, the distributions of axial and circumferential strains over one quarter of the cylinder are shown in Figures 4-19 and 4-20, respectively. These may be compared with Figures 4-11 and 4-10 for the case of internal pressure loading. The midplane strains at 90% of the classical buckling load are quite high for this laminate, and material failure might be expected due to the levels of strain in the boundary layer region. It can be clearly seen that over much of the cylinder the response is greatest near the maximum radius of curvature at s/C = 0, and decreases near the minimum radius of curvature at s/C = 1/4. While these responses clearly vary with both axial and circumferential coordinates, there is less variation for both strains in the circumferential direction than was the case for the internal pressurized cylinder. Further, the variation of strain in the circumferential direction decreases greatly near the midspan of the cylinder. At midspan, the circumferential strain increases only vary slightly from s/C = 0 to s/C = 1/4, while for the axial strain, there is even less variation with the circumferential coordinate at midspan. Indeed, at midspan, the difference between the axial midplane strain at s/C = 0 and s/C = 1/4 is less then 3%. It should also be noted that the average axial midplane strain at midspan is very closely approximated by the relation

$$\varepsilon_x^{avg}\Big|_{x=0} = -\Delta/L, \tag{4.6}$$

where -Δ is the applied axial end-shortening, and L is the axial length of the cylinder.

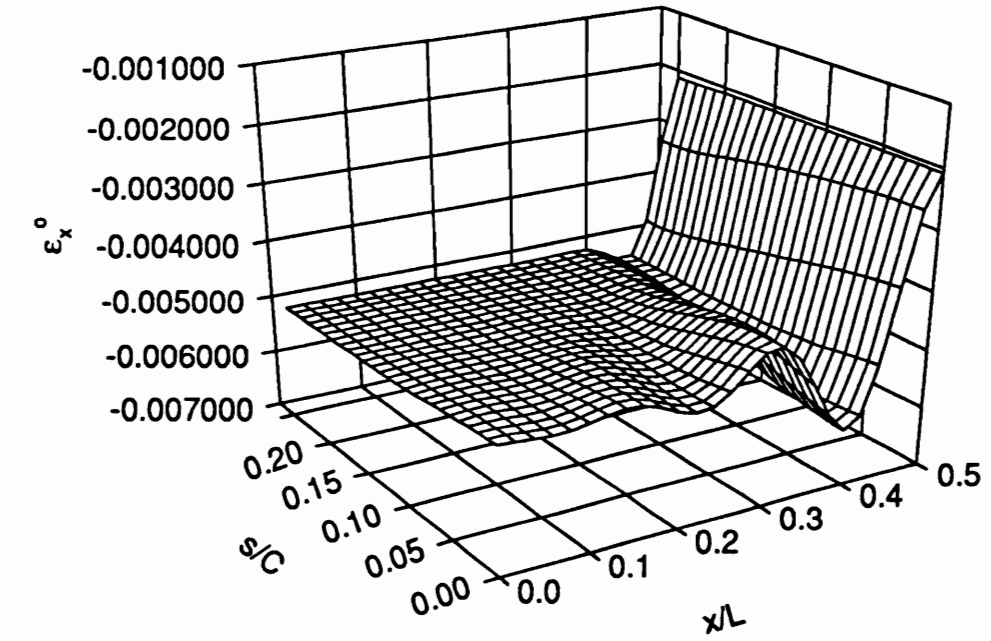

Figure 4-19 Axial Midplane Strain Over One Quarter of the Cylinder, Axial End-Shortening.

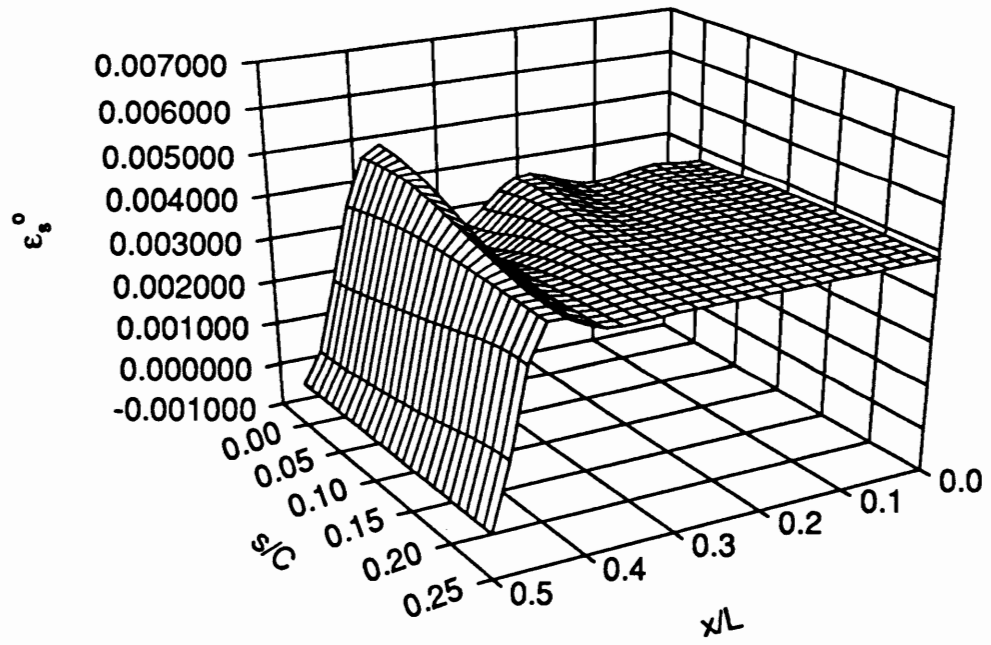

Figure 4-20 Circumferential Strain Over One Quarter of the Cylinder, Axial End-Shortening.

The distributions of the stress resultants N_x and N_s are also given over the quarter cylinder in Figures 4-21 and 4-22, respectively. These may be compared with Figures 4-12 and 4-13 for the case of internal pressure loading. In the case of N_x, the variations are very small, and could not be discerned if Figure 4-21 was graphed to the same scale as Figure 4-22. Still it is possible to note that this quantity changes most rapidly along s/C = 0, the flattest part of the ellipse, while the greatest compressive load occurs at s/C = 1/4, the stiffest, most highly curved region of the cylinder. By contrast, the circumferential stress resultant, N_s, is

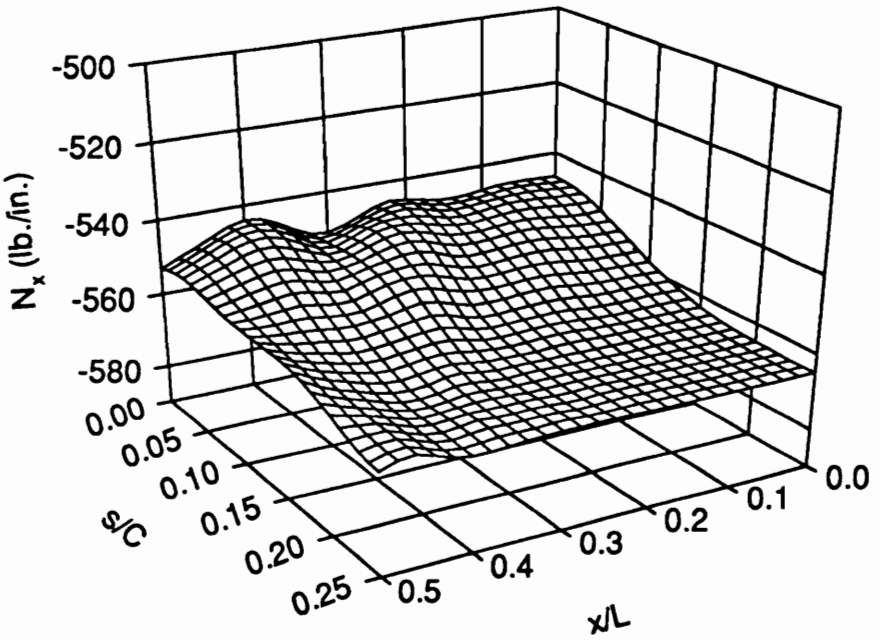

Figure 4-21 N_x Over One Quarter of the Cylinder, Axial End-Shortening.

virtually zero near the midspan of the cylinder and remains comparatively small throughout most of the length of the cylinder, approaching the size of N_x only near the clamped ends.

Lastly, it should be noted that a way in which to estimate the response of an elliptical cylinder at a particular s/C location is to calculate the response for a circular cylinder having the same radius as the radius of curvature of the elliptical cylinder at that point. Clearly, this would not work well in the case of internal pressure, as the radial displacement, for instance, is negative over much of the circumference for an elliptical cylinder, but never would be negative for any approximating circular cylinder. For the case of axial compression, however, this can often provide a reasonable approximation to the response that might be expected at a particular circumferential location. To illustrate this point, the results of Figure 4-17 are compared in Figure 4-23 with the exact nonlinear solutions for two circular cylinders axially compressed by the same value of end-shortening as the elliptical cylinder. One circular cylinder has a radius equal to the

ellipse's maximum radius of curvature, while the other cylinder has a radius equal to the ellipse's minimum radius of curvature, which occurs at s/C = 1/4. As can be seen from the figure, the response at the minimum

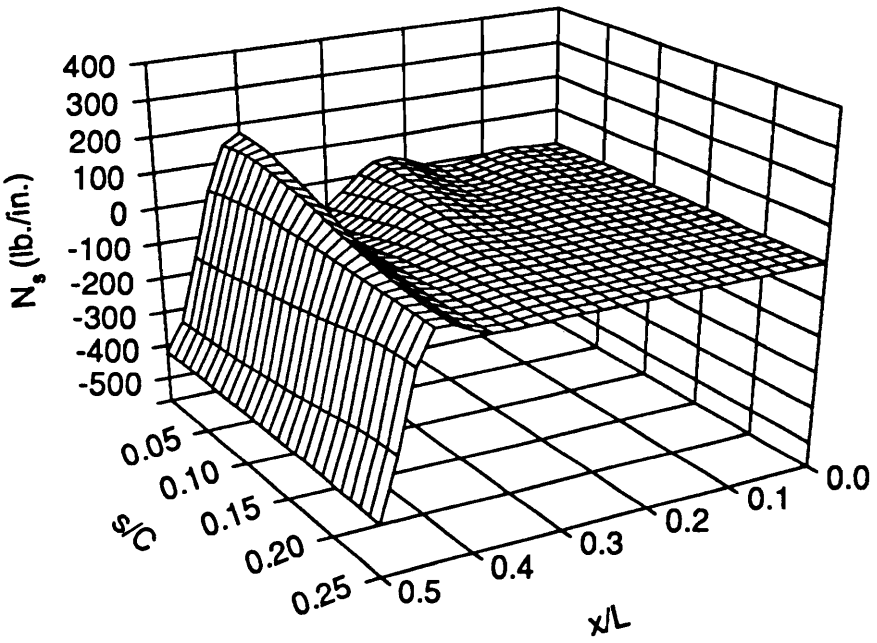

Figure 4-22 N_s Over One Quarter of the Cylinder, Axial End-Shortening.

radius of curvature, at s/C = 1/4, can be well predicted by the solution for a circular cylinder with the same radius. However, at the maximum radius of curvature, s/C = 0, the solution for a circular cylinder does not provide as good a prediction for the response of the ellipse. In addition to displacements, responses such as stress resultants can also be approximated using this method. An example of these results is given in Fig. 4-24, which represents the moment resultant M_x plotted as a function of the normalized axial coordinate at s/C = 0 and s/C = 1/4 and compared with the approximate circular solutions. Notice that for this quantity as well, even a simple axial load results in responses that vary with the circumferential coordinate, and the length of the boundary layer associated with the clamped end conditions varies with the circumferential coordinate, the boundary layer being longer at the circumferential location with the maximum radius of curvature. At the minimum radius of curvature, the response of the elliptical cylinder is quite well predicted by the solution for a circular cylinder with the same radius. At the maximum radius of curvature, such a solution does not provide as close agreement, but provides a better prediction for M_x than for the radial displacement. The discrepancies between the prediction at s/C = 0 are due largely to the fact that these

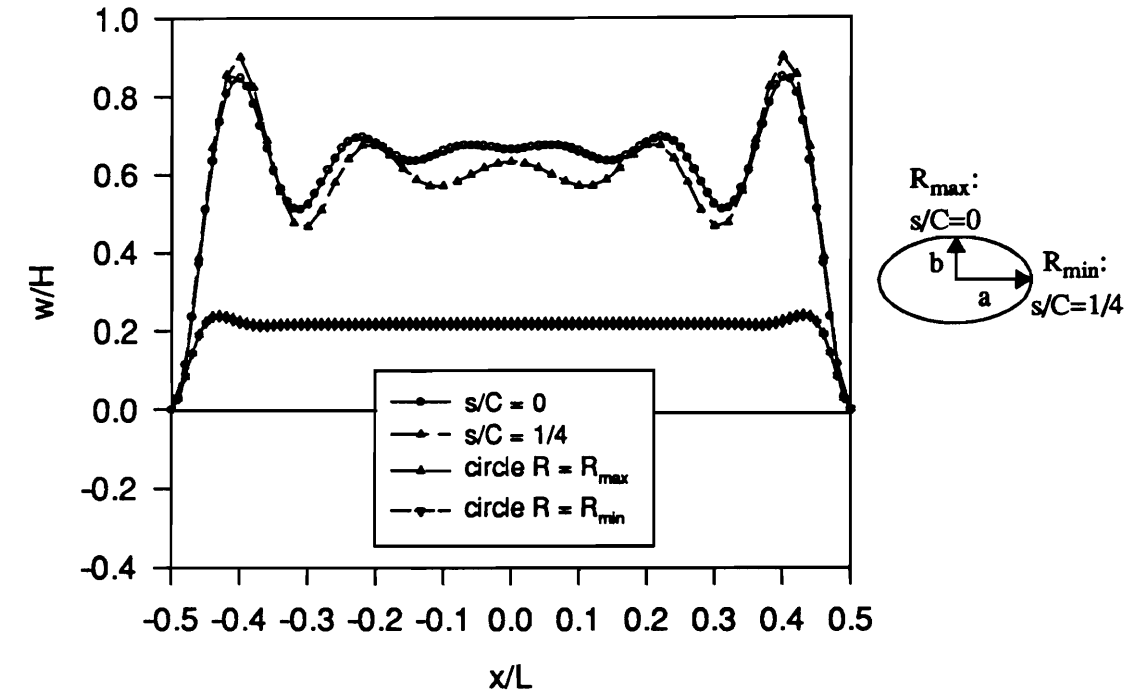

Figure 4-23 Comparison of Normalized Radial Displacements at s/C = 0 and s/C = 1/4 with Approximate Circular Cylinder Solutions, Axial End-Shortening.

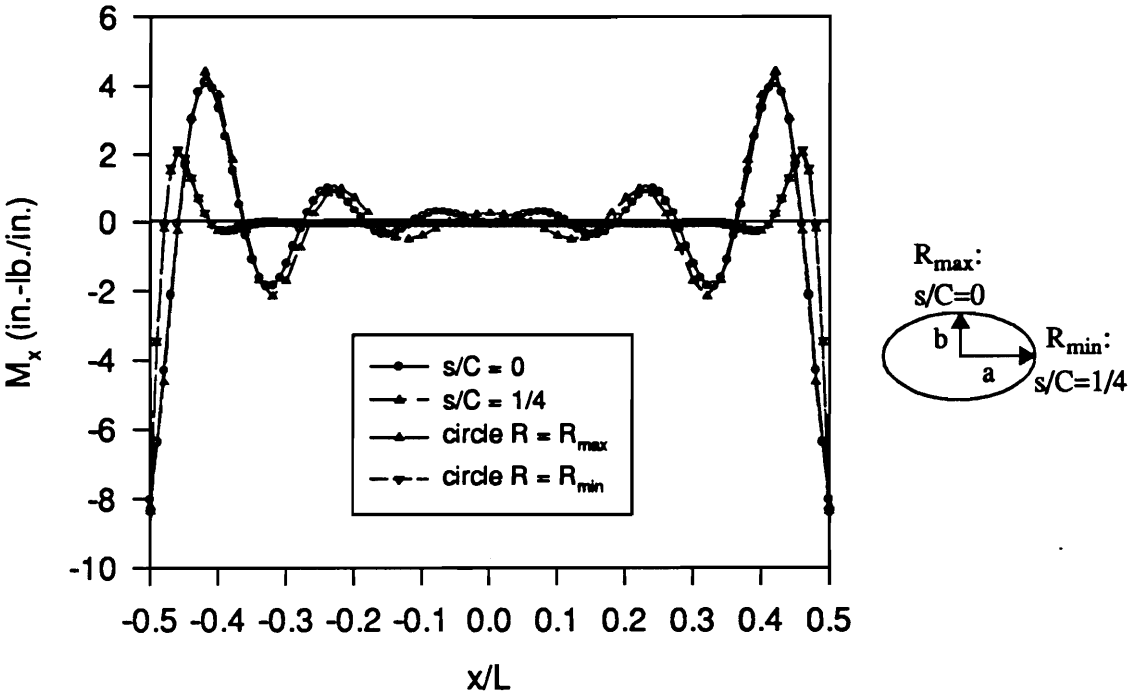

Figure 4-24 Comparison of M_x at s/C = 0 and s/C = 1/4 with Approximate Circular Cylinder Solutions, Axial End-Shortening.

results are taken in the far prebuckling range. Although not shown here, at lower levels of axial compression, $\Delta < 0.75\Delta_{cr}$ the results are uniformly close for all values of s/C.

Internal Pressure and Axial Compression

In order to illustrate the effects of combined pressure and axial loads, results are given in this section for the clamped $(+45_2/-45_2)_s$, elliptical cylinder with b/a = 0.70 subjected to 1 atm. internal pressure and axial end-shortening to 90% of buckling. The normalized radial displacement plotted against the normalized axial coordinate at s/C = 0 and s/C = 1/4 is shown in Figure 4-25. In comparing these results with Figure 4-17, for axial compression alone, it can be seen that the addition of even a small amount of internal pressure has the effect of flattening out the response at s/C = 0 and decreasing the length of the boundary layer, while increasing the peaks in the boundary layer by about 20%. At s/C = 1/4, the addition of internal pressure does not affect the peak values much in the boundary layer, but does result in a decrease of displacements near the midspan of the cylinder. It might be expected that for greater values of internal pressure, the radial displacement at the minimum radius of curvature would become negative, as it does with pure internal pressure loading. Thus the addition of internal pressure decreases the variation of the radial displacement in the axial direction, but increases the variation in the circumferential direction.

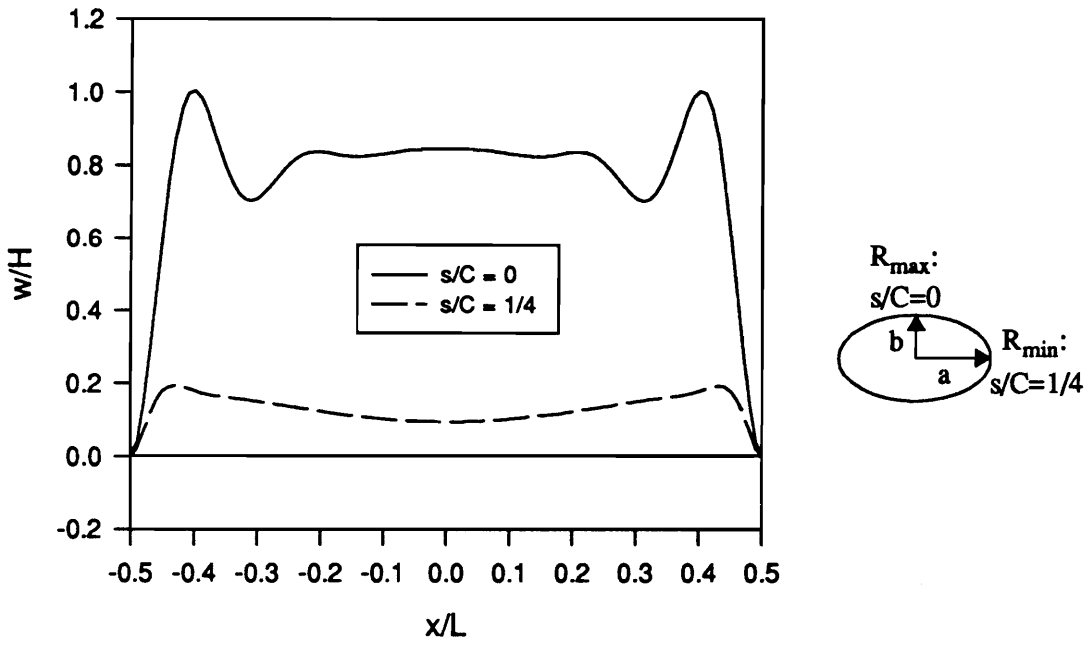

Figure 4-25 Normalized Radial Displacement at s/C = 0 and s/C = 1/4, Combined Loading.

For comparison with Figure 4-18, the normalized radial displacements at s/C = -1/8 and s/C = 1/8 are also given in Figure 4-26. The skewing of the deformed shape is still evident in the antisymmetry of the response at s/C = -1/8 to the response at s/C = 1/8, but is somewhat decreased from the amount seen in the case of axial end-shortening alone. The boundary layers at these locations are also shorter and flatter due to the addition of pressure, but show only a small increase in their peak values.

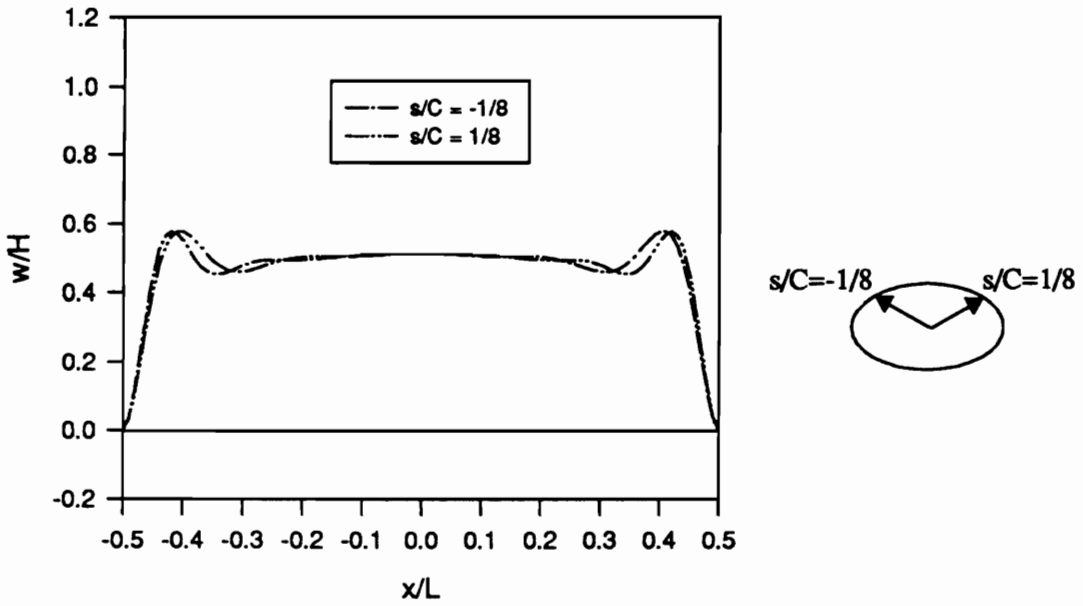

Figure 4-26 Normalized Radial Displacement at s/C = -1/8 and s/C = 1/8, Combined Loading.

The distributions of the axial and circumferential midplane strains over one quarter of the cylinder, $0.0 \le x/L \le 0.5$ and $0.0 \le s/C \le 0.25$, are shown in Figures 4-27 and 4-28, respectively. In both cases the presence of internal pressure results in a small decrease in the variation of the strains with axial coordinate by comparison to the case of axial end-shortening alone, shown in Figures 4-19 and 4-20. This is paid for, however, by an increase in the circumferential variation of both quantities, and by increases in the peak strains as well as the overall levels of strain.

The distribution of N_x over the quarter cylinder, which results from a combination of the above strains, is shown in Figure 4-29. The addition of only 1 atm. internal pressure completely changes the character of the distribution for N_x as compared to the case for no internal pressure in Figure 4-21. The variation in both the axial and circumferential directions increases considerably, while the average value of N_x actually decreases slightly from that for pure axial compression. The overall changes in the value of this stress resultant over the cylinder remain fairly small, however, although the shape of the distribution now more closely resembles that for N_x for the cylinder with only an internal pressure load, Figure 4-12. The circumferential stress

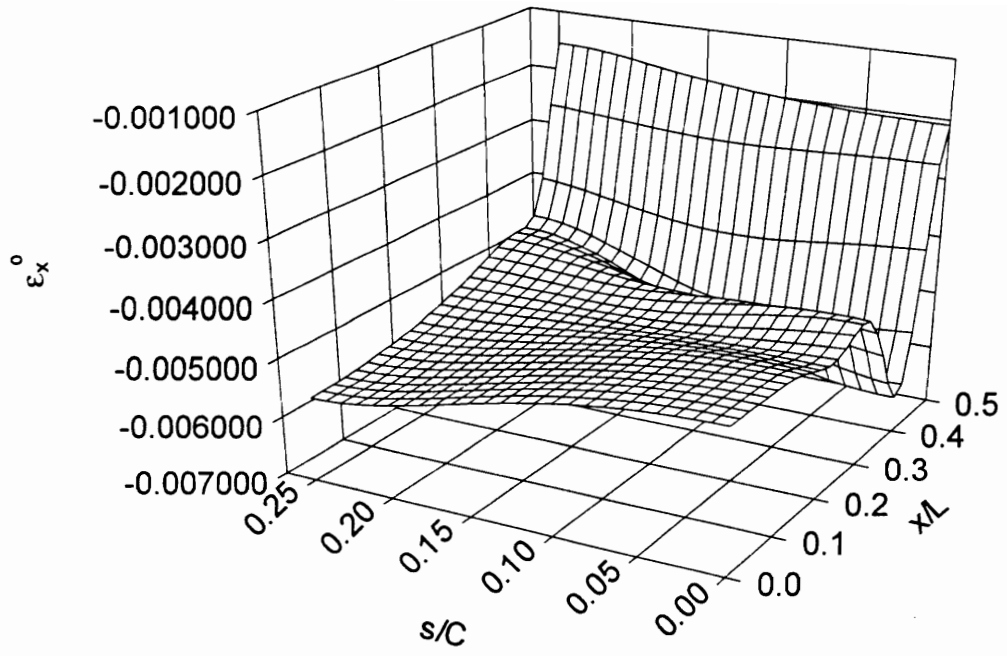

Figure 4-27 Axial Strain Over One Quarter of the Cylinder, Combined Loading.

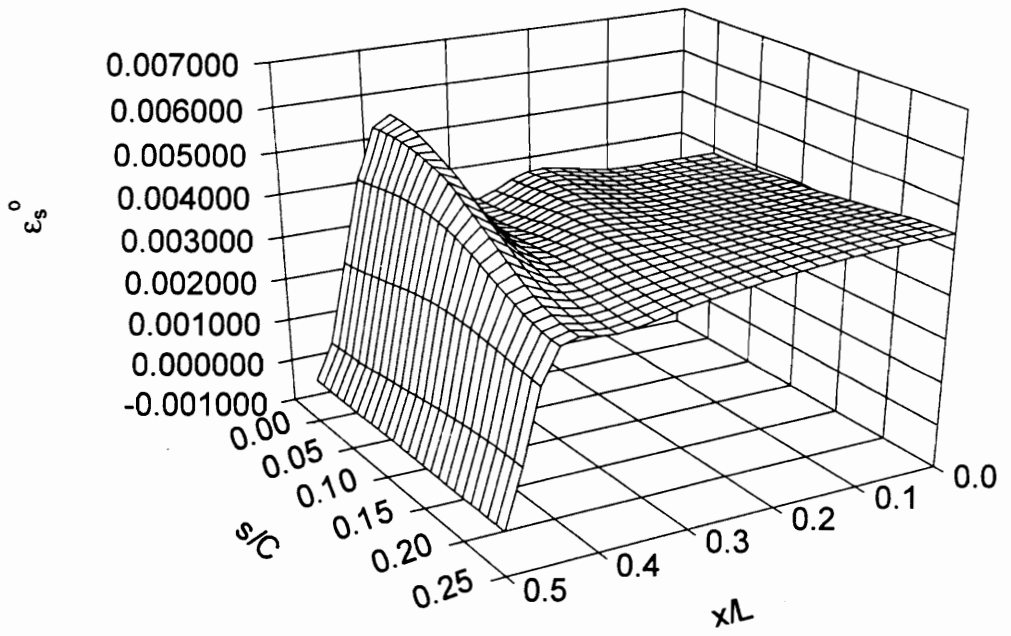

Figure 4-28 Circumferential Strain Over One Quarter of the Cylinder, Combined Loading.

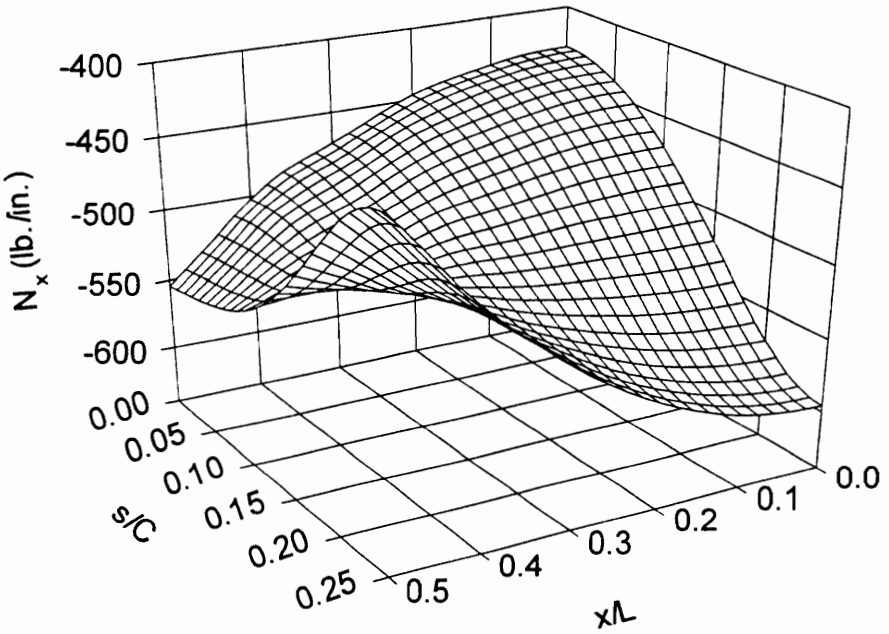

Figure 4-29 N_x Over One Quarter of the Cylinder, Combined Loading.

The circumferential stress resultant, N_s, is plotted as a function of the axial and circumferential coordinates over the quarter cylinder in Figure 4-30. This figure may be compared with Figure 4-22 which shows this quantity for the case of axial compression only. Unlike, N_x, this stress resultant shows no such clear change in its character due to the addition of internal pressure. Rather, as with the circumferential strain, there is a slight decrease in the variation of this response with the axial coordinate, accompanied by an increase in the variation with the circumferential coordinate and an increase in its peak values.

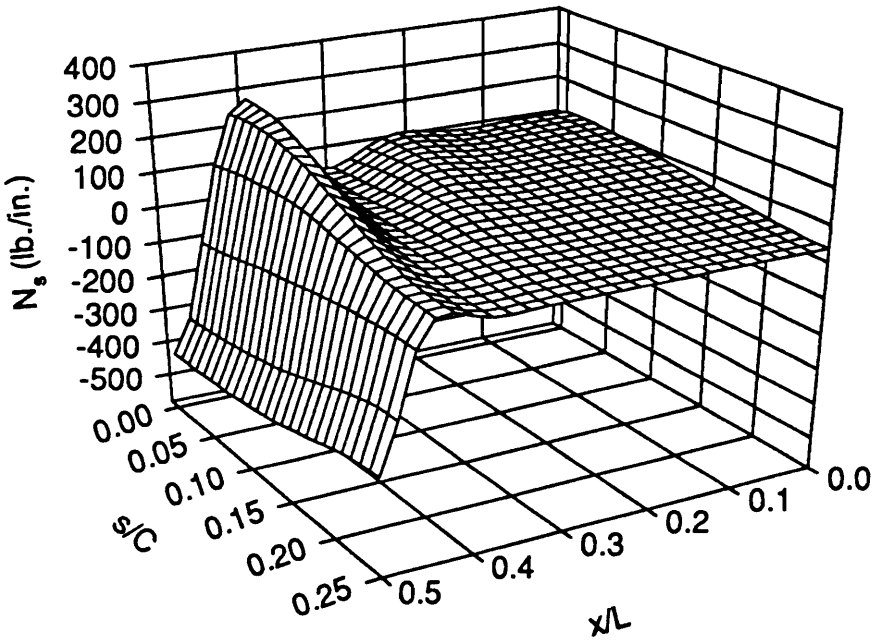

Figure 4-30 N_s Over One Quarter of the Cylinder, Combined Loading.

Lastly, it is instructive to make a more direct comparison between the results for cylinders axially compressed to 90% of the buckling load, with and without the addition 1 atm. of internal pressure. In Figure 4-31 the circumferential midplane strain at midspan is shown as a function of the circumferential coordinate between s/C = 0 and s/C = 1/4 for both of these cases. That there is an increase in the circumferential strains at midspan induced by the addition of a low level of internal pressure is made evident in Figure 4-31. The circumferential strain under combined loading is everywhere greater than the circumferential strain resulting from pure axial end-shortening, and is particularly greater in the more highly curved regions closer to the minimum radius of curvature at s/C = 1/4. Also, while the changes in the value of this strain change very slowly between s/C = 1/8 and s/C = 1/4 without internal pressure, the addition of pressure results in a rapid increase in strain levels in this region. This comparison between combined loading and pure axial loading is also made for the normalized radial displacement in Figure 4-32. Once again, it can be seen that the addition of internal pressure leads to a greater variation with the circumferential coordinate. Even with only axial compression, the tendency of the less stiff, lower curvature areas of the elliptical cross-section to deflect more results in the deformed shape of the cross-section approaching a more circular shape. When the influence of internal pressure, which also causes the cross-section to become more circular, is added to this effect, this increased change in the radial displacement with the circumferential coordinate naturally

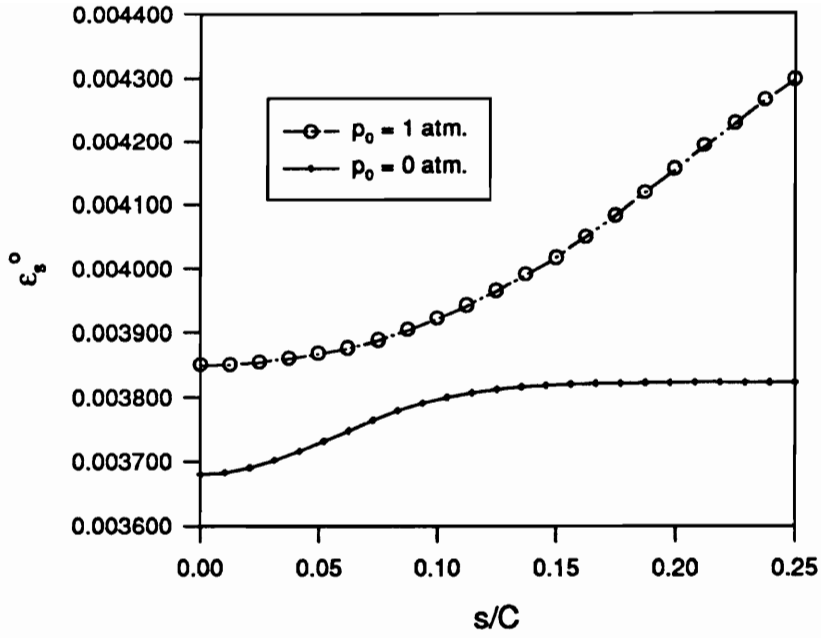

Figure 4-31 Comparison of Midspan Circumferential Midplane Strain, Axial End-Shortening at 90% of Buckling for Pressurized and Unpressurized Cylinders.

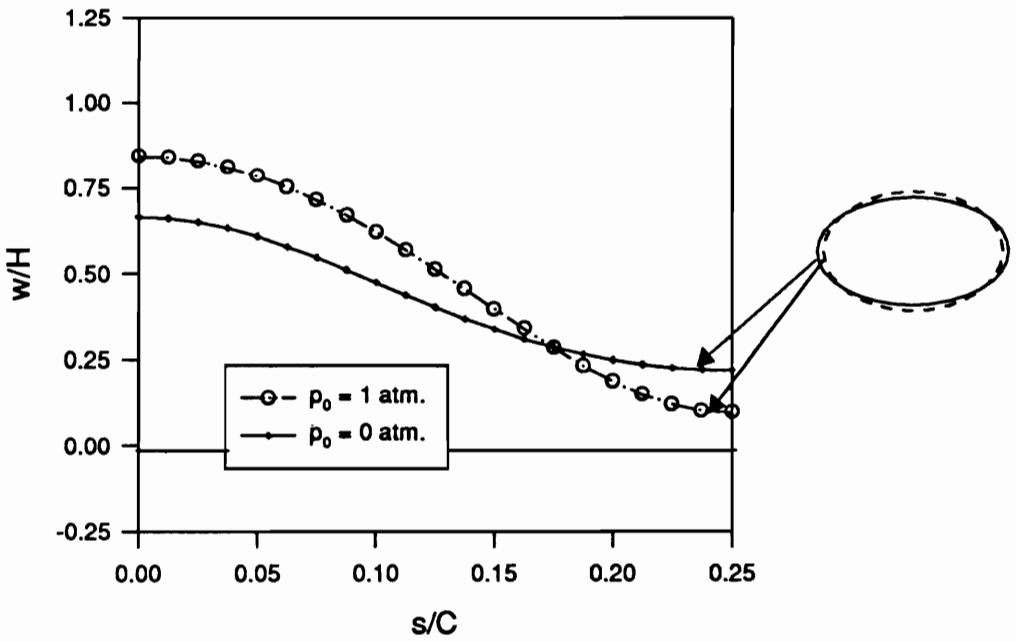

Figure 4-32 Comparison of Midspan Normalized Radial Displacement, Axial End-Shortening at 90% of Buckling for Pressurized and Unpressurized Cylinders.

results. In addition, with internal pressure added the maximum value of radial displacement at s/C = 0, and the minimum value at s/C =1/4, are both, as expected, more extreme than the maximum and minimum values obtained for pure axial compression.

It is clear that the response of elliptical cylinders to simple load conditions is not necessarily simple. In all cases, the response is dependent upon both the axial and circumferential coordinates. This is true even in the "membrane" region of such cylinders. In order to properly design structures using noncircular cylinders, these issues must be understood. The present analysis provides an efficient tool for studying the behavior of elliptical cylinders in response to simple load conditions, with the additional benefit that physical issues can be studied by examining the coefficient functions in the series and their dependence on the axial coordinate.

Analytical studies must be supplemented, however, with experimental results. In the next chapter, the accompanying experimental portion of this research is discussed, and in ch. 6 the experimental results are compared with analytical results.

Chapter 5.0 Description of Experiments

Several major tasks were undertaken in preparation for the experimental component of the present investigation. The first task was to develop the specifications for the graphite-epoxy test specimens. It was decided that the smallest practical ratio of semi-minor axis to semi-major axis would be b/a = 0.70. For convenience of manufacture and fixturing, it was further decided to hold the major axis constant for all cross sections, and to only vary the minor axis such that ratios of b/a = 0.70, 0.85, and 1.00 would be obtained. Because the analysis is restricted to thin shells, it was also necessary that $R_{min}/H > 50$. These factors and other size considerations resulted in an eight-ply wall construction and a semi-major axis of 5.0 in. (127 mm). After obtaining suitable mandrels, the second major task was to develop a workable method to lay-up and cure the specimens within the constraints of the available facilities. Lastly, it was necessary to design test fixtures. This required developing a design for functional and economical end caps appropriate for low level internal pressure as well as axial compression to failure.

These preparatory tasks resulted in the production of three 20 in. (508 mm) long aluminum mandrels, nine graphite-epoxy test specimens, three sets of end caps, and other associated hardware and procedures. Details of the specimen production may be found in Appendix B. Details of the resulting specimens, end caps, and testing procedure will be described in the following sections.

Test Fixtures

Three sets of end caps, one set for each cross sectional shape, were designed and fabricated for the experimental program. A schematic of a specimen in this fixture is shown in Figure 5-1. In order to provide test fixtures which could be used for both axial compression and internal pressure, end caps were designed with elliptical grooves machined into aluminum plates. Details of the bottom end cap for the case b/a = 0.70 are shown in Figure 5-2. One-inch deep grooves were machined into a 2.5 in. thick aluminum plate. The grooves were made 0.75 in. wide to allow for ease of positioning and potting of the cylinders, and care was taken to ensure that the bottom of the groove and the back surface of the end cap were flat and parallel to each other.

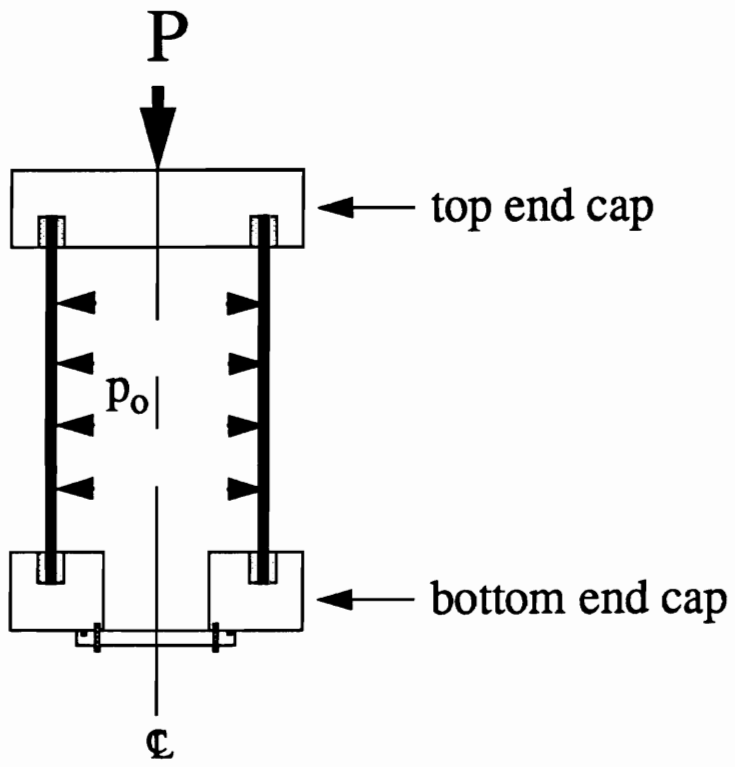

Figure 5-1 Schematic of Test Specimen in Fixture.

The corners of the aluminum end caps were removed due to limitations on the length of the probe that would be used to measure geometric imperfections in the cylinders after potting (see Appendix A), as well as to reduced their weight. It should be noted that excess bulk was provided in the design of these end caps so that they might be more easily modified for future tests involving much higher levels of internal pressure.

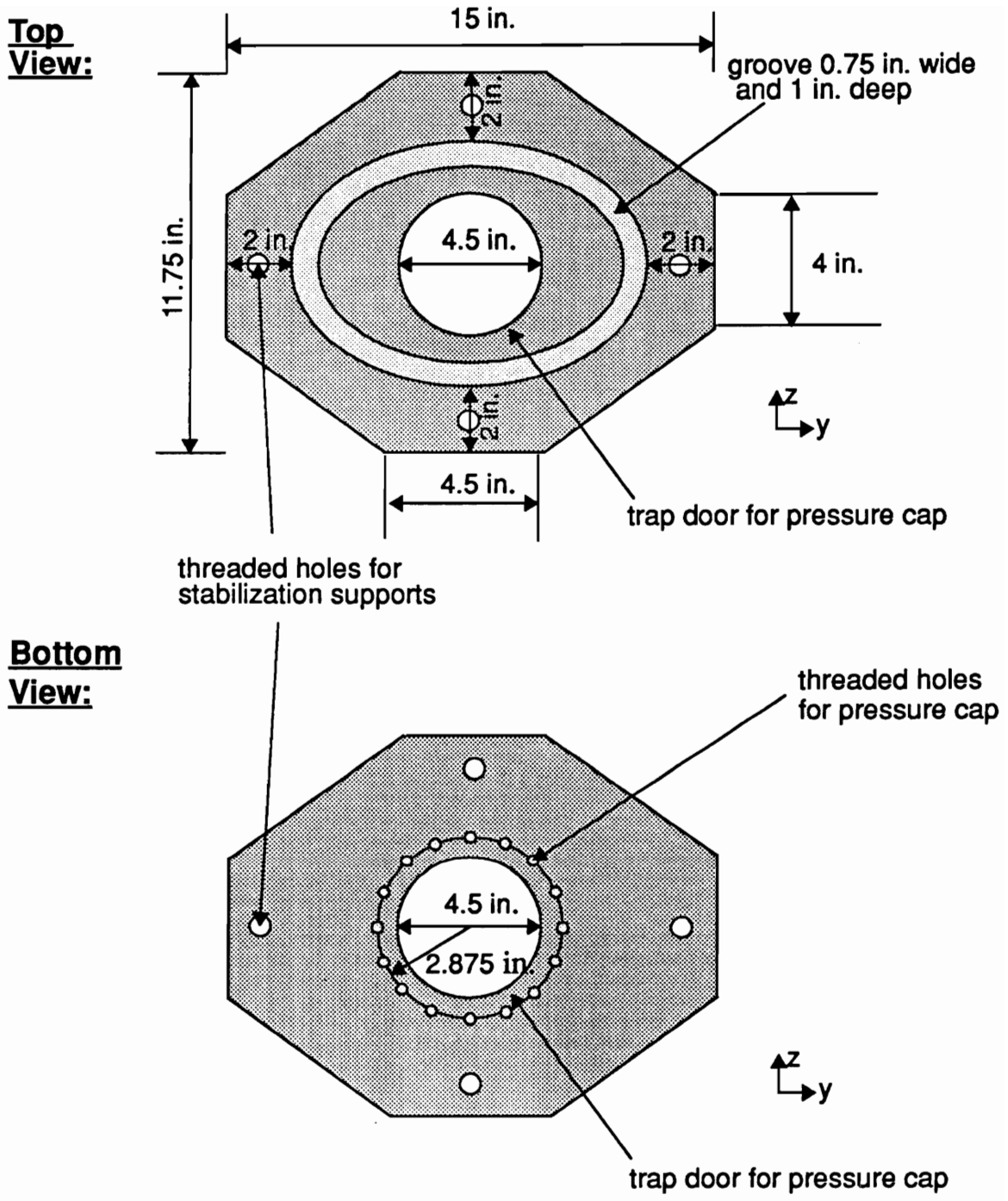

Figure 5-2 Details of the Bottom End Cap for Cylinders with b/a = 0.70: Top and Bottom Views.

To accommodate the pressure port and wiring for the internal strain gages, a circular 'trap door' was cut into each bottom end cap. In order to use a pre-existing pressure cap with a specially designed compact instrumentation feed-through, the size of the trap door was made the same for each bottom end cap. A schematic of this pressure and instrumentation feed-through and the attached pressure cap is shown in Figure 5-3. It should be noted that some leaking was known to occur around the wire insulation on this

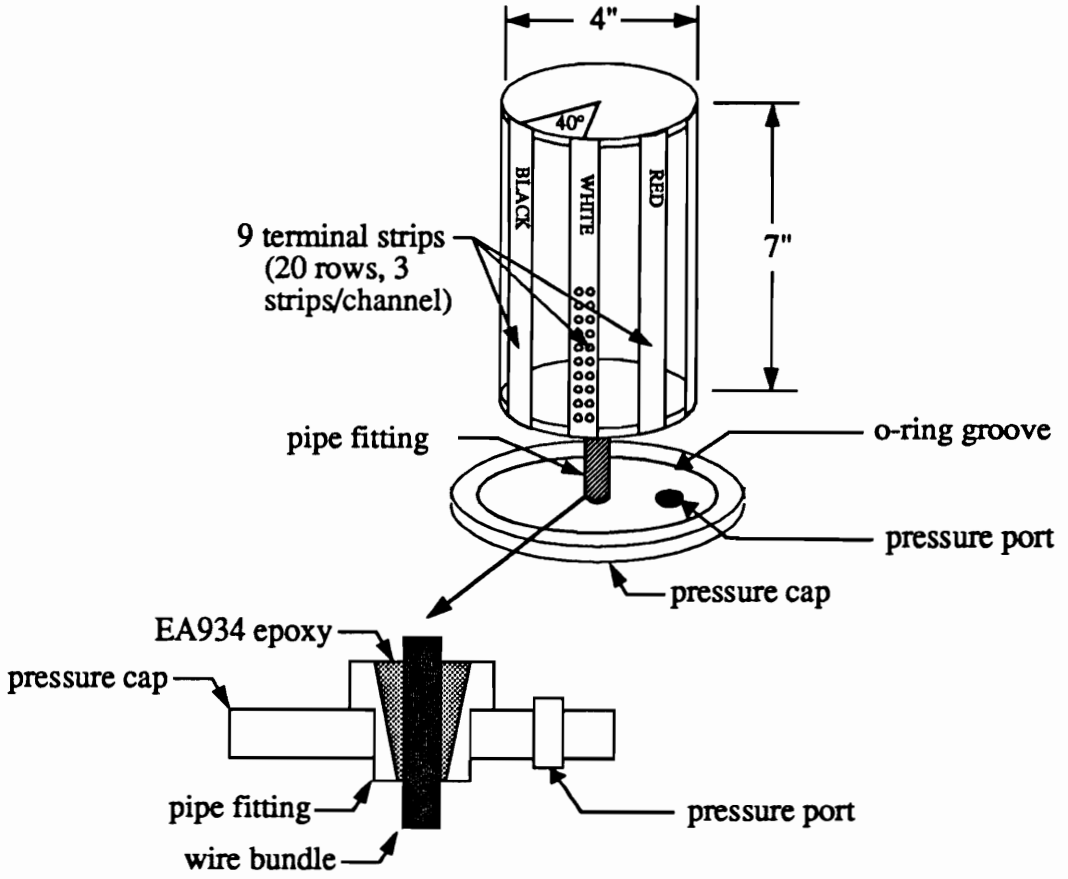

Figure 5-3 Schematic of Pressure Cap and 60 Channel Instrumentation Feed-Through.

feed-through, but in tests by the designer [50] the leak rate was found to be only 0.4 atm./min. at 10 atm. internal pressure. The bottom side of each bottom end cap contained a ring of threaded holes by which this pressure cap could be attached. In addition, four threaded holes were placed in each end cap so that long, threaded rods could be used to stabilize the whole assembly for transport.

Specimens

Nine eight-ply graphite-epoxy specimens, three lay-ups for each of the three cross sections, were fabricated and tested. The lay-ups studied were a quasi-isotropic $(\pm 45/0/90)_s$, an axially-stiff $(\pm 45/0_2)_s$, and a circumferentially-stiff $(\pm 45/90_2)_s$. The nominal semi-major axis for all specimens was 5.00 in. (127 mm), and all specimens were cut to the same length, 14.5 in. (368 mm), resulting in a gage length of 12.5 in. (327 mm). This provided a length-to-radius ratio of 2.9 for the circular cylinders. For the elliptical cross section cylinders with b/a = 0.85 and b/a = 0.70, the length-to-radius ratios ranged from just under two to just over six for b/a = 0.70, and from just under 2.5 to just over four for b/a =0.85. The specimen lay-ups and parameters are summarized in Table 5-1. The cylinder thicknesses given in this table were averaged from 32 caliper measurements taken at four axial and eight circumferential locations. The values reported as 'best fits' for the semi-major and semi-minor axes were calculated using data from the measurements of the outer surfaces of the cylinders, as described in Appendix A.

Table 5-1 Summary of Test Specimen Parameters.

aspect ratio	Lay-up	Avg. H, in.	best fit. a, in.	best fit b, in.	best fit b/ best fit a	L/R_{max}	R_{min}/H
b/a = 1.00	$(\pm 45/0/90)_s$	0.0438	4.987	4.978	0.998	2.91	113.84
	$(\pm 45/0_2)_s$	0.0443	4.981	4.979	0.999	2.91	112.35
	$(\pm 45/90_2)_s$	0.0437	4.990	4.979	0.998	2.90	113.68
b/a = 0.85	$(\pm 45/0/90)_s$	0.0439	4.980	4.248	0.853	2.48	82.52
	$(\pm 45/0_2)_s$	0.0442	4.983	4.243	0.852	2.48	81.75
	$(\pm 45/90_2)_s$	0.0440	4.980	4.250	0.853	2.48	82.44
b/a = 0.70	$(\pm 45/0/90)_s$	0.0440	4.980	3.511	0.705	2.05	56.27
	$(\pm 45/0_2)_s$	0.0439	4.990	3.494	0.700	2.04	55.72
	$(\pm 45/90_2)_s$	0.0445	4.989	3.504	0.702	2.04	55.30

All specimens were fabricated from 12- in. wide Hercules AS4/3501-6 graphite-epoxy tape. A C-Scan of each specimen was conducted to assess the specimen's initial condition. The cylinders were then cut to length and their ends machined flat and parallel. The fabrication, nondestructive evaluation, and machining of the specimens are described in Appendix B.

The specimens were instrumented after being cut to length. As a matter of convenience, prior to potting, the interior of each specimen was strain gaged. Specimen ends were potted using epoxy in the elliptical

grooves of the end caps described above. After potting, shape imperfection data were obtained by accurate measurement of the cylinder's outer surface shape. Details of the surface shape measurement are given in Appendix A. Once the outer surface had been measured, gages were mounted on the exterior surface. In order to reuse the end caps, it was necessary after each test to heat the epoxy to remove the previous specimen and then machine out the remaining epoxy in preparation for potting the next cylinder.

In preparation for testing, the specimen was painted white to improve visualization of the deformations. The internal strain gage leads were attached to the instrumentation feed-through in the pressure cap. An O-ring and fresh vacuum grease were applied to the pressure cap and it was then bolted to the bottom end cap. A spacing ring with four two-inch wide grooves in the bottom was placed under the bottom end cap in order to run the interior strain gage leads out of the bottom of the assembly, as well as to run an air hose out from pressure port in the pressure cap. The specimen was then ready to be tested once the instrumentation and data acquisition setups were completed.

Fabrication of the circular and elliptical cross section mandrels was performed by Iowa-American Machine & Mfg. Co., Inc. of Osceola, Iowa, under contract to VPI&SU. Fabrication of the test fixtures, machining, and potting of the test specimens was performed under contract to NASA-LaRC by Advex Corporation of Hampton, Virginia. Surface measurements were performed by the Quality Assurance and Inspection Office laboratory at NASA-LaRC. The strain gages were applied by Modern Machine and Tool Co., Inc. of Newport News, Virginia, also under contract to NASA-LaRC.

Instrumentation and Data Acquisition

A typical test setup is shown in Figure 5-4. A total of 101 channels of data was acquired electronically during each test at a rate of approximately one reading of all channels per second. Applied loads were measured with a calibrated load cell and displacements measured with direct current differential transducers (DCDT's). Surface strains were measured by back-to-back strain gages. The gages and associated wiring, running axially, can be seen in the figure. Both video recordings and still photographs were taken for all tests. A shadow moire interferometry setup also was used during the testing, but did not prove to be useful due to the variable curvature of the specimens.

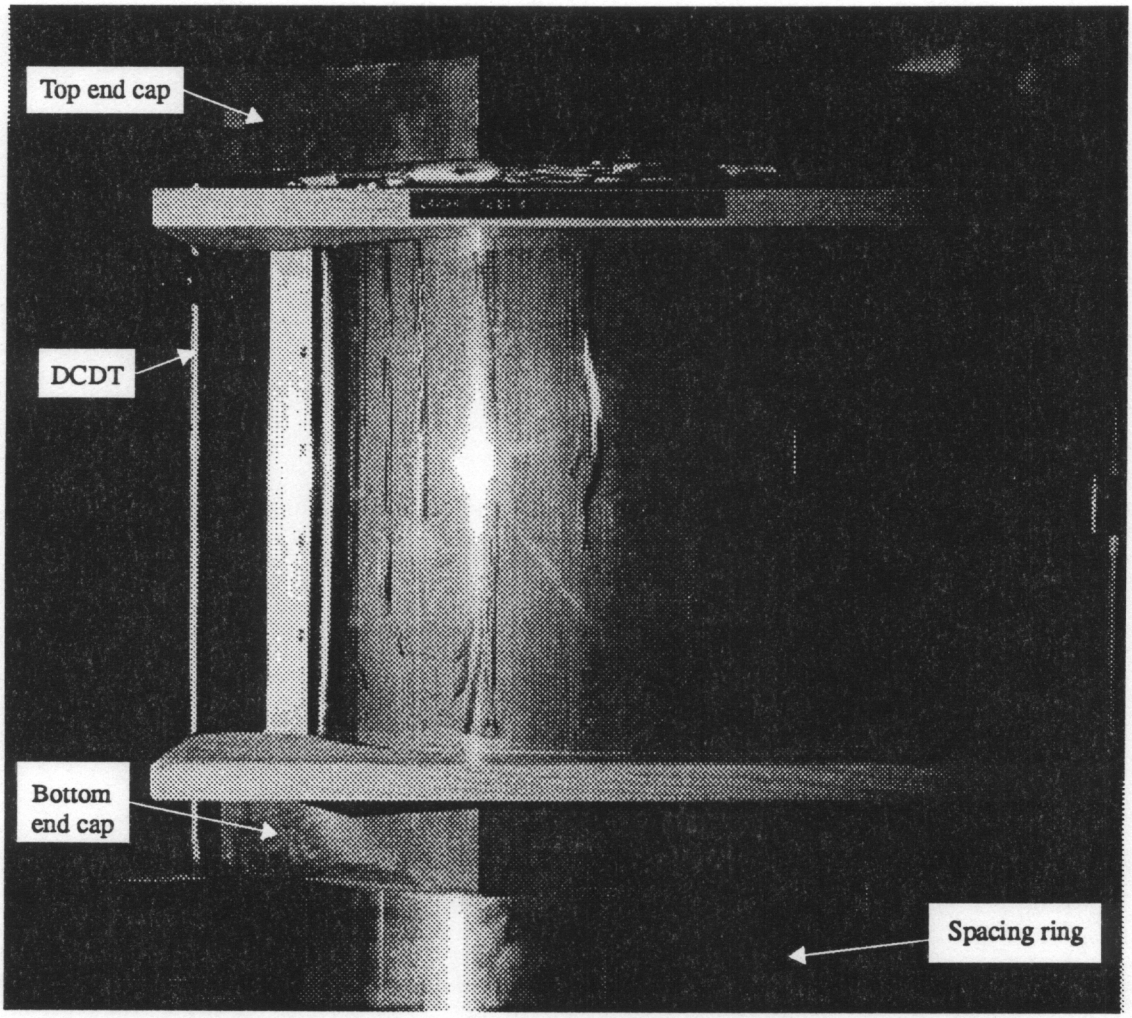

Figure 5-4 Typical Test Set-Up.

Back-to-back surface strains were measured at 44 locations on each cylinder. The general strain gage pattern for all test specimens is shown in Figure 5-5. It can be seen from this pattern that the majority of the gages are oriented axially, with the circumferential locations s/C = 0 and s/C = 1/4 being instrumented most heavily. Two axial locations, x/L = 0.0440 and x/L = 0.0, however, also contain several circumferential gages in order to investigate the circumferential strain under internal pressure and combined loading in both the membrane and boundary-layer regions. Radial displacements were also measured at these axial locations with DCDT's positioned at s/C = -1/2, -3/8, and -1/4. The locations of these DCDT's are indicated on Figure 5-5 by solid circles. The solid squares in Figure 5-5 indicate the position of DCDT's measuring axial displacement.

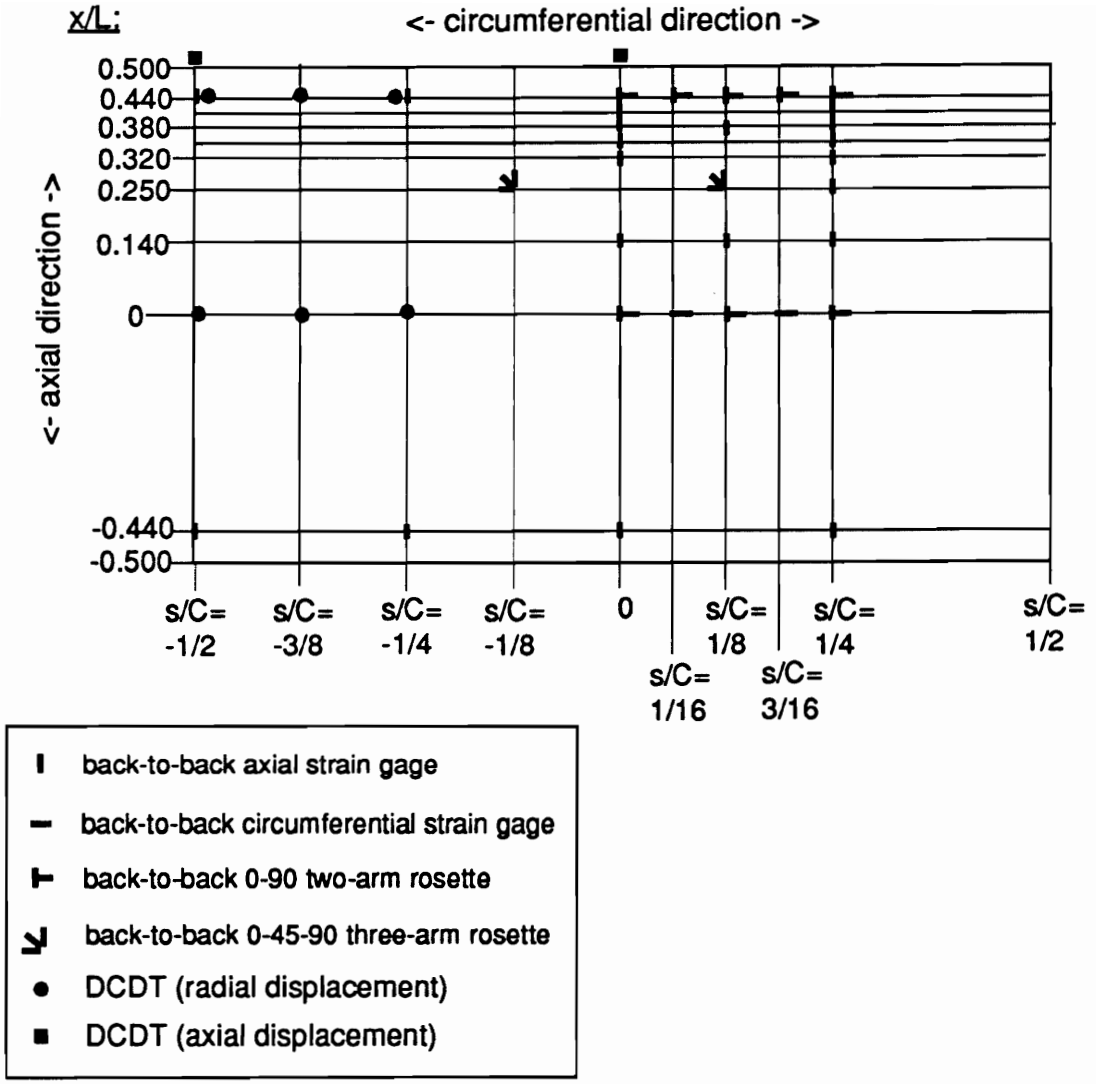

Figure 5-5 Typical Instrumentation Pattern.

Test Procedure

Three types of tests were run on each specimen: (1) 1 atm. internal pressure with zero end displacement, (2) 1 atm. internal pressure with compressive axial displacement to

$$\frac{\Delta}{L} = \frac{P}{E_x CH} = -0.000500, \tag{5.1}$$

and, (3) axial compression to failure with no internal pressure. These tests were conducted in the Structural Mechanics Laboratory at NASA-LaRC.

For the first test, pressure was controlled manually using an air pump with a regulator. The cylinders were loaded at roughly 0.33 atm. per minute until 1 atm. internal pressure was achieved and then unloaded at roughly the same loading rate. This method was also used for the second set of tests. For these second tests the cylinders were reloaded to 1 atm. internal pressure, after which a specified level of compressive axial displacement was applied using the screw-driven load frame. All loads were then released and the test repeated using the opposite load path, i.e., compressive axial displacement followed by internal pressure. No internal pressure was applied for the final test, in which the compressive axial displacement was increased until buckling, or material failure, of the specimen occurred. The specimen was held in ths state to observe the condition of the specimen and mark the deformation pattern.

Chapter 6.0 Comparison of Experimental and Analytical Results

The measured and observed experimental responses for the cylinders studied here are discussed and compared with the predicted responses in this chapter. The experimental data are first used to discuss the symmetry and uniformity of the test set up. Then for each load case the effects of cylinder ellipticity are discussed using results from the set of three $(\pm 45/0/90)_s$ cylinders. Following that, the effects of material orthotropy are discussed by comparing the results for the cylinders with b/a = 0.70 for each lay-up. Results for the other cylinders not discussed in this chapter are given, for completeness, in Appendix C. The test results are then compared to numerical predictions based on both perfect and geometrically imperfect cylinders. Prebuckling deflections and strain distributions are discussed and compared in detail. Buckling loads are also compared to predicted values based upon classical estimates as well as linear and nonlinear finite element results which include initial shape imperfections. Lastly, the postbuckling and failure characteristics observed during the tests are described.

Symmetry and Uniformity of Specimen Load State

Representative examples of the symmetry and uniformity of the cylinders' response in the experimental set-up are given in Figures 6-1 and 6-2 for the case of internal pressure and axial compression, respectively. These results are shown for the cylinder with a cross sectional aspect ratio of b/a = 0.70. In both figures, the axial midplane strains are graphed versus load parameter for the gages located near the top and bottom end caps, and at the circumferential locations at the ends of the minor and major diameters of the cross section (see Figure 5-5 for details).

As might be expected from the results shown in Figure 4-11, for internal pressure loads a distinct difference can be seen in Figure 6-1 between the axial midplane strains produced at the ends of the minor diameter (s/C = 0, 1/2) and those occurring at the ends of the major diameter (s/C = ±1/4). Comparing the results at the ends of the major diameter, an almost perfect symmetry of the response can be seen to exist both about the center of the cross section and about the midspan of the cylinder. The results at the ends of the minor diameter are not as perfectly uniform, but still show a reasonable degree of symmetry. At these locations the strain levels are much smaller and any normal scatter would be more evident. From these results, and similar results for the other cylinders, it was concluded that the pressure loading experimental set-up was loading the cylinders as intended.

The axial strains in Figure 6-2 are plotted versus the normalized load parameter P/P_{cr}, where P is the experimental axial load and P_{cr} is the classical buckling for the elliptical cylinder which is given in eqn. 4.2.

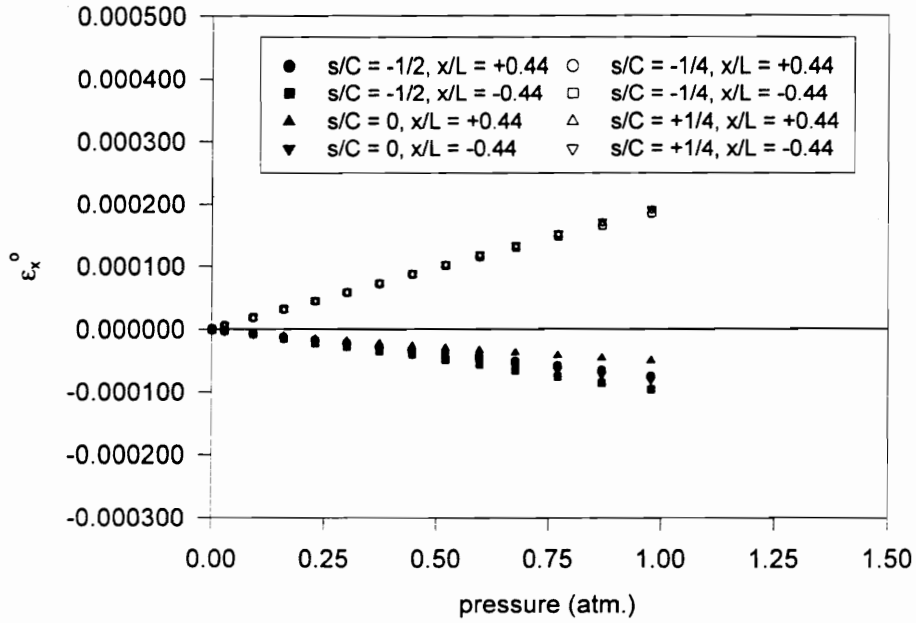

Figure 6-1 Symmetry Check for $(\pm 45/0/90)_s$ Cylinder, b/a = 0.70, Internal Pressure Loading.

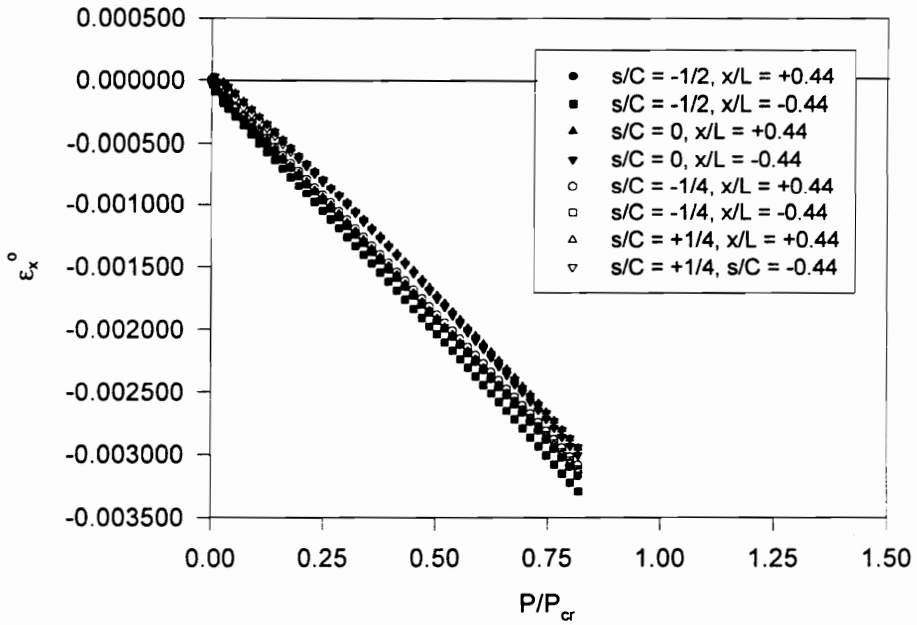

Figure 6-2 Symmetry Check for $(\pm 45/0/90)_s$ Cylinder, b/a = 0.70, Axial Compression Loading.

Unlike the results for the case of internal pressure, for axial end-shortening there is very little difference between the axial strains at different circumferential locations near the end caps. Once again the axial strains at s/C = ±1/4 are quite uniform, while those at s/C = 0, 1/2 are less so. In this case, however, at least some of the lack of uniformity is due to an initial nonlinear 'soft' response, which could be due to flexibility in the end fittings. For $P/P_{cr} > 0.25$, the results are quite linear and largely parallel, demonstrating that extraneous load states, such as bending, were kept to a minimum. Therefore, from these results, as well as those for the other cylinders, it was concluded that the axial loading experimental set-up was loading the specimens as intended.

Internal Pressure

Effects of Cylinder Geometry

As discussed in ch. 4, for internal pressure loads the response of elliptical cylinders, unlike circular cylinders, varies with the circumferential coordinate of the cylinder. This is illustrated in Figures 6-3 - 6-6, which show the normalized radial responses at midspan of the three $(\pm 45/0/90)_s$ cylinders discussed here as a function of internal pressure. For the most severely elliptical cross section considered in this study, b/a = 0.70, these results are shown in Figure 6-3. In this figure, experimental data taken at the cylinder midspan at s/C = 0, 1/8 and 1/4 are compared with the analysis results for the perfect cylinder, and STAGS predictions for the imperfect cylinder. A similar set of results are shown in Figure 6-4 for the cylinder having a mild

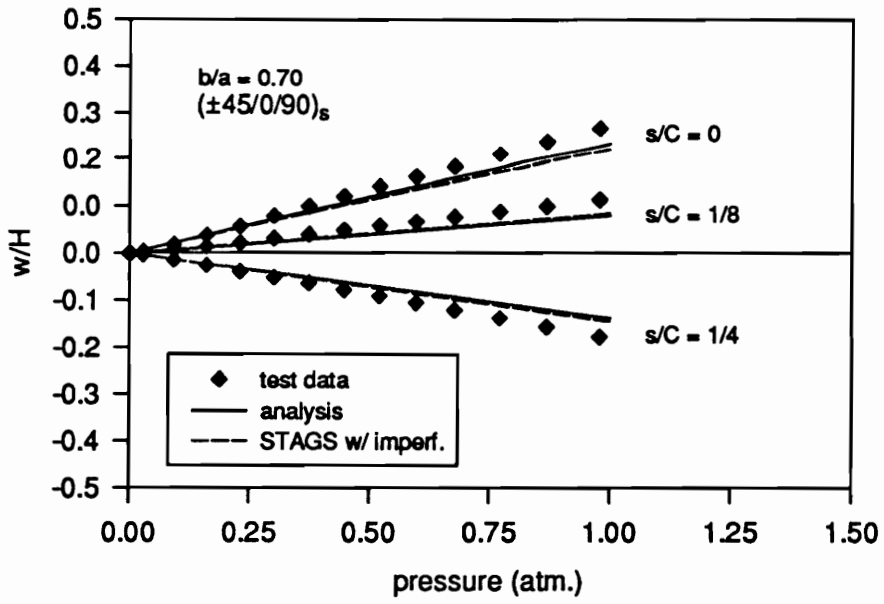

Figure 6-3 Normalized Radial Displacement at Midspan for the $(\pm 45/0/90)_s$ Cylinder, b/a = 0.70, Internal Pressure Loading to 1 Atm.

ellipticity (b/a = 0.85). For comparison, results for the circular cylinder, b/a = 1.00, are shown in Figure 6-5. In each of these cases there is good agreement between the experimental and predicted results. However,

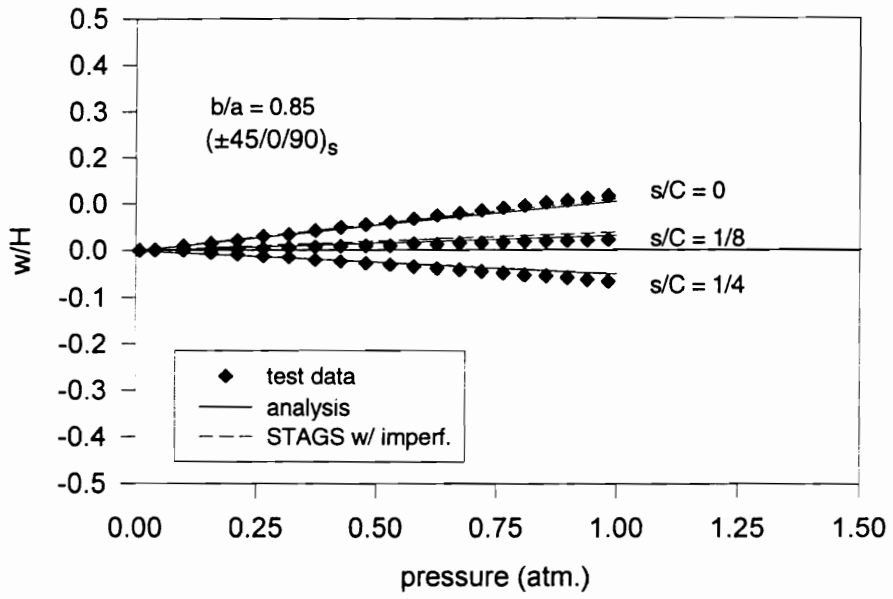

Figure 6-4 Normalized Radial Displacement at Midspan for the $(\pm 45/0/90)_s$ Cylinder, b/a = 0.85, Internal Pressure Loading to 1 Atm.

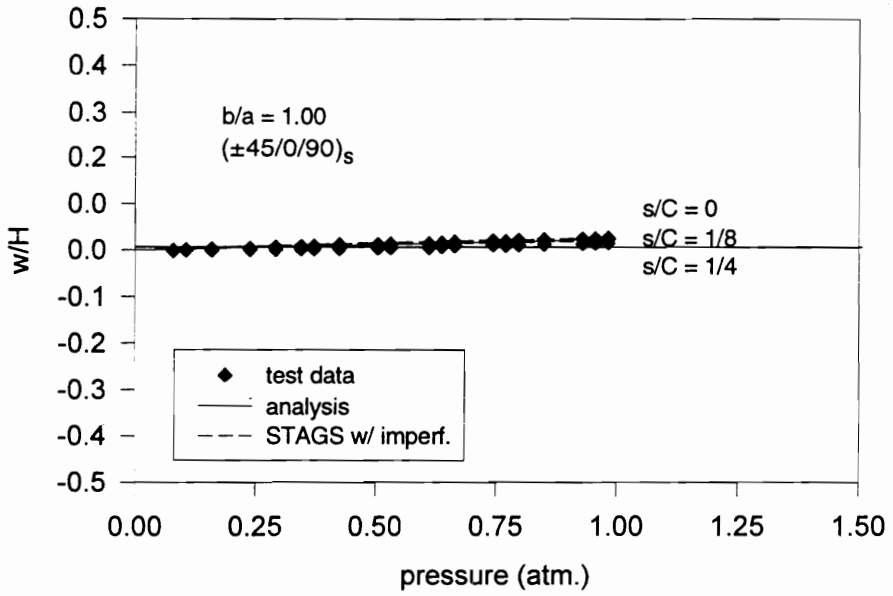

Figure 6-5 Normalized Radial Displacement at Midspan for the $(\pm 45/0/90)_s$ Cylinder, b/a = 1.00, Internal Pressure Loading to 1 Atm.

for the cylinders with b/a = 0.70 and b/a = 0.85, the experimental results show deflections greater than those predicted by the analyses. There is little difference, however, between the results calculated using the perfect and imperfect cylinder geometries. As expected for the circular cylinder, little difference can be seen between the measured results at the three circumferential locations. What differences there are can be assumed to be primarily a measure of the imperfections. The results shown in Figures 6-3 and 6-4 clearly confirm that for elliptical cylinders, even under very low pressure, the radial responses vary circumferentially, with the radial displacements becoming negative near the minimum radius of curvature (s/C = 1/4). As previously noted, this is due to the tendency of the elliptical cross sections to become more circular when loaded by internal pressure.

Although the results in Figures 6-3, 6-4, and 6-5 have all been plotted to the same scale, for further ease of comparison the analytical results at s/C = 0 and s/C = 1/4 for the perfect $(\pm 45/0/90)_s$ cylinders of each cross section are shown together in Figure 6-6. From this figure it can be clearly seen that the tendency of the cross section to become more circular under internal pressurization increases as the ellipticity of the cross section becomes more extreme.

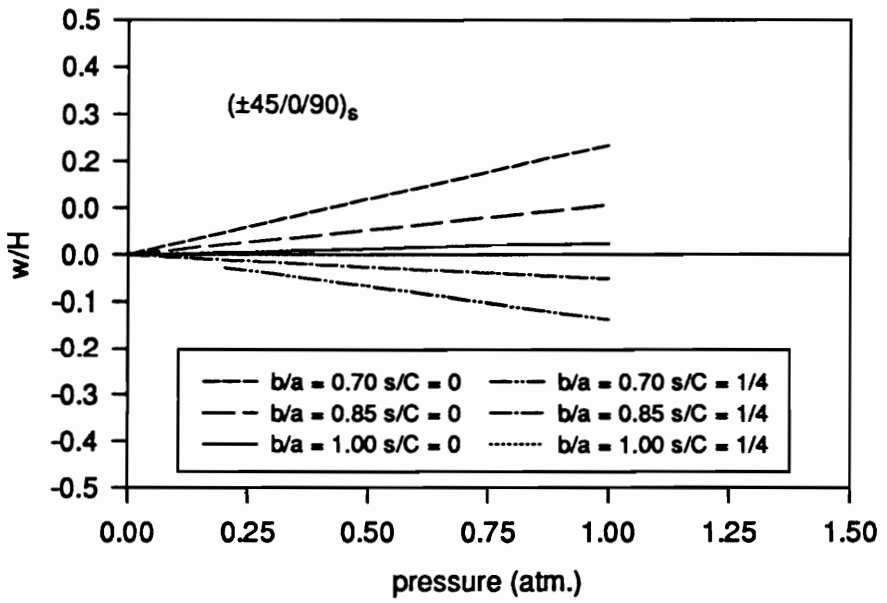

Figure 6-6 Comparison of Analytical Results for Normalized Radial Displacement at Midspan for the $(\pm 45/0/90)_s$ Cylinders, Internal Pressure Loading to 1 Atm.

This point is further illustrated in the following figures, which show the circumferential midplane strains, and the associated bending strains, $\kappa_s^o * H/2$, at midspan as functions of the internal pressure for the $(\pm 45/0/90)_s$ cylinders. The circumferential strains for the cylinder with b/a = 0.70 at the circumferential

locations s/C = 0, 1/8, and 1/4 are shown in Figure 6-7, and the corresponding bending strains at the same circumferential locations are shown in Figure 6-8. The circumferential midplane strain clearly varies with

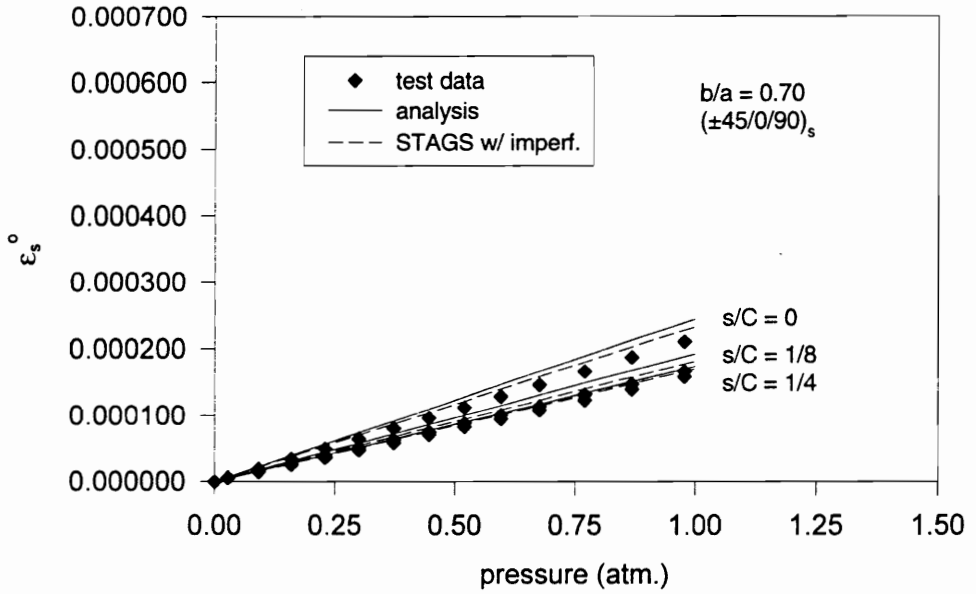

Figure 6-7 Circumferential Midplane Strain at Midspan for the $(\pm 45/0/90)_S$ Cylinder, b/a = 0.70, Internal Pressure Loading to 1 Atm.

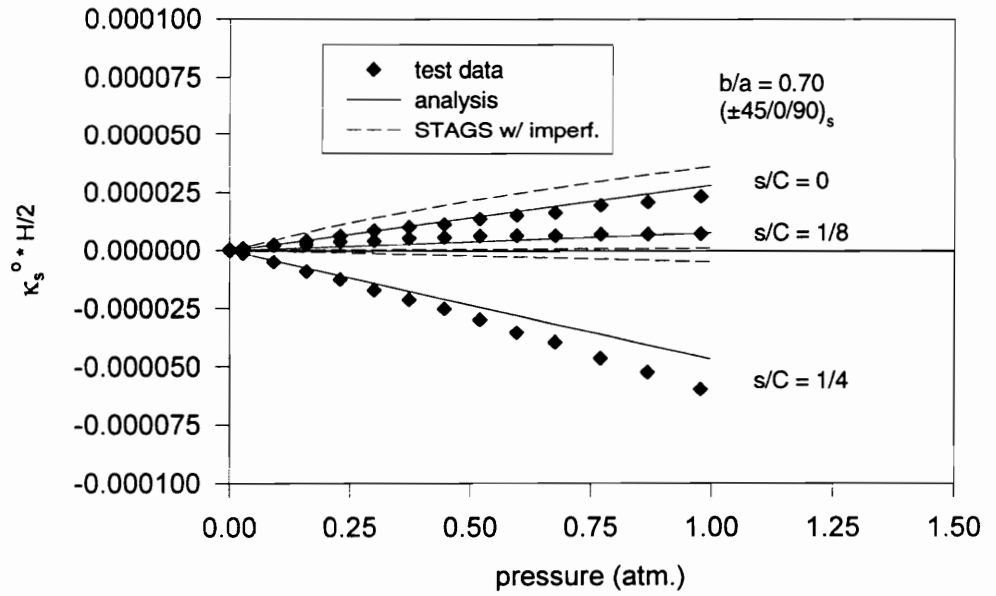

Figure 6-8 Circumferential Bending Strain at Midspan for the $(\pm 45/0/90)_S$ Cylinder, b/a = 0.70, Internal Pressure Loading to 1 Atm.

circumferential coordinate, although less dramatically than does the radial displacement. The bending strains, however, do exhibit a wide spread in the values between circumferential locations, varying from positive values at s/C = 0 to negative values at s/C = 1/4. This variation in the sign of the circumferential bending strains might be expected as they are related to the second derivative of the radial displacements with respect to the circumferential coordinate and the displacements are such that the cylinder is becoming more circular. Notice also that, even in the midspan "membrane" region of the cylinder, the magnitude of the circumferential bending strain is nearly one-half of the value of the circumferential midplane strain.

As can be seen, both the circumferential midplane and bending strains from STAGS and from the analysis agree fairly well with the experimental results. It is important to note that Figure 6-7 would suggest that the cylinder in the experiment with b/a = 0.70 was stiffer in the hoop direction than was assumed in the analyses. That is counter to Figure 6-3 which suggests that the cylinder in the experiment was softer. The addition of initial shape imperfections through the STAGS finite element model makes only a slight improvement over the results obtained from the analysis for the perfect cylinder for the circumferential midplane strains. However for the circumferential bending strains, oddly, the results from the imperfect cylinder at s/C = 1/4 deviate somewhat from the test data, while the prediction for the perfect cylinder matches the test data closely. It should be noted that for all three $(\pm 45/0/90)_s$ cylinders, despite attempting to keep the ends fixed against axial movement, a small degree of axial expansion ($\Delta/L < 0.000050$) occurred. This was due to the lack of complete control of the load frame within which the pressurization tests were conducted. Therefore, while the analysis for the geometrically perfect cylinders also assumed perfect boundary conditions, i. e., no axial expansion, the STAGS models included initial shape imperfections and this deviation from ideal end conditions, the magnitude of the deviation being determined from the axial DCDT data.

For the cylinder with b/a = 0.85, the circumferential midplane strains versus applied internal pressure are given in Figure 6-9, and the bending strains versus internal pressure in Figure 6-10. This cylinder's cross section is a mild ellipse, and the gradients of these responses are milder than those for the more severely elliptical cylinder with b/a = 0.70, especially the bending responses. Nevertheless, these responses are different from those for the circular cylinder, which are shown in Figure 6-11 for the circumferential strains, and in Figure 6-12 for the bending strains, where the slight variation with circumferential location is primarily attributable to initial shape imperfections. For these quantities, the cylinder with b/a = 0.85, and to a lesser extent the circular cylinder, represent the first examples examined here in which results from STAGS which include shape imperfections and lack of ideal end fixation make a definite improvement in the correlation with the experimental data, as compared to the correlation of the experimental data with the analytical results for the perfect cylinders.

A clearer view of the distribution of the circumferential midplane strain at midspan can be gained by plotting the circumferential strain at 1 atm. internal pressure against the normalized circumferential

coordinate, s/C, over one quarter of the cylinders' cross sections. Plots of this type for the $(\pm 45/0/90)_S$ cylinders with b/a = 0.70, 0.85, and 1.00 are given in Figures 6-13, 6-14, and 6-15, respectively. In all three

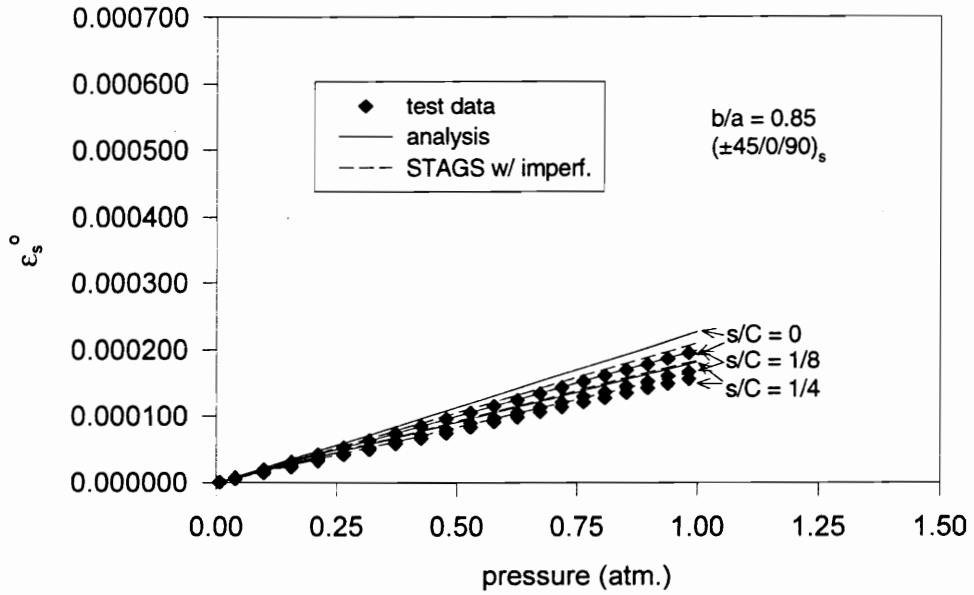

Figure 6-9 Circumferential Midplane Strain at Midspan for the $(\pm 45/0/90)_S$ Cylinder, b/a = 0.85, Internal Pressure Loading to 1 Atm.

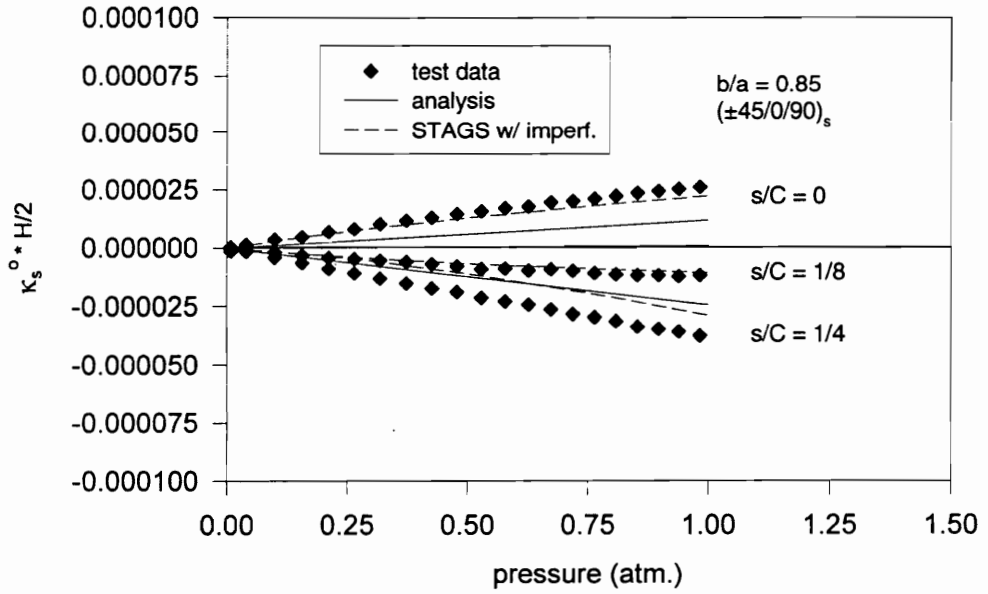

Figure 6-10 Circumferential Bending Strain at Midspan for the $(\pm 45/0/90)_S$ Cylinder, b/a = 0.85, Internal Pressure Loading to 1 Atm.

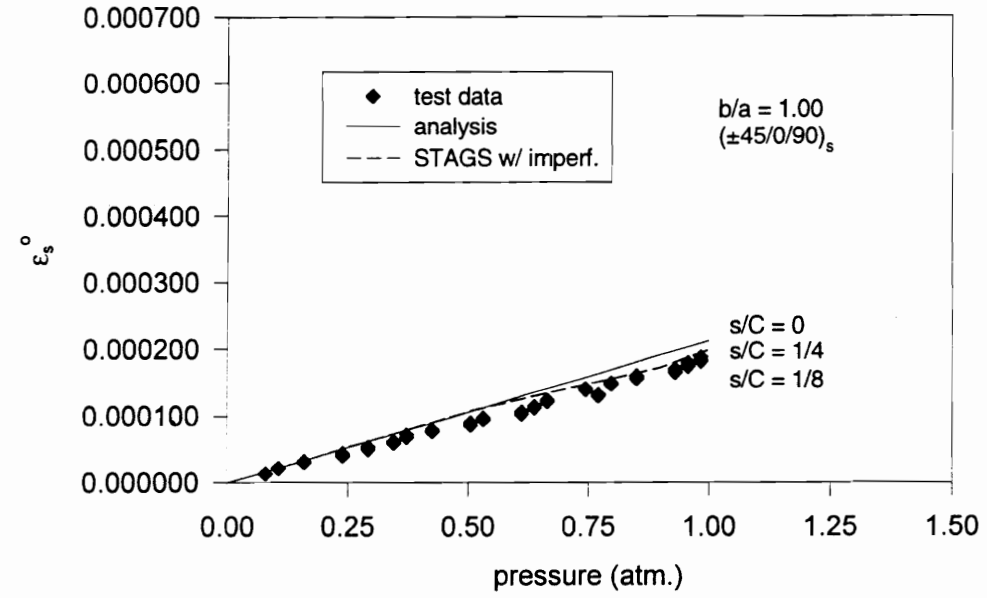

Figure 6-11 Circumferential Midplane Strain at Midspan for the $(\pm 45/0/90)_s$ Cylinder, b/a = 1.00, Internal Pressure Loading to 1 Atm.

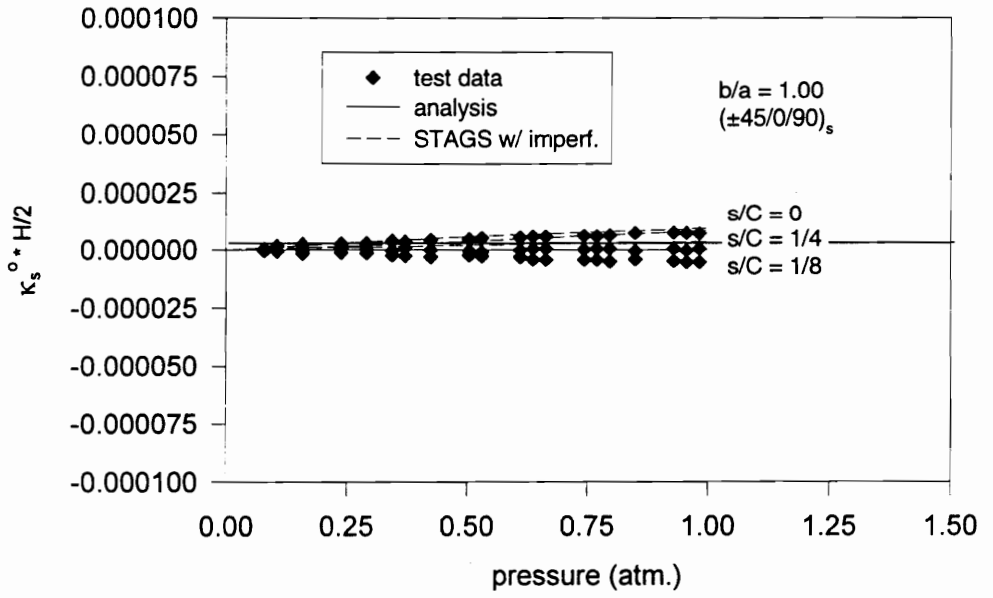

Figure 6-12 Circumferential Bending Strain at Midspan for the $(\pm 45/0/90)_s$ Cylinder, b/a = 1.00, Internal Pressure Loading to 1 Atm.

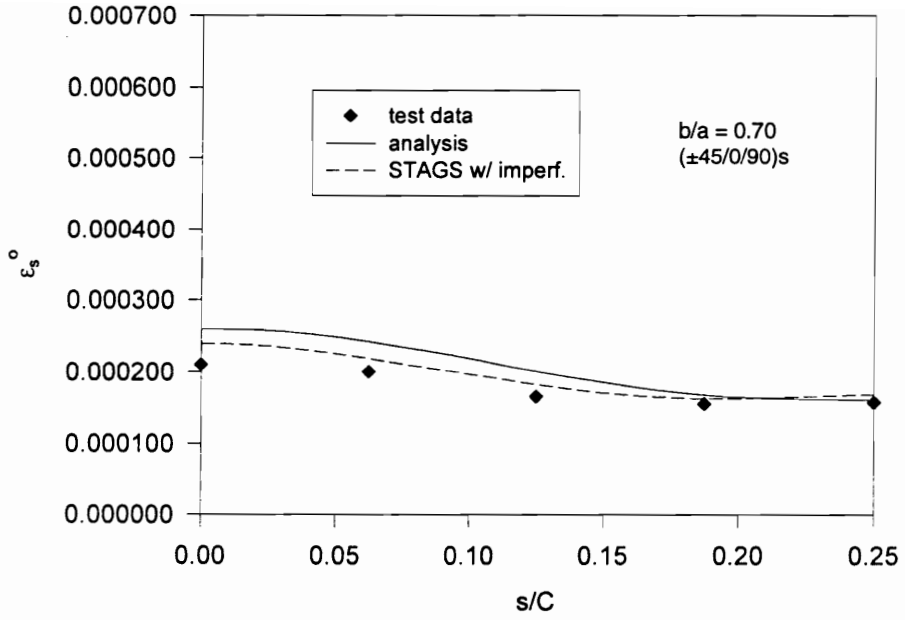

Figure 6-13 Circumferential Midplane Strain vs. s/C at Midspan for the $(\pm 45/0/90)_S$ Cylinder, b/a = 0.70, 1 Atm. Internal Pressure.

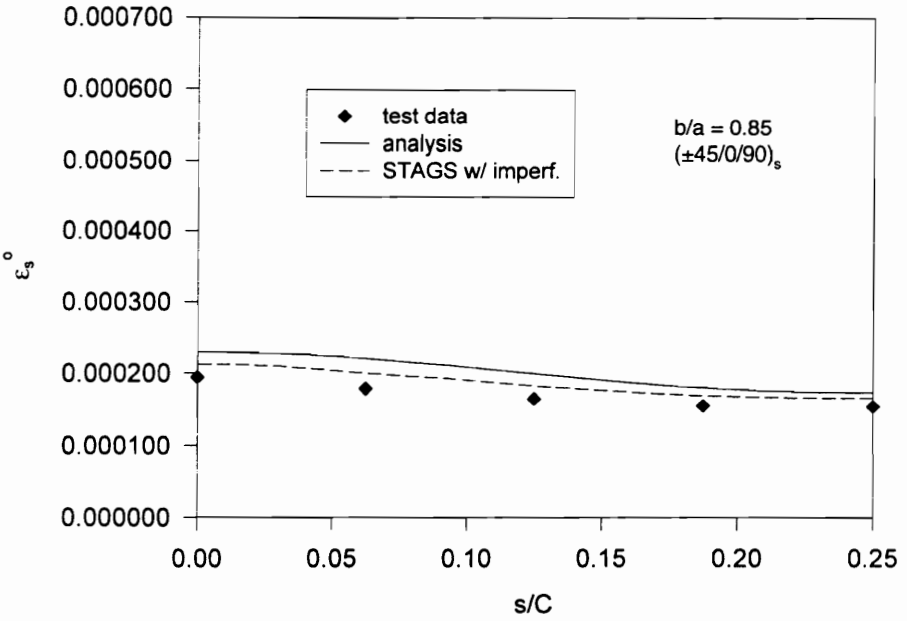

Figure 6-14 Circumferential Midplane Strain vs. s/C at Midspan for the $(\pm 45/0/90)_S$ Cylinder, b/a = 0.85, 1 Atm. Internal Pressure.

cases, the experimental strains are slightly lower than the calculated strains, with STAGS results for the imperfect cylinders closer than the results calculated from the analysis for the perfect cylinders. The improved correlation for the imperfect cylinder is due primarily to the downward shift resulting from the inclusion of the nonideal end conditions in the form of a small amount of axial expansion. This is especially clear for the case of the circular cylinder, shown in Figure 6-15. Figures 6-13 - 6-15 again point to the cylinders in the experiments being stiffer in the hoop direction, in contrast to Figures 6-3 - 6-5 which suggest the opposite.

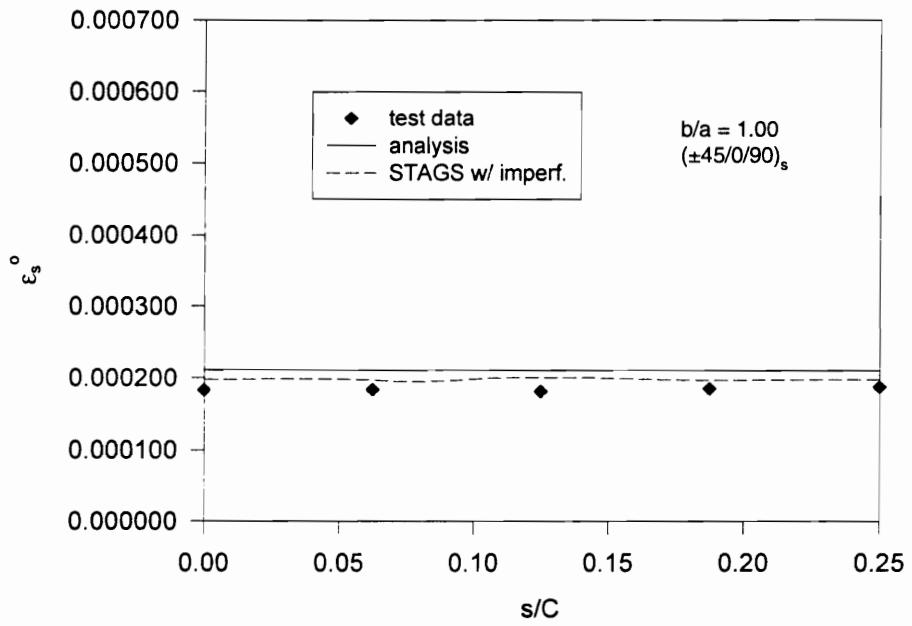

Figure 6-15 Circumferential Midplane Strain vs. s/C at Midspan for the $(\pm 45/0/90)_s$ Cylinder, b/a = 1.00, 1 Atm. Internal Pressure.

In order to provide a better comparison of the way in which the circumferential strain distribution varies with varying cross sectional ellipticity, the analytical results for all three perfect $(\pm 45/0/90)_s$ cylinders are graphed together in Figure 6-16. It can be seen that the variation of circumferential strain with circumferential coordinate also increases with increasing ellipticity of the cross section, especially in the region of the maximum radius of curvature, the flattest part of the ellipse.

Lastly, the axial midplane strain at a load level of 1 atm. of internal pressure is shown as a function of the normalized axial coordinate, x/L, at two circumferential locations, s/C = 0 and s/C = 1/4. The axial strains recorded from the experimental data and calculated for the perfect and imperfect cylinders are compared in Figures 6-17, 6-18, and 6-19 for the $(\pm 45/0/90)_s$ cylinders with b/a = 0.70, 0.85, and 1.00, respectively. The effects of the lack of perfectly fixed end conditions can be seen in a small shift of the results from STAGS, as

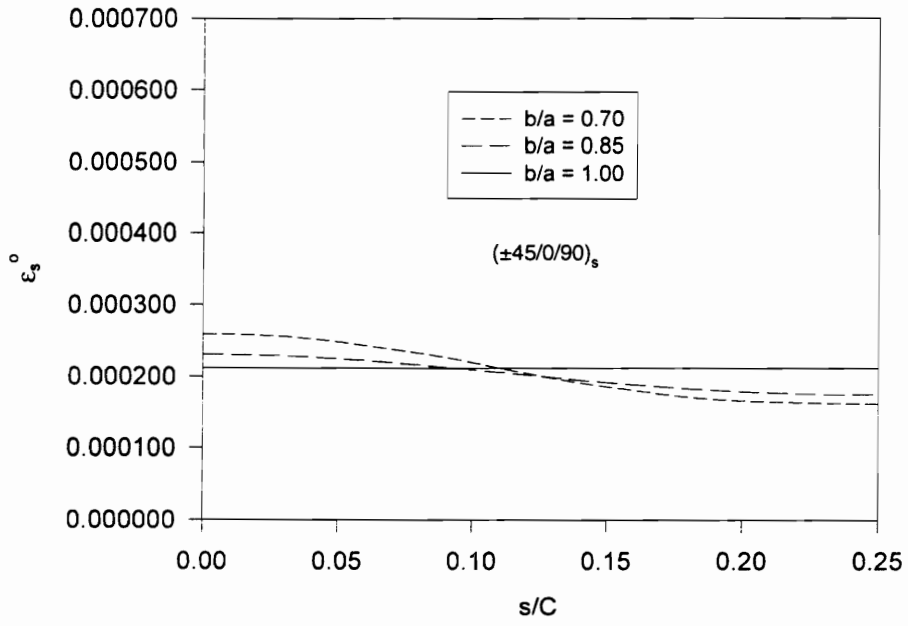

Figure 6-16 Comparison of Analytical Results for Circumferential Midplane Strain vs. s/C at Midspan for the $(\pm 45/0/90)_S$ Cylinders, 1 Atm. Internal Pressure.

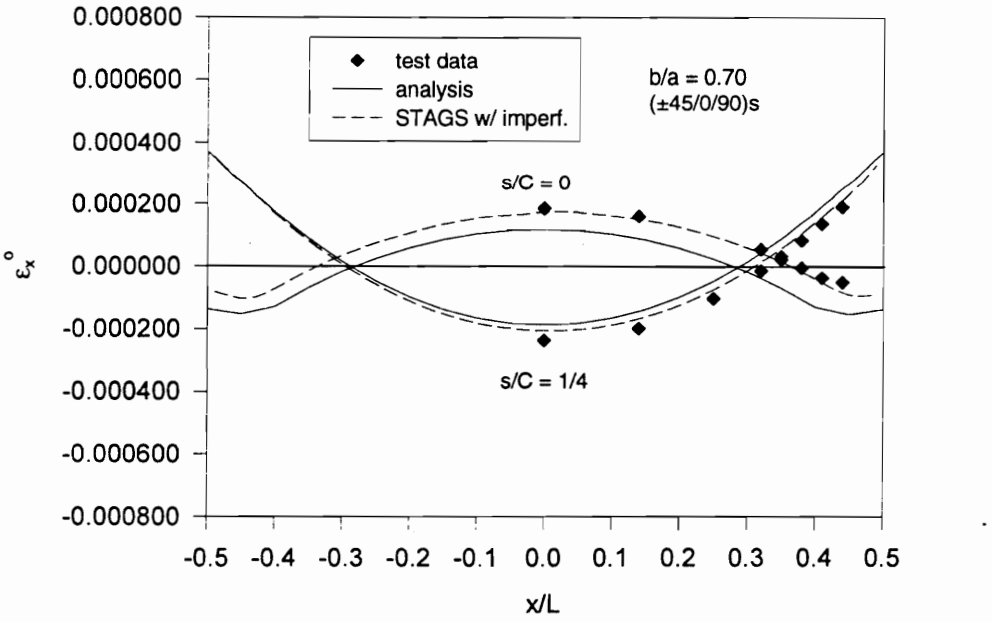

Figure 6-17 Axial Midplane Strain vs. x/Lfor the $(\pm 45/0/90)_S$ Cylinder, b/a = 0.70, 1 Atm. Internal Pressure.

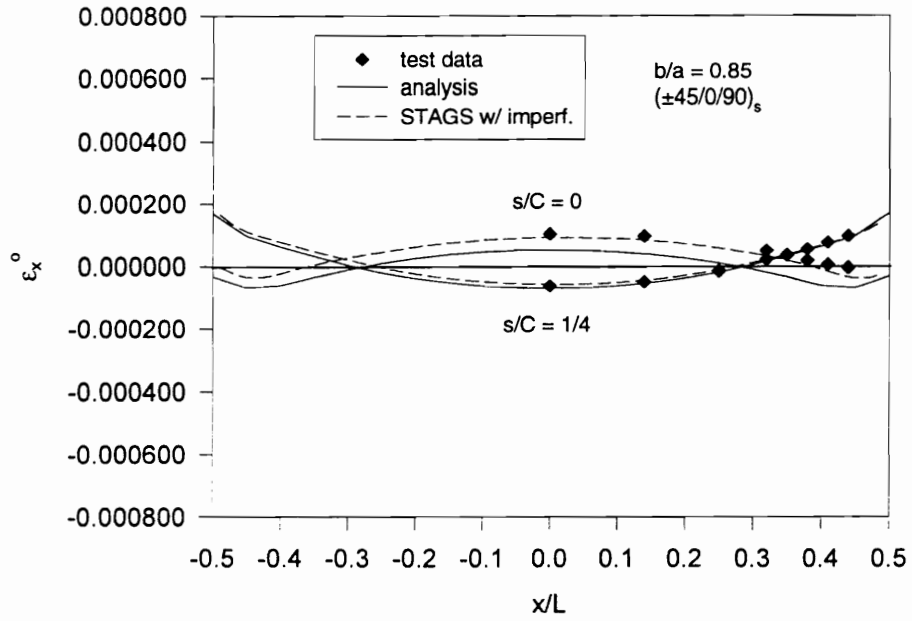

Figure 6-18 Axial Midplane Strain vs. x/L for the $(\pm 45/0/90)_s$ Cylinder, b/a = 0.85, 1 Atm. Internal Pressure.

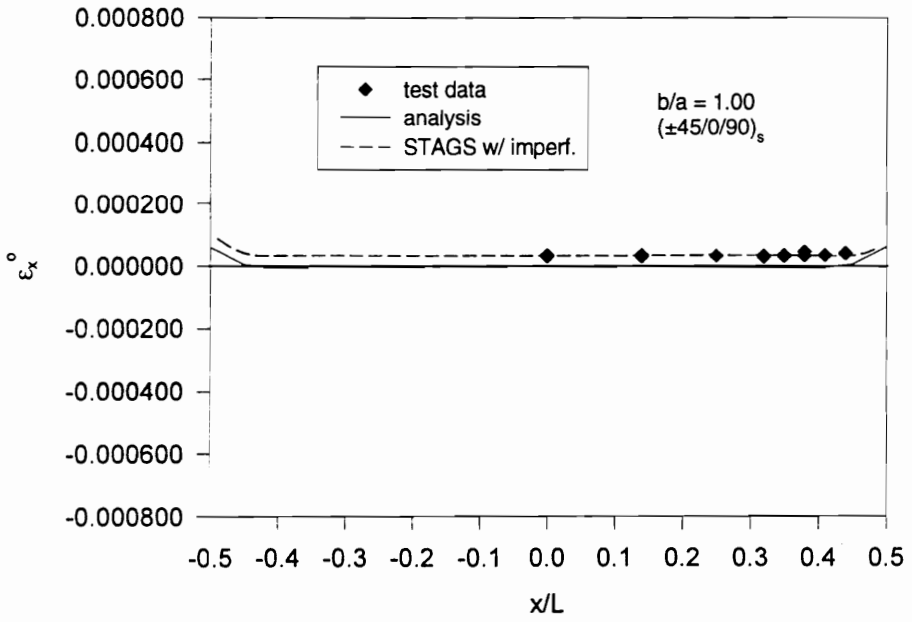

Figure 6-19 Axial Midplane Strain vs. x/L for the $(\pm 45/0/90)_s$ Cylinder, b/a = 1.00, 1 Atm. Internal Pressure.

compared to the results from the analysis for the perfect cylinders. Again, this can be seen most clearly in the results for the circular cylinder, shown in Figure 6-19. Unlike the results for circumferential strain, however, the consideration of geometric imperfections in the elliptical cylinders results in a somewhat greater spread in axial strains between s/C = 0 and s/C = 1/4 over most of the cylinders' lengths. In all three cases, there is excellent agreement between the experimental data and the results predicted from the STAGS models of the imperfect cylinders. It is safe to say, however, that the primary difference between the STAGS finite element results with initial imperfections and the analytical results is the inclusion of an unwanted amount of lengthening of the cylinders in the experiments. To be noted is the good agreement in axial stiffness of the cylinders in the experiments as compared to the cylinders in the analyses.

For ease of cross comparison, the analytical results for all three perfect $(\pm 45/0/90)_s$ cylinders are graphed together in Figure 6-20. From this figure, as well as the previous three figures, it can be seen that even at low pressure, with the ends largely restrained against axial movement, significant midplane axial strains are produced in the elliptical cylinders. Indeed, the axial strains at midspan are as great as the circumferential strains (see Figure 6-16). This is in agreement with the results discussed in ch. 4. Further, the axial strains vary with both the axial and circumferential coordinates, with the sign of the strain changing with both axial and circumferential location. As with the other quantities examined here, these tendencies become more pronounced as the ellipticity of the cross section becomes more extreme.

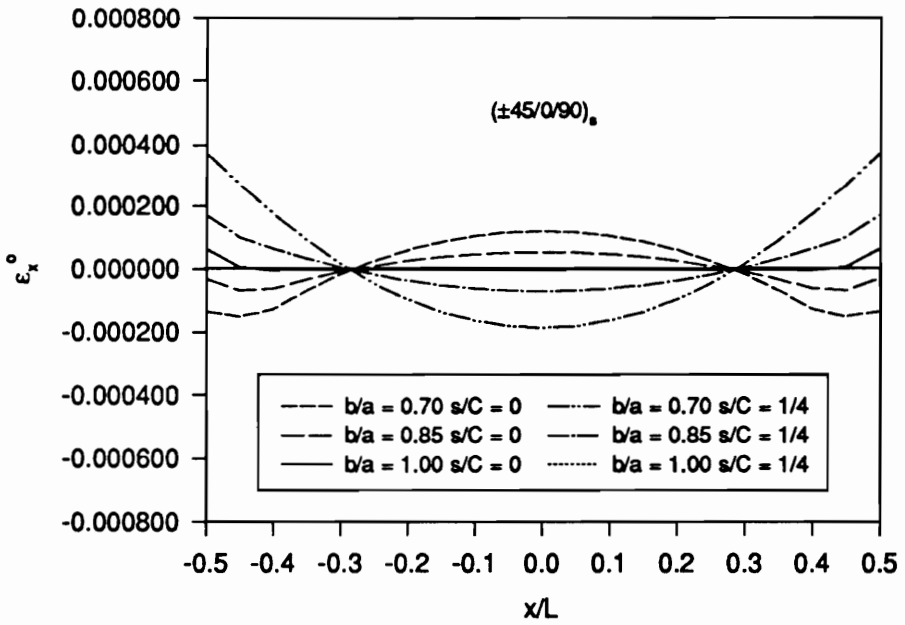

Figure 6-20 Comparison of Analytical Results for Axial Midplane Strain vs. x/L for the $(\pm 45/0/90)_s$ Cylinders, 1 Atm. Internal Pressure.

Effects of Cylinder Orthotropy

In order to illustrate the effects of material orthotropy on the responses of pressurized elliptical cylinders, results are given in this section for the axially-stiff $(\pm 45/0_2)_s$ and the hoop-stiff $(\pm 45/90_2)_s$ cylinders with the most severely elliptical cross section studied here, b/a = 0.70. For each case, experimental results are compared with the analysis results for the perfect cylinder, and STAGS predictions for the imperfect cylinder. These results are discussed and compared with those given in the previous section for the $(\pm 45/0/90)_s$ cylinder, b/a = 0.70. It should be noted that both the set of axially-stiff and the set of hoop-stiff cylinders displayed trends similar to those discussed above for the quasi-isotropic cylinders with regard to the sensitivity of their responses to cylinder ellipticity. The results for the $(\pm 45/0_2)_s$ and $(\pm 45/90_2)_s$ cylinders, b/a = 0.85 and b/a = 1.00, can be found in Appendix C.

The normalized radial displacement at midspan is given as a function of the internal pressure load at three circumferential locations, s/C = 0, 1/8, and 1/4, in Figure 6-21 for the $(\pm 45/0_2)_s$ cylinder and in Figure 6-22 for $(\pm 45/90_2)_s$ cylinder. These figures may be compared with Figure 6-3, which gives a similar set of relations for the $(\pm 45/0/90)_s$ cylinder, b/a = 0.70. As was the case for the quasi-isotropic cylinder, reasonable agreement can be seen for both of these cylinders between the calculated and experimental results. In these cases as well, the cylinders in the experiments appear to be softer in the hoop direction than was assumed in the analyses. There is little difference between the results calculated based upon perfect and imperfect cylinder geometries. The radial displacements also clearly vary with circumferential location for these elliptical cylinders, with the radial displacements at the minimum radius of curvature, s/C = 1/4, becoming negative, as was also the case for the quasi-isotropic elliptical cylinders.

In order to provide a clearer means for comparing these results for the radial displacements, the analytical results at s/C = 0 and s/C = 1/4 for the three cylinders with cross sectional aspect ratio b/a = 0.70 are given together in Figure 6-23. The values at s/C = 0 for the $(\pm 45/0_2)_s$ and $(\pm 45/90_2)_s$ cylinders are very close, and slightly greater than those obtained for the $(\pm 45/0/90)_s$ cylinder of the same cross section. At s/C = 1/4, however, a progression can be seen from the smaller negative value of the radial displacement for the axially-stiff cylinder to the largest negative value of radial displacement for the hoop-stiff cylinder. This indicates that the increased negative radial displacement response of the $(\pm 45/90_2)_s$ cylinder is due to the increased circumferential stiffness, as both A_{22} and D_{22} are greatest for this lay-up. That A_{22} will have this sort of influence can be seen by examining the membrane theory solution (see ref. 9), for which the normalized radial displacement at midspan is given by

$$\frac{w(0,s)}{H} = p_o R(s)\left\{\left(a_{22} - \frac{a_{12}^2}{a_{11}}\right)R(s) - \frac{L^2}{8}\left(a_{66} + \frac{a_{12}}{3}\right)\frac{d^2R}{ds^2} + a_{11}\left(\frac{L^4}{384}\right)\frac{d^3R}{ds^3}\right\}, \qquad (6.1)$$

where the a_{ij} are the elements of the inverse of the stiffness matrix, i. e., $[a] = [A]^{-1}$. Because R(s), the

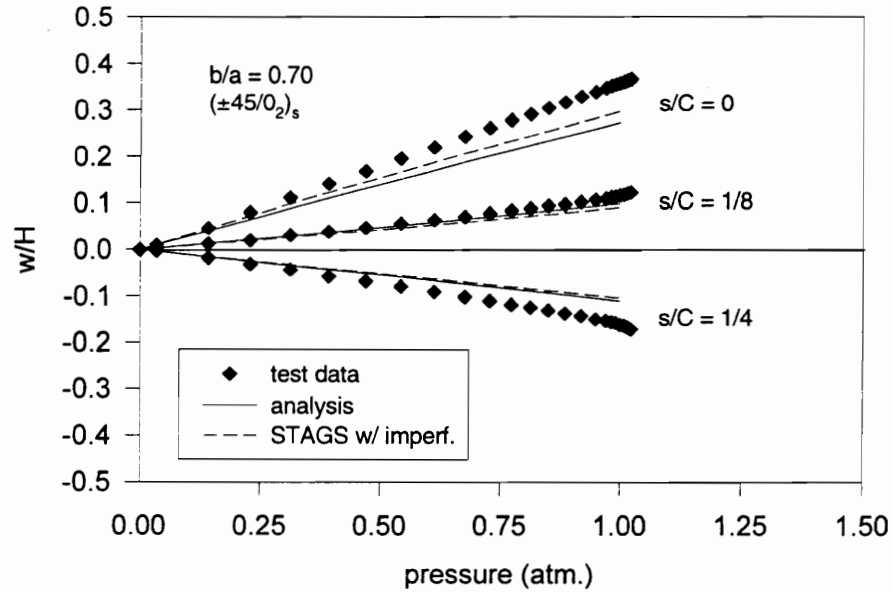

Figure 6-21 Normalized Radial Displacement at Midspan for the $(\pm 45/0_2)_s$ Cylinder, b/a = 0.70, Internal Pressure Loading to 1 Atm.

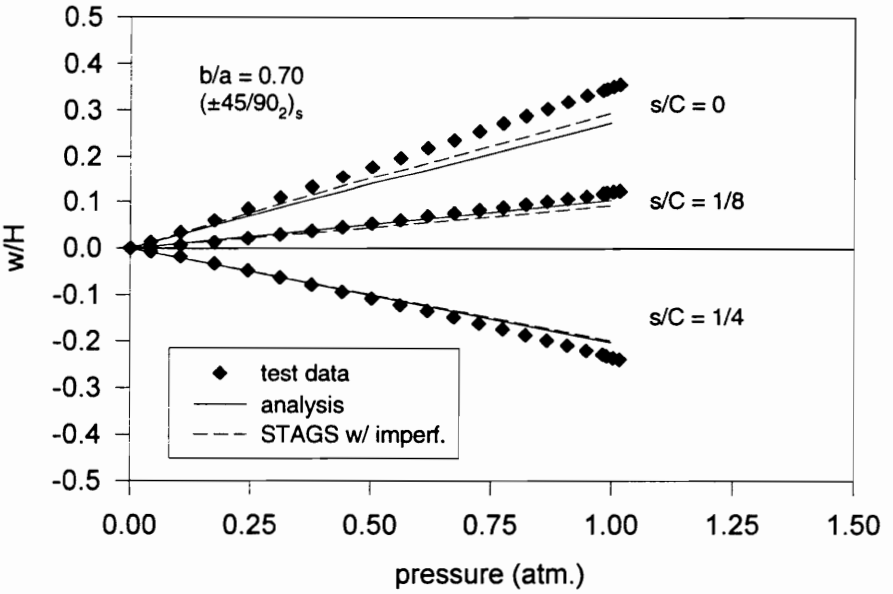

Figure 6-22 Normalized Radial Displacement at Midspan for the $(\pm 45/90_2)_s$ Cylinder, b/a = 0.70, Internal Pressure Loading to 1 Atm.

function describing the radius of curvature of the cross section, is the same for each of these cylinders, the difference in the values of the radial displacement at a given circumferential location for these cylinders is due to the differences in the stiffnesses. In particular, at s/C = 1/4, the term multiplying $a_{11} = A_{22}/\det[A]$ has the greatest influence. Therefore the hoop-stiff cylinder would be expected to have the largest negative value at this point. In general, the orthotropic elliptical cylinders exhibit larger variations in radial displacement with circumferential location than do the quasi-isotropic elliptical cylinders, with the largest variation occurring for the $(\pm 45/90_2)_s$ cylinder, b/a = 0.70.

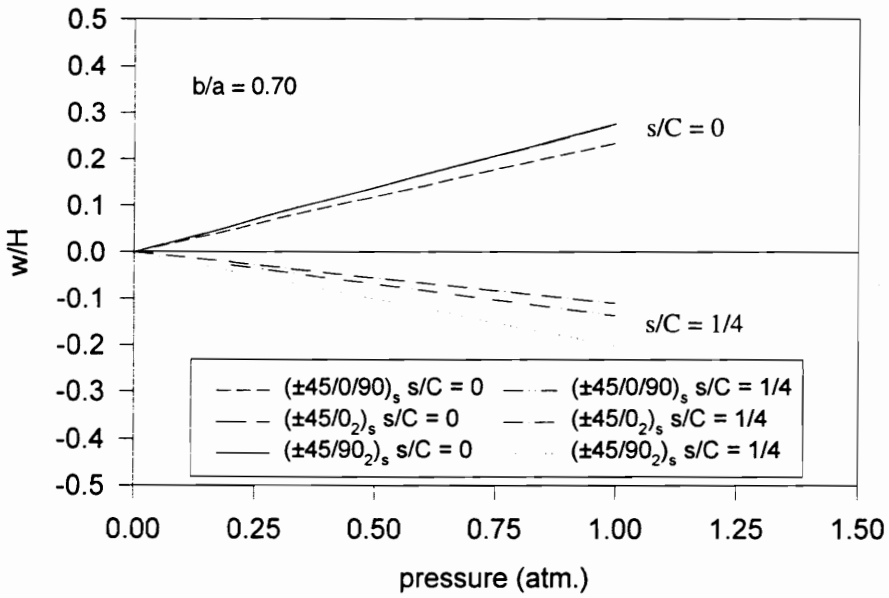

Figure 6-23 Comparison of Analytical Results for Normalized Radial Displacement at Midspan for the $(\pm 45/0/90)_s$, $(\pm 45/0_2)_s$, and $(\pm 45/90_2)_s$ Cylinders, b/a = 0.70, Internal Pressure Loading to 1 Atm.

The circumferential midplane strains, and their associated bending strains, κ_s*H/2, at midspan for the $(\pm 45/0_2)_s$ and $(\pm 45/90_2)_s$ cylinders, b/a = 0.70, are also plotted against internal pressure in the following figures. For the $(\pm 45/0_2)_s$ cylinder, the circumferential midplane strains at s/C = 0, 1/8, and 1/4, are shown in Figure 6-24, and the corresponding bending strains at the same circumferential locations are shown in Figure 6-25. For the $(\pm 45/90_2)_s$ cylinder, these circumferential midplane strains are given in Figure 6-26 and the associated circumferential bending strains are given in Figure 6-27. In each case, the circumferential strain varies with circumferential location, as was the case for the $(\pm 45/0/90)_s$ cylinder having the same cross section. As might be expected, the cylinder having a hoop-stiff lamination exhibits the lowest levels of circumferential midplane strains and the smallest variation of circumferential midplane strain with

circumferential position, the values at s/C = 0 and s/C = 1/8 being almost indistinguishable. The largest circumferential midplane strains and the largest circumferential variation in these strains occur in the $(\pm 45/0_2)_s$ cylinder, b/a = 0.70, which has the lowest stiffness in the circumferential direction. The results for the quasi-isotropic cylinder, b/a = 0.70, shown in Figure 6-7, are intermediate to these two sets of results. Notice also that the distribution of the circumferential midplane strains for the $(\pm 45/90_2)_s$ cylinder is reversed from that for the other two cylinders, the strains being are greatest at s/C = 1/4 and least at s/C = 0.

The circumferential bending strains for these cylinders also exhibit a clear spread in the values between the three circumferential locations, varying from positive at s/C = 0 to negative at s/C =1/4. These results are similar to those discussed in the previous section for the $(\pm 45/0/90)_s$ cylinder, b/a = 0.70, which are shown in Figure 6-8. Indeed the magnitudes of the bending strains for all three of the cylinders with a b/a = 0.70 cross sectional aspect ratio are quite similar, though the bending strains at s/C = 1/4 for the $(\pm 45/90_2)_s$ cylinder are the greatest among these cylinders. This is true despite the fact that D_{22} is largest for this lay-up. The difference that should be noted in studying these graphs is in the magnitudes of these bending strains in comparison to with the associated circumferential midplane strains for a each cylinder. It was noted from the discussion of the quasi-isotropic cylinder that the magnitude of the circumferential bending strains reached over 40% of the value of the circumferential midplane strain. For the $(\pm 45/0_2)_s$ cylinder, the circumferential bending strain is at most 20% of the midplane strain, while for the $(\pm 45/90_2)_s$ cylinder at s/C =1/4 the magnitude of the circumferential bending strain is nearly equal to the value of the corresponding circumferential midplane strain.

In each of these cases, the results from the analysis for the perfect cylinders and the STAGS results for the imperfect cylinders agree reasonably well with the experimental data. The inclusion of initial geometric imperfections through STAGS generally improves this correlation, especially in the case of the circumferential bending strains at s/C = 0 for the $(\pm 45/0_2)_s$ cylinder. For the $(\pm 45/90_2)_s$ cylinder, as with the quasi-isotropic cylinders, a small axial displacement occurred during the internal pressure test and this deviation from ideal end conditions was included in the STAGS model of the imperfect cylinder. The inclusion of this deviation from ideal end fixation is primarily responsible for the excellent correlation between the experimental data and the STAGS results, as compared to the correlation between the experimental data and the analytical results for the perfect cylinder, for the circumferential midplane strains in the $(\pm 45/90_2)_s$ cylinder.

In order to provide a better view the distribution of the circumferential midplane strains at midspan, the circumferential midplane strains at a load level of 1 atm. of internal pressure are graphed as a function of the normalized circumferential coordinate for the $(\pm 45/0_2)_s$ cylinder in Figure 6-28 and for the $(\pm 45/90_2)_s$ cylinder in Figure 6-29. A similar plot of the circumferential midplane strain results for the $(\pm 45/0/90)_s$

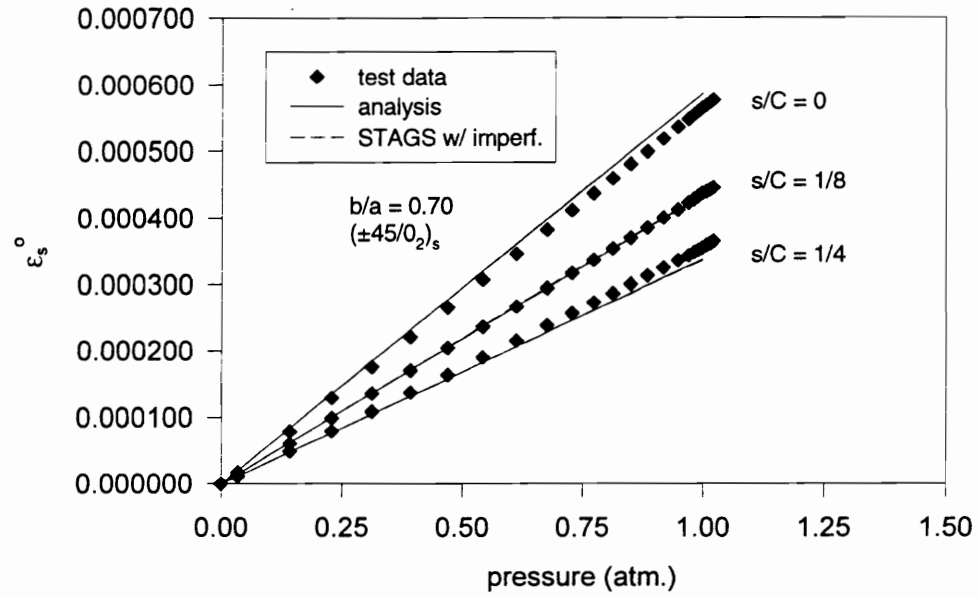

Figure 6-24 Circumferential Midplane Strain at Midspan for the $(\pm 45/0_2)_s$ Cylinder, b/a = 0.70, Internal Pressure Loading to 1 Atm.

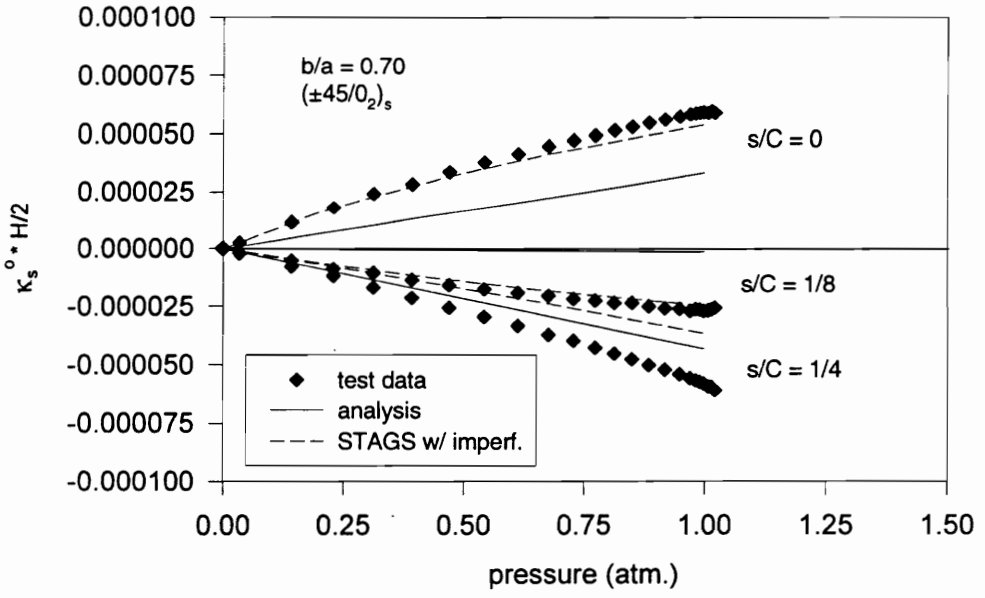

Figure 6-25 Circumferential Bending Strain at Midspan for the $(\pm 45/0_2)_s$ Cylinder, b/a = 0.70, Internal Pressure Loading to 1 Atm.

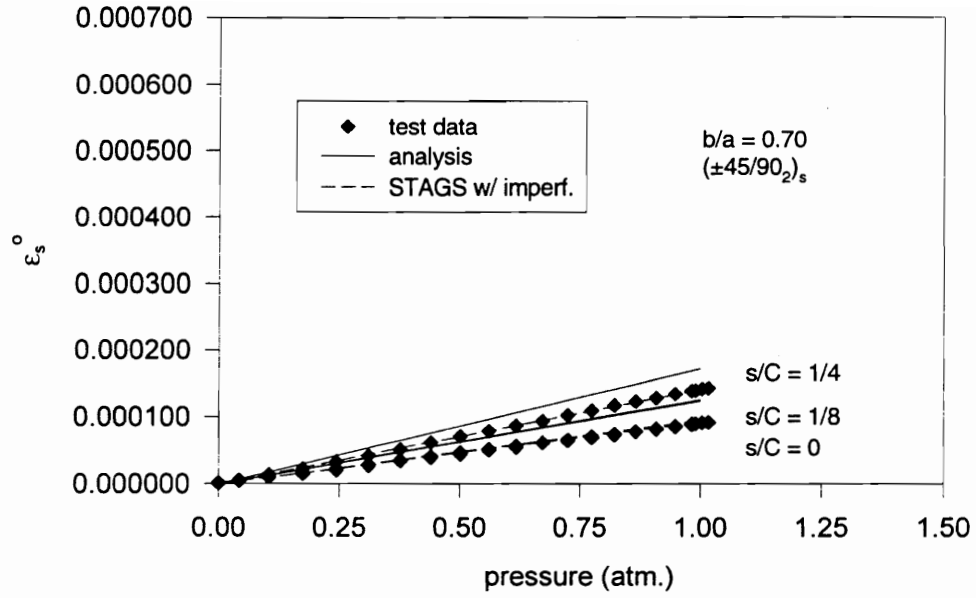

Figure 6-26 Circumferential Midplane Strain at Midspan for the $(\pm 45/90_2)_s$ Cylinder, b/a = 0.70, Internal Pressure Loading to 1 Atm.

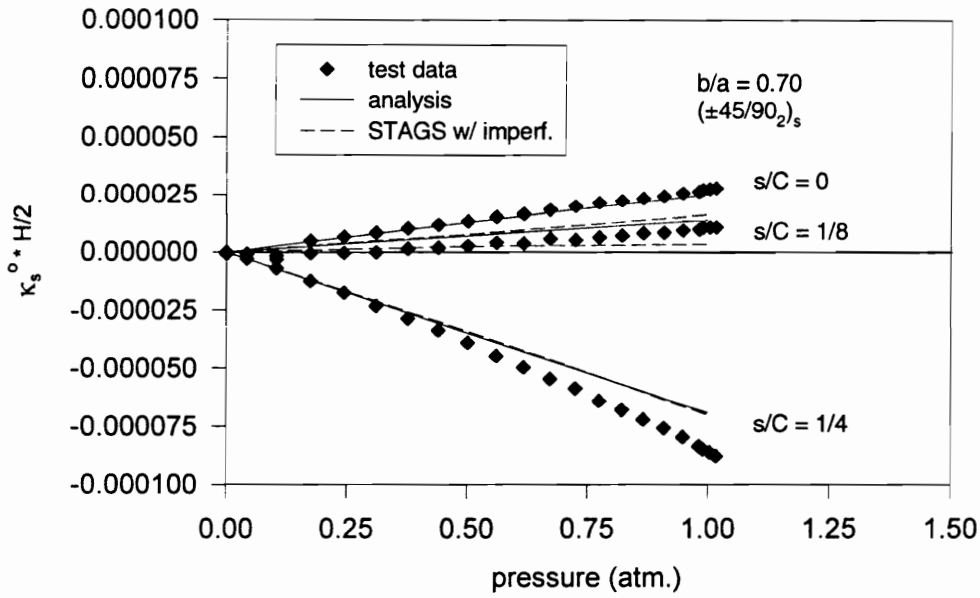

Figure 6-27 Circumferential Bending Strain at Midspan for the $(\pm 45/90_2)_s$ Cylinder, b/a = 0.70, Internal Pressure Loading to 1 Atm.

cylinder, b/a = 0.70, was given previously in Figure 6-13. In these graphs, the circumferential variation of the circumferential strains can be seen even more clearly. In each of these cases, there is good agreement between the measured and calculated results, with the STAGS results for the imperfect cylinders providing a closer correlation with the experimental data. Particularly for the $(\pm 45/90_2)_s$ cylinder, this improved correlation is due to the shift in circumferential midplane strain values resulting from taking into account the lack of ideal end fixation.

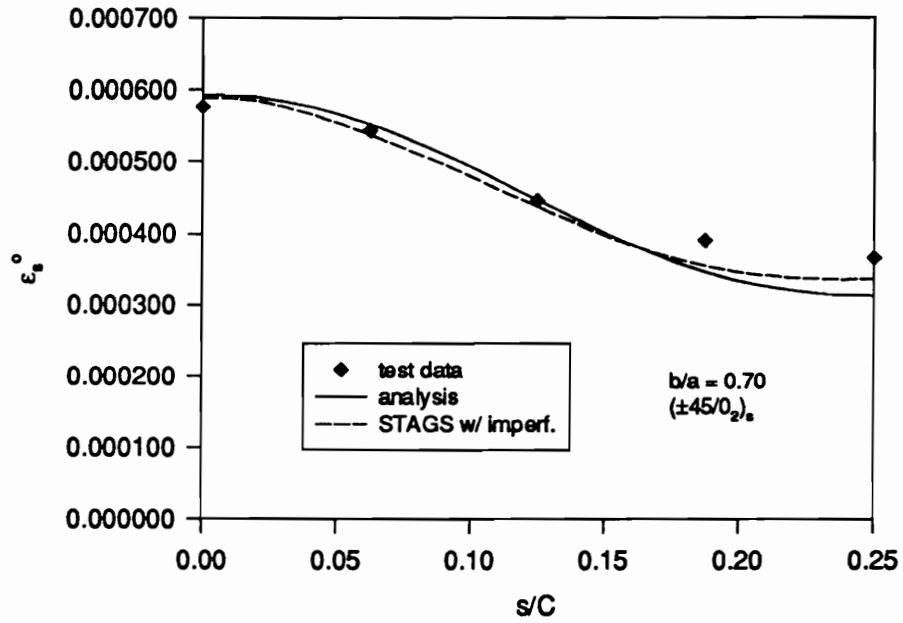

Figure 6-28 Circumferential Midplane Strain vs. s/C at Midspan for the $(\pm 45/0_2)_s$ Cylinder, b/a = 0.70, 1 Atm. Internal Pressure.

Although the circumferential midplane strain results for all of the cylinders are plotted to the same scale, for further ease of comparison the analytical results for each of the cylinders having b/a = 0.70 cross sectional aspect ratio are also shown together in Figure 6-30. As noted earlier, the overall levels of circumferential midplane strain increase from the lowest for the cylinder with a hoop-stiff lay-up, the $(\pm 45/90_2)_s$ cylinder, to the highest for the cylinder which is softest in the circumferential direction, the $(\pm 45/0_2)_s$ cylinder. The largest variation in circumferential strain with circumferential coordinate can also be seen in the $(\pm 45/0_2)_s$ cylinder, with the least variation occurring in the hoop-stiff cylinder. Interestingly, in the $(\pm 45/90_2)_s$ cylinder, the circumferential midplane strains vary in the opposite way from the $(\pm 45/0/90)_s$ and $(\pm 45/0_2)_s$ cylinders, increasing from s/C = 0 to s/C = 1/4. This would seem to indicate that the increased hoop stiffness is an equalizer of sorts as the circumferential midplane strains for this lay-up, even with

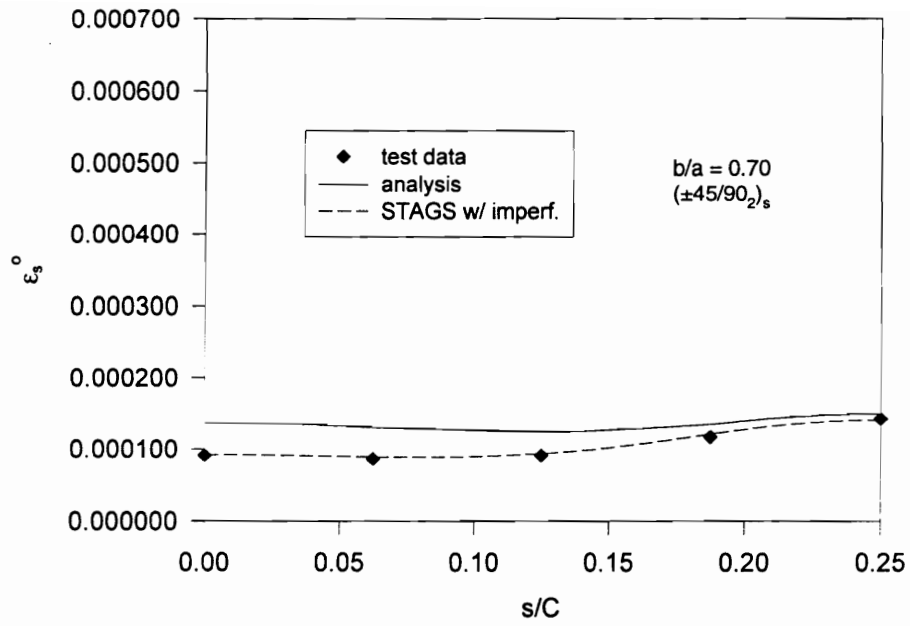

Figure 6-29 Circumferential Midplane Strain vs. s/C at Midspan for the $(\pm 45/90_2)_s$ Cylinder, b/a = 0.70, 1 Atm. Internal Pressure.

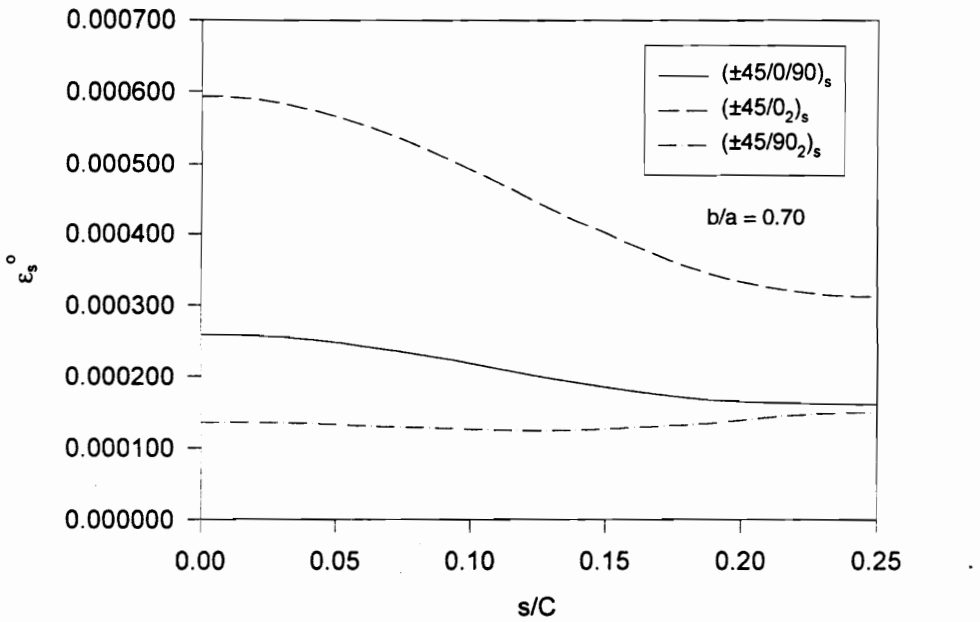

Figure 6-30 Comparison of Analytical Results for Circumferential Midplane Strain vs. s/C at Midspan for the $(\pm 45/0/90)_s$, $(\pm 45/0_2)_s$, and $(\pm 45/90_2)_s$ Cylinders, b/a = 0.70, 1 Atm. Internal Pressure.

b/a = 0.70, look more like strains for a circular cylinder. The primary difference, however, is that there would be no bending strains for a circular cylinder and Figure 6-27 shows otherwise for the elliptical cylinder. Furthermore, by comparing the strains results with those for the radial displacements, given in Figure 6-23, it can be seen that w/R is by no means the dominant term in the circumferential midplane strain, as would be the case for circular cylinders. If it were, since these three cylinders have the same equation for 1/R(s), the $(\pm 45/90_2)_s$ cylinder which experienced the largest magnitudes of radial displacement would also have the highest circumferential midplane strains. This is not the case, however. As discussed in ch. 4, unlike circular cylinders, elliptical cylinders undergo nonzero circumferential displacements when pressurized, thus the derivative of the circumferential displacement with respect to the circumferential coordinate, $\partial v / \partial s$, has large influence on the values of the circumferential midplane strains.

Finally, the axial midplane strains at 1 atm. of internal pressure are plotted against the normalized axial coordinate, x/L, at two circumferential locations, s/C = 0 and s/C = 1/4. These axial strains are shown for the $(\pm 45/0_2)_s$ cylinder in Figure 6-31 for the $(\pm 45/0_2)_s$ cylinder and for the $(\pm 45/90_2)_s$ cylinder in Figure 6-32. These results may be compared with those for the $(\pm 45/0/90)_s$ cylinder, b/a = 0.70, given in Figure 6-17. Again, the effects of the lack of perfect end fixation for the $(\pm 45/90_2)_s$ cylinder can be seen in the shift of the STAGS results for the imperfect cylinder as compared to the analytical results for the perfect cylinder. For both cylinders, there is good agreement between the experimental data and the analyses. Indeed, for the $(\pm 45/90_2)_s$ cylinder the agreement between the experimental results and the results predicted by the STAGS model is excellent. Unlike the case of circumferential strain, the consideration of geometric imperfections in these cylinders results in a somewhat greater circumferential variation in axial strains over most of the cylinders' length. This is consistent with the results discussed above for the quasi-isotropic elliptical cylinders. Also it is very evident, by comparing Figures 6-31 and 6-32, that the degree of orthotropy has a strong influence on the magnitude and distribution of the axial strains, even in the ideal analytical case, where there are no imperfections and the boundary conditions are ideal.

In order to more easily compare these axial strain distributions, the analytical results for all three perfect cylinders, b/a = 0.70, are shown together in Figure 6-33. From this figure, as well as Figures 6-31, 6-32 and 6-17, it is obvious that even at low pressure, with the ends largely restrained against axial movement, significant midplane axial strains are produced in all of these elliptical cylinders. The $(\pm 45/90_2)_s$ cylinder, being softest in the axial direction, exhibits the greatest axial midplane strains, while those for the axially-stiff cylinder are lowest. By comparing these results with those given for the circumferential midplane strains in Figure 6-30, it can be seen that there is a trade off between the axial and circumferential midplane strain distributions in the elliptical cylinders. For the quasi-isotropic cylinder, the levels of axial and circumferential strains at midspan were nearly equal. The $(\pm 45/0_2)_s$ cylinder shows the lowest levels and

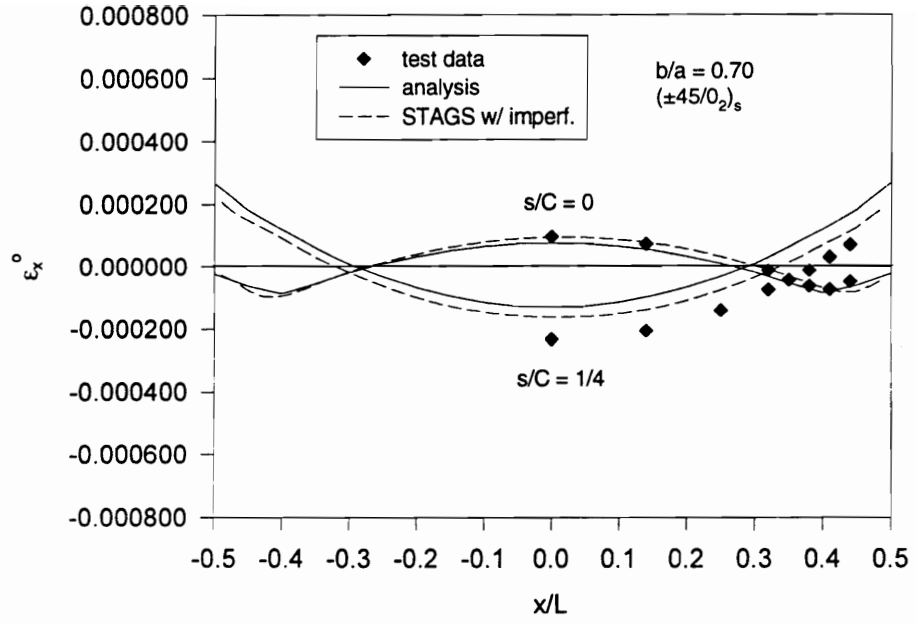

Figure 6-31 Axial Midplane Strain vs. x/L for the $(\pm 45/0_2)_s$ Cylinder, b/a = 0.70, 1 Atm. Internal Pressure.

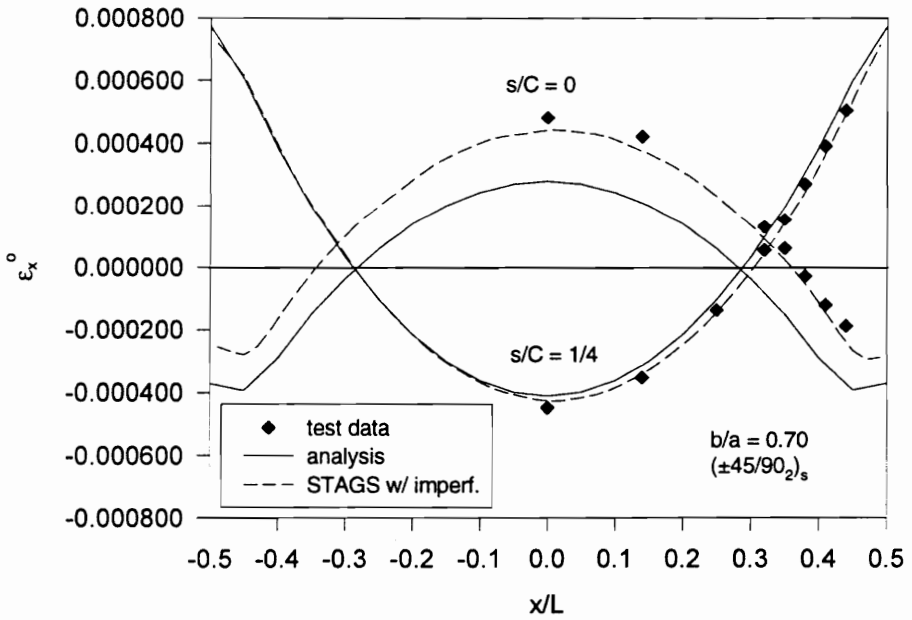

Figure 6-32 Axial Midplane Strain vs. x/L for the $(\pm 45/90_2)_s$ Cylinder, b/a = 0.70, 1 Atm. Internal Pressure.

lowest gradients in axial midplane strain, but the largest values and largest gradient in circumferential midplane strains. The $(\pm 45/90_2)_s$ cylinder exhibits the lowest circumferential midplane strains and very little variation in these strains with circumferential coordinate, however, it is subject to the largest gradient in axial midplane strains, as well as magnitudes of axial midplane strain at midspan which are nearly four times higher than the magnitudes of the circumferential midplane strains.

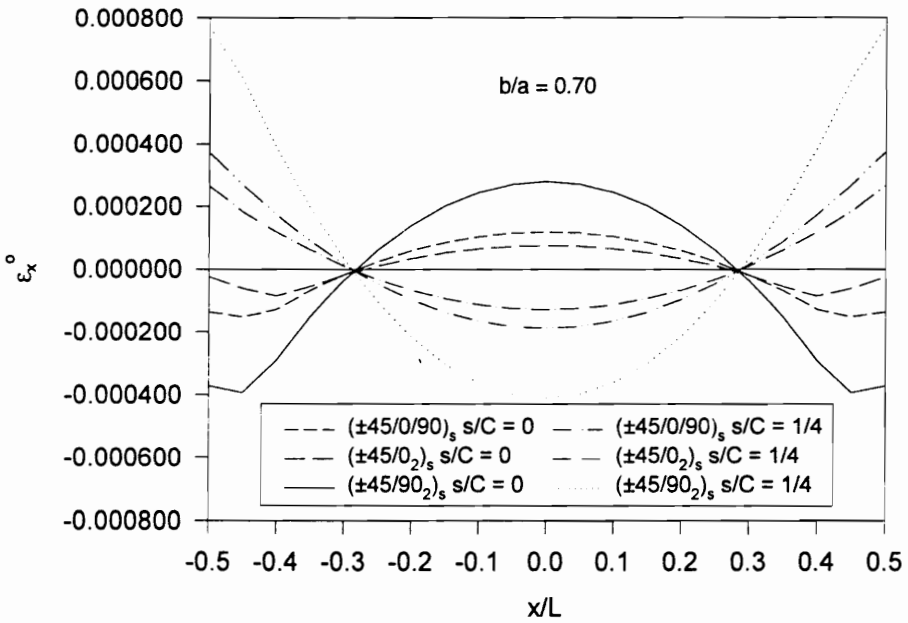

Figure 6-33 Comparison of Analytical Results for Axial Midplane Strain vs. x/L for the $(\pm 45/0/90)_s$, $(\pm 45/0_2)_s$, and $(\pm 45/90_2)_s$ Cylinders, b/a = 0.70, 1 Atm. Internal Pressure.

While at the low level of pressure investigated here the magnitudes of the strains are low, clearly, as discussed in ch. 4, the gradient in the strains, and therefore the stresses, can be large. This presents the potential for large interlaminar stresses developing in elliptical cylinders, even at relatively low pressure loads. However, an accurate examination of this issue over a significant range of internal pressure would require a fully nonlinear analysis of the interlaminar stresses, which is beyond the scope of the present investigation.

The results presented here show that even with low pressure levels, there are distinct differences in response among cylinders due both to geometry and to orthotropy. This has been both predicted and observed, and the comparison between the predictions and observations is good.

Axial Compression

In this section, experimental and analytical results are compared for cylinders in axial compression. This was the last test run on each cylinder, in which loading was increased until buckling and/or material failure of the cylinder occurred. Those cylinders were held in the buckled state to observe the condition of the specimen and mark the deformation pattern.

Prebuckling

As discussed in ch. 4, the prebuckling responses of elliptical cylinders in axial compression can, for some quantities, show significant dependence on circumferential location, while other quantities exhibit almost as little circumferential variation as a circular cylinder. Both of these types of prebuckling responses are shown in the figures discussed below. For clarity, the results shown in these figures have been truncated at the buckling values obtained in the experiments as well as by each analysis. Recall that for the analysis the buckling load is assumed to be given by eqn. 4.2. The buckling values obtained from STAGS and from the experiments will be discussed in a later section.

Effects of Cylinder Geometry

In Figures 6-34 and 6-35 the normalized radial displacements of the $(\pm 45/0/90)_s$ cylinder with b/a = 0.70 are plotted against the axial load, normalized by P_{cr} the classical buckling load, which is defined in eqn. 4.2. In Figure 6-34 the response at the cylinder's midspan is shown, while the response in the boundary layer, near the end cap, is shown in Figure 6-35. In both of these figures, the experimental data taken at the circumferential locations s/C = 0, 1/8 and 1/4 are compared with the results of the analysis for the perfect cylinder, and the STAGS results for the imperfect cylinder. Except at the s/C = 0 position near the end cap, where the experimental response much exceeds the predicted response, reasonably good agreement can be seen between the test data and the analytical results. Measuring the radial displacements near the end caps is not as precise as measuring these displacements at midspan. At midspan, the radial displacement response does not change as rapidly with axial position as it does near the end cap. This can be seen in Figure 4-6. Not having the displacement transducer at the exact axial location near the end cap where the predictions are being made will result in a greater difference between predictions and measurements than not having the displacement transducer in the exact axial location near midspan. In general, in Figures 6-34 and 6-35 there is little difference between the results calculated for the perfect and imperfect cylinder geometries.

It is clear that, at both axial locations, the radial deformations are much greater at the maximum radius of curvature, s/C = 0. In comparing these results with those shown in Figure 6-3 for the midspan radial displacements of this cylinder when loaded by internal pressure, it should be noted that even in the boundary

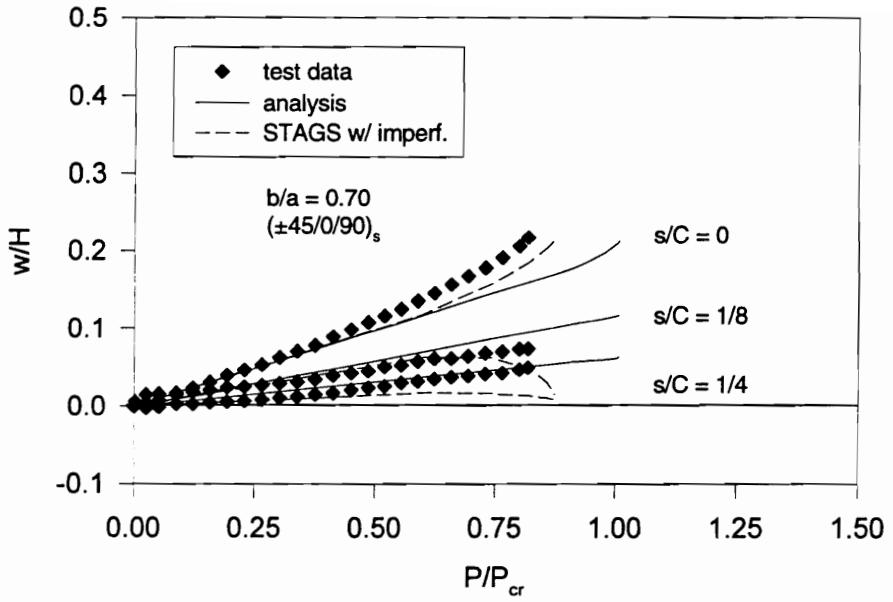

Figure 6-34 Normalized Radial Displacement at Midspan vs. P/P_{cr} for the $(\pm 45/0/90)_s$ Cylinder, b/a = 0.70.

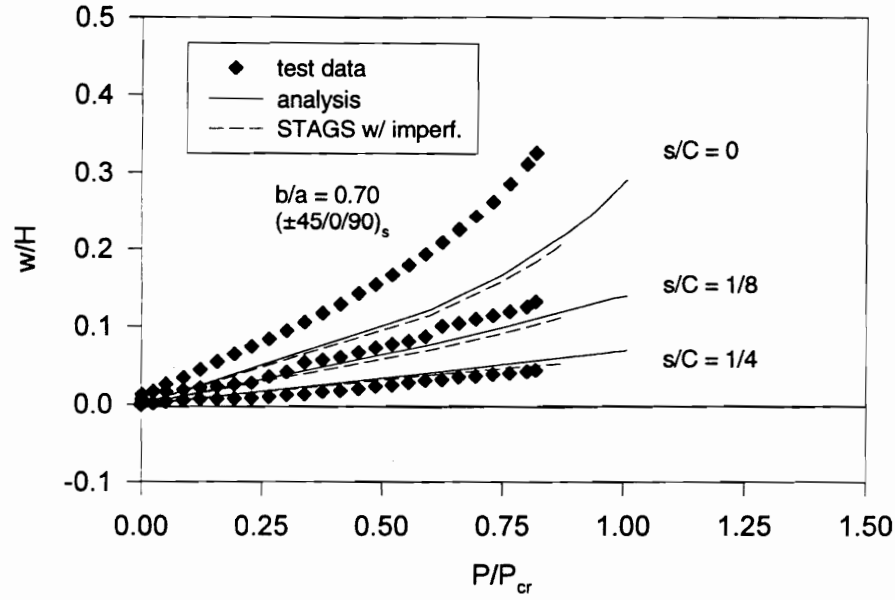

Figure 6-35 Normalized Radial Displacement near the End Cap vs. P/P_{cr} for the $(\pm 45/0/90)_s$ Cylinder, b/a = 0.70.

layer of the cylinder, at a high level of axial compression, the largest radial displacements are still only slightly greater than those generated by an internal pressure load of only 1 atm. The spread in the values of the radial displacements for the axially compressed cylinder is also lower. The radial responses at the minimum radius of curvature, s/C = 1/4, are close to zero but not negative, as was the case when the cylinder was loaded by internal pressure. With axial compression, the cylinder expands outward at all radial locations.

Similar results are shown for the cylinder with b/a = 0.85 in Figures 6-36 and 6-37 for the radial responses of this cylinder at midspan and near the end cap, respectively. For comparison, results for the circular cylinder, b/a = 1.00, are shown in Figure 6-38 for the radial response at midspan, and in Figure 6-39 for the response near the end cap. In these figures as well, a reasonably good agreement is shown between the experimental and predicted responses, except at s/C = 1/4 at the midspan of the mildly elliptical cylinder where the measured response is quite low by comparison to the calculated results. Unlike the response to internal pressure, there is a relatively small but noticeable difference between the radial displacements at the three circumferential locations for the axially loaded circular cylinder. This difference in the experimental radial displacements is also predicted by the STAGS results for the imperfect circular cylinder. In general, the radial responses of the mildly elliptical cylinder are intermediate to the responses of the more severely elliptical cylinder and the circular cylinder.

A more complete view of the deformations of these cylinders, and particularly of the influence of initial geometric imperfections upon these deformation patterns, is presented in Figures 6-40 - 6-42. In each of these figures, the deformed shape for both the perfect and imperfect cylinder, obtained from the STAGS finite element program, is shown at a load level equal to the greatest prebuckling load obtained for the imperfect cylinder, i. e., the load obtained just prior to buckling. Contour lines are also given on these graphs for the radial displacements. Note that the potted ends of the cylinders are represented in these STAGS models by restricting radial and circumferential displacements along nodes on the portions of the ends which would be in end fixtures.

The deformed shapes for the $(\pm 45/0/90)_s$ cylinder with b/a = 0.70 with and without imperfections are shown in Figure 6-40. In viewing the deformations for the perfect cylinder, clearly the largest deformations occur near the flattest part of the elliptical cross-section, the maximum radii of curvature at s/C = 0 and 1/2, and the amplitude and the wavelength of the boundary layer vary circumferentially. There is also a degree of symmetry about the major and minor diameters for the case of the perfect cylinder.This symmetry is obviously disrupted by the presence of initial geometric imperfections, which strongly influence the cylinder's deformations. With the perfect cylinder, it is seen that indeed the radial displacements do not change significantly with axial location near the midspan of the cylinder. Near the end caps, the radial displacements do change rapidly with axial location. However, for the imperfect cylinder, at the flattest part of the cylinder the radial displacement at midspan changes with axial location as rapidly as it does near the

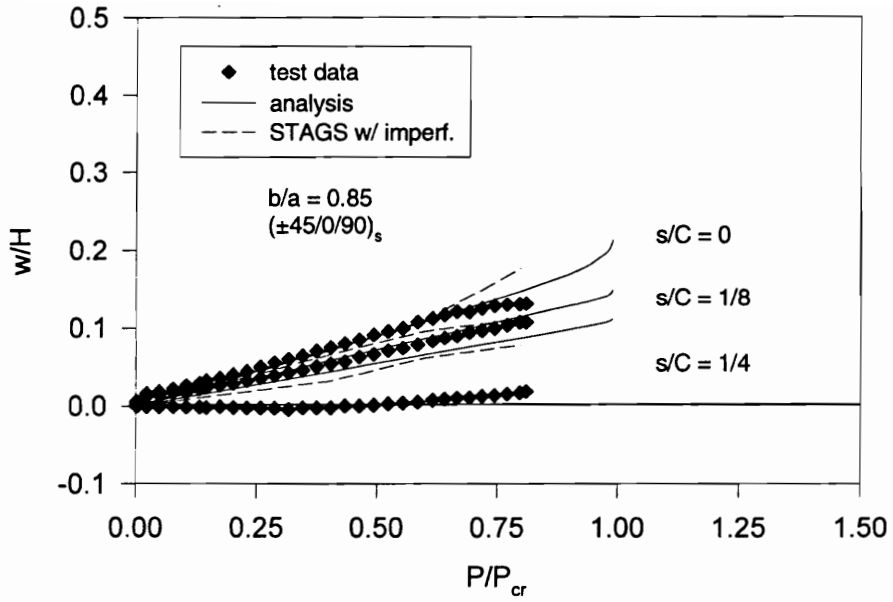

Figure 6-36 Normalized Radial Displacement at Midspan vs. P/P_{cr} for the $(\pm 45/0/90)_s$ Cylinder, b/a = 0.85.

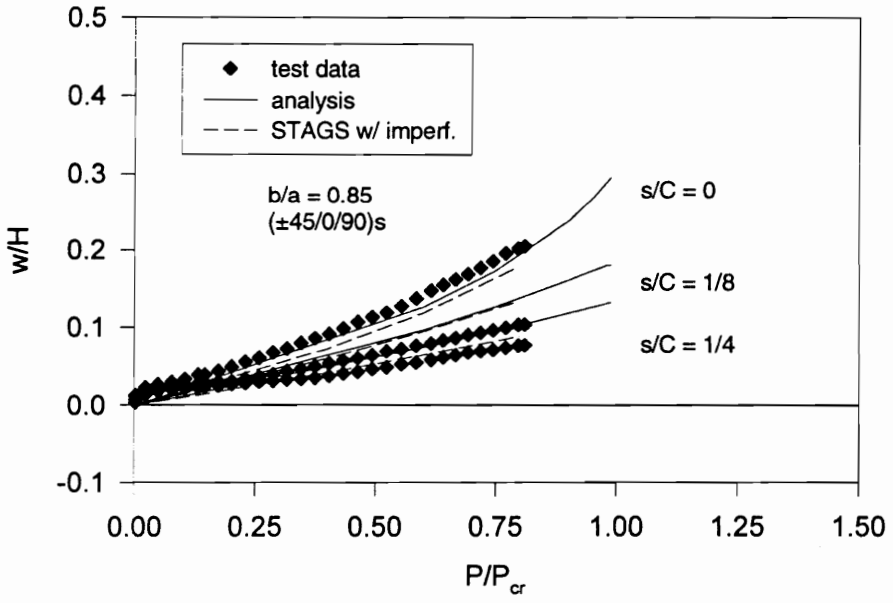

Figure 6-37 Normalized Radial Displacement near the End Cap vs. P/P_{cr} for the $(\pm 45/0/90)_s$ Cylinder, b/a = 0.85.

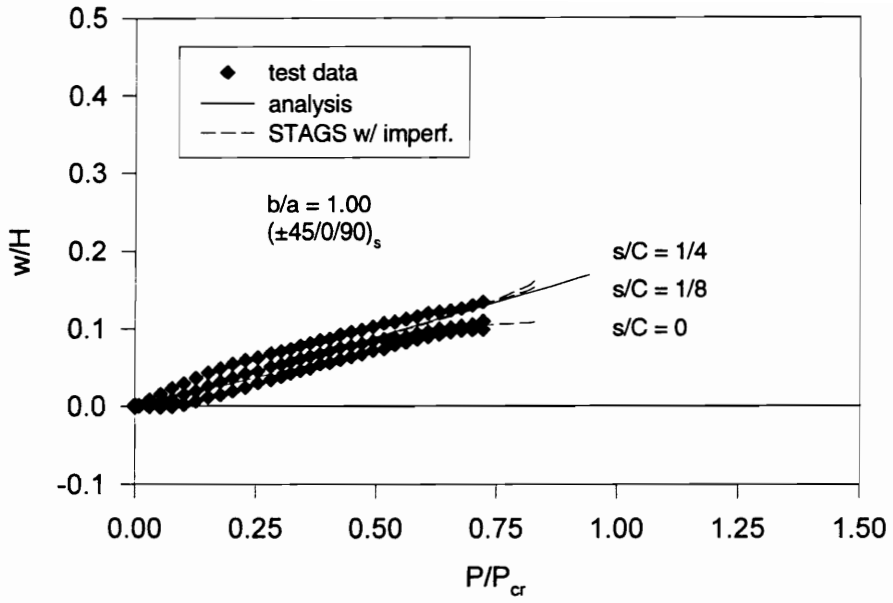

Figure 6-38 Normalized Radial Displacement at Midspan vs. P/P_{cr} for the $(\pm 45/0/90)_s$ Cylinder, b/a = 1.00.

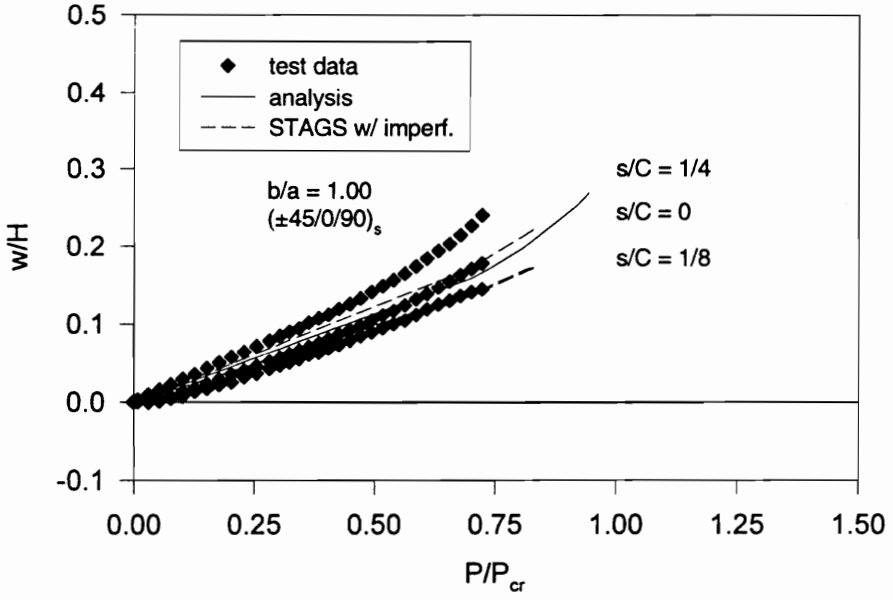

Figure 6-39 Normalized Radial Displacement near the End Cap vs. P/P_{cr} for the $(\pm 45/0/90)_s$ Cylinder, b/a = 1.00.

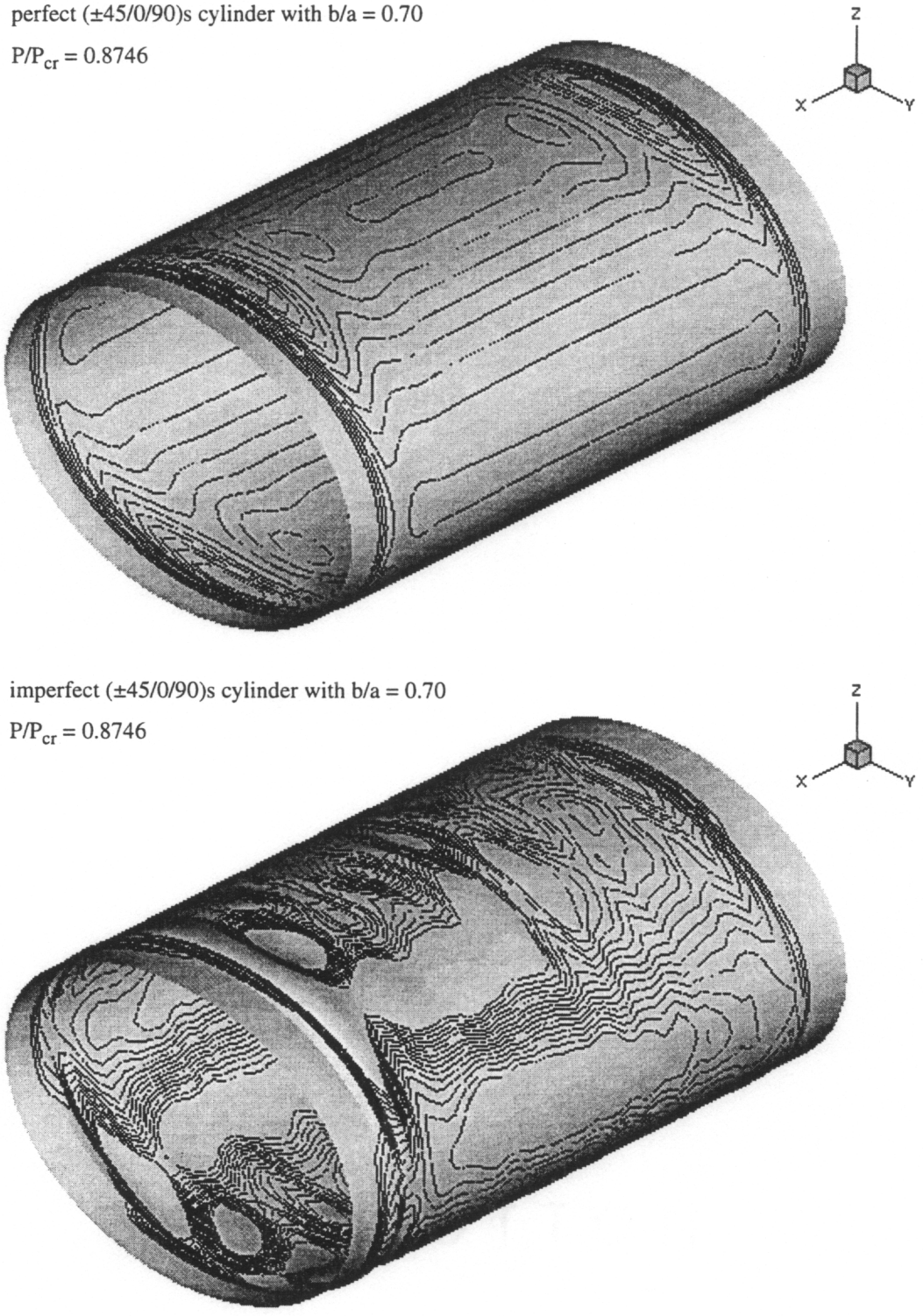

Figure 6-40 Deformed Shapes of the Perfect and Imperfect $(\pm 45/0/90)_s$ Cylinder with b/a = 0.70.

end caps. Thus the discrepancies between predictions and experiments in Figures 6-34 - 6-39 could well be due to even small inaccuracies in the axial placement of the displacement transducers. Note, however, that with imperfections the largest deformations still occur near the flattest part of the elliptical cylinder. Note also with the imperfect cylinder how sensitive the measure of radial displacement near s/C = 0 is to axial location. Even a small axial misalignment of a DCDT might easily result in a large difference between the measured and predicted results. This may explain, in part, the poor agreement at s/C = 0 in Figure 6-35.

The deformed shapes of the perfect and imperfect $(\pm 45/0/90)_s$ cylinders with b/a = 0.85 and b/a = 1.00 are shown in Figures 6-41 and 6-42, respectively. Although the milder, b/a = 0.85, perfect elliptical cylinder undergoes less variation in radial displacements with circumferential location than the cylinder with b/a = 0.70, it still exhibits a deformation pattern characteristic of an elliptical cylinder, with the amplitude and wavelength of the boundary layer varying circumferentially and the greatest deformations occurring near the flattest parts of the cylinder. By comparison, the response of the perfect circular cylinders are simple and circumferentially uniform. For both the elliptical cylinder with b/a = 0.85 and the circular cylinder, the presence of initial geometric imperfections results in a great change in the deformation patterns. While the imperfect cylinder with b/a = 0.85 still exhibits slightly greater deformations in the flattest regions of the cylinder, the deformed shape of the mildly elliptical cylinder with imperfections is more similar to the deformed shape of the imperfect circular cylinder than to the deformed shape of the more severely elliptical cylinder with imperfections.

In Figures 6-43 and 6-44 the axial midspan strains, and the associated bending strains, $\kappa_x^o * H/2$, at midspan for the $(\pm 45/0/90)_s$ cylinder with b/a = 0.70 are shown as functions of the normalized axial load. The axial midspan strains at the circumferential locations s/C = 0, 1/8, and 1/4 are shown in Figure 6-43 and the corresponding bending strains are shown in Figure 6-44. These axial strains are also shown in Figure 6-45 for the mildly elliptical cylinder, with the bending strains versus normalized load given in Figure 6-46. For the circular cylinder, the axial midplane strains and bending strains are plotted as functions of axial load in Figures 6-47 and 6-48, respectively.

The axial bending strains at midspan are quite small for all of these cylinders, being less than 10% of the axial midplane strains at midspan. The agreement between the measured and calculated bending strains for the elliptical cylinders is good, with poorer correlation occurring for the circular cylinder. For both of the elliptical cylinders, the bending strains in the stiffer region near the minimum radius of curvature are nearly zero, while the largest bending strains are in the flattest part of the cross section, near the maximum radius of curvature. Strangely, the greatest circumferential variation in the bending strains occurs in the circular cylinder, although this degree of difference is predicted by the STAGS analysis for the cylinder with initial shape imperfections.

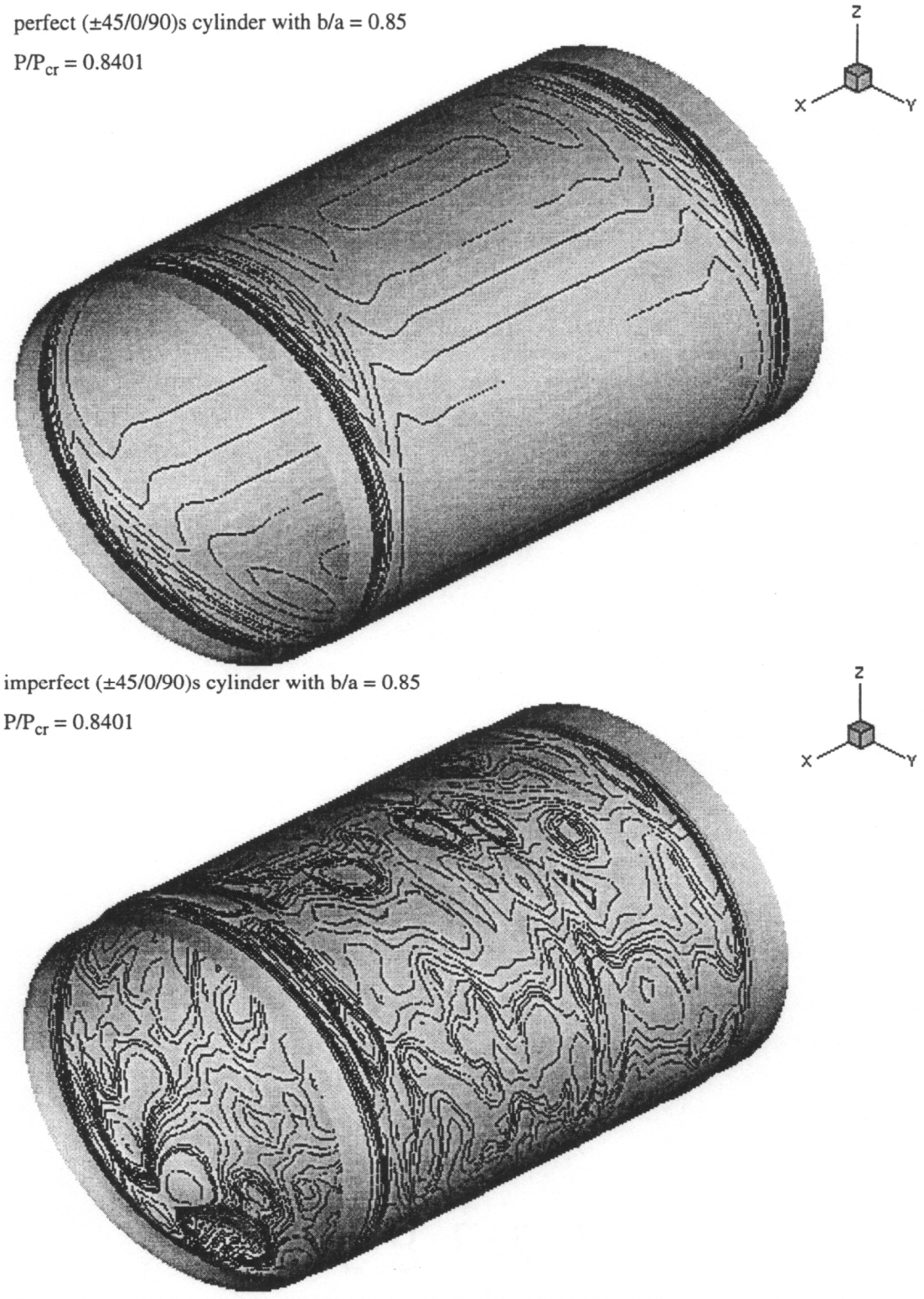

Figure 6-41 Deformed Shapes of the Perfect and Imperfect $(\pm 45/0/90)_s$ Cylinder with b/a = 0.85.

perfect (±45/0/90)s cylinder with b/a = 1.00

$P/P_{cr} = 0.8324$

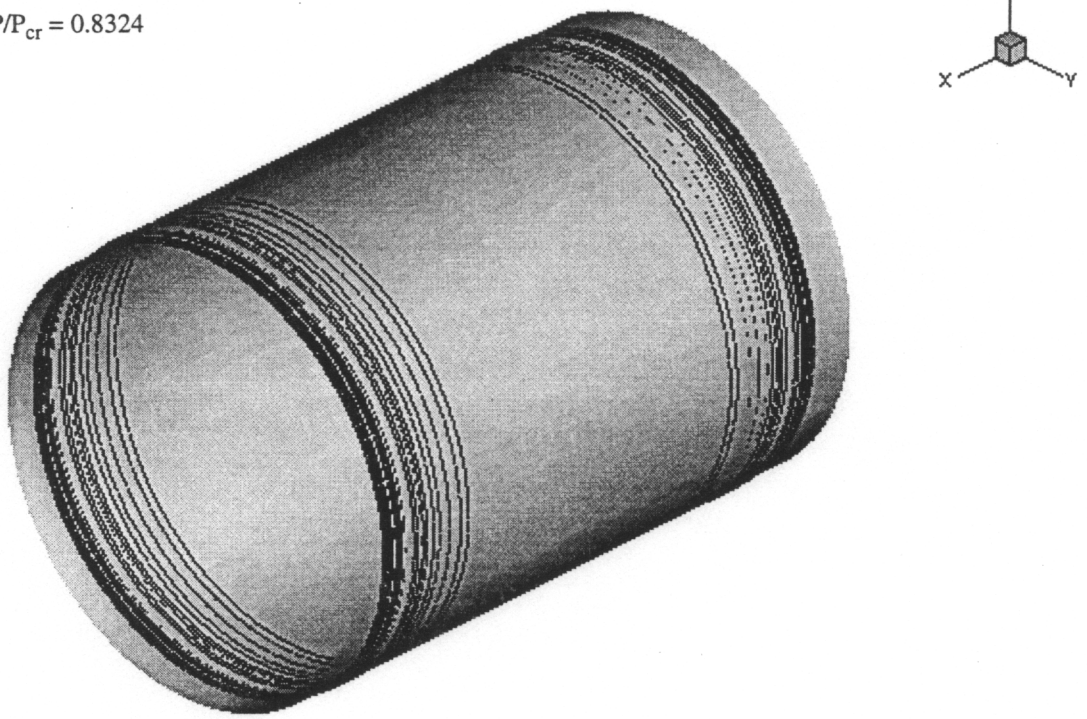

imperfect (±45/0/90)s cylinder with b/a = 1.00

$P/P_{cr} = 0.8324$

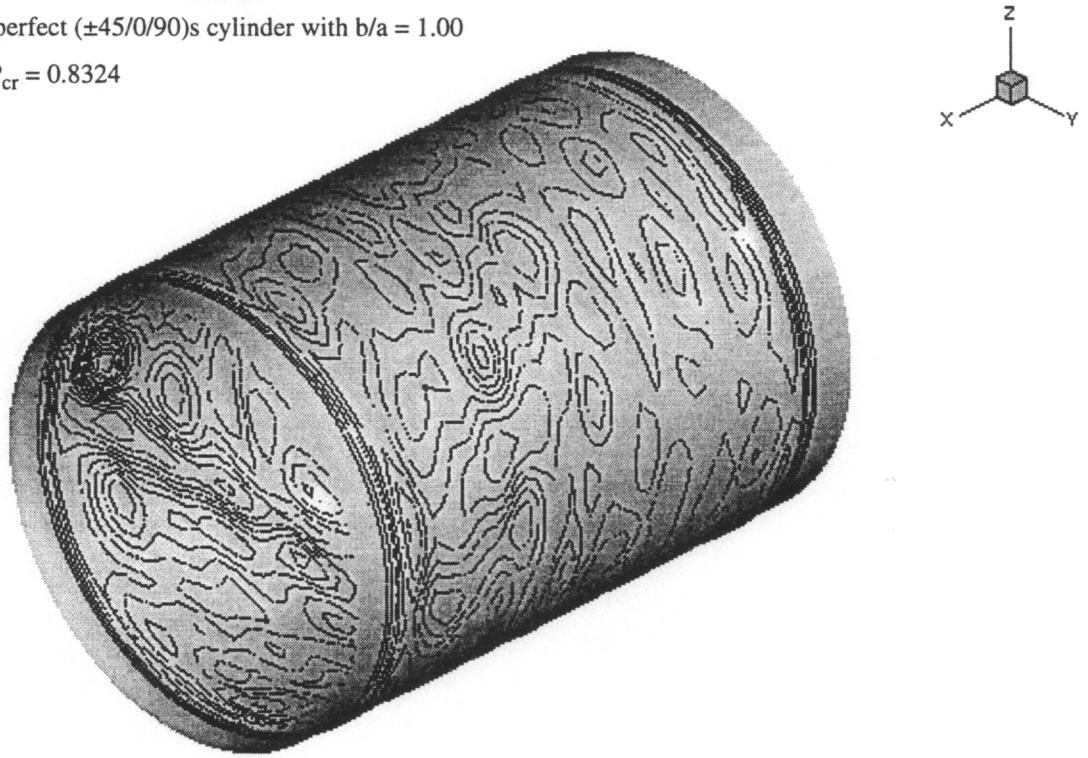

Figure 6-42 Deformed Shapes of the Perfect and Imperfect $(\pm 45/0/90)_s$ Cylinder with b/a =1.00.

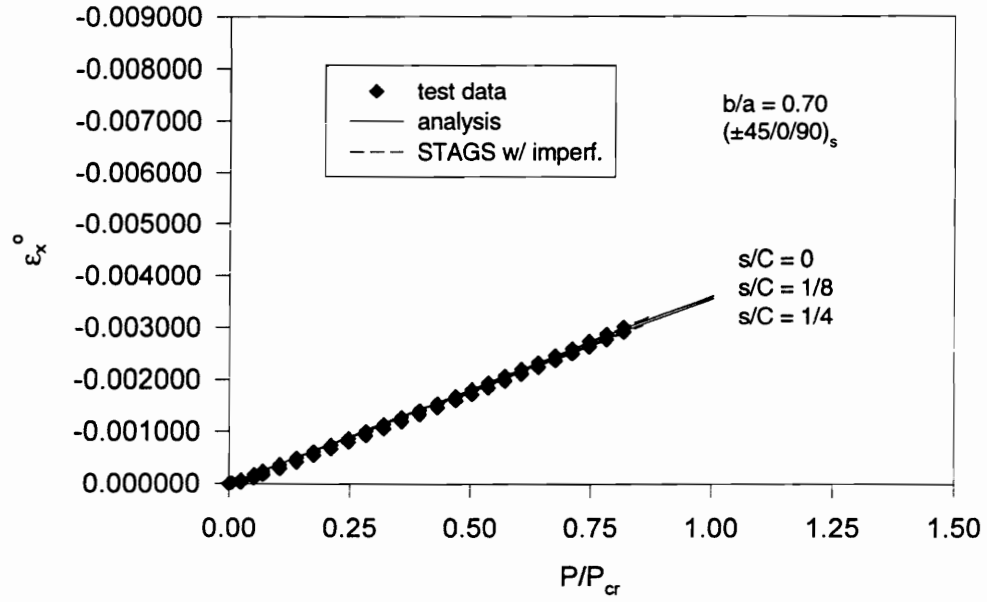

Figure 6-43 Axial Midplane Strain at Midspan vs. P/P_{cr} for the $(\pm 45/0/90)_s$ Cylinder, b/a = 0.70.

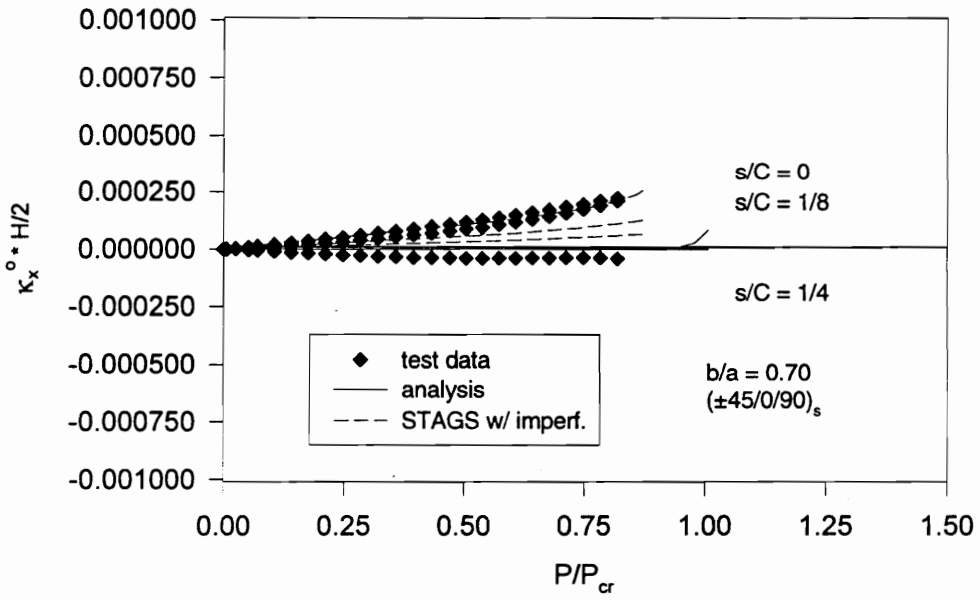

Figure 6-44 Axial Bending Strain at Midspan vs. P/P_{cr} for the $(\pm 45/0/90)_s$ Cylinder, b/a = 0.70.

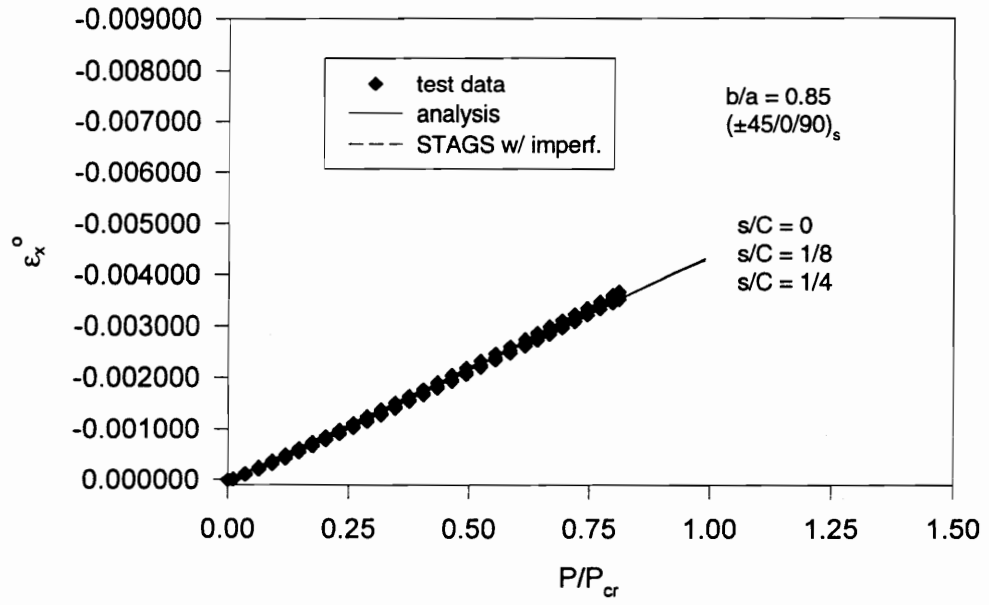

Figure 6-45 Axial Midplane Strain at Midspan vs. P/P_{cr} for the $(\pm 45/0/90)_s$ Cylinder, b/a = 0.85.

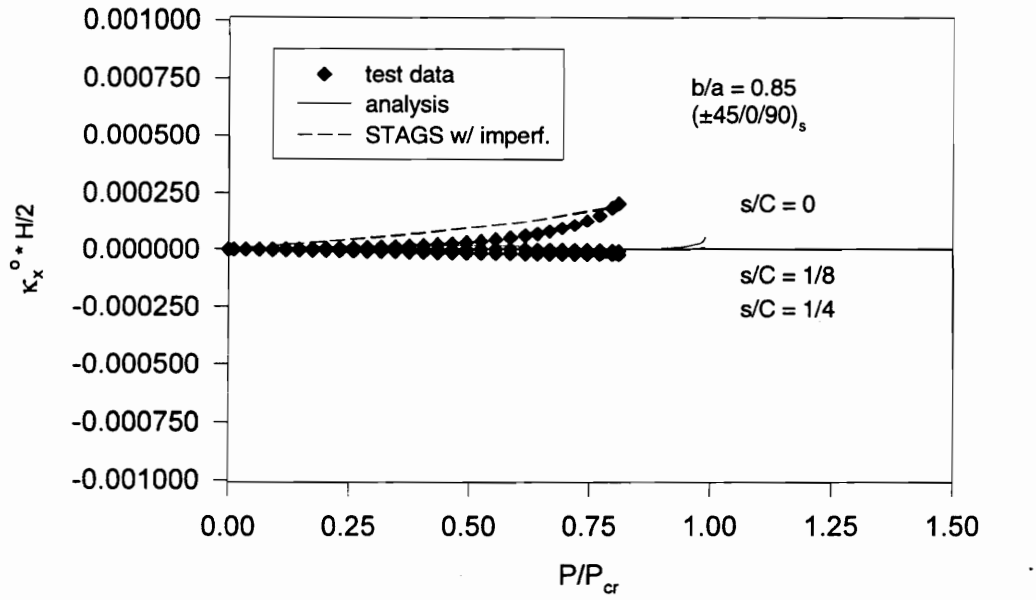

Figure 6-46 Axial Bending Strain at Midspan vs. P/P_{cr} for the $(\pm 45/0/90)_s$ Cylinder, b/a = 0.85.

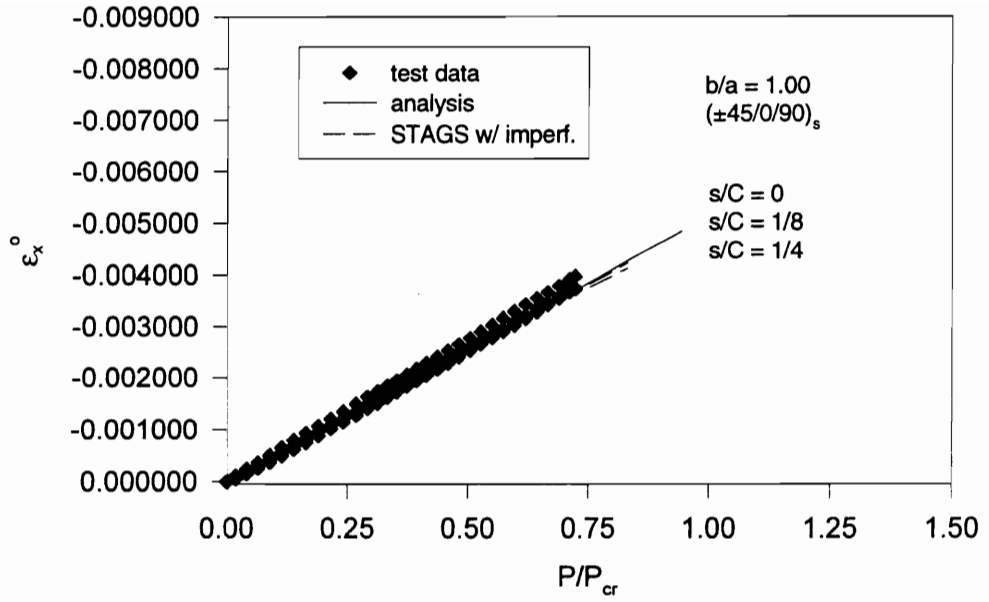

Figure 6-47 Axial Midplane Strain at Midspan vs. P/P_{cr} for the $(\pm 45/0/90)_s$ Cylinder, b/a = 1.00.

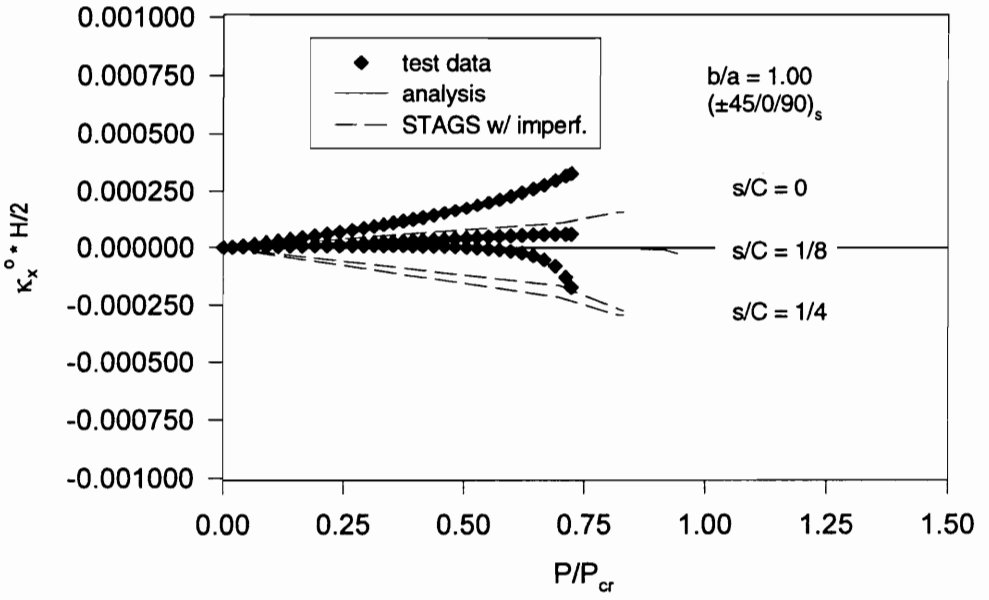

Figure 6-48 Axial Bending Strain at Midspan vs. P/P_{cr} for the $(\pm 45/0/90)_s$ Cylinder, b/a = 1.00.

For all of these cylinders the plots of axial midplane strain against normalized axial load show excellent agreement between the experimental data and the analytical results for both the perfect and imperfect cylinders. The axial midplane strain results at midspan exhibit extremely little variation with circumferential location, which is in agreement with the observations made in ch. 4. Indeed, perhaps the greatest difference between the axial strains in the three circumferential locations can be found in the circular cylinder. The variation in the results for the circular cylinder can be attributed in part to the presence of a ply seam near the s/C = 1/4 position on the cylinder, near the strain gage location.

There is very little variation in the circumferential midplane strain at midspan for elliptical cylinders loaded in axial compression. This is illustrated in Figures 6-49 - 6-53, which show the circumferential midplane strain at midspan plotted against the normalized circumferential coordinate. The circumferential strain plotted over one quarter of the cross section for the cylinder with b/a = 0.70 is given at a load level of $P/P_{cr} = 0.50$ in Figure 6-49 and at $P/P_{cr} = 0.75$ in Figure 6-50. A similar set of results is given for the cylinder with b/a = 0.85 in Figure 6-51 at a load of $P/P_{cr} = 0.50$ and in Figure 6-52 at $P/P_{cr} = 0.75$. The circular cylinder buckled before reaching a load level of $P/P_{cr} = 0.75$, so circumferential strain as a function of circumferential coordinate is shown for the circular cylinder only at $P/P_{cr} = 0.50$. These results are given in Figure 6-53. In all of these figures, excellent agreement can be seen between the test data and the analytical results for both the perfect and imperfect cylinders. For this quantity, the inclusion of imperfections in the analysis, in each of these cases, makes only a small improvement in the correlation between the experimental data and the predicted results. As can be seen, in contrast to the circumferential strain results for the elliptical cylinders loaded by internal pressure (see Figures 6-13 and 6-14), when the circumferential strain is plotted as a function of the circumferential coordinate for axially compressed elliptical cylinders, the relationships are nearly flat. Indeed, most of the variation in circumferential strain is due to the shape imperfections in the cylinders. This is true even at $P/P_{cr} = 0.75$, which for these two elliptical cylinders represents roughly 93% of the maximum experimental load attained by these cylinders. The circular cylinder at P/Pcr = 0.50 shows a greater degree of variation in circumferential strain at midspan than either of the elliptical cylinders at either load level, as it has larger imperfections.

Lastly, axial midplane strain is plotted as a function of normalized axial coordinate at two circumferential locations, s/C = 0 and s/C = 1/4. The axial strains for the cylinder with b/a = 0.70 are shown at load levels of $P/P_{cr} = 0.50$ in Figure 6-54 and at $P/P_{cr} = 0.75$ in Figure 6-55. These results for the mildly elliptical cylinder are shown in Figures 6-56 and 6-57 for loads of $P/P_{cr} = 0.50$ and $P/P_{cr} = 0.75$, respectively. The axial strain distribution for the circular cylinder at $P/P_{cr} = 0.50$ is given in Figure 6-58. In each of these figures, the analytical results, and especially the STAGS results for the imperfect cylinders, agree fairly well with the experimental results, although once again the worst correlation exists for the circular cylinder. At least one

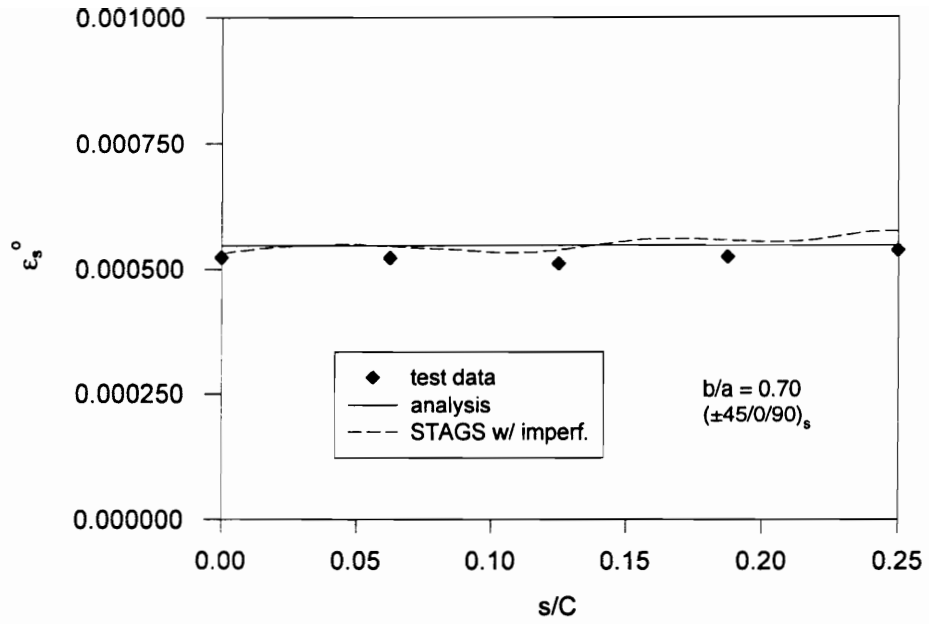

Figure 6-49 Circumferential Midplane Strain vs. s/C at Midspan for the $(\pm 45/0/90)_s$ Cylinder, b/a = 0.70, $P/P_{cr} = 0.50$.

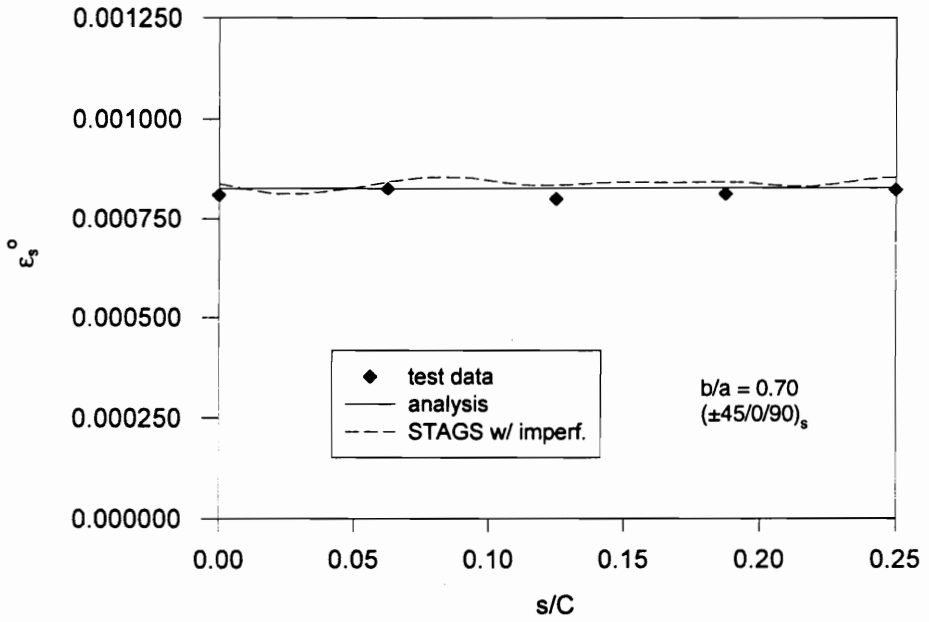

Figure 6-50 Circumferential Midplane Strain vs. s/C at Midspan for the $(\pm 45/0/90)_s$ Cylinder, b/a = 0.70, $P/P_{cr} = 0.75$.

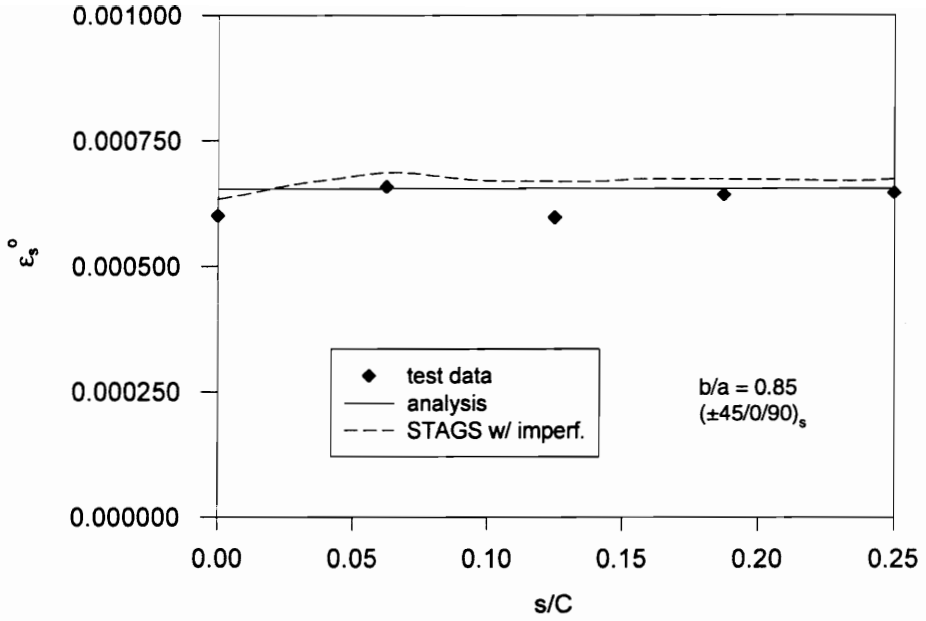

Figure 6-51 Circumferential Midplane Strain vs. s/C at Midspan for the $(\pm 45/0/90)_S$ Cylinder, b/a = 0.85, $P/P_{cr} = 0.50$.

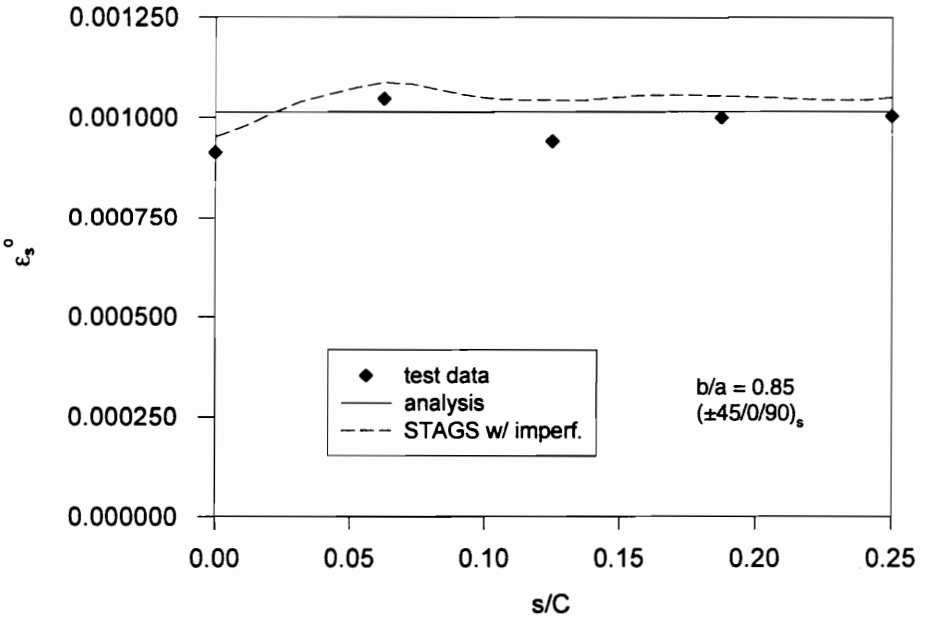

Figure 6-52 Circumferential Midplane Strain vs. s/C at Midspan for the $(\pm 45/0/90)_S$ Cylinder, b/a = 0.85, $P/P_{cr} = 0.75$.

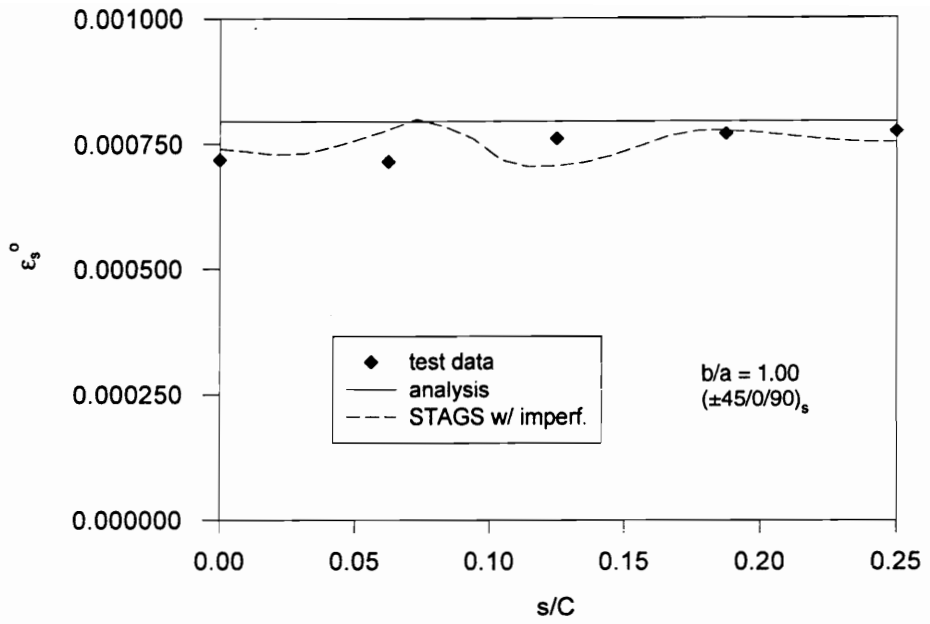

Figure 6-53 Circumferential Midplane Strain vs. s/C at Midspan for the $(\pm 45/0/90)_s$ Cylinder, b/a = 1.00, $P/P_{cr} = 0.50$.

strain gage at the s/C = 1/4 position in the circular cylinder gives an unexpectedly low reading, which may be due to damage developing in the ply seam near this gage. For all cases, very good agreement can be seen between the test data and the analyses near the midspan and throughout much of the length of the cylinders. The greatest discrepancies between the measured and predicted results occurs in the boundary layers. The shape of the boundary layer is sensitive to a number of issues, but particularly to boundary conditions. While the boundary conditions of the test specimens closely approximate clamped conditions, it is known that a slight flexibility of the boundary support, can significantly affect the shape of the boundary layer [48].

The character of the axial strain distribution for the elliptical cylinders under axial compression is again quite different from the response of these cylinders to internal pressure (see Figures 6-17 and 6-18). The axial strains for axially compressed elliptical cylinders are nearly uniform with respect to circumferential location at midspan and throughout most of the length of the cylinders, but diverge in the region of the boundary layer. In comparing Figure 6-54 with Figure 6-55, and Figure 6-56 with 6-57, it can be seen that changes in the load level primarily affect the axial strain distribution by increasing the amplitude of the response in the boundary layer. In the area of the boundary layer, the region of the cylinder near the minimum radius of curvature is stiffest and exhibits the highest axial strains, while the lowest are found in the region of the maximum radius of curvature. The average lengths of the boundary layers for two elliptical

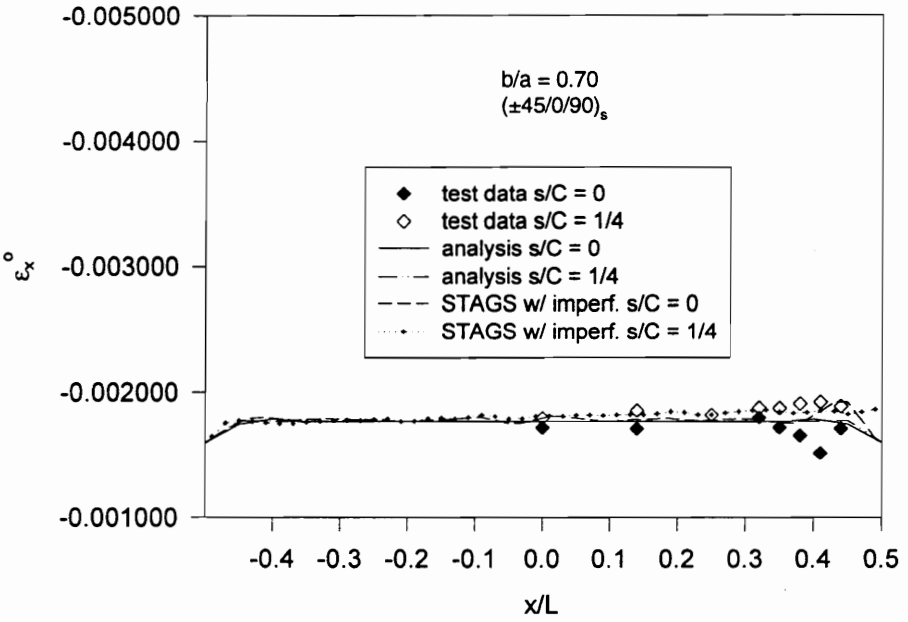

Figure 6-54 Axial Midplane Strain vs. x/L for the $(\pm 45/0/90)_s$ Cylinder, b/a = 0.70, $P/P_{cr} = 0.50$.

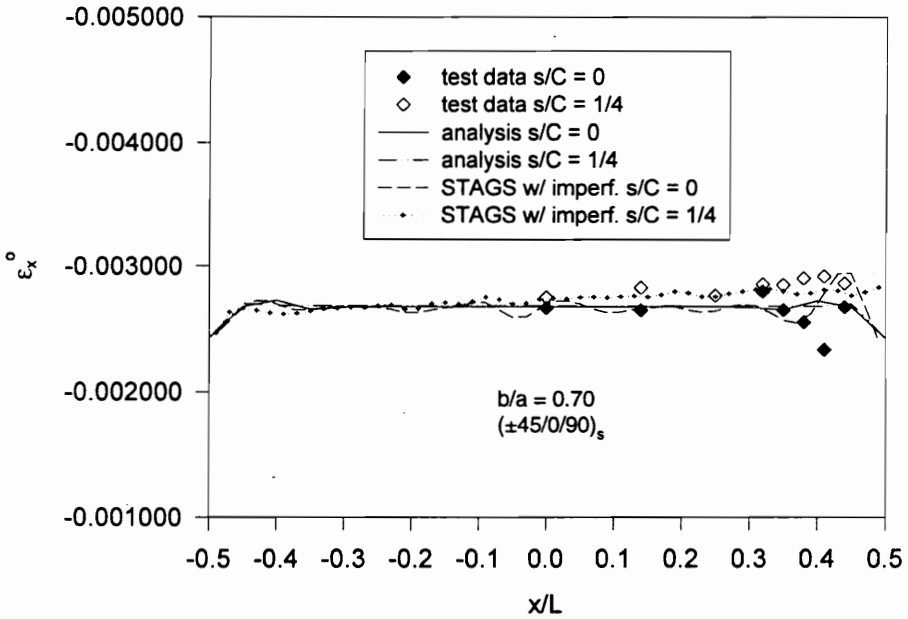

Figure 6-55 Axial Midplane Strain vs. x/L for the $(\pm 45/0/90)_s$ Cylinder, b/a = 0.70, $P/P_{cr} = 0.75$.

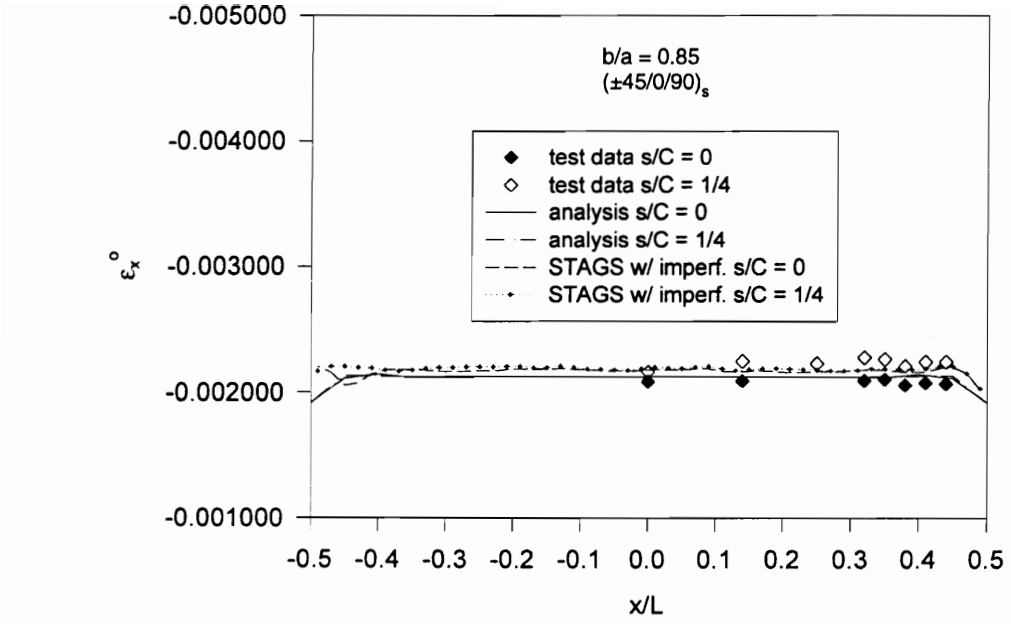

Figure 6-56 Axial Midplane Strain vs. x/L for the $(\pm 45/0/90)_s$ Cylinder, b/a = 0.85, $P/P_{cr} = 0.50$.

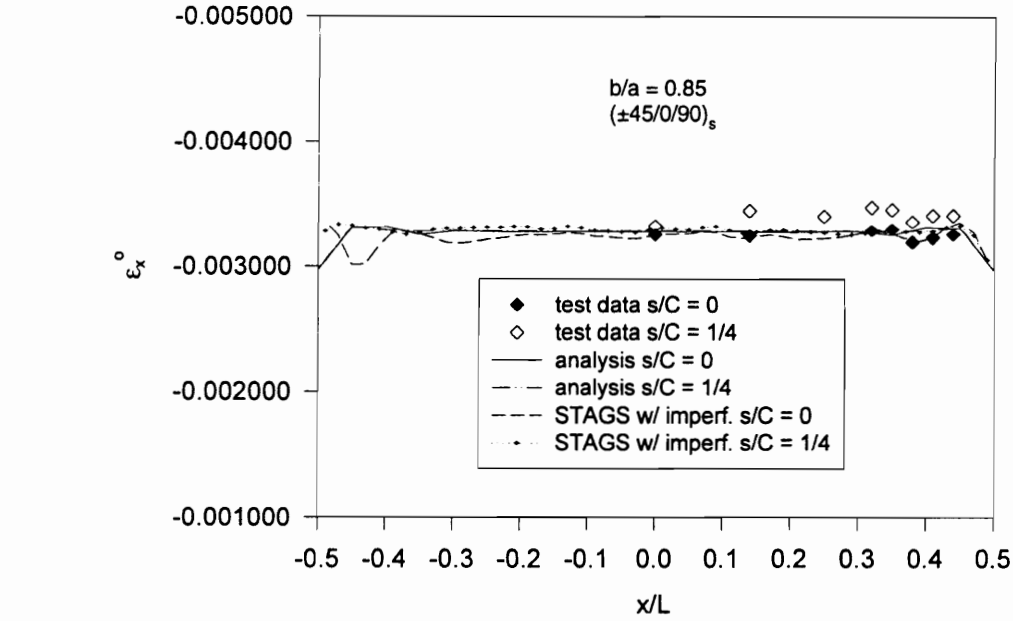

Figure 6-57 Axial Midplane Strain vs. x/L for the $(\pm 45/0/90)_s$ Cylinder, b/a = 0.85, $P/P_{cr} = 0.75$.

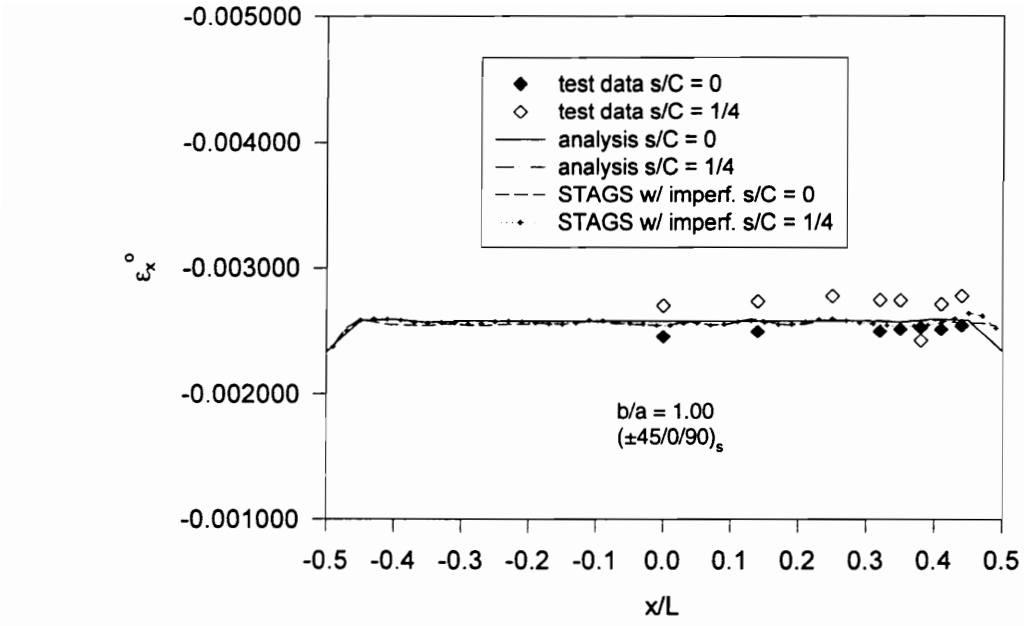

Figure 6-58 Axial Midplane Strain vs. x/L for the $(\pm 45/0/90)_s$ Cylinder, b/a = 1.00, $P/P_{cr} = 0.50$.

cylinders are roughly the same. However, the cylinder with a more severely elliptical cross section shows a definite difference between the boundary layer responses at s/C = 0 and s/C = 1/4, having higher strains, but a flatter response, at s/C = 1/4, and lower strains, but a higher amplitude and longer extent of the boundary layer, at s/C = 0. The mildly elliptical cylinder, however, exhibits a distribution of axial strain in the boundary layer which more closely resembles the response of a circular cylinder, showing little difference between the responses at s/C = 0 and s/C = 1/4.

Effects of Cylinder Orthotropy

As was the case for pressure loading, the effects of material orthotropy upon elliptical cylinders under axial compression will be discussed in the context of the three elliptical cylinders having b/a = 0.70, with the other cases shown for reference in Appendix C.

For comparison with Figures 6-34 and 6-35 for the $(\pm 45/0/90)_s$ cylinder with b/a = 0.70, the normalized radial displacements are given as a function of the normalized axial load in Figures 6-59 and 6-60 for the $(\pm 45/0_2)_s$ cylinder with b/a = 0.70, and in Figures 6-61 and 6-62 for the $(\pm 45/90_2)_s$ cylinder with b/a = 0.70. The responses at cylinder midspan are shown in Figures 6-59 and 6-61, while the responses in the boundary layer, near the end cap, are shown in Figures 6-60 and 6-62. In all of these figures, the experimental data measured at three circumferential positions, s/C = 0, 1/8, and 1/4, are compared with the results of the analysis for the perfect cylinder and the STAGS results for the imperfect cylinder. Good agreement can be

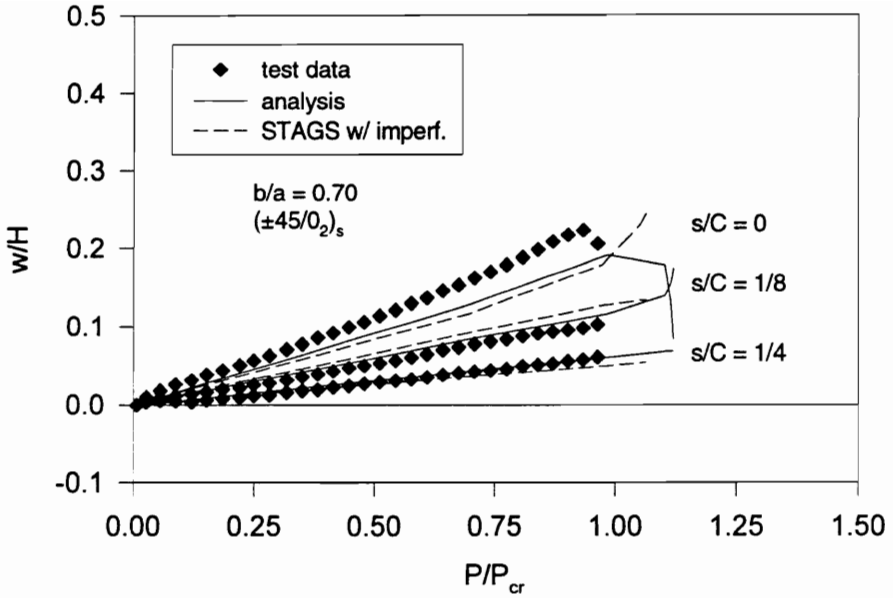

Figure 6-59 Normalized Radial Displacement at Midspan vs. P/P_{cr} for the $(\pm 45/0_2)_s$ Cylinder, b/a = 0.70.

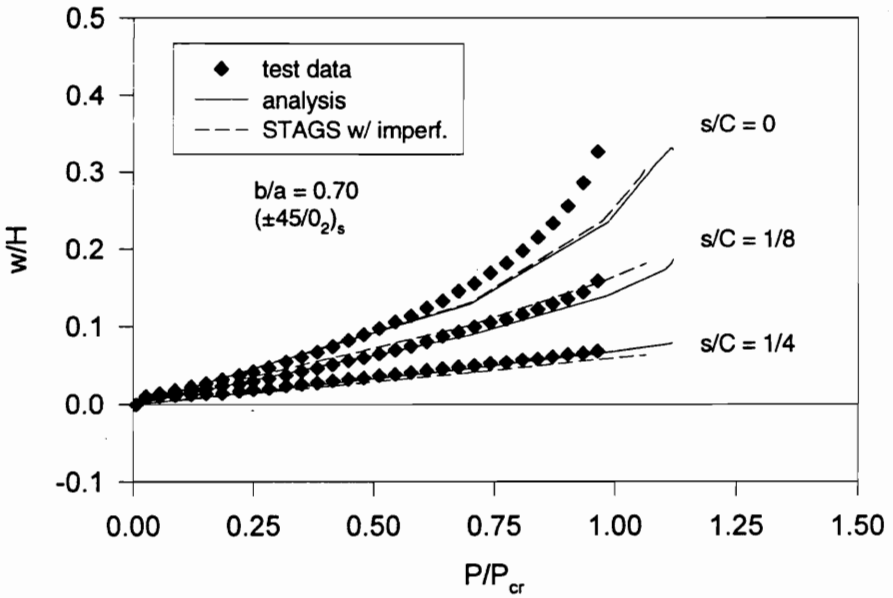

Figure 6-60 Normalized Radial Displacement near the End Cap vs. P/P_{cr} for the $(\pm 45/0_2)_s$ Cylinder, b/a = 0.70.

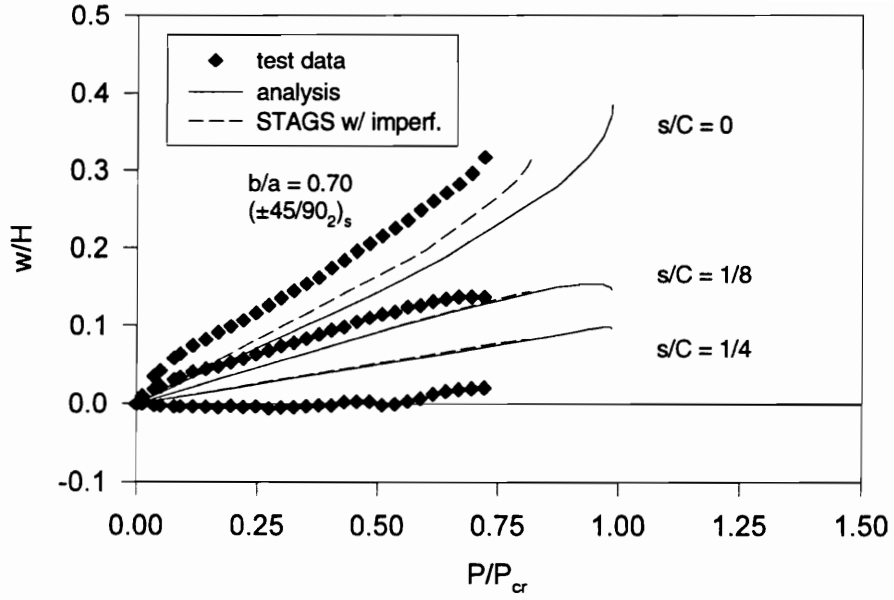

Figure 6-61 Normalized Radial Displacement at Midspan vs. P/P_{cr} for the $(\pm 45/90_2)_s$ Cylinder, b/a = 0.70.

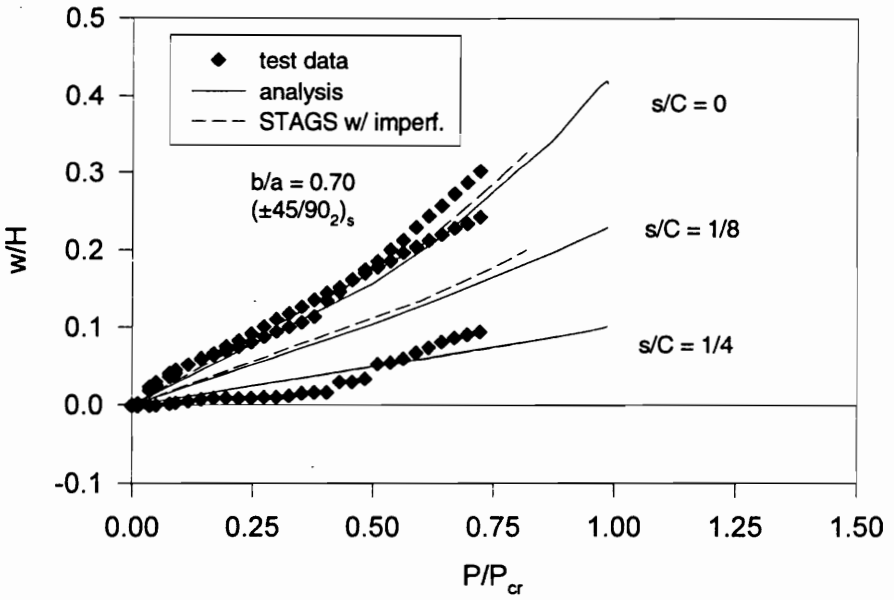

Figure 6-62 Normalized Radial Displacement near the End Cap vs. P/P_{cr} for the $(\pm 45/90_2)_s$ Cylinder, b/a = 0.70.

seen between the predicted and measured responses for the $(\pm 45/0_2)_s$ cylinder, while the correlation for the $(\pm 45/90_2)_s$ cylinder is, in general, poorer, especially at s/C = 1/8 near the end cap due to the presence of a ply seam near the DCDT position. As was the case for the quasi-isotropic cylinders, the inclusion of imperfections does not result in large differences in the predicted responses as compared to those for the perfect cylinder. The most significant improvement in the correlation between the experimental and analytical results due to the inclusion of imperfections in the analysis can be seen in the $(\pm 45/90_2)_s$ cylinder at s/C = 0 at midspan. However, at midspan for the $(\pm 45/0_2)_s$ cylinder at s/C = 0 the analysis for the perfect cylinder agrees more closely with the experimental results than does the analysis for the imperfect cylinder.

Clearly, as was the case for the quasi-isotropic elliptical cylinder, at both axial locations the radial displacements are greatest at s/C = 0, the maximum radius of curvature. For all three of the cylinders having b/a = 0.70 the radial displacements in the boundary layer reach similar levels, with the quasi-isotropic cylinder having the greatest experimentally measured radial displacements. Note that for the orthotropic cylinders, even at a high level of axial compression, the largest radial displacements are less than those generated by only 1 atm. of internal pressure loading (see Figures 6-21 and 6-22, for example). At midspan, the quasi-isotropic and axially-stiff cylinders reach similar levels of radial displacements from s/C = 0 to s/C = 1/4. The primary difference between these two cylinders lies in the fact that the $(\pm 45/0_2)_s$ cylinder exhibits a sharp downturn in the value of the radial displacement at s/C = 0 just prior to buckling. The hoop-stiff cylinder exhibits the greatest radial deformations at midspan, reaching levels, unlike the other two cylinders, comparable to those in the boundary layer. The variation of radial displacement with circumferential position is greatest for the $(\pm 45/90_2)_s$ cylinder, with the measured displacement at s/C = 1/4 being very close to zero.

A better view of the predicted deformation patterns of these cylinders, as well as the effects of including initial geometric imperfections upon these deformation patterns, can be seen in Figures 6-63 and 6-64 for the $(\pm 45/0_2)_s$ cylinder and the $(\pm 45/90_2)_s$ cylinder, respectively. These figures can be compared to Figure 6-40 for the $(\pm 45/0/90)_s$ cylinder with b/a = 0.70. As in Figure 6-40, in these figures the deformed shapes obtained from the STAGS finite element program are shown for both the perfect and imperfect cylinders at a load level equal to the largest load obtained for the imperfect cylinder. The contour lines shown on these plots represent radial displacements. Again, for the perfect cylinders, there is a degree of symmetry about the major and minor diameters as well as about the cylinders' midspan, but this symmetry is largely lost due to the inclusion of initial geometric imperfections. For both of these orthotropic cylinders, as was the case for quasi-isotropic cylinder, the largest deformations and the greatest axial variation in these deformations occurs near the maximum radii of curvature, s/C = 0 and 1/2, and the smallest deformations with the least axial variation occur near the minimum radii of curvature, s/C = ±1/4. This is true for both the perfect and imperfect cases. In comparing the results for the perfect cylinders, notice that for comparable load levels the

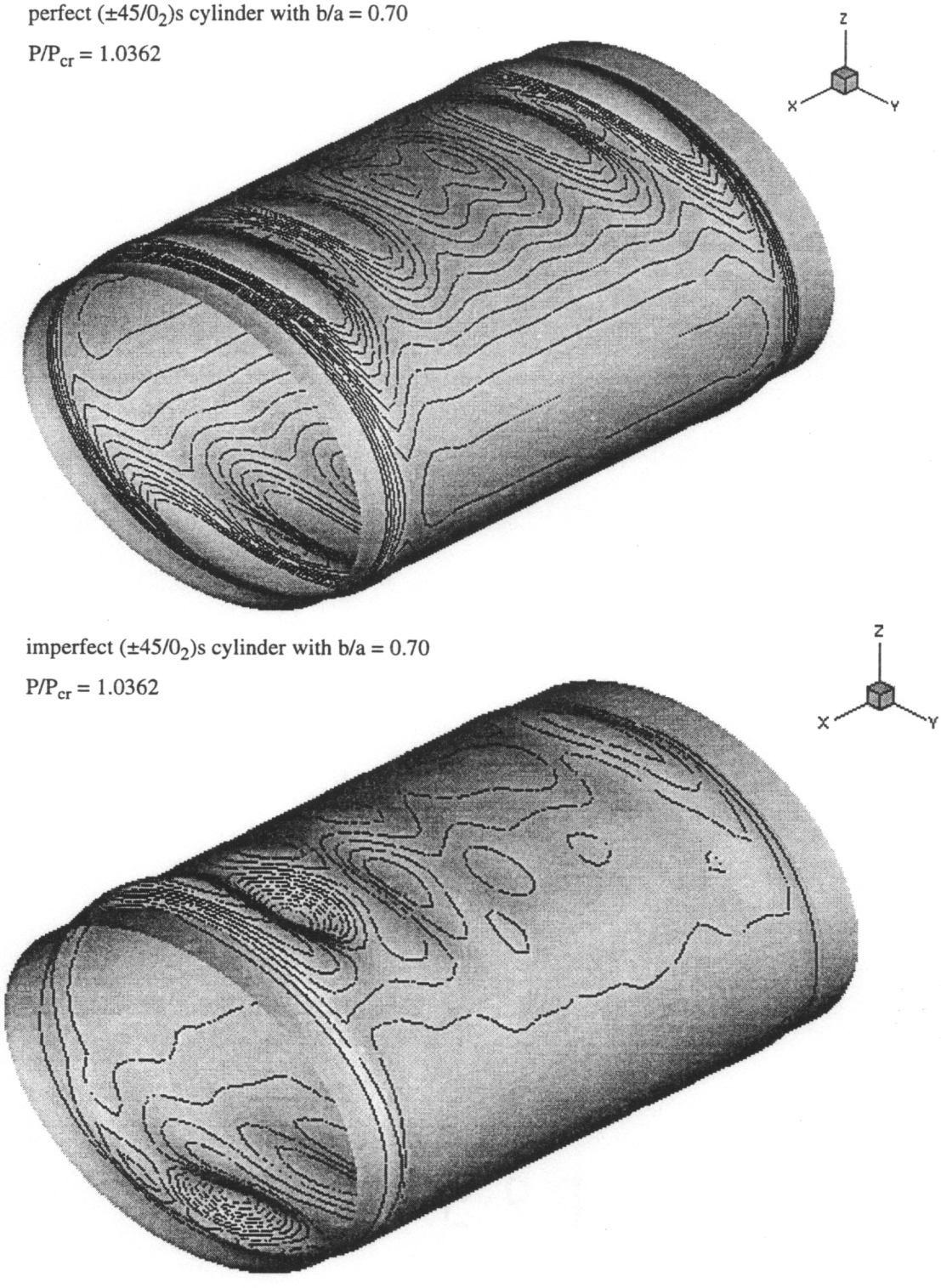

Figure 6-63 Deformed Shapes of the Perfect and Imperfect $(\pm 45/0_2)_s$ Cylinder with b/a = 0.70.

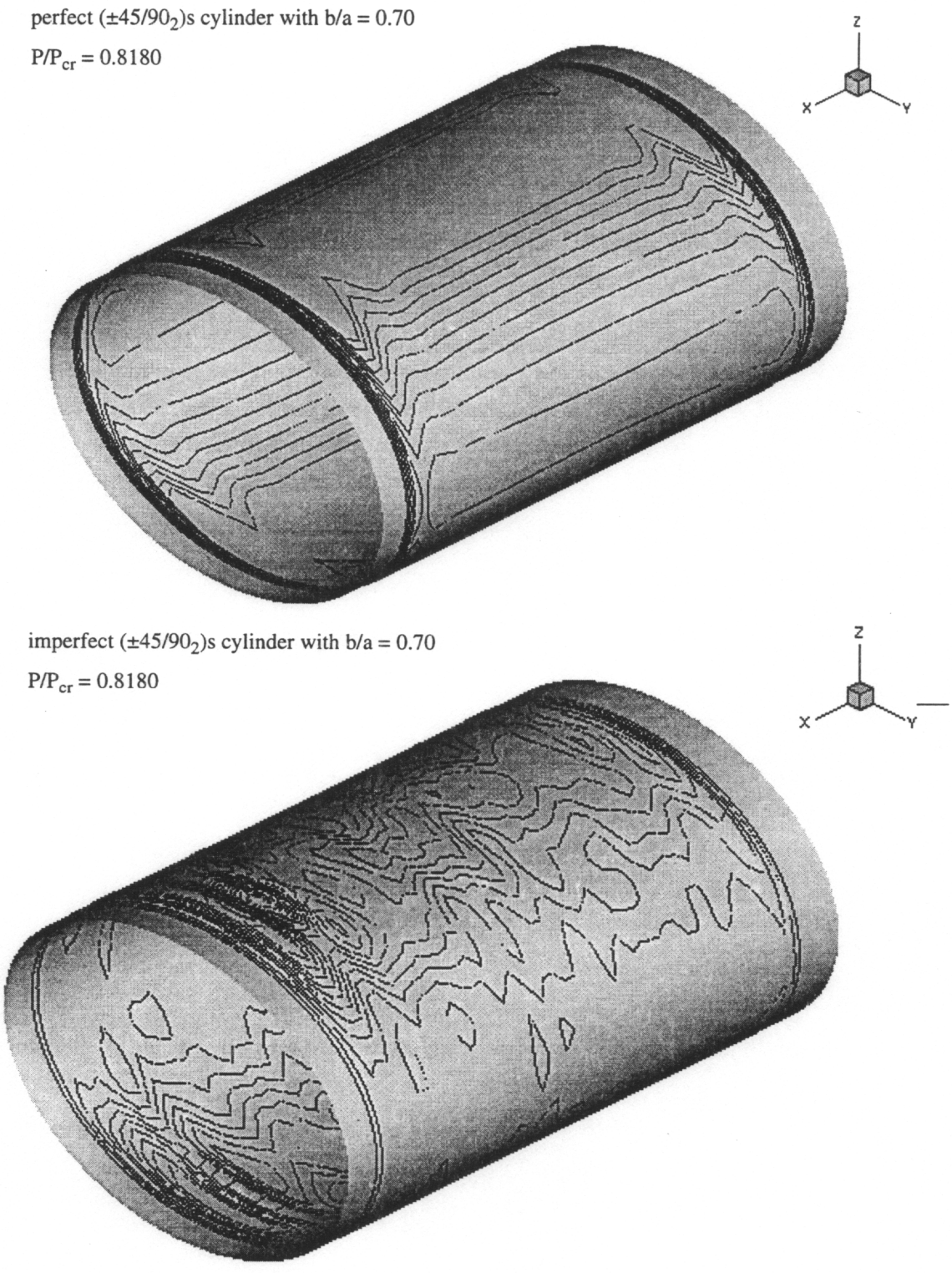

Figure 6-64 Deformed Shapes of the Perfect and Imperfect $(\pm 45/90_2)_s$ Cylinder with b/a = 0.70.

axially-stiff cylinder exhibits the greatest variations in radial displacements and the hoop-stiff cylinder the smallest variations, with the quasi-isotropic cylinder response being intermediate. This changes with the inclusion of imperfections, however, with the largest gradients in radial displacements occurring in the quasi-isotropic cylinder and the smallest variations in the $(\pm 45/0_2)_s$ cylinder. As with the quasi-isotropic cylinder, it is evident form the results for the imperfect hoop-stiff cylinder that a small misplacement, axially or circumferentially, of a displacement transducer might contribute to a significant difference between the measured and predicted results.

In Figures 6-65 - 6-68 the axial midplane strains and associated bending strains are shown as functions of the normalized axial load at midspan for the orthotropic cylinders with b/a = 0.70. These figures may be compared with Figures 6-43 and 6-44 which show corresponding results for the quasi-isotropic cylinder with b/a = 0.70. The axial midplane strains at the circumferential locations s/C = 0, 1/8, and 1/4 about the cylinder midspan are given in Figure 6-65 for the $(\pm 45/0_2)_s$ cylinder and in Figure 6-67 for the $(\pm 45/90_2)_s$ cylinder. The corresponding bending strains, κ_x*H/2, are given for the $(\pm 45/0_2)_s$ cylinder in Figure 6-66 and for the $(\pm 45/90_2)_s$ cylinder in Figure 6-68.

The axial bending strains for these cylinders are quite small, as they were for the $(\pm 45/0/90)_s$ cylinder as well. Indeed, for the axially-stiff cylinder, the axial bending strains at midspan are very close to zero and exhibit only a very small variation with circumferential position. A clearer circumferential variation in the axial bending strains can be seen for the hoop-stiff cylinder, although the values of these strains remain low, well under 10% of the associated axial midplane strains. In both cases, the agreement is quite good between the experimental results and those calculated for the cylinders with initial shape imperfections, with somewhat poorer correlation with the results for the perfect cylinders.

In comparing the axial midplane strains at midspan for the three cylinders with b/a = 0.70, the primary difference is in the slope of the responses, with the axially-stiff cylinder giving the stiffest response and the hoop-stiff cylinder showing the softest response, as would be expected. As was the case for the quasi-isotropic cylinder, for both of these orthotropic elliptical cylinders the axial strain results at midspan show virtually no circumferential variation. Indeed, no real difference can be observed at all in the $(\pm 45/0_2)_s$ cylinder between the axial strains recorded at the three circumferential locations. For these cylinders, as was the case for the quasi-isotropic cylinders, there is excellent agreement between the experimental data and the analytical results for both the perfect and imperfect cases.

The close agreement between the predicted and measured relations for the axial midplane strain as a function of axial load, which had also been observed in Figures 6-43, 6-45 and 6-47, is further illustrated in Table 6-1 by the excellent agreement in effective axial Young's modulus as calculated from the experimental data and from the analyses for the perfect and imperfect cylinders. For the analysis for the perfect cylinders,

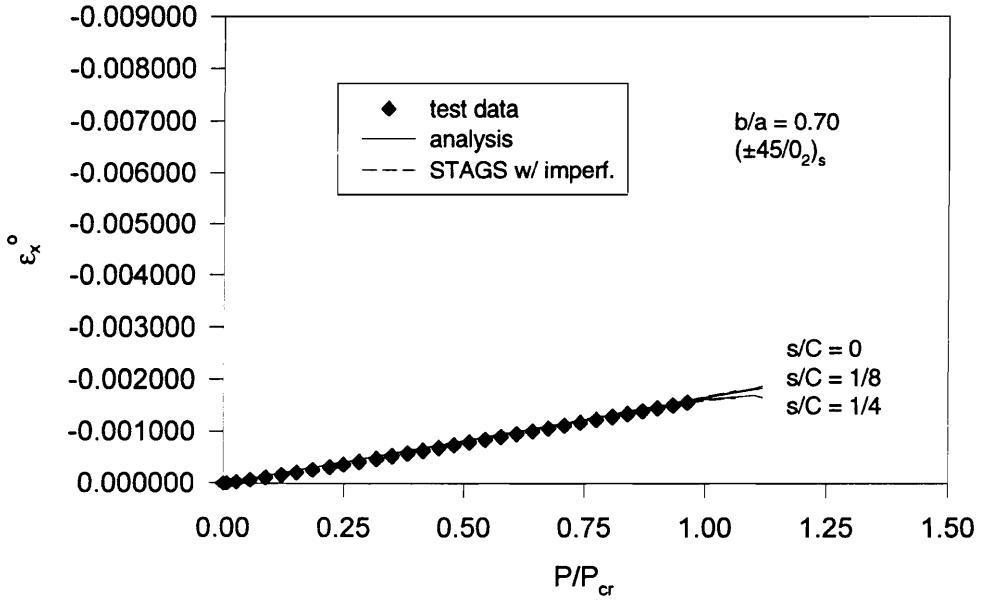

Figure 6-65 Axial Midplane Strain at Midspan vs. P/P$_{cr}$ for the $(\pm 45/0_2)_s$ Cylinder, b/a = 0.70.

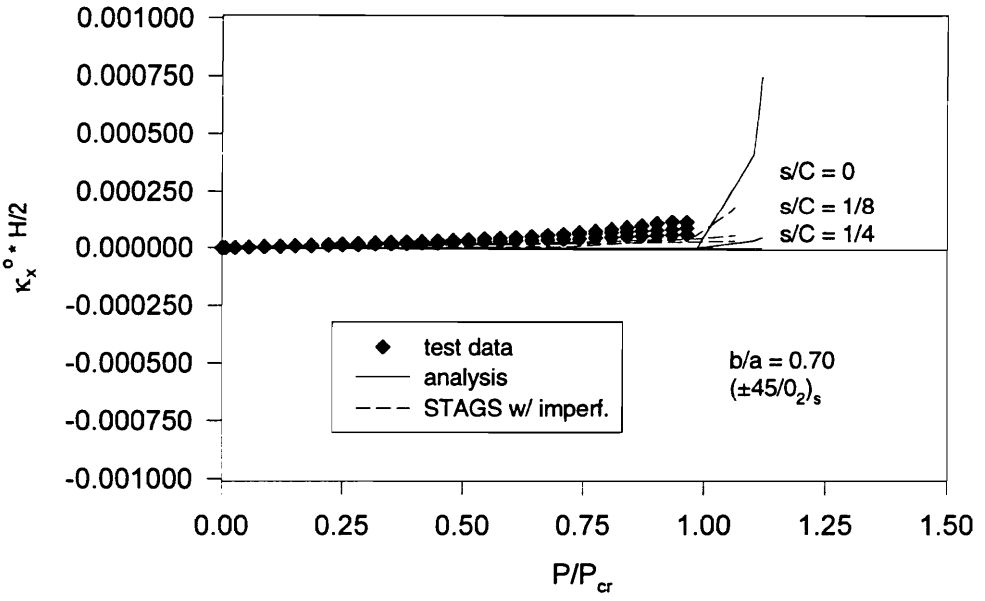

Figure 6-66 Axial Bending Strain at Midspan vs. P/P$_{cr}$ for the $(\pm 45/0_2)_s$ Cylinder, b/a = 0.70.

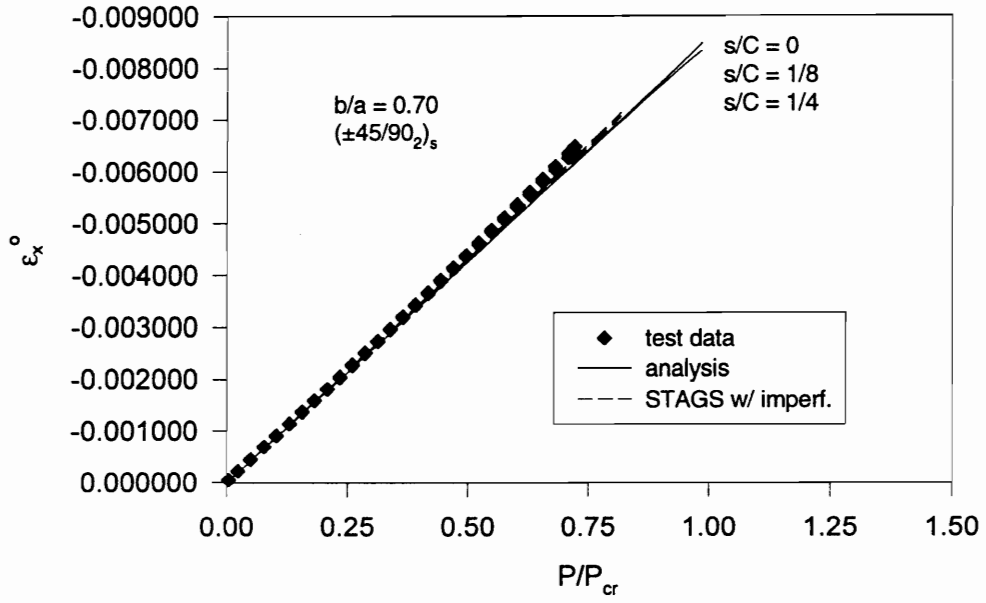

Figure 6-67 Axial Midplane Strain at Midspan vs. P/P_{cr} for the $(\pm 45/90_2)_s$ Cylinder, b/a = 0.70.

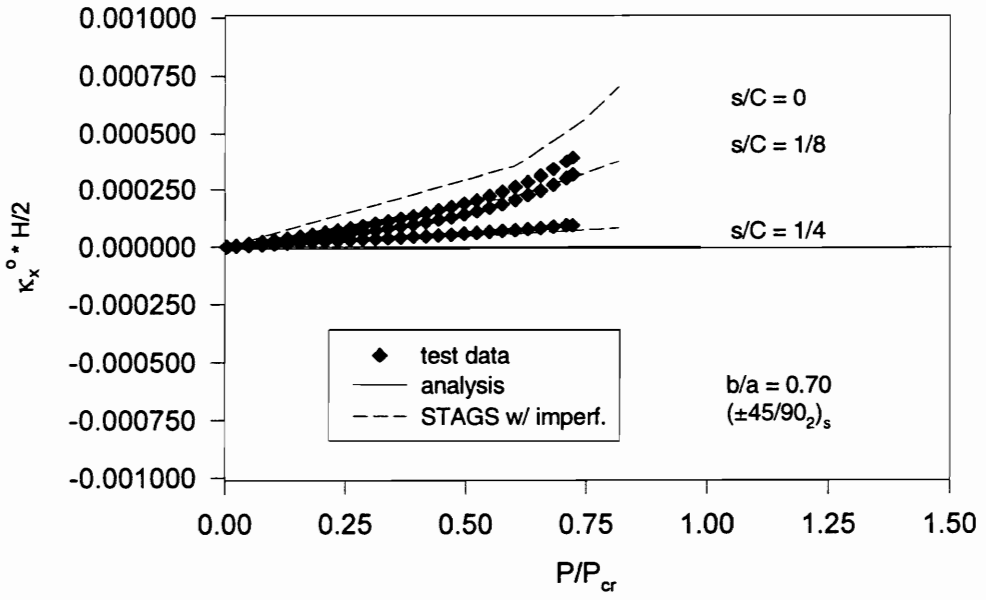

Figure 6-68 Axial Bending Strain at Midspan vs. P/P_{cr} for the $(\pm 45/90_2)_s$ Cylinder, b/a = 0.70.

the effective axial Young's modulus may be given by the mathematical definition:

$$E_x = \det[A] / (A_{22}H) = (A_{11}A_{22} - A_{12}^2) / (A_{22}H) . \quad (6.2)$$

For both the experimental data and the STAGS analysis for the imperfect cylinders, the modulus is calculated at each of the three circumferential locations, s/C = 0, 1/8 and 1/4, based upon a least-squares fit of the data used the plots of axial midplane strain versus axial load, such as those given above. Averages of these results from the three circumferential locations are also given in Table 6-1 for each of the three cylinders.

The best correlation in these results within a given cylinder can be seen in the cylinder with b/a = 0.70, while the worst comparison can be found in the results for the quasi-isotropic circular cylinder. The low value of the modulus calculated from the experimental data at s/C = 1/4 in this circular cylinder may be partly due to the presence of a ply seam near that position on the cylinder. Still, the degree to which imperfections, rather than cross sectional shape, contribute to local variations in the modulus can be seen in that the values at s/C = 0, 1/8, and 1/4 varies as much within the circular cylinder as within the elliptical cylinders.

All of the values of the effective axial Young's modulus shown in Table 6-1 are, however, quite close to one another, with the differences being at worst 7%. This agreement is good not only within a given cylinder, but among the three cylinders as well. Indeed, the average moduli calculated from the experimental results are within 5% of each other.

As was the case for the quasi-isotropic cylinders (see Figures 6-49 - 6-53), there is little or no circumferential variation in the circumferential midplane strains for the orthotropic cylinders. This can be seen in Figures 6-69 - 6-71, in which the circumferential midplane strain at midspan is given as a function of the normalized circumferential coordinate over one quarter of the cross section for the orthotropic cylinders with b/a = 0.70 at a given level of axial load. These results are shown for the $(\pm 45/0_2)_s$ cylinder at a load level of $P/P_{cr} = 0.50$ in Figure 6-69, and at a load level of $P/P_{cr} = 0.75$ in Figure 6-70. Similar results are given in Figure 6-71 for the $(\pm 45/90_2)_s$ cylinder at $P/P_{cr} = 0.50$. This cylinder buckled prior to attaining a load level of $P/P_{cr} = 0.75$, so results are shown only at $P/P_{cr} = 0.50$. In each of these figures, the function describing the circumferential midplane strain versus circumferential location for the perfect cylinders is virtually flat. Any variations seem to be primarily to initial shape imperfections. For the $(\pm 45/90_2)_s$ cylinder, the inclusion of imperfections provides a closer match with the experimental data. However, for the $(\pm 45/0_2)_s$ cylinder, as was the case for the $(\pm 45/0/90)_s$ cylinder with b/a = 0.70, the consideration of shape imperfections in the analysis makes little difference in the correlation between the experimental and the predicted results. In each of these cases, very good agreement can be seen between the test data and the analytical results for both the perfect and imperfect cylinders.

Table 6-1 Effective young's Modulus: E_x (10^{-6}) psi

Cross section	Circum. Location	$(\pm 45/0_2)_s$			$(\pm 45/0/90)_s$			$(\pm 45/90_2)_s$		
		experi-mental	STAGS w/ imperf.	det[A]/ A_{22}*H	experi-mental	STAGS w/ imperf.	det[A]/ A_{22}*H	experi-mental	STAGS w/ imperf.	det[A]/ A_{22}*H
b/a = 1.00	s/C = 0	10.394	10.573	10.822	7.2140	7.4587	7.3431	3.3028	3.4055	3.2243
	s/C = 1/8	10.630	10.789		7.2753	7.5526		3.1682	3.3119	
	s/C = 1/4	10.725	11.080		6.9931	7.4278		3.2007	3.3457	
	Average	10.583	10.814		7.1608	7.4797		3.2239	3.3544	
b/a = 0.85	s/C = 0	10.595	10.904	10.822	7.0304	7.3162	7.3431	3.1654	3.2886	3.2243
	s/C = 1/8	10.649	10.514		7.1613	7.2995		3.3263	3.1879	
	s/C = 1/4	10.340	10.541		6.9659	7.2281		3.1586	3.1706	
	Average	10.528	10.653		7.0525	7.2812		3.2167	3.2157	
b/a = 0.70	s/C = 0	10.638	10.984	10.822	7.1274	7.1394	7.3431	3.0734	3.1234	3.2243
	s/C = 1/8	10.686	10.642		7.2028	7.4245		3.0473	3.0739	
	s/C = 1/4	10.706	10.681		7.0767	6.9281		3.0486	3.1197	
	Average	10.676	10.769		7.1356	7.1640		3.0564	3.1057	

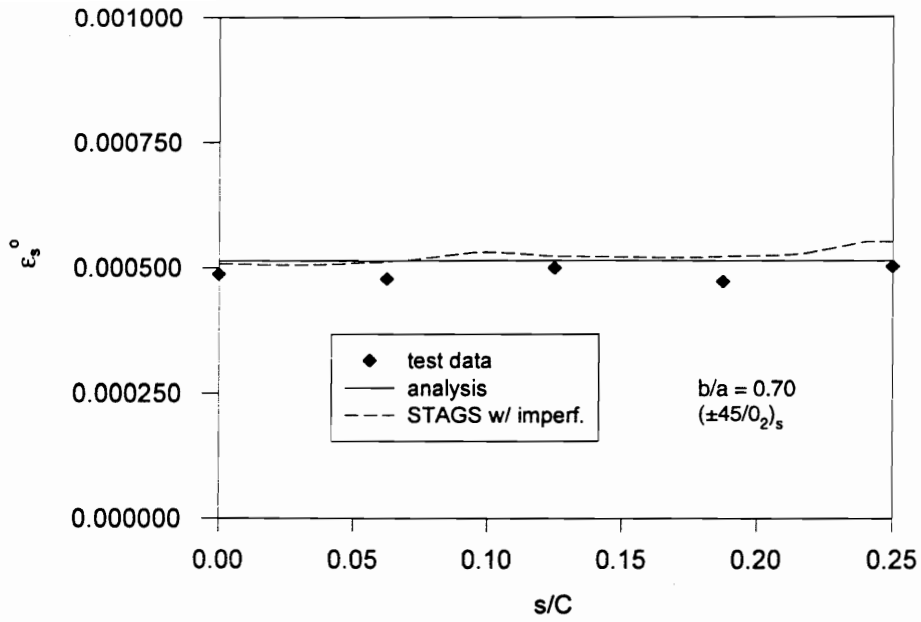

Figure 6-69 Circumferential Midplane Strain vs. s/C at Midspan for the $(\pm 45/0_2)_s$ Cylinder, b/a = 0.70, $P/P_{cr} = 0.50$.

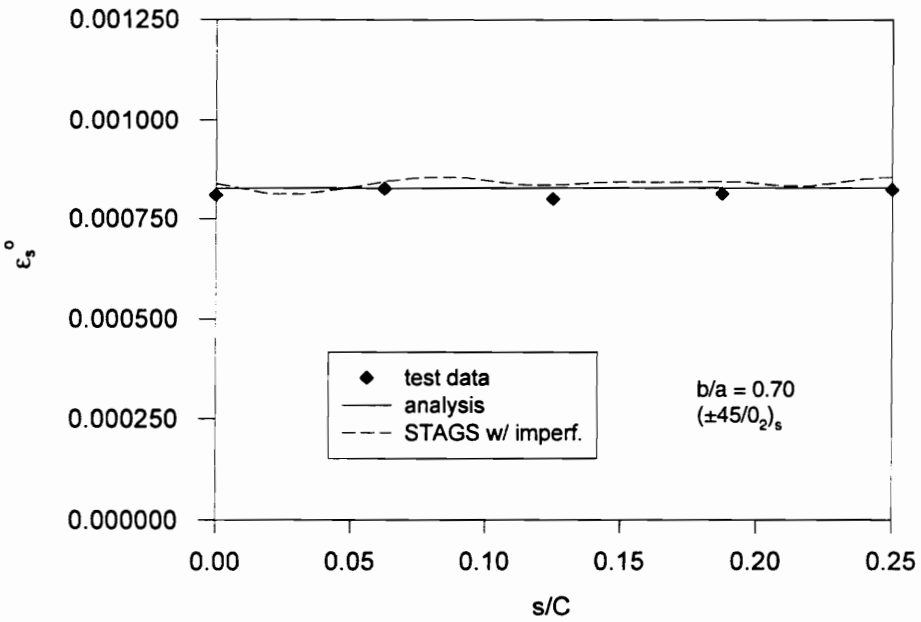

Figure 6-70 Circumferential Midplane Strain vs. s/C at Midspan for the $(\pm 45/0_2)_s$ Cylinder, b/a = 0.70, $P/P_{cr} = 0.75$.

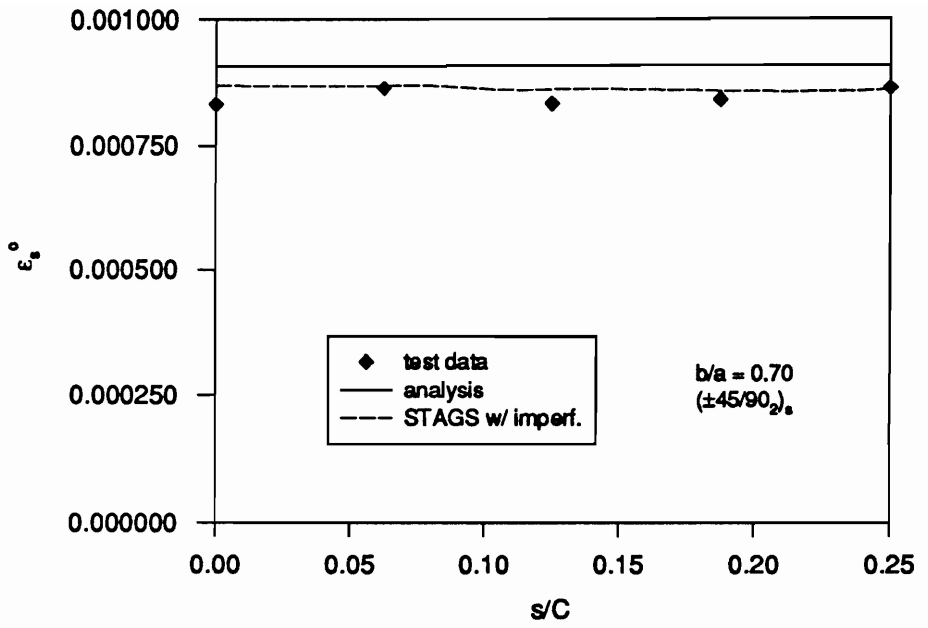

Figure 6-71 Circumferential Midplane Strain vs. s/C at Midspan for the $(\pm 45/90_2)_s$ Cylinder, b/a = 0.70, $P/P_{cr} = 0.50$.

Finally, for comparison with Figures 6-54 and 6-55 for the quasi-isotropic cylinder with b/a = 0.70, axial midplane strains in the orthotropic cylinders with b/a = 0.70 are shown as functions of the normalized axial coordinate at two circumferential positions, s/C = 0 and 1/4. These results are given for the $(\pm 45/0_2)_s$ cylinder in Figures 6-72 and 6-73 for axial loads of $P/P_{cr} = 0.50$ and $P/P_{cr} = 0.75$, respectively. The axial strain distribution for the $(\pm 45/90_2)_s$ cylinder at $P/P_{cr} = 0.50$ is shown in Figure 6-74. Note that the results for the $(\pm 45/0_2)_s$ cylinder have been graphed on a different scale from those for the $(\pm 45/90_2)_s$ and $(\pm 45/0/90)_s$ cylinders both due to the low levels of strain in this cylinder and in order to show more clearly the comparison between the experimental and analytical results.

For the $(\pm 45/0_2)_s$ cylinder the comparison is excellent between the experimental data and the analytical results for both the perfect and imperfect cylinders. Of these cylinders with b/a = 0.70, this one exhibits the shallowest boundary layer with the least circumferential variation in the amplitude and length. Shape imperfections also seem to have the least influence upon the axial strain distribution in this cylinder, although the degree of imperfections in this cylinder is not significantly less than that of the other two cylinders with b/a = 0.70 (see Appendix A). The correlation between experimental data and analytical predictions is also good for the $(\pm 45/90_2)_s$ cylinder, especially at s/C = 0. In comparing the analytical results for the perfect cylinders with b/a = 0.70, the greatest circumferential variation in the amplitude and length of the boundary layer is predicted to occur in the $(\pm 45/90_2)_s$ cylinder. The inclusion of shape imperfections,

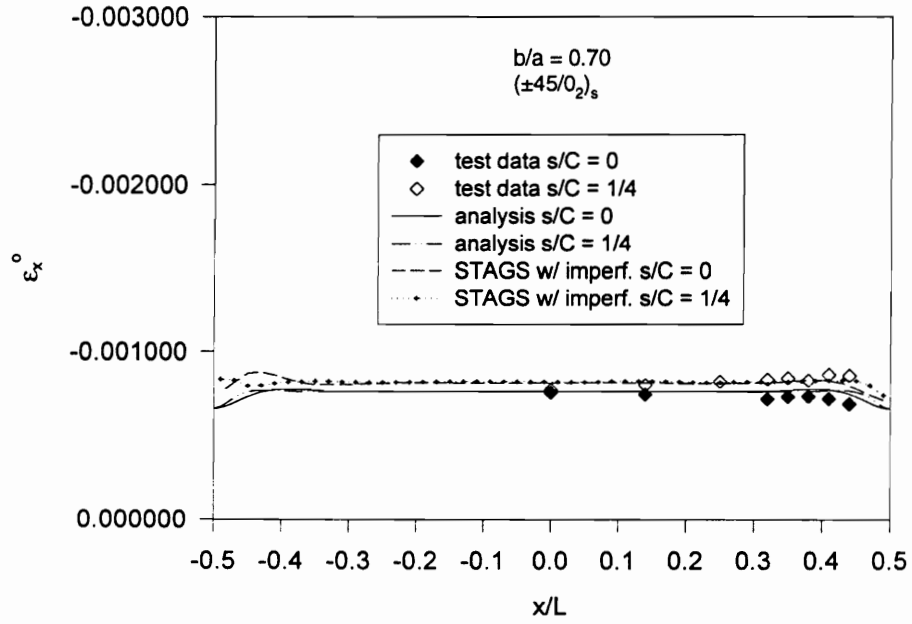

Figure 6-72 Axial Midplane Strain vs. x/L for the $(\pm 45/0_2)_s$ Cylinder, b/a = 0.70, $P/P_{cr} = 0.50$.

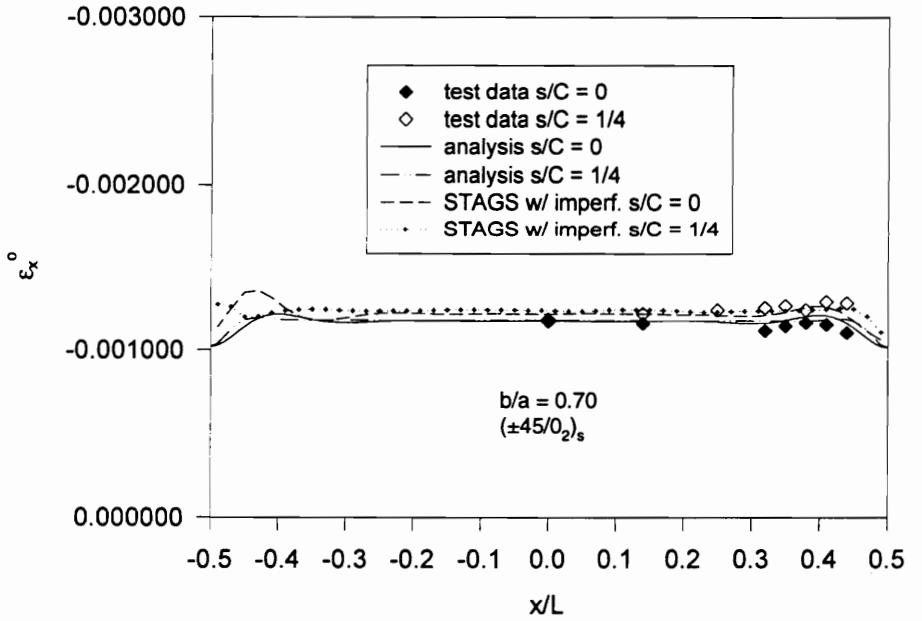

Figure 6-73 Axial Midplane Strain vs. x/L for the $(\pm 45/0_2)_s$ Cylinder, b/a = 0.70, $P/P_{cr} = 0.75$.

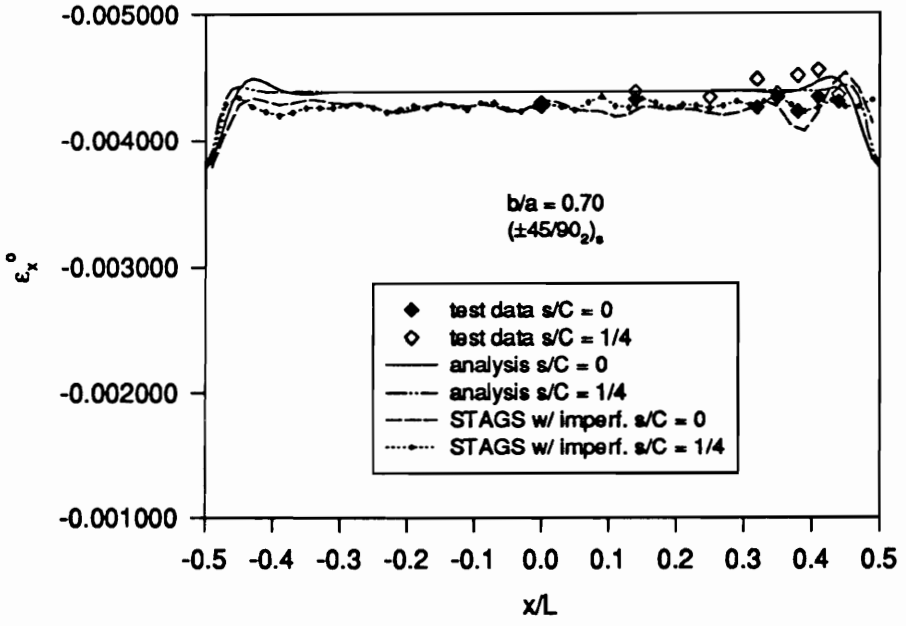

Figure 6-74 Axial Midplane Strain vs. x/L for the $(\pm 45/90_2)_s$ Cylinder, b/a = 0.70, $P/P_{cr} = 0.50$.

however, alters the character of the response so that the $(\pm 45/90_2)_s$ cylinder and the $(\pm 45/0/90)_s$ cylinder exhibit similar degrees of variation in their axial midplane strain distributions.

Buckling, Postbuckling and Failure

As stated earlier, all cylinders were loaded in axial compression to buckling and/or material failure. Each of the $(\pm 45/0/90)_s$ and $(\pm 45/0_2)_s$ cylinders discussed here buckled. Recall that the cylinders were loaded by a known axial end shortening (see Figure 3-1) and as such, buckling was associated with a sudden decrease in applied load, accompanied by an audible snap. The experimental buckling load is determined from the highest load achieved prior to the drop in load which accompanied buckling. The $(\pm 45/90_2)_s$ cylinder with b/a = 0.70 also buckled in this manner. However, the $(\pm 45/90_2)_s$ cylinders with b/a = 0.85 and b/a = 1.00 experienced material failure, in the form of a thin band of a 'brooming' type failure, which propagated swiftly around the circumference of the cylinder, prior to buckling. An illustration of the observed response of the cylinders that experienced material failure is given in Figure 6-75. A photograph of the failed $(\pm 45/90_2)_s$ cylinder with b/a = 0.85 is shown in Figure 6-76.

It was observed also, that both the circular and elliptical cylinders, although damaged, fully recovered their initial shapes after unloading.

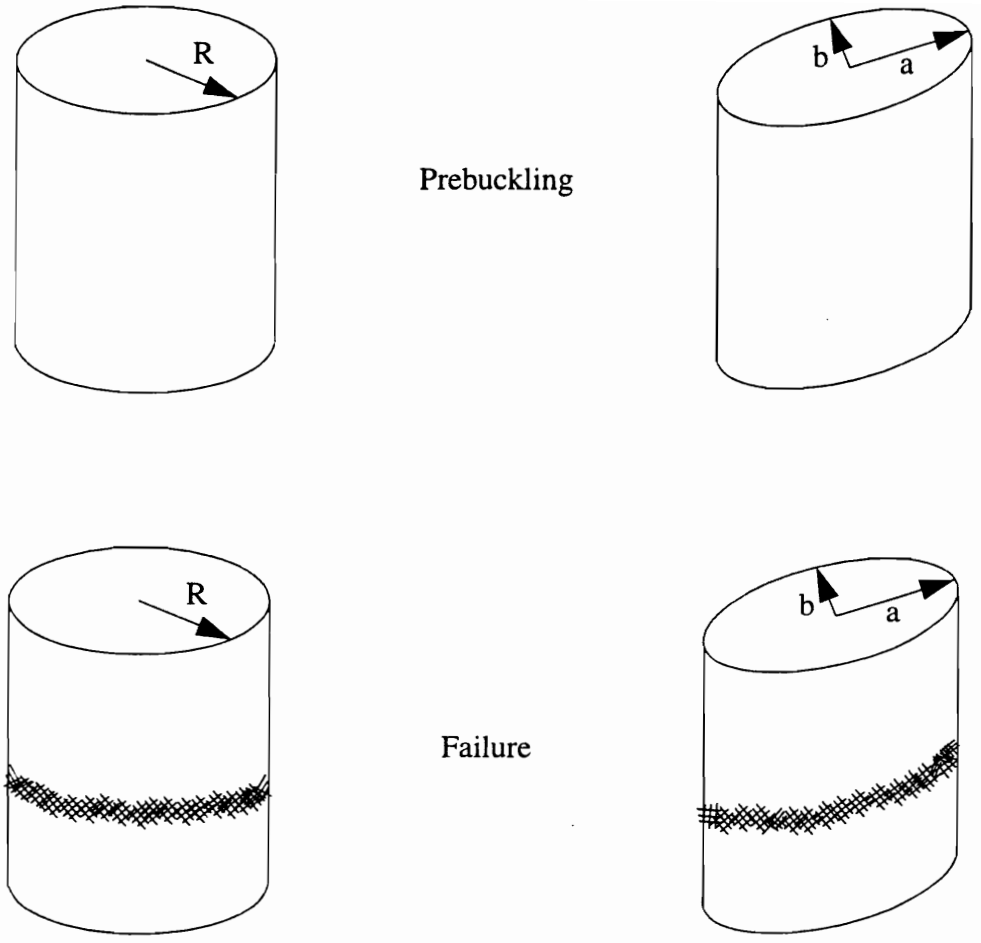

Figure 6-75 Illustration of Axial Compression to Material Failure for the $(\pm 45/90_2)_s$ Cylinders, b/a = 0.85 and b/a = 1.00.

A comparison of experimental and analytical buckling loads for the cylinders studied here is presented in Table 6-2. In the first three columns of this table, the experimental buckling load, P_{cr}^{exp}, is normalized by three different analytically predicted buckling loads. The first, P_{cr} is the classical buckling load from eqn. 4.2, which for an elliptical cylinder is the classical buckling load for a circular cylinder having a radius equal to the maximum radius of curvature of the elliptical cross section. The other two are determined from fully nonlinear collapse analyses conducted with the STAGS finite element code (see ch. 3) for both the perfect cylinder, $P_{cr}^{nl,perf.}$, and the cylinder modelled including measured shape imperfections, $P_{cr}^{nl,imperf.}$. The last two columns of Table 6-2 compare the analytical predictions by showing both sets of the nonlinear buckling loads predicted by the STAGS models, normalized by the classical buckling load, P_{cr}

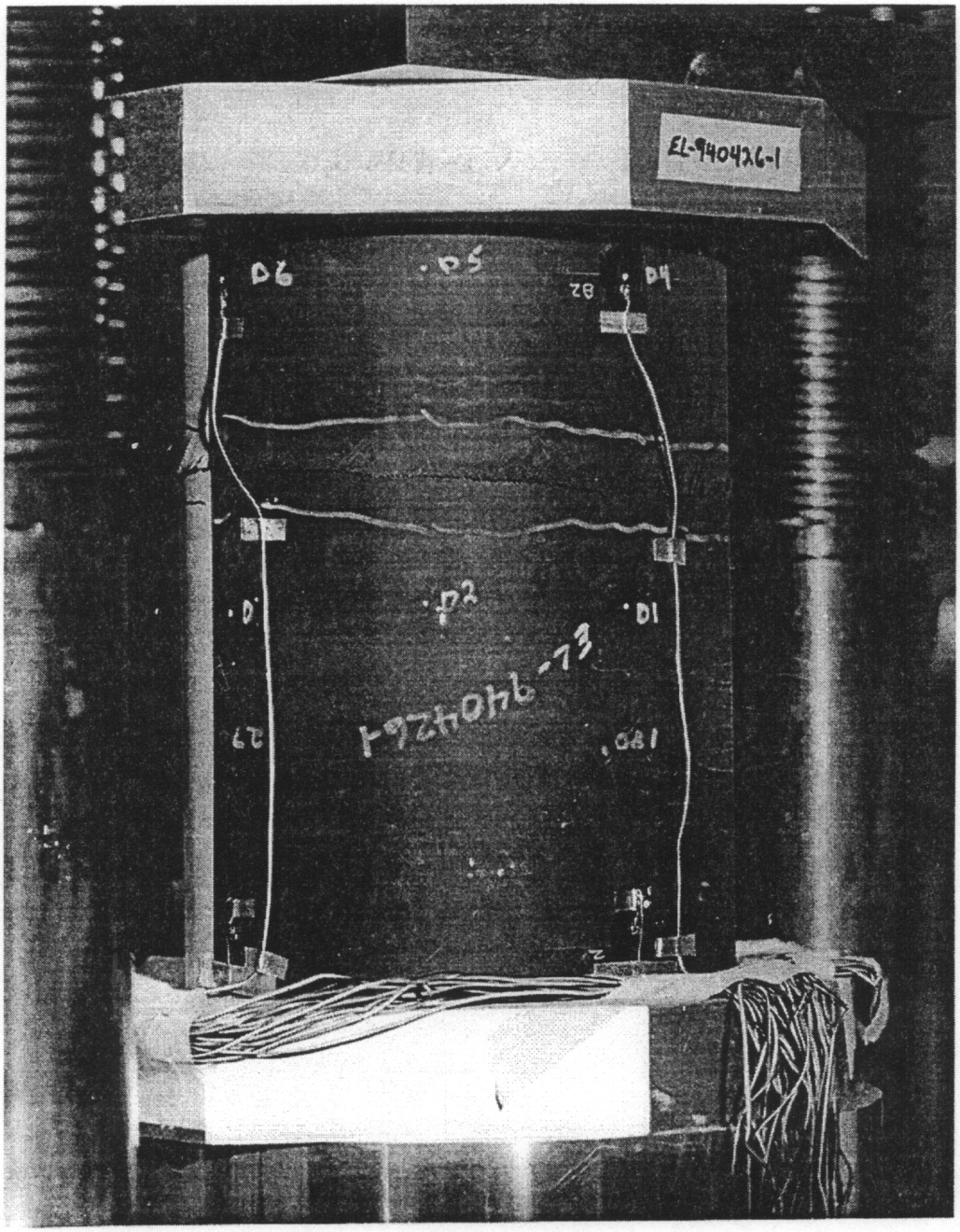

Figure 6-76 Failed $(\pm 45/90_2)_s$ Elliptical Cylinder, b/a = 0.85.

Table 6-2 Buckling Results for All Cylinders.

Lay -up	Cross Section	$(P_{cr}^{exp})/(P_{cr})$	$(P_{cr}^{exp})/(P_{cr}^{nl,perf.})$	$(P_{cr}^{exp})/(P_{cr}^{nl,imperf.})$	$(P_{cr}^{nl,perf.})/(P_{cr})$	$(P_{cr}^{nl,imperf.})/(P_{cr})$
$(\pm 45/0/90)_s$	b/a = 1.00	0.7232	0.7661	0.8687	0.9440	0.8324
	b/a = 0.85	0.8109	0.8026	0.9652	0.9898	0.8401
	b/a = 0.70	0.8187	0.8123	0.9360	1.008	0.8746
$(\pm 45/0_2)_s$	b/a = 1.00	0.8948	0.8913	0.9174	1.0039	0.9754
	b/a = 0.85	0.9321	0.8700	0.8990	1.0713	1.0368
	b/a = 0.70	0.9716	0.8677	0.9377	1.1198	1.0362
$(\pm 45/90_2)_s$	b/a = 1.00*	---	---	---	0.8009	0.7520
	b/a = 0.85*	---	---	---	0.9244	0.7371
	b/a = 0.70	0.7219	0.7319	0.8826	0.9864	0.8180

* Cylinders in which material failure occurred prior to buckling. The $(\pm 45/90_2)_s$ circular cylinder (b/a = 1.00) failed at $P/P_{cr} = 0.4549$, while the $(\pm 45/90_2)_s$ cylinder with b/a = 0.85 failed at $P/P_{cr} = 0.5962$.

Examining the first column, it is seen that both of the quasi-isotropic elliptical cylinders buckled at roughly 81% of the classical buckling load, while the quasi-isotropic circular cylinder buckled at approximately 72% of the classical prediction, as did the $(\pm 45/90_2)_s$ cylinder with b/a = 0.70. For the axially-stiff cylinders, the classical buckling prediction gave very good results, the cylinder with b/a = 0.70 buckling at 97%, the cylinder with b/a = 0.85 at 93%, and the circular cylinder at better than 89% of the classical buckling load. Comparisons of the STAGS results for the perfect cylinder, $P_{cr}^{nl,perf.}$, with the experimental results, the second column, is revealing. Despite the much greater computational cost of calculating the nonlinear buckling load for the perfect cylinders, for all of these cylinders very little was gained using this method as opposed to the formula for the classical buckling load. For the $(\pm 45/0/90)_s$ circular cylinder, there is less than a 6% improvement in the prediction of the experimental buckling load using $P_{cr}^{nl,perf.}$ rather than P_{cr}, while for the $(\pm 45/0/90)_s$ elliptical cylinders and the $(\pm 45/90_2)_s$ cylinder with b/a = 0.70 the difference is virtually nonexistent. For the $(\pm 45/0_2)_s$ cylinders, $P_{cr}^{nl,perf.}$ actually provides a nonconservative prediction relative to the classical buckling load. The inclusion of measured shape imperfections, however, makes a definite improvement in the prediction of the experimental buckling load for all but the $(\pm 45/0_2)_s$ elliptical cylinders. The nonlinear buckling loads calculated from the imperfect $(\pm 45/0/90)_s$ elliptical cylinder models are within 7% of the experimental buckling load and $P_{cr}^{nl,imperf.}$ for the $(\pm 45/90_2)_s$ cylinder with b/a = 0.70 is within 12%, a significant improvement for only a small increase in computational expense as compared to

the collapse analyses for the perfect cylinders. Including imperfections in the STAGS model for the circular cylinders also improves the result, bringing the buckling prediction to within 14% of the experimentally determined buckling load for the $(\pm 45/0/90)_s$ circular cylinder and within 9% for the $(\pm 45/0_2)_s$ circular cylinder. The fourth and fifth columns reiterate the findings of the first three columns, but in a slightly different format. What is surprising is that the axially-stiff elliptical cylinders do not seem as sensitive to imperfections, or the approximations inherent in arriving at the simple formula for P_{cr} as the other cylinders.

It should be noted that a frame-by-frame review of the video recording of the buckling of the $(\pm 45/0/90)_s$ circular cylinder revealed the growth of a small, localized damage area prior to buckling. This damage area occurred on the nodal line of the buckled pattern and may have contributed to the cylinder buckling at a lower load level than could be determined using shape imperfections alone. Attempts to model this damage area as either a small point moment or localized variation in thickness were not, however, effective in producing any significant improvement in the predicted load.

An illustration is given in Figure 6-77 which compares the observed responses of circular and elliptical cylinders to axial compression, from prebuckling to buckling, postbuckling and material failure, for those cylinders that did not experience material failure prior to buckling. For both the circular and elliptical cylinders, buckling occurs suddenly with little or no visible prebuckling deformations. Buckling, in all cases, is accompanied by a decrease in applied load and an audible snap. When a circular cylinder buckles, the buckling pattern is a classic diamond-pattern which forms a continuous ring of buckles around the midsection of the cylinder. Significant material failure occurs simultaneously at the nodal lines of the buckles and the load drops precipitously to a very low level. For an elliptical cylinder, the initial buckling pattern is generally characterized by a single diamond-shaped buckle, not accompanied by visible material failure, appearing in the midspan of the cylinder, near the maximum radius of curvature of the cross section, the flattest part of the ellipse. This single buckle often occurs on only one side of the cylinder. The appearance of this initial buckling shape is followed by a change to another shape with two or three diamond-shaped buckles across the region of the maximum radii of curvature, the flattest parts of the cylinder. At the same time, as the load transfers from the buckled flatter regions of the cylinder to the stiffer, more highly curved areas of the cylinder's circumference, a 'brooming' type of material failure occurs in this highly curved area near the minimum radii of curvature of the cross section. At this point, material failure is also visibly apparent at the nodal lines of the buckles and the cylinder is capable of carrying only a very small amount of applied load. A photograph of this state is shown in Figure 6-78 for the $(\pm 45/0/90)_s$ cylinder with cross sectional aspect ratio of $b/a = 0.70$. The extent of the region of the circumference that buckles and that in which the material fails is dependent upon the cross sectional shape. The buckled area is shorter, and the failed area larger, for the more severely elliptical cylinder.

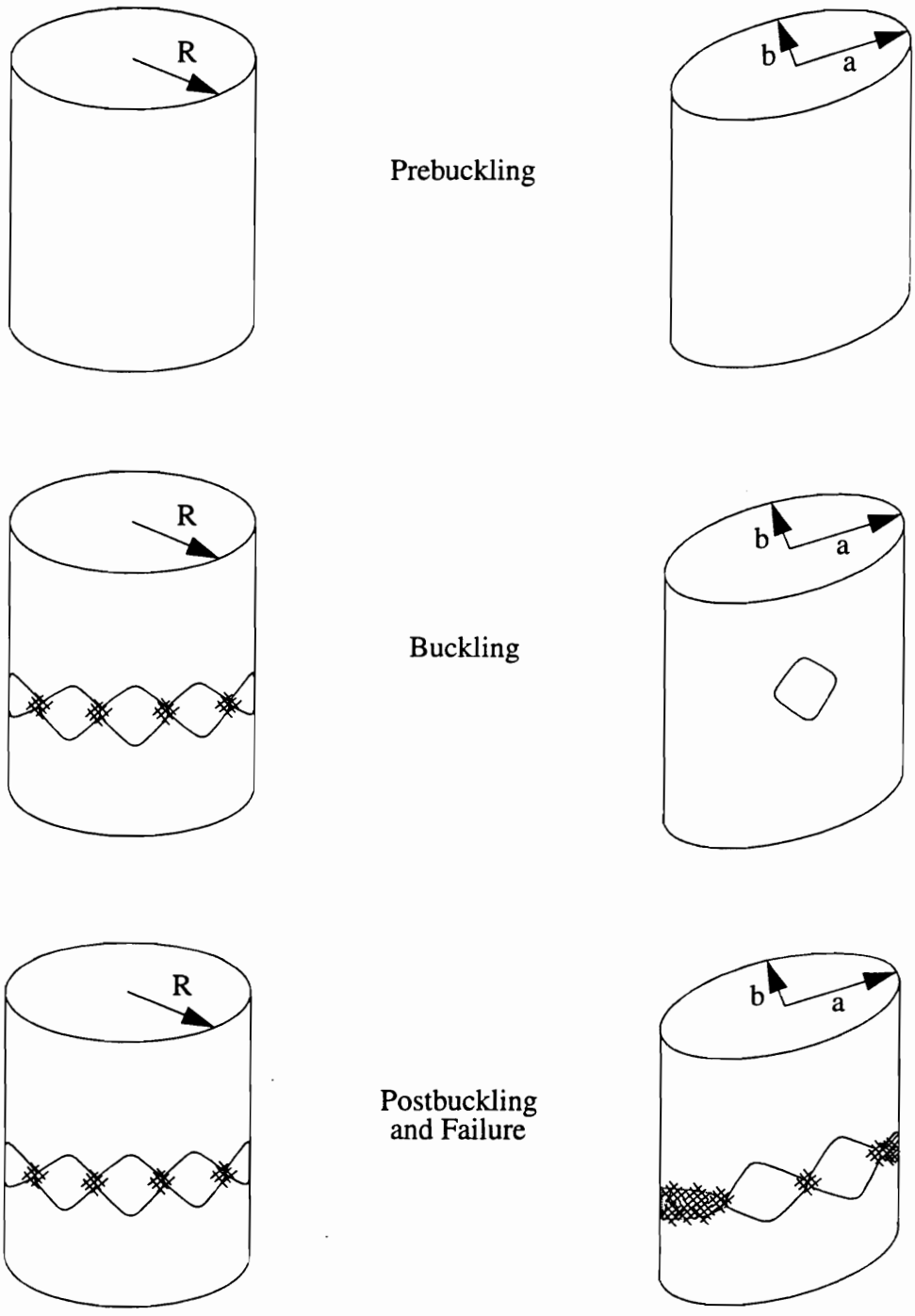

Figure 6-77 Illustration of Axial Compression to Postbuckling and Failure for Circular and Elliptical Cylinders.

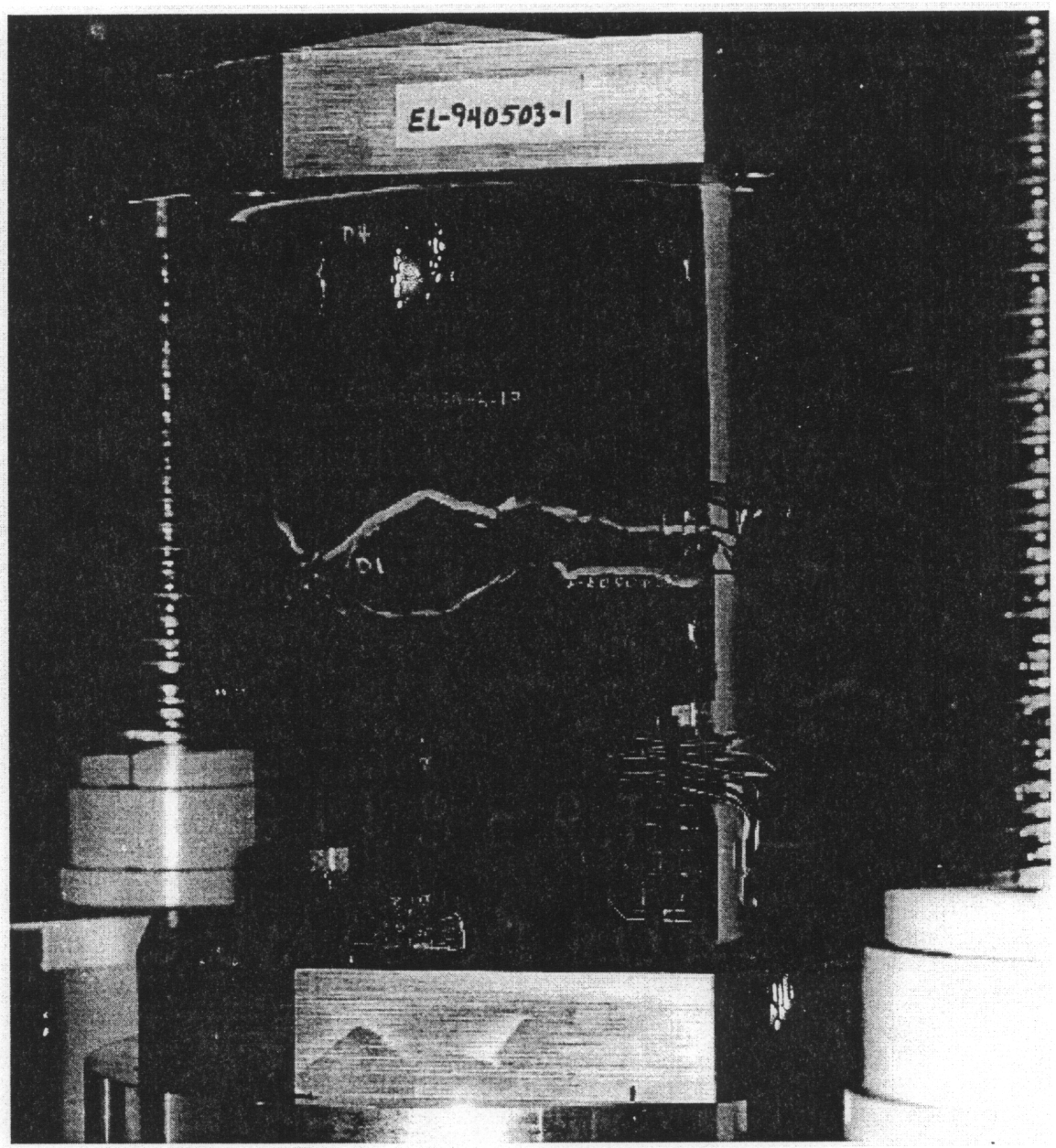

Figure 6-78 Buckled $(\pm 45/0/90)_s$ Cylinder, b/a = 0.70.

For both of the $(\pm 45/0/90)_s$ elliptical cylinders studied here, the appearance of this initial buckling shape is followed very swiftly by this change to another shape with two or three diamond-shaped buckles across the flattest parts of the cylinder. In the $(\pm 45/90_2)$s cylinder with b/a = 0.70, material failure occurs in several regions of the cylinder shortly after the appearance of an initial buckle on one side of the cylinder. Hence this case represents the only elliptical cylinder in which the final buckled pattern is not roughly symmetric about the cylinder's major and minor diameters.

For the $(\pm 45/0_2)_s$ elliptical cylinders this transistion is slower and more distinct. Unlike the quasi-isotropic cylinders, after a drop in load following the appearance of a single buckle, the load held or actually increases again until the cylinder snaps into a shape with two or three buckles across both of the flatter sections of the cylinders. It is interesting that for the $(\pm 45/0_2)_s$ cylinder with b/a = 0.70 the load achieved prior to this change of buckled shape is actually slightly greater than the load acheived prior to initial buckling. This is demonstrated in Figure 6-79 which shows the experimental load versus end-displacement, both normalized by their critical experimental values, for the $(\pm 45/0_2)_s$ cylinders with b/a = 0.70, 0.85 and 1.00. In this figure, the end displacement shown is the average of the two DCDT's which measured the axial displacement of the top end cap. In contrast to the circular $(\pm 45/0_2)_s$ cylinder, both of the $(\pm 45/0_2)_s$ elliptical cylinders continued to carry a percentage of the load after initial buckling occurred. It appears that this percentage decreases with the degree of ellipticity of the cylinder cross section. For the other elliptical cylinders, after an initial buckle appears, the cylinder progresses rapidly to failure. As the load transfers to the stiffer regions of the cylinders near the tightly curved minimum radii of curvature, the material in these regions quickly fails. For the axially-stiff elliptical cylinders, however, the material does not fail so quickly, so that the combination of material orthotropy and geometry results in some postbuckling strength.

Combined Internal Pressure and Axial Compression

Finally, results are given in this section for combined internal pressure and axial compression. In ch. 4, combined loading results were given for a cylinder at a high level of axial load with a low pressure load. In order to ensure that the cylinders were not damaged prior to final tests of pure axial compression to failure, the combined loading tests conducted here were done for 1 atm. internal pressure and a relatively low level of axial compression, specifically

$$\frac{P}{E_x CH} = \frac{\Delta}{L} = -0.000500\,. \tag{6.3}$$

This level of applied axial load was less than 20% of the classical buckling load for any of the cylinders.

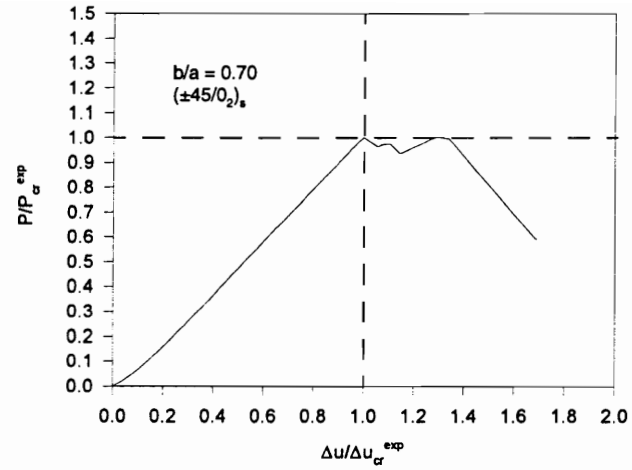

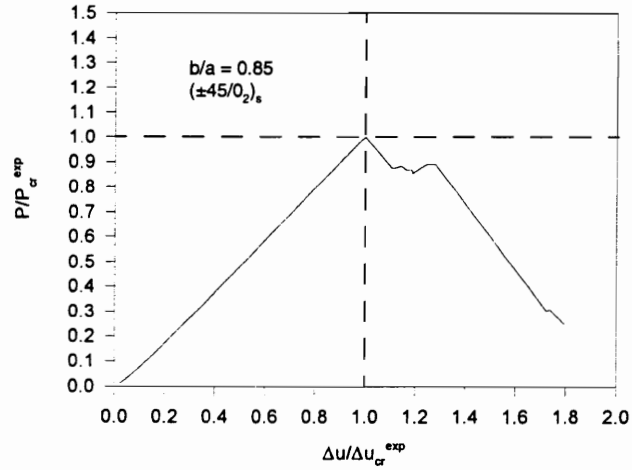

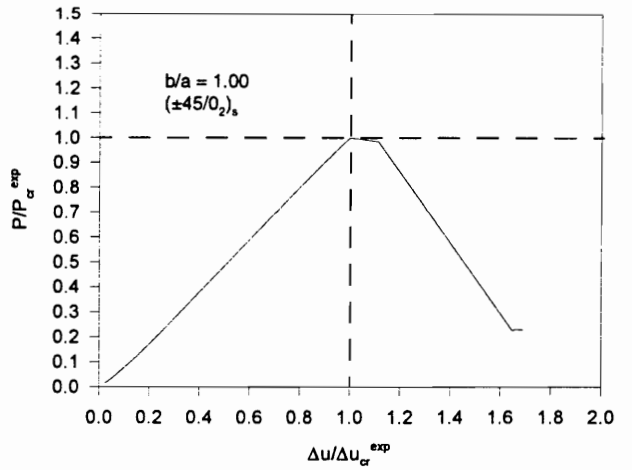

Figure 6-79 Normalized Load vs. End Displacement Experimental Results for the $(\pm 45/0_2)_S$ Cylinders.

As discussed in ch. 4, there can be a difference between linear and nonlinear predictions for cylinders only loaded by 1 atm. pressure. Two combined load tests were therefore run, applying the loads in different order to determine if there might be a dependence on load path. No appreciable difference, however, was detected between the results of these two tests. In the following discussion, results are given for strain distributions at the maximum level of combined loading, internal pressure = 1 atm. and $P/(E_xCH) = -0.000500$.

Effects of Geometry

The distribution of circumferential midplane strain at midspan as a function of normalized circumferential coordinate is given in Figures 6-80, 6-81, and 6-82 for the $(\pm 45/0/90)_s$ cylinders with b/a = 0.70, 0.85 and 1.00, respectively. In all three cases, the agreement between the predicted results and the experimental data is fairly good. The worst correlation between the analyses and the test data can be seen in the results for the circular cylinder, which has nearly as great a variation in circumferential strains as the b/a = 0.85 elliptical cylinder. For both of the elliptical cylinders, the STAGS results for the imperfect cylinders are closer to the experimental strains than the results calculated from the analysis for the perfect cylinders. Here, this is due to the inclusion of imperfections alone, as no difference in the end conditions has been included in the STAGS analysis for the imperfect cylinders relative to the analysis of the prefect cylinders.

These plots may be compared with similar plots for the quasi-isotropic cylinders under pure internal pressure in Figures 6-13 - 6-15, and those given for pure axial compression in Figures 6-49 - 6-53. For the ellipses, the results given for combined loading resemble more closely those for internal pressure alone, having, unlike the results for pure axial loading, a noticeable variation in circumferential strain with the circumferential coordinate. This variation is very slightly decreased as compared to the results for pressure alone. For all three cylinders, however, the primary difference between these results for combined loading and those for pure internal pressure is an upward shift in the average value of the circumferential strain. This can be more clearly seen by comparing Figure 6-83, in which the analytical results for all three cylinders under the combined load are given, with Figure 6-16, the corresponding graph for internal pressure alone.

The axial midplane strain for the combined load is shown as a function of the normalized axial coordinate, x/L, at two circumferential locations, s/C = 0 and s/C = 1/4. The axial strains recorded from the experimental data and those calculated for the perfect and imperfect cylinders are compared in Figures 6-84, 6-85, and 6-86 for the cylinders with b/a = 0.70, 0.85, and 1.00, respectively. As was the case for internal pressure alone, the consideration of geometric imperfections in the elliptical cylinders results in a somewhat greater circumferential variation in axial strains over most of the cylinders' lengths, perhaps due in part to the slightly lower effective Young's modulus of the imperfect cylinders (see Table 6-1). In all three cases, there

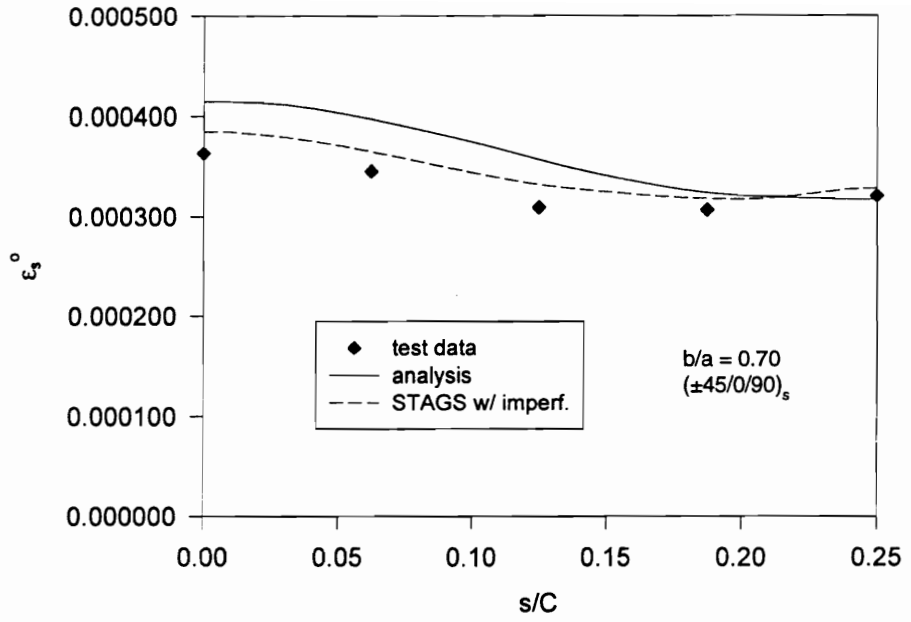

Figure 6-80 Circumferential Midplane Strain vs. s/C at Midspan for the $(\pm 45/0/90)_S$ Cylinder, b/a = 0.70, Combined Loading.

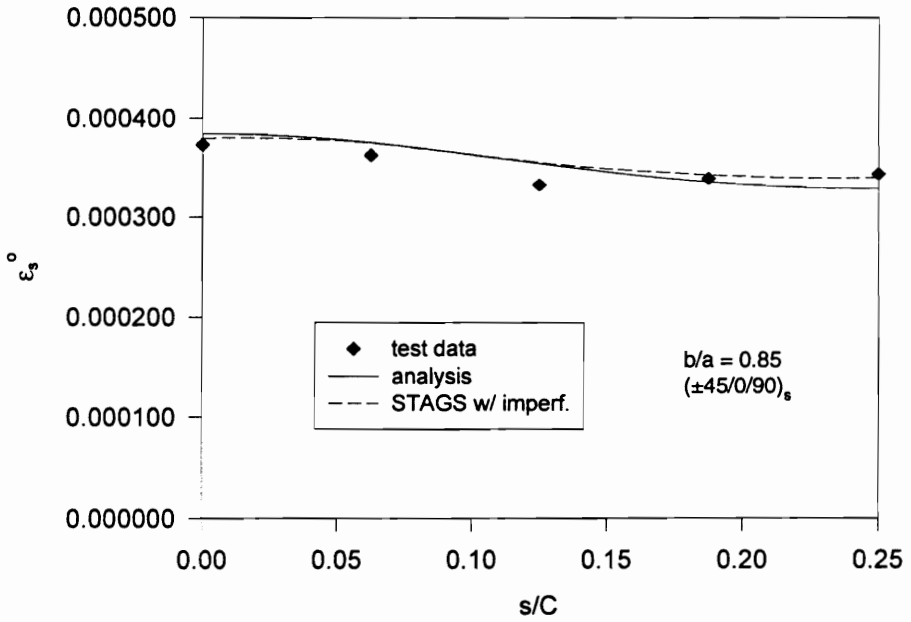

Figure 6-81 Circumferential Midplane Strain vs. s/C at Midspan for the $(\pm 45/0/90)_S$ Cylinder, b/a = 0.85, Combined Loading.

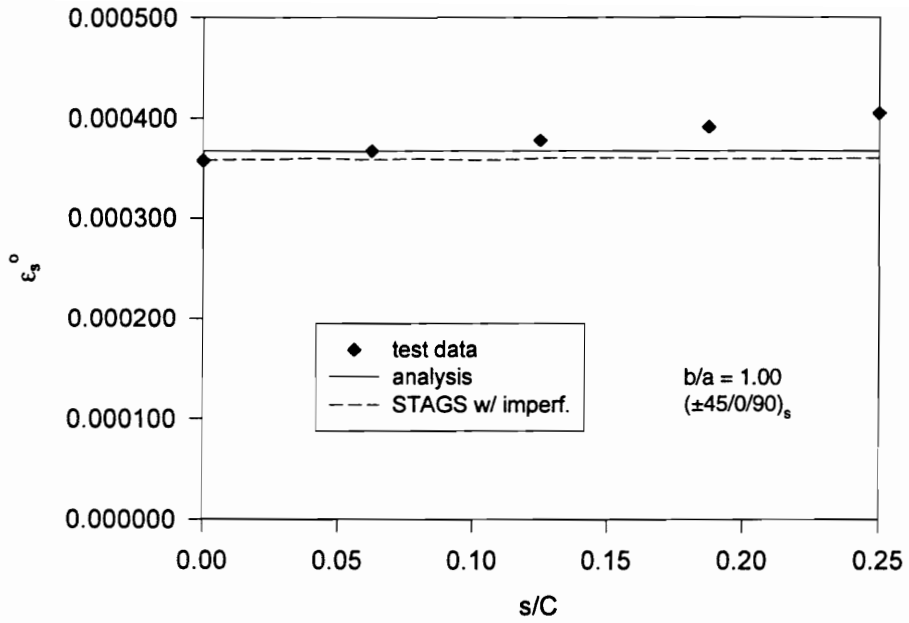

Figure 6-82 Circumferential Midplane Strain vs. s/C at Midspan for the $(\pm 45/0/90)_S$ Cylinder, b/a = 1.00, Combined Loading.

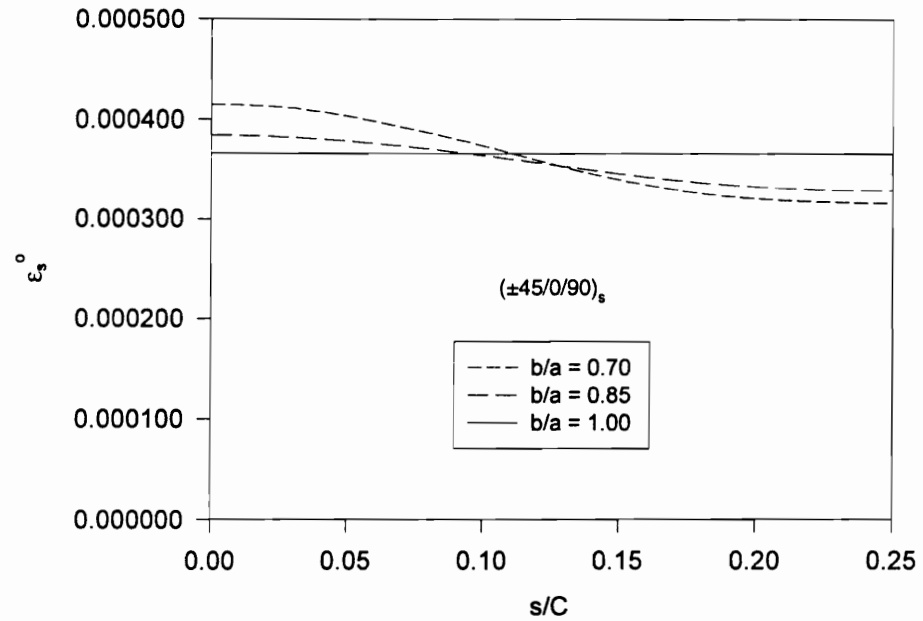

Figure 6-83 Comparison of Analytical Results for Circumferential Midplane Strain vs. s/C at Midspan for the $(\pm 45/0/90)_S$ Cylinders, Combined Loading.

is good agreement between the experimental data and the results predicted from the STAGS models of the imperfect cylinders. Again, the worst correlation can be seen in the results for the circular cylinder, shown in Figure 6-86, which shows nearly as great a difference between axial strains at s/C = 0 and s/C =1/4 as the cylinder with a cross sectional aspect ratio of b/a = 0.85. As noted previously, this may be partially due to the presence of a ply seam near the s/C = 1/4 position on this cylinder.

These plots may be compared with similar plots for pure internal pressure in Figures 6-17 - 6-19, and those given for pure axial compression in Figures 6-54 - 6-58. As was the case for circumferential strain, the axial strain results given for the elliptical cylinders under combined loading resemble more closely those for internal pressure alone, having, unlike the results for pure axial loading, a distinct variation in axial strain with both the axial and circumferential coordinate over the entire length of the cylinder. These variations are slightly decreased as compared to the results for pressure alone, especially nearer to the ends of the cylinders. For all three cylinders, however, the primary difference between these results for combined loading and those for pure internal pressure is the shift in average value of the axial strain by -0.00500. This can be more clearly seen by comparing Figure 6-87, in which the analytical results for all three cylinders under the combined load are given, with Figure 6-20, the corresponding graph for internal pressure alone.

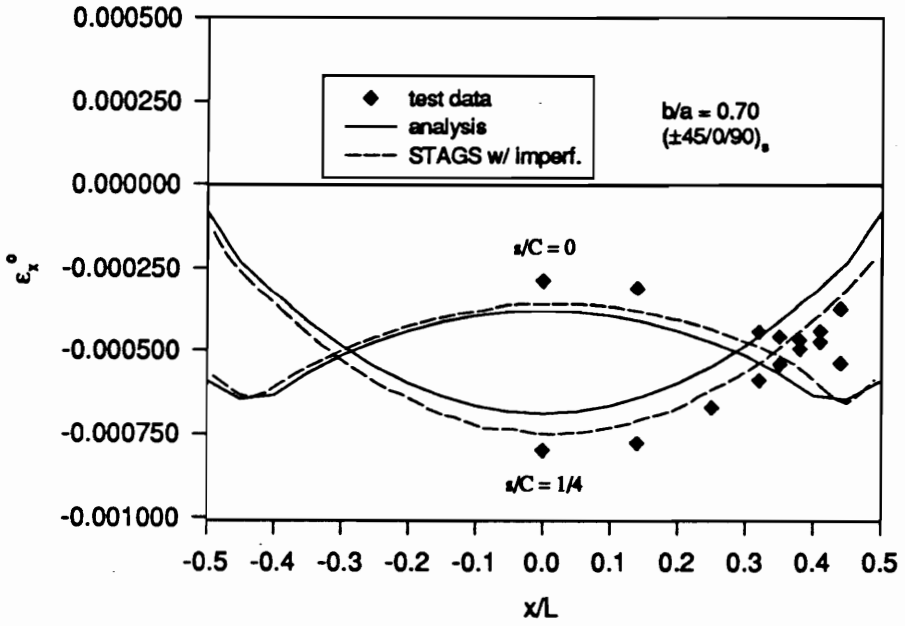

Figure 6-84 Axial Midplane Strain vs. x/Lfor the $(\pm 45/0/90)_s$ Cylinder, b/a = 0.70, Combined Loading.

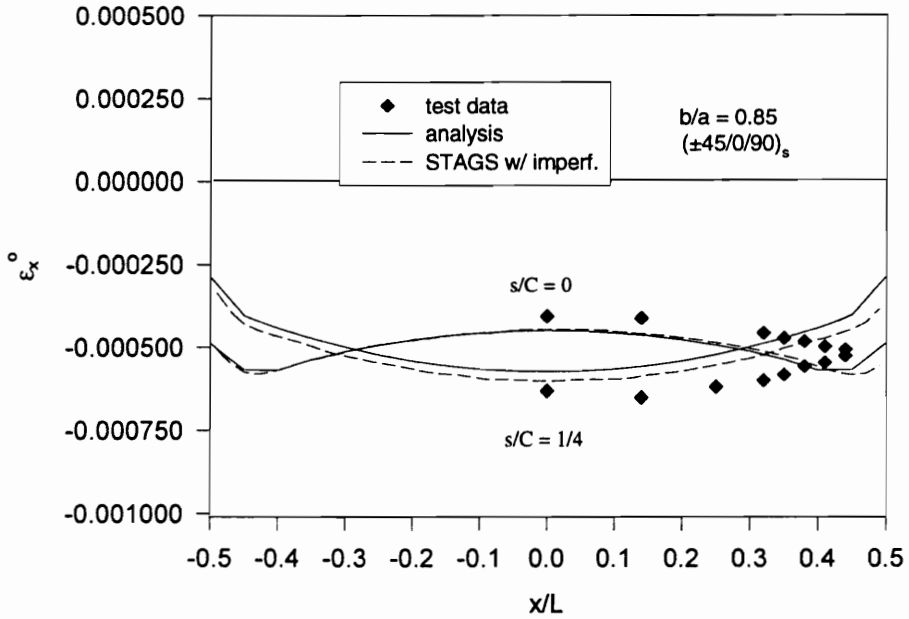

Figure 6-85 Axial Midplane Strain vs. x/L for the $(\pm 45/0/90)_S$ Cylinder, b/a = 0.85, Combined Loading.

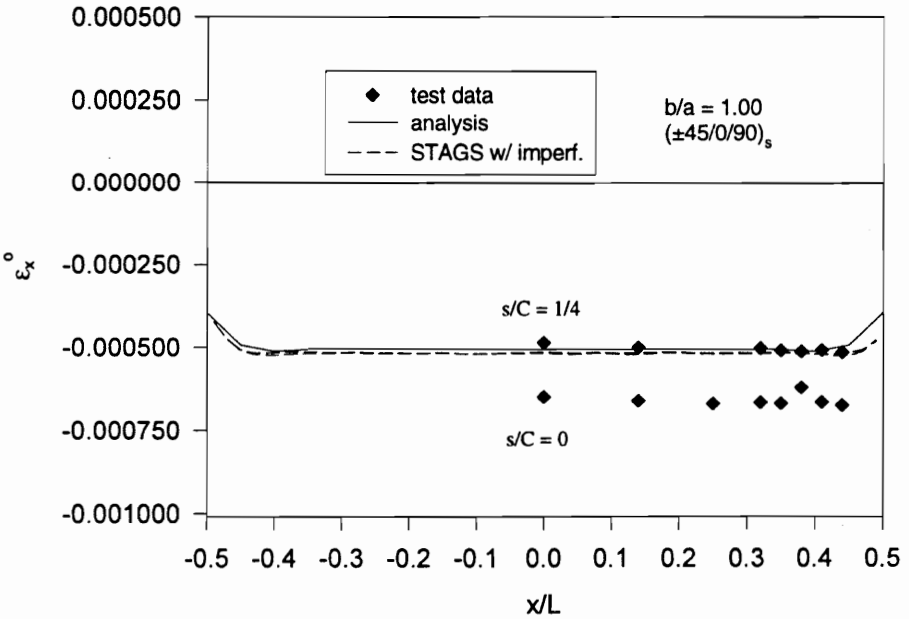

Figure 6-86 Axial Midplane Strain vs. x/L for the $(\pm 45/0/90)_S$ Cylinder, b/a = 1.00, Combined Loading.

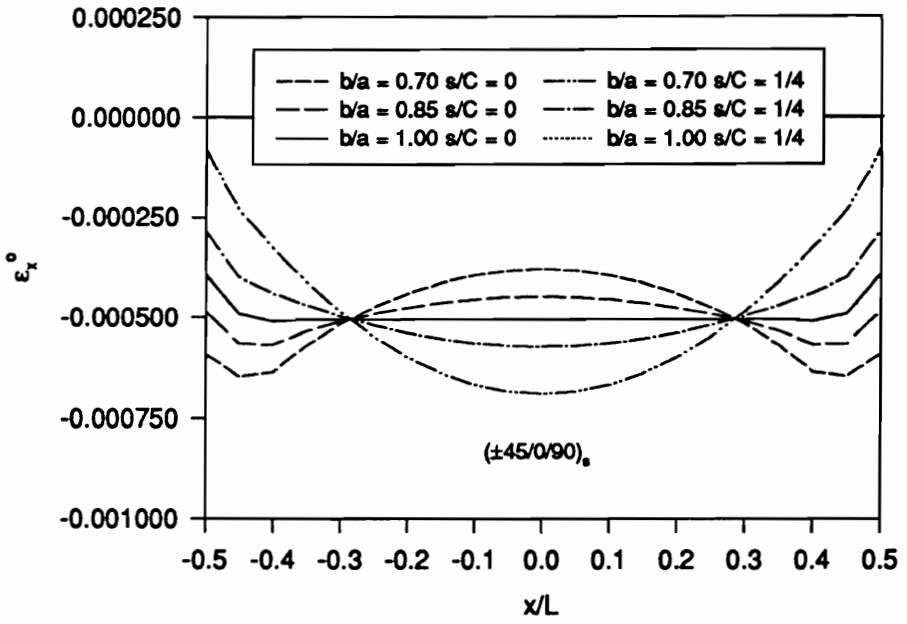

Figure 6-87 Comparison of Analytical Results for Axial Midplane Strain vs. x/L at Midspan for the $(\pm 45/0/90)_s$ Cylinders, Combined Loading.

It can be seen from these figures that even with only a small axial load added to the internal pressure load, the magnitudes of the circumferential and axial strains are increased relative to the case of internal pressure alone, while the gradients in these quantities with axial and circumferential location remain essentially the same, but still are large. As with all other quantities and load cases discussed here, these tendencies become more pronounced as the ellipticity of the cross section increases.

Effects of Orthotropy

In order to illustrate the effects of material orthotropy upon elliptical cylinders under combined loading, the circumferential midplane strain distributions at midspan are shown in Figure 6-88 for $(\pm 45/0_2)_s$ cylinder with b/a = 0.70, and in Figure 6-89 for the $(\pm 45/90_2)_s$ cylinder with b/a = 0.70. Similar results for the $(\pm 45/0/90)_s$ cylinder with b/a = 0.70 were given above in Figure 6-80. For these cases, the agreement between the measured data and the predicted results is fairly good. For the $(\pm 45/90_2)_s$ cylinder, the inclusion of shape imperfections results in a very close match with the experimental results, while for the $(\pm 45/0_2)_s$

cylinder, consideration of initial imperfections makes little improvement in the correlation between experimental and analytical results.

The highest levels of circumferential strain and the largest circumferential gradient in this strain can be seen in the axially-stiff elliptical cylinder shown in Figure 6-88. Note that this figure is plotted on a scale which is shifted upward by comparison with Figures 6-80 and 6-89 due to the much higher levels of circumferential strain for the $(\pm 45/0_2)_s$ cylinder. The lowest strain levels and smallest circumferential variation in circumferential strain occur in the hoop-stiff cylinder, with the quasi-isotropic cylinder giving results intermediate to those of the orthotropic cylinders. These plots may be compared with Figures 6-28 and 6-29, which show similar results for pure internal pressure, and Figures 6-69 - 6-71, for the case of pure axial compression. As was the case for the quasi-isotropic elliptical cylinder, the results for combined loading for the orthotropic elliptical cylinders more closely resemble the results for internal pressure alone, having an identifiable circumferential variation in the circumferential strains at midspan. Although this variation is very slightly decreased by comparison to the results for pressure alone, the primary difference, for both cylinders, is in an upward shift in the average value of the circumferential strain. This was also the case for the quasi-isotropic cylinder. This effect can be seen more clearly by comparing Figure 6-90, in which the perfect cylinder results are given together for all three cylinders with b/a = 0.70, with Figure 6-30, the corresponding graph for internal pressure alone. Also, by comparing the results of Figure 6-90 with those

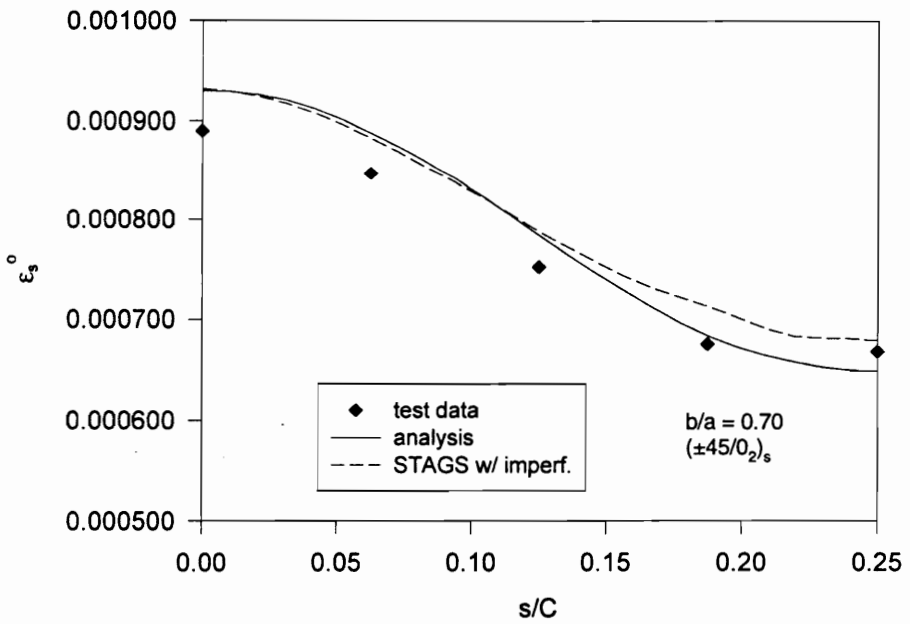

Figure 6-88 Circumferential Midplane Strain vs. s/C at Midspan for the $(\pm 45/0_2)_s$ Cylinder, b/a = 0.70, Combined Loading.

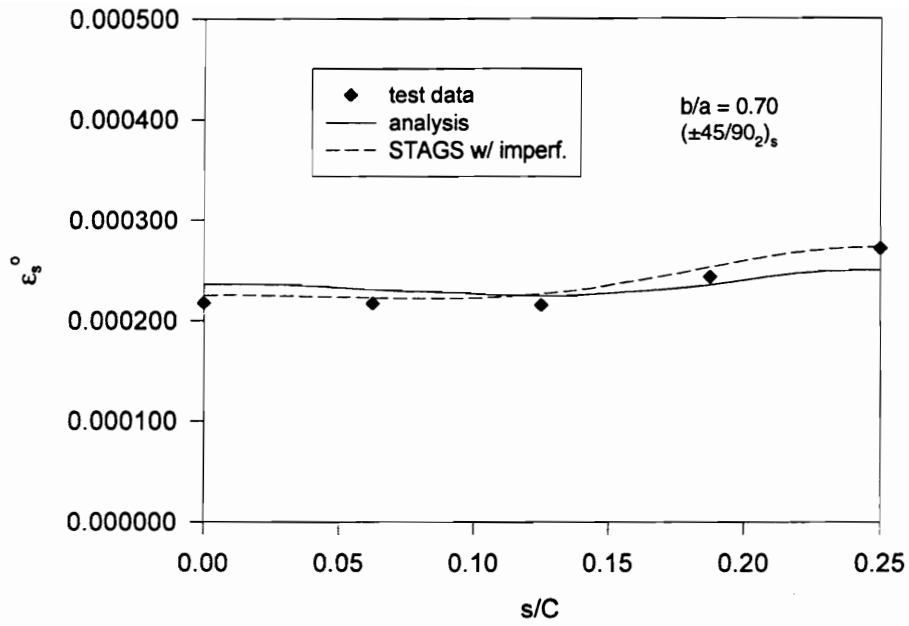

Figure 6-89 Circumferential Midplane Strain vs. s/C at Midspan for the $(\pm 45/90_2)_s$ Cylinder, b/a = 0.70, Combined Loading.

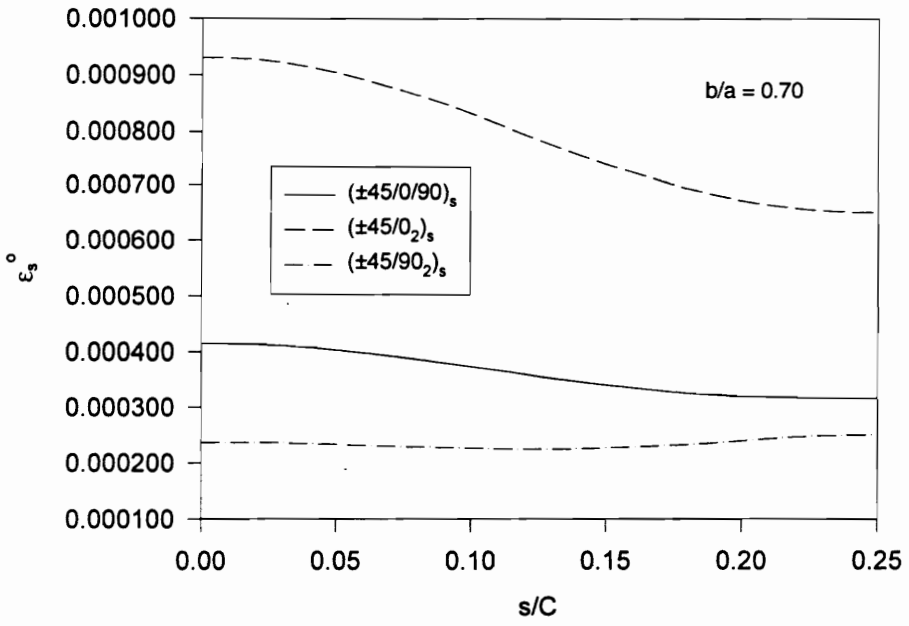

Figure 6-90 Comparison of Analytical Results for Circumferential Midplane Strain vs. s/C at Midspan for the $(\pm 45/0/90)_s$, $(\pm 45/0_2)_s$, and $(\pm 45/90_2)_s$ Cylinders, b/a = 0.70, Combined Loading.

in Figure 6-83, which gives the analytical combined load results for the quasi-isotropic perfect cylinders, it can be seen that material orthotropy has a greater influence upon distribution of circumferential strains in a noncircular cylinder than does the cross sectional ellipticity on these strains in a quasi-isotropic cylinder.

Lastly, the axial midplane strain for the orthotropic cylinders with b/a = 0.70 under combined load is plotted against the normalized axial coordinate at two circumferential locations, s/C = 0 and s/C = 1/4. These results are shown for the $(\pm 45/0_2)_s$ cylinder in Figure 6-91, and for the $(\pm 45/90_2)_s$ cylinder in Figure 6-92. Similar results were given above for the quasi-isotropic cylinder with b/a = 0.70 in Figure 6-84. These results may also be compared with Figures 6-31 and 6-32 for these orthotropic cylinders loaded by pure internal pressure, and Figures 6-72 - 6-74 for the case of pure axial compression.

For these cylinders, there is excellent agreement between the experimental and the analytical results for the imperfect cylinders, with somewhat poorer, but still reasonably good, agreement between the experimental data and the analyses for the perfect cylinders. As was the case for the $(\pm 45/0/90)_s$ elliptical cylinder, as well as these cylinders when loaded by pressure alone, the inclusion of initial shape imperfections in the analysis results in a somewhat greater circumferential variation in the axial strains over most of the midsection of the cylinder. As also was observed in the quasi-isotropic elliptical cylinder, the axial strain results for these orthotropic elliptic cylinders are very similar in character to the results obtained for pressure loading alone. The circumferential variations in axial strains for the combined load are somewhat decreased, particularly near the ends of the cylinder, but different from the pure internal pressure case primarily in a roughly -0.000500 shift in the average value of the axial strain.

Like the case of pressure only, for combined loading the axially-stiff cylinder exhibits the lowest levels of axial strain as well as the least axial and circumferential variation in the axial strains. The axial strain distribution in the quasi-isotropic cylinder is only slightly greater. The hoop-stiff cylinder undergoes the greatest axial strains and has the largest gradients in these strains. Note that Figure 6-92 for the $(\pm 45/90_2)_s$ cylinder is plotted to a larger scale due to the much larger range of axial strains experienced by this cylinder. Indeed, unlike the axially-stiff and quasi-isotropic elliptical cylinders, the hoop-stiff cylinder under combined loading undergoes a sign change in the axial strain near the ends of the cylinder along the s/C = 1/4 circumferential position.

For ease of comparison, the analytical results based upon the perfect cylinder geometry for the three cylinders with b/a = 0.70 under combined loading are shown together in Figure 6-93. These may also be compared with Figure 6-33, a similar graph for the cylinders with b/a = 0.70 loaded by pressure only, and with Figure 6-87, for the three perfect quasi-isotropic cylinders under combined loading. In comparing Figures 6-93 and 6-87, it appears that, as was seen for the circumferential strains, for a noncircular cylinder material orthotropy has a greater effect on the axial strain profile than does cylinder ellipticity for a quasi-isotropy cylinder.

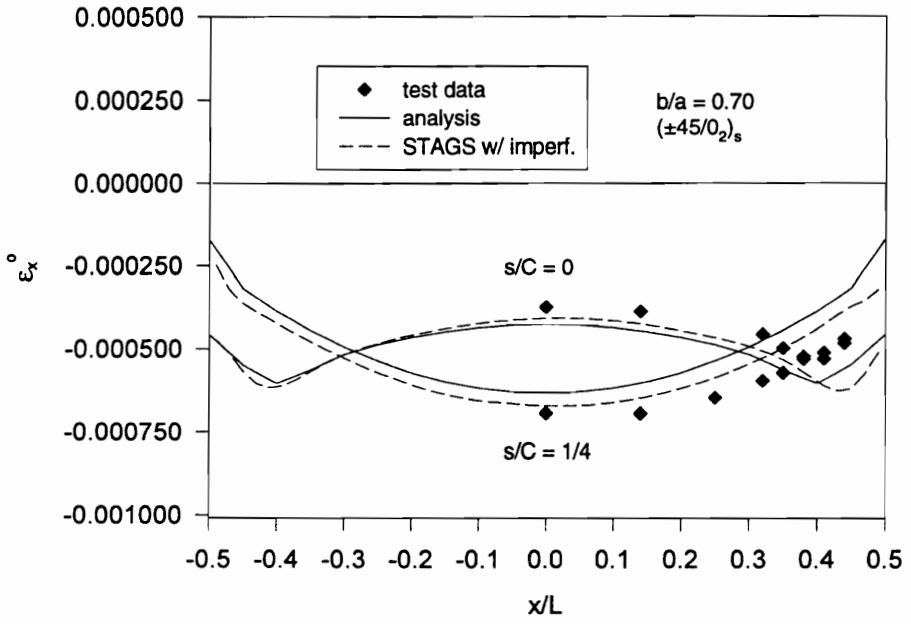

Figure 6-91 Axial Midplane Strain vs. x/L for the $(\pm 45/0_2)_s$ Cylinder, b/a = 0.70, Combined Loading.

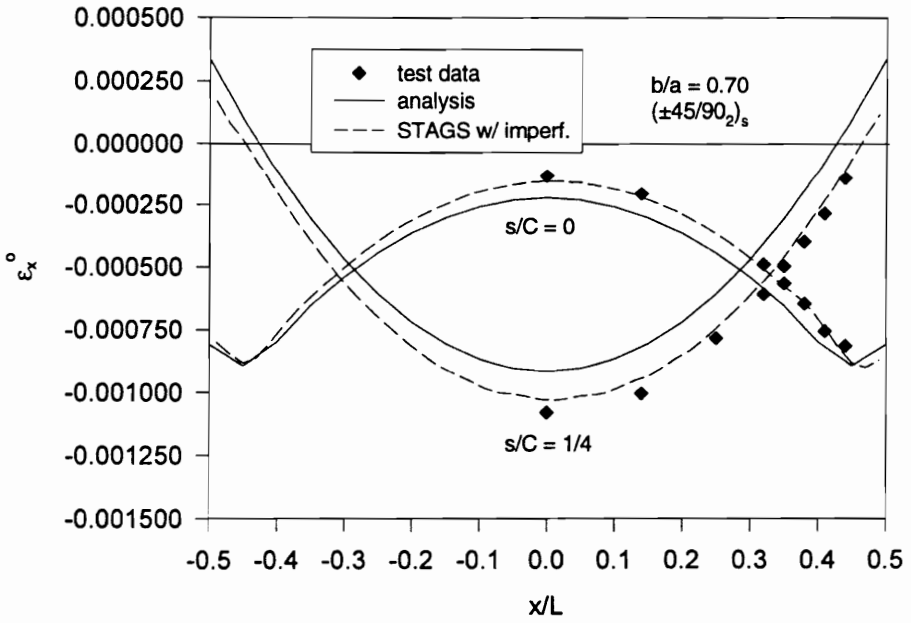

Figure 6-92 Axial Midplane Strain vs. x/L for the $(\pm 45/90_2)_s$ Cylinder, b/a = 0.70, Combined Loading.

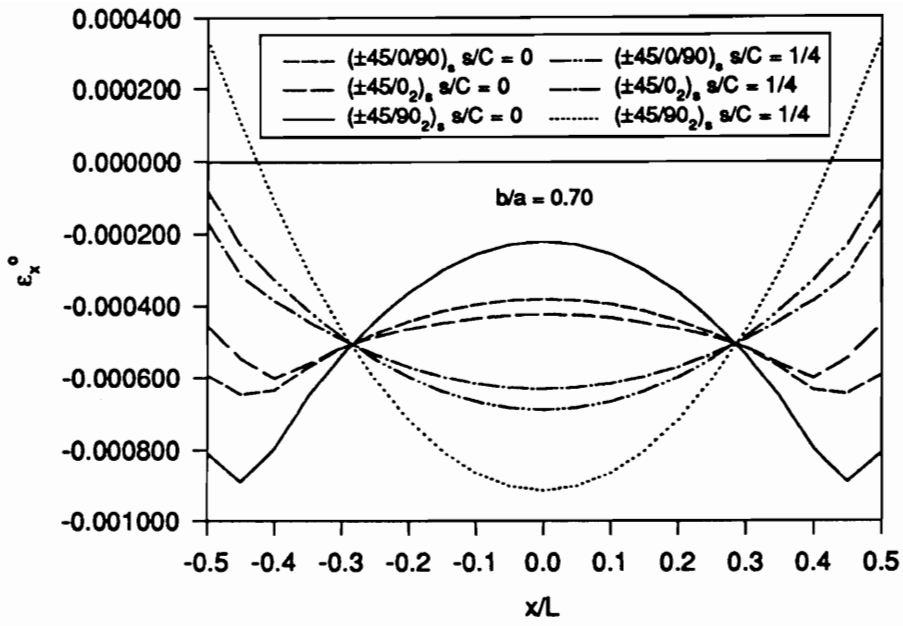

Figure 6-93 Comparison of Analytical Results for Axial Midplane Strain vs. x/L for the (±45/0/90)$_s$, (±45/0$_2$)$_s$, and (±45/90$_2$)$_s$ Cylinders, b/a = 0.70, Combined Loading.

Because the results for these cylinders under combined loading most closely resemble the results for loading by pressure alone, the same trade offs between the axial and circumferential midplane strain distributions exist for combined loading as have been discussed previously for pure internal pressure. With only a small axial load added to the internal pressure load, the magnitudes of the circumferential and axial strains are increased, while the gradients in these quantities with axial and circumferential location remain large. While the gradients in the strains for elliptical cylinders under combined pressure and axial loads are in general large, there are distinct differences in response among cylinders due both to geometry and to orthotropy. This can be seen both in the analytical predictions and the experimental results, and the comparison between the predicted and measured results is good.

In this chapter experimentally measured results have been compared with analytical predictions based upon both perfect and imperfect geometry for three load cases: internal pressure, axial compression, and a combination of internal pressure and axial loading. These comparisons have been made in the prebuckling range. Buckling, postbuckling, and material failure have also been examined for the case of axial compression. These results have been discussed and compared for composite cylinders varying in both orthotropy and geometry.

Chapter 7.0 Conclusions and Recommendations for Future Work

This chapter concludes an analytical and experimental study of the effects of cross sectional ellipticity, material orthotropy, and initial geometric imperfections upon the response of composite elliptical cylinders to internal pressure, axial compression, and combined pressure and axial loads. Because future transport fuselages may involve noncircular cross sections, it is necessary to understand how the lack of axisymmetry, in combination with material orthotropy, affects the response of composite cylinders of noncircular cross section to such simple load conditions, such as axial compression and internal pressure. To this end, nine cylinders with three lay-ups and three cross sectional aspect ratios have been studied here in detail. A large amount of information has been presented. A summary of the study and its conclusions, as well as recommendations for future work, are presented below.

For this study a semi-closed form series solution was developed which provides an efficient analytical tool with which to examine the prebuckling responses of perfect noncircular cylinders. Further, physical insight into the character of these responses can be gained by studying the coefficient functions in the series and their dependence on the axial coordinate. In addition, the STAGS finite element code was used to verify the series solution and to examine the influence of initial shape imperfections on the prebuckling and buckling responses by incorporating accurately measured imperfection data from each cylinder into the finite element models. Lastly, nine cylinders were fabricated and tested using a fixture constructed for this project to allow for both axial compression and internal pressurization. The internal pressure, combined loading, and axial compression tests performed on each of these cylinders have provided valuable data for verifying the analyses, and have added unique data to the literature.

For each of these load cases, it is clear that the response of elliptical cylinders to simple load conditions is not necessarily simple. This is true even in the "membrane" region of such cylinders. Elliptical cylinders differ from circular cylinders in that their responses vary with both the axial and the circumferential coordinate. Indeed, the circumferential displacement field for an elliptical cylinder, unlike that of a circular cylinder, is both nonzero and nontrivial. The degree to which the responses of a given elliptical cylinder will vary in the axial or circumferential direction is dependent upon the ellipticity and the material orthotropy of the cylinder. For cylinders with any given level of material orthotropy, the axial and circumferential variation in the cylinders' responses increase with increasing ellipticity.

These issues are most evident for the case of internal pressure. In this case, the responses can vary dramatically due to the tendency of elliptical cylinders to become more circular when internally pressurized.

As a result, for instance, the radial displacements actually become negative near the minimum radii of curvature of the cross section, and the magnitudes of the circumferential displacements can reach values near to the maximum of the radial displacement. As a result, coupling can result in counterintuitive responses. For instance, unlike circular cylinders, the maximum radial displacement for a pressurized hoop-stiff elliptical cylinder is greater than that for a similar elliptical quasi-isotropic cylinder. This is reversed, however, for circumferential midplane strains due to the large influence of the variation of the circumferential displacement with the circumferential coordinate. Overall, however, material orthotropy has a greater influence upon distribution of circumferential strains in a pressurized noncircular cylinder than does the degree of cross sectional ellipticity.

Significant midplane axial strains are also produced in the elliptical cylinders, even at low pressure and with the ends largely restrained against axial movement. The axial strains for all of the elliptical cylinders vary with both the axial and circumferential coordinates, with the sign of the strain changing with both axial and circumferential location. For quasi-isotropic elliptical cylinders, the axial strains at midspan are as great as the circumferential strains. There is a trade off here between the axial and circumferential midplane strain distributions in the elliptical cylinders for the different levels of material orthotropy. The axially-stiff elliptical cylinders show the lowest levels and lowest gradients in axial midplane strain, but the largest values and largest gradient in circumferential midplane strains. The hoop-stiff elliptical cylinders exhibit the lowest circumferential midplane strains and very little variation in these strains with circumferential coordinate. However, they are subject to the largest gradient in axial midplane strains, as well as magnitudes of axial midplane strain at midspan which are nearly four times higher than the magnitudes of the circumferential midplane strains. For each case, these tendencies increase with increasing ellipticity of the cross section. Thus there are distinct differences in response among cylinders due both to geometry and orthotropy.

In some ways, the response of elliptical cylinders to relatively high prebuckling axial compression loads is less dramatic than the response to even low levels of internal pressure. In particular, the radial displacements, while still exhibiting significant circumferential variation, nowhere become negative and even in the boundary layer region reach magnitudes only slightly greater than those produced at midspan by only 1 atm. of internal pressure. The degree of circumferential variation in the circumferential midplane strains is much lower. The character of the axial strain distribution for the elliptical cylinders under axial compression is also quite different from the response of these cylinders to internal pressure. The axial strains for axially compressed elliptical cylinders are nearly uniform with respect to circumferential location at midspan and throughout most of the length of the cylinders, but diverge in the region of the boundary layer. In elliptical cylinders, unlike circular cylinders, both the length and the amplitude of the boundary layer vary with circumferential location, with greatest length and amplitude occurring near the maximum radii of curvature

circumferential location, with greatest length and amplitude occurring near the maximum radii of curvature of the cross section, which is the flattest part of the ellipse, and the shortest length and least amplitude occurring near the minimum radii of curvature in the most highly curved regions of the cylinder. This boundary response is highly dependent upon both geometry and material orthotropy. However, like circular cylinders, the greatest influence upon the responses in the boundary layer is the presence of initial geometric imperfections. This is again unlike the case for pressure loading. The responses to internal pressures loads are only slightly influenced by initial shape imperfections. Quite the opposite is true for the case of axial compression loading, although this influence is somewhat less in the more severely elliptical cylinders than in the mildly elliptical or the circular cylinders. This could be best observed in comparing the predicted deformed shapes of perfect and imperfect cylinders. For the cylinders with b/a = 0.70, although the presence of imperfections could greatly alter the magnitude of a displacement at a given location, the deformed shape of any of these imperfect elliptical cylinders is still dominated by the deformation pattern characteristic of the perfect elliptical cylinder. Further, for the $(\pm 45/0_2)_s$ cylinder with b/a = 0.70 shape imperfections also seem to have the least influence upon the axial strain distribution in this cylinder, although the degree of imperfections in this cylinder is not significantly less than that of the other two cylinders with b/a = 0.70. Of the cylinders with b/a = 0.70, this one also exhibits the shallowest boundary layer with the least circumferential variation in the amplitude and length. For both the elliptical cylinders with b/a = 0.85 and the circular cylinders, the presence of initial geometric imperfections results in a great change in the deformation patterns. While the imperfect cylinders with b/a = 0.85 still exhibit slightly greater deformations in the flattest regions of the cylinder, the deformed shapes of the mildly elliptical cylinders with imperfections are more similar to the deformed shapes of the imperfect circular cylinders than to the deformed shapes of the more severely elliptical cylinders with imperfections.

Due to the relatively low levels of pressure and axial end shortening used for the combined loading studies, the trends in the results for this case most closely resembled those observed for pressure loading, but with a shift in the levels of the strains. Thus the gradients in the strains, and therefore the stresses, remain large as in the case of pressure loading alone, but the overall levels of the strains are increased. While, due to safety concerns, no cylinders were tested with pressure and high levels of axial compression, analysis indicates the effects of pressurization can be great enough that the addition of even small pressure loads to elliptical cylinders with high axial loads can result in much larger variations in strains and displacements than would be seen for axial load alone, greatly increasing the likelihood of material failure occurring prior to buckling.

Each of the cylinders in this study was also tested in axial compression to buckling and/or material failure. For the hoop-stiff circular and mildly elliptical cylinders, material failure occurred prior to buckling. For the remaining cylinders, which did not fail prior to buckling, buckling occurred suddenly with little or no visible prebuckling deformations. In these cases, buckling was accompanied by an audible snap.

A comparison of the experimental and analytical buckling loads indicates that P_{cr}, the classical buckling load which is calculated by using the maximum radius of curvature of the elliptical cylinder in the classical buckling load formula for a circular cylinder, provides an estimate nearly as good, or in some cases better than, the prediction given by a nonlinear collapse analysis conducted with the STAGS finite element model for the perfect cylinder. Despite the much greater computational cost of the collapse analysis, for all of the cylinders very little was gained by using this method as opposed to the formula for the classical buckling load. The inclusion of initial geometric imperfections in the model for the collapse analysis, however, makes a significant improvement in the prediction of the experimental buckling load for all but the axially-stiff cylinders, for only a small increase in computational expense as compared to the cost for the collapse analyses for the perfect cylinders.

Elliptical and circular cylinders also differ in the way that they buckle. When a circular cylinder buckles, the buckling pattern is a classic diamond-shaped pattern which forms a continuous ring around the midsection of the cylinder. The load drops immediately to a very low level and obvious material damage occurs at the nodal lines of the buckles. For an elliptical cylinder, initial buckling is characterized by a single diamond-shaped buckle appearing in the flattest part of the midsection of the cylinder, often on only one side of the cylinder. At this point the cylinder may still be carrying a significant amount of load. The appearance of this initial buckle is followed by a transition to another shape with two or three diamond-shaped buckles across the flattest parts of the midsection and on both sides of the cylinder. At the same time, as the load transfers to the more highly curved regions of the cross section, material failure occurs near midspan in these highly curved regions and material failure also becomes visibly apparent at the nodal lines of the buckles. After this, the load drops to a very low level. The extent of the region of the circumference that buckles and that in which material failure occurs is dependent primarily upon the cross sectional shape. The buckled area is shorter, and the failed area larger, for the more severely elliptical cylinders. The percentage of load which is held after the appearance of the initial buckle is dependent upon both material orthotropy and cross sectional shape. In particular, for the axially-stiff elliptical cylinders, unlike the other cylinders, after a drop in load following the appearance of a single buckle, the load holds or actually increases again until the cylinder snaps into a shape with two or three buckles across both of the flatter sections of the cylinders. Indeed the axially-stiff cylinder with $b/a = 0.70$ reaches a load prior to this change of buckled shape that is actually slightly greater than the load achieved prior to initial buckling. In contrast to the circular cylinder, both of the axially-stiff elliptical cylinders could continue to carry a percentage of the load after initial buckling occurred. It appears that this percentage decreases as the degree of ellipticity of the cylinder cross section decreases. For the other elliptical cylinders, after an initial buckle appears a lower level of load is held and the cylinder progresses rapidly to failure. As the load transfers to the stiffer regions of the cylinders near the tightly curved minimum radii of curvature, the material in these regions quickly fails. For the

axially-stiff elliptical cylinders, however, the material does not fail so quickly, so that the combination of material orthotropy and geometry results in some postbuckling strength. It is likely that with a less brittle matrix material this effect could be further enhanced.

For all of the load conditions of interest in this study, the responses have been both predicted and observed, and the comparison between the predictions and observations has been, in general, good. Indeed, the worst correlation between experimental and analytical results has often occurred in the circular rather than the elliptical cylinders. However, only a limited number of experimental specimens were tested in this study in order to confirm the trends predicted by the analyses. More experimental work will be necessary in the future in order to supplement these results. And, although the agreement between experimental and analytical results has been relatively good, future work should examine the effects of including shear deformable terms in the analysis. Also of importance for future study is the issue of interlaminar stresses, particularly for pressurized elliptical cylinders. As mentioned previously, even with low levels of internal pressure and low magnitudes of strains, the gradients in the strains, and therefore the stresses, can be quite large presenting the possibility that large interlaminar stresses could develop. An accurate examination of this issue over a full range of internal pressure will require a fully nonlinear analysis of the interlaminar stresses. Other recommendations for future research include considering other load conditions, such as bending, as well as studying the addition of rings, stiffeners, and cutouts in elliptical cylinders.

For all of these load cases studied here, it is also clear that material orthotropy and geometry combine to effect the overall response of noncircular cylinders. In this study only symmetrically laminated elliptical cylinders with spatially uniform material properties have been examined. However, the effects of nonsymmetric laminates, other cross sectional shapes, or spatially nonuniform material properties, e.g., cylinders produced by tow placement or by joining differently laminated segments, remain to be investigated.

The understanding gained through this investigation, as well as the knowledge to be gained by future studies of the issues outlined above, will be necessary to develop efficient designs for structural components utilizing noncircular composite cylinders.

References

1. Stein, M., "Some Recent Advances in the Investigation of Shell Buckling," *AIAA J.* , vol. 6, no. 12, pp. 2339-2345, 1968.
2. Arbocz, J., "Past, Present, and Future of Shell Stability Analysis", N82-17537, NASA, 1981.
3. Simitses, G. J., "Buckling and Postbuckling of Imperfect Cylindrical Shells: A Review," *Appl. Mech. Rev.*, vol. 39, no. 10, pp. 1517-1524, 1986.
4. Novozhilov, V. V., *The Theory of Thin Shells*, Noordhoff, Groningen, Netherlands, 1959.
5. Flügge, W., *Stresses in Shells*, Springer-Verlag, New York, 1960.
6. Dym, C. L., *Introduction to the Theory of Shells*, Hemisphere, New York, 1990.
7. Gavelya, S. P., and Sharapova, D. I., "Deformation of Noncircular Cylindrical Shells," *Prikl. Mekh.*, vol. 22, no. 1, pp. 63-68, 1986.
8. Shirokawa, K., and Morita, M., "Vibration and Buckling of Cylinders with Elliptical Cross Section," *J. Sound Vib.*, vol. 84, no. 1, pp. 121-131, 1982.
9. K. Marguerre, "Stability of the Cylindrical Shell of Variable Curvature", NASA TM 1302, 1951.
10. Romano, F., and Kempner, J., "Stress and Displacement Analysis of a Simply Supported Noncircular Cylindrical Shell Under Lateral Pressure," *PIBAL Report No. 415,* Polytechnic Institute of Brooklyn, Brooklyn, N. Y., 1958.
11. Romano, F., and Kempner, J., "Stresses in Short Noncircular Cylindrical Shells Under Lateral Pressure," *J. Appl. Mech.*, vol. 9, no. 4, pp. 669-674, 1962.
12. Vafakos, W. P., Romano, F., and Kempner, J., "Clamped Short Oval Cylindrical Shells Under Hydrostatic Pressure," *J. Aerospace Sci.,* vol. 29, no. 11, pp. 1347-1357, 1962.
13. Vafakos, W. P., Nissel, N., and Kempner, J., "Energy Solution for Simply Supported Oval Shells," Polytech. Inst. Brooklyn, PIBAL Rept. 667, August 1963.
14. Vafakos, W. P., Nissel, N., and Kempner, J., "Energy Solution for Simply Supported Oval Shells," *AIAA J.*, vol. 2, no. 3, pp. 555-557, 1964.
15. Kempner, J.and Chen, Y.-N., "Large Deflections of an Axially Compressed Oval Cylindrical Shell," *PIBAL Report No. 694*, Polytechnic Institute of Brooklyn, Brooklyn, N. Y., 1964.
16. Kempner, J.and Chen, Y.-N., "Large Deflections of an Axially Compressed Oval Cylindrical Shell," *Proc. IX Inter. Cong. Appl. Mech.*, Munich, Germany, 1964; Springer-Verlag, Berlin, pp. 299-305, 1965.
17. Kempner, J.and Chen, Y.-N., "Buckling and Postbuckling of an Axially Compressed Oval Cylindrical Shell," *Proc. Symp. on the Theory of Shells*, Houston, Texas, pp. 141-175, 1967.
18. Almroth, B. O., "Postbuckling Behavior of Axially Compressed Circular Cylinders," *AIAA J.* , vol. 1, no. 3, pp. 630-633, 1963.

19. Hutchinson, J. W., "Buckling and Initial Postbuckling Behavior of Oval Cylindrical Shells Under Axial Compression," *J. Appl. Mech.*, vol. 35, no. 1, pp. 66-72, 1968.

20. Kempner, J.and Chen, Y.-N., "Large Deflections of an Axially Compressed Oval Cylindrical Shell," *Proc. XII Inter. Cong. Appl. Mech.*, Stanford, Calif., 1968; Springer-Verlag, Berlin, pp. 246-256, 1969.

21. Almroth, B. O., Brogan, F. A., and Marlowe, M. B., "Collapse Analysis for Elliptic Cones," *AIAA J.*, vol. 9, no. 1, pp. 32-37, 1971.

22. Tennyson, R. C., Booten, M., Caswell, R. D., "Buckling of Imperfect Elliptical Cylindrical Shells under Axial Compression," *AIAA J.*, vol. 9, no.2, pp. 250-255, 1971.

23. Feinstein, G., Chen, Y. N., Kempner, J., "Buckling of Clamped Oval Cylindrical Shells under Axial Loads," *AIAA J.*, vol. 9, no. 9, pp. 1733-1738, 1971.

24. Volpe, V., Chen, Y. N., and Kempner, J., "Buckling of Orthogonally Stiffened Finite Oval Cylindrical Shells Under Axial Compression," *AIAA J.*, vol. 8, no. 5, pp. 571-579, 1980.

25. Sun, G., "Buckling and Initial Postbuckling Behavior of Laminated Oval Cylindrical Shells Under Axial Compression," *J. Appl. Mech.*, vol. 58, no. 3, pp. 848-850, 1991.

26. Soldatos, K. P., "Nonlinear Analysis of Transversely Shear Deformable Laminated Composite Cylindrical Shells - Part I: Derivation of Governing Equations," *J. Pressure Vessel Tech.*, vol. 114, no. 1, pp.105-109, 1992.

27. Soldatos, K. P., "Nonlinear Analysis of Transversely Shear Deformable Laminated Composite Cylindrical Shells - Part II: Buckling of Axially Compressed Cross-Ply Circular and Oval Cylinders," *J. Pressure Vessel Tech.*, vol. 114, no. 1, pp.110-114, 1992.

28. Sheinman, I., and Firer, M., "Buckling and Post-Buckling of Laminated Noncircular Cylindrical Shells," *AIAA J.*, vol. 32, no. 3, pp. 384-393, 1994.

29. Firer, M., and Sheinman, I., "Nonlinear Analysis of Laminated Noncircular Cylindrical Shells," *Int. J. Solids Structures*, vol. 32, no. 10, pp. 1405-1416, 1995.

30. Soldatos, K. P., "A Flügge-Type Theory for the Analysis of Anisotropic Laminated Non-Circular Cylindrical Shells," *Int. J. Solids Structures*, vol. 20, no. 2, pp.107-120, 1984.

31. Hui, D., and Du, I. H. Y., "Effects of Axial Imperfections on Vibrations of Anti-symmetric Cross-Ply Oval Cylindrical Shells," *J. Appl. Mech.*, vol. 53, no. 3, pp. 675- -680, 1986.

32. Suzuki, K. and Leissa, A. W., "Analysis of Free Vibrations of Noncircular Thick Cylindrical Shells Having Circumferentially Varying Thickness," *Int. J. Solids Structures*, vol. 26, no. 3, pp. 255-270, 1990.

33. Leissa, A. W., *Vibration of Shells*, NASA SP - 288, 1973.

34. Sewall, J. L., and Pusey, C. G., "Vibration Study of Clamped-Free Elliptical Cylindrical Shells," *AIAA J.*, vol. 9, no. 6, pp. 1004-1011, 1971.

35. Yao, J. C., and Jenkins, W. C., "Buckling of Elliptic Cylinders under Normal Pressure," *AIAA J.*, vol. 8, no. 1, pp. 22-27, 1970.

36. Slepov, B. I., "Vibrations and Stability of an Elliptical Shell," *NASA TT F-12*, March 1969.

37. Kempner, J., Vafakos, W. P., and Nissel, N., "Reinforced Oval Cylinder - Comparison of Theory and DTMB Tests," *J. Appl. Mech.*, vol. 31, pp. 710-711, 1964.

38. Feinstein, G., Erickson, B., Kempner, J., "Stability of Oval Cylindrical Shells," *J. Exp. Mech.*, vol. 9, no. 9, pp. 514-520, 1971.

39. Mushtari, K. M., and Galimov, K. Z., *Nonlinear Theory of Thin Elastic Shells*, Israel Program for Scientific Translation, O. T. S., U. S. Dept. of Commerce, Washington, 1957.

40. Vekua, I. N., *Shell Theory: General Methods of Construction*, Pitman Advanced Publishing Program, Boston, 1986.

41. Koiter, W. T., "On the Nonlinear Theory of Thin Elastic Shells", *Koninklijke Nederlandse Akademie von Wetenschappen, Proc., Series B*, vol. 69, pp. 1-54, 1966.

42. Nemeth, M. P., "Nondimensional Parameters and Equations for Buckling of Symmetrically Laminated Thin Elastic Shallow Shells," *NASA Tech. Mem. No. 104060*, Mar. 1991.

43. Brogan, F. A., Rankin, and C. C., Cabiness, H. D., "Stuctural Analysis of General Shells", Vol. 2: STAGS User Manual, Version 2.0, *LMSC P032594*, Lockheed Palo Alto Research Laboratory, Palo Alto, CA, June, 1994.

44. Leissa, A. W., and Qatu, M. S., "Equation of Elastic Deformation of Laminated Composite Shallow Shells," *J. Appl. Mech.*, vol. 58, no. 1, pp. 181-188, 1991.

45. Dym, C. L., and Shames, I. H., *Energy and Finite Element Methods in Structural Mechanics*, Hemisphere Publishing Co., New York, pp. 71-100, 1985.

46. Wolfram, S., *Mathematica: A System for Doing Mathematics by Computer*, Addison-Wesley Publishing Co., Redwood City, CA, 1991.

47. IMSL MATH/Library User's Manual, IMSL Inc., Houston, TX., pp. 660-671, 1987.

48. Fuchs, J. P., "Numerical And Experimental Investigation of the Bending Response of Thin-Walled Composite Cylinders." Ph. D. dissertation in Engineering Mechanics, Virginia Polytechnic Institute and State University, Sept. 1993, available University Microfilms, Ann Arbor, MI, order number 9403851.

49. Hu, S., Bark, J. S., and Nairn, J. A., "On the Phenomenon of Curved Microcracks in $[(S)/90_n]_s$ Laminates: Their Shapes, Initiation Angles and Locations," *Composites Sci. and Tech.*, vol. 47, no. 2, p. 321-329, 1994.

50. Fuchs, J. P., personal communication, Sept. 1994.

Appendix A Initial Imperfections

The external surface of each specimen was accurately measured using a Brown & Sharpe validator coordinate measurement system, resulting in a three dimensional geometric representation of the surface of each cylinder. Axial data points were spaced 1/8 in. (~ 3 mm) while circumferential data points were spaced every $\theta = 2^{\circ}$, where

$$\begin{aligned} y &= a\sin\theta \\ z &= b\cos\theta, \end{aligned} \tag{A.1}$$

and the Cartesian coordinates, y and z, are the same as those shown in Figure 3-1. This description of the outer surface with the coordinates y and z defined in terms of a new angle, θ, was adopted for ease of programming the measurement system. This form allowed for an easily measured and easily visualized angle which also provided a spacing over the circumference which was reasonably uniform. The angle θ is related to the angle ϕ, used in the analysis by

$$\phi = \operatorname{atan}\left(\frac{a}{b}\tan\theta\right). \tag{A.2}$$

Figure A-1 is a schematic of the measurement setup. The cylinder with end caps was positioned vertically on the measurement table. The contact probe indexed in the circumferential direction and performed scans along the axial direction.

These external surface data were then used to calculate a 'best fit' perfect elliptical cylinder using the least-squares method. The differences between the measured data and this 'best fit' perfect cylinder were then calculated in order to obtain 'raw data' in the form of radial imperfections relative to the perfect cylinder at each point. It should be noted that because, as detailed in Ch. 3, the exterior surfaces of these cylinders are not precisely elliptical in cross-section, several approximations were necessary both to measure the cylinder surface and to calculate the 'best fit' cylinder. The largest errors introduced in the radial imperfections by these approximations, however, are estimated to be on the order of 5% of the laminate thickness.

The calculated imperfections were then reduced to obtain Fourier series coefficients to describe the midsurface imperfections, as described in [A1]. The measured imperfections are assumed to be of the form

$$\frac{\bar{w}(x,\theta)}{H} = \sum_{k}\sum_{l}\left(\cos\frac{k\pi x}{L}\left[A_{kl}\cos l\theta + B_{kl}\sin l\theta\right] + \sin\frac{k\pi x}{L}\left[C_{kl}\cos l\theta + D_{kl}\sin l\theta\right]\right), \tag{A.3}$$

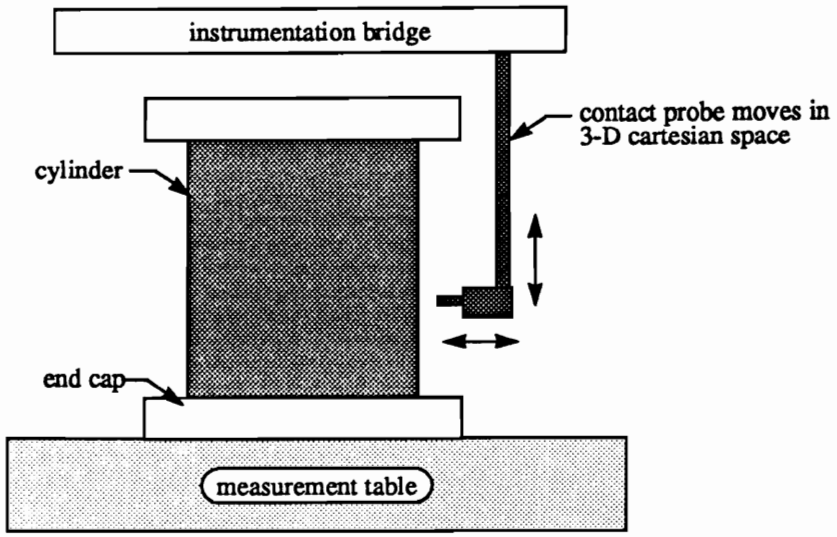

Figure A-1 Imperfection Measurement Set-up.

where A_{kl}, B_{kl}, C_{kl}, and D_{kl} are the Fourier coefficients. The number of *half* waves in the axial direction is given by k while the number of *full* waves in the circumferential direction is given by l. The Fourier coefficients are then included in the STAGS finite element analysis of each specimen through the user-written subroutine *dimp*, which can describe the measured imperfection as either a perturbation of the geometry or include its effects in the strain-displacement relations. In these analyses, the imperfections were included as perturbations of the initial mesh geometry which was based on the 'best fit' perfect data.

Plots of the imperfection data for EL-940503-1 (the $(\pm 45/0/90)_s$ cylinder with axes ratio b/a = 0.70) are illustrated in Figure A-2. Three representations of the imperfection data are shown: (a) the deviation of the measured data from the best fit ellipse, referred to as 'raw data', (b) the Fourier series representation of this data, referred to as 'reduced data', and, (c) the map of the perturbations of the mesh in the STAGS model resulting from the use of the Fourier representation. These are the three levels of reduction necessary to go from measured data to a STAGS model with accurately represented shape imperfections. As indicated by this figure, all three representations closely match each other, so that very little loss of accuracy results from this method of reducing the measured data to mesh perturbations. Note that the imperfection amplitude is approximately ±30 % of the wall thickness for this specimen.

The 'raw data' maps for each set of cylinders with a given cross section are given in Figures A-3 - A-5.

References

A1. Cartalas, Ch., van der Hoeven, H.J.C., Klompé, "Guide to the Data Reduction of Imperfection Surveys on Circular Shells", Memorandum M-622, Delft University of Technology, 1989.

(a) Raw Data

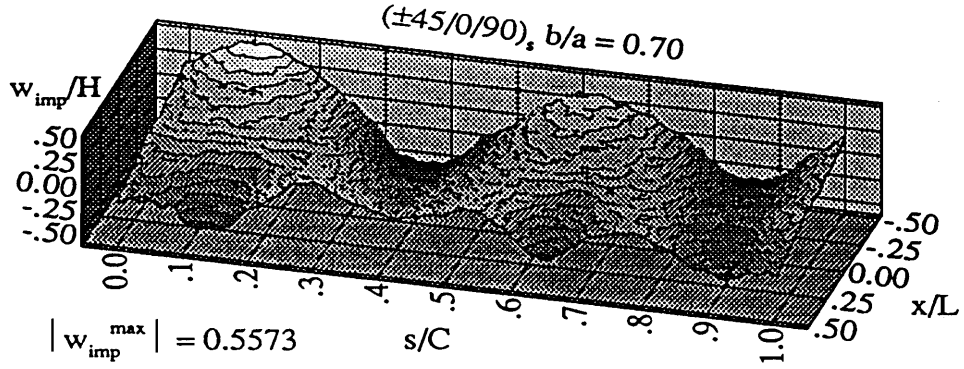

(b) Reduced Data

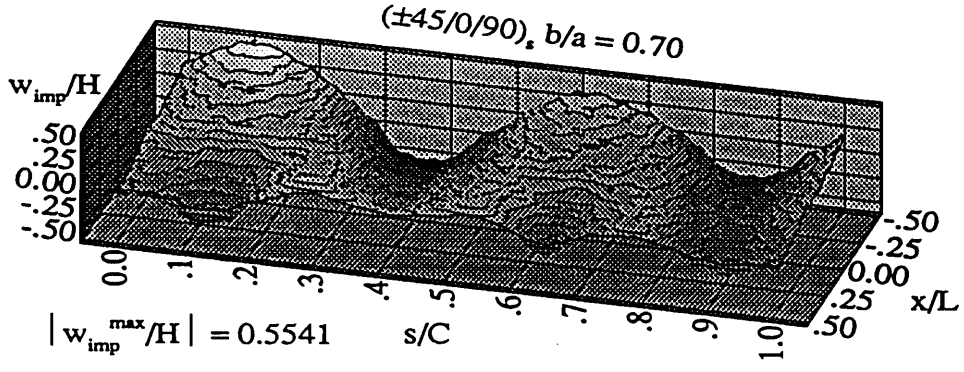

(c) STAGS Imperfection

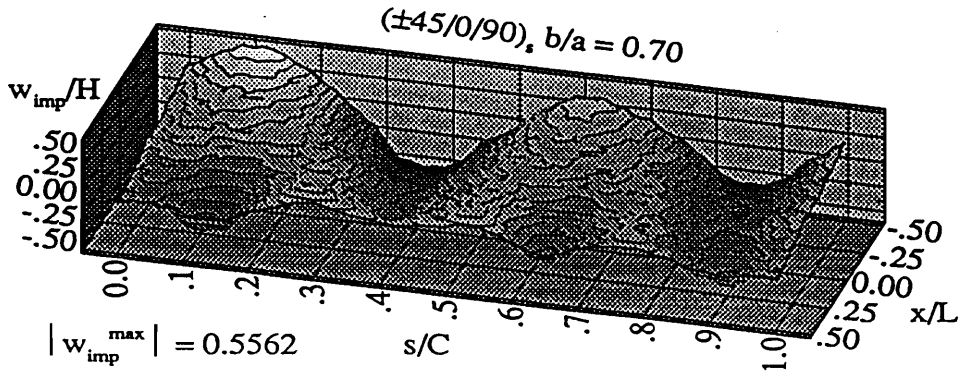

$0 \le k \le 49, 0 \le l \le 90$

Figure A-2 Measured Geometric Imperfection Data for $(\pm 45/0/90)_S$ Cylinder with b/a = 0.70.

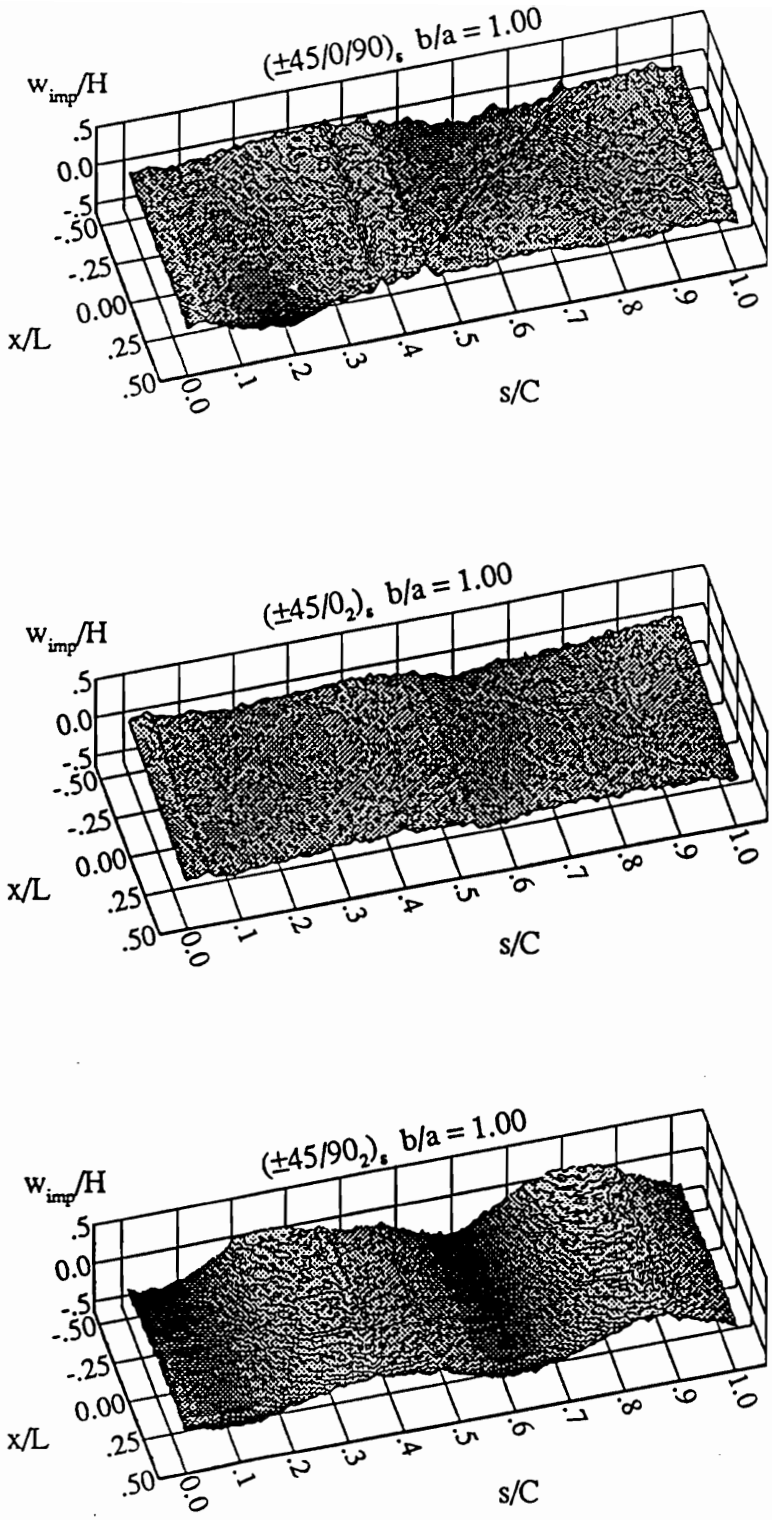

Figure A-3 Measured Geometric Imperfections for the Cylinders with b/a = 1.00.

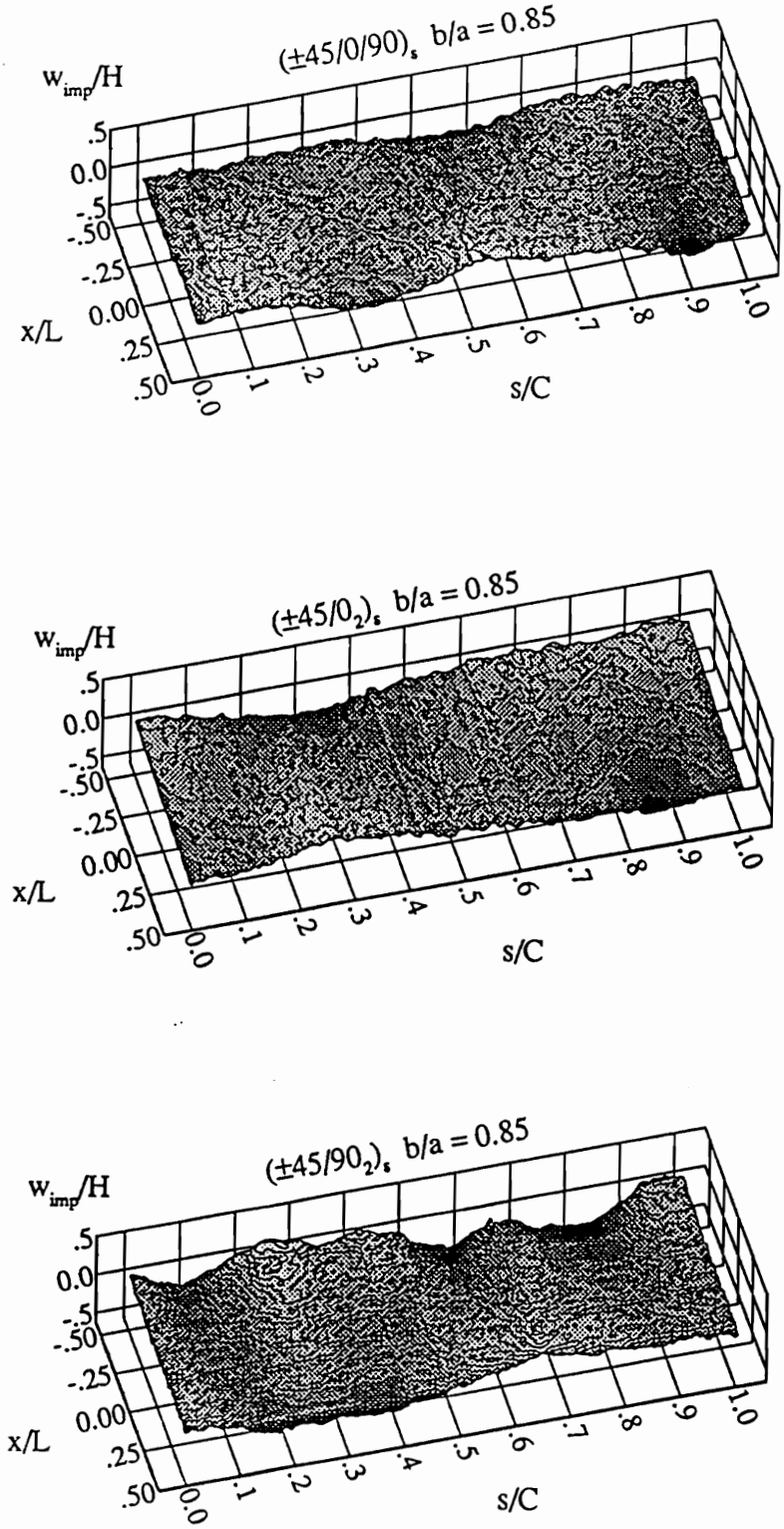

Figure A-4 Measured Geometric Imperfections for the Cylinders with b/a = 0.85.

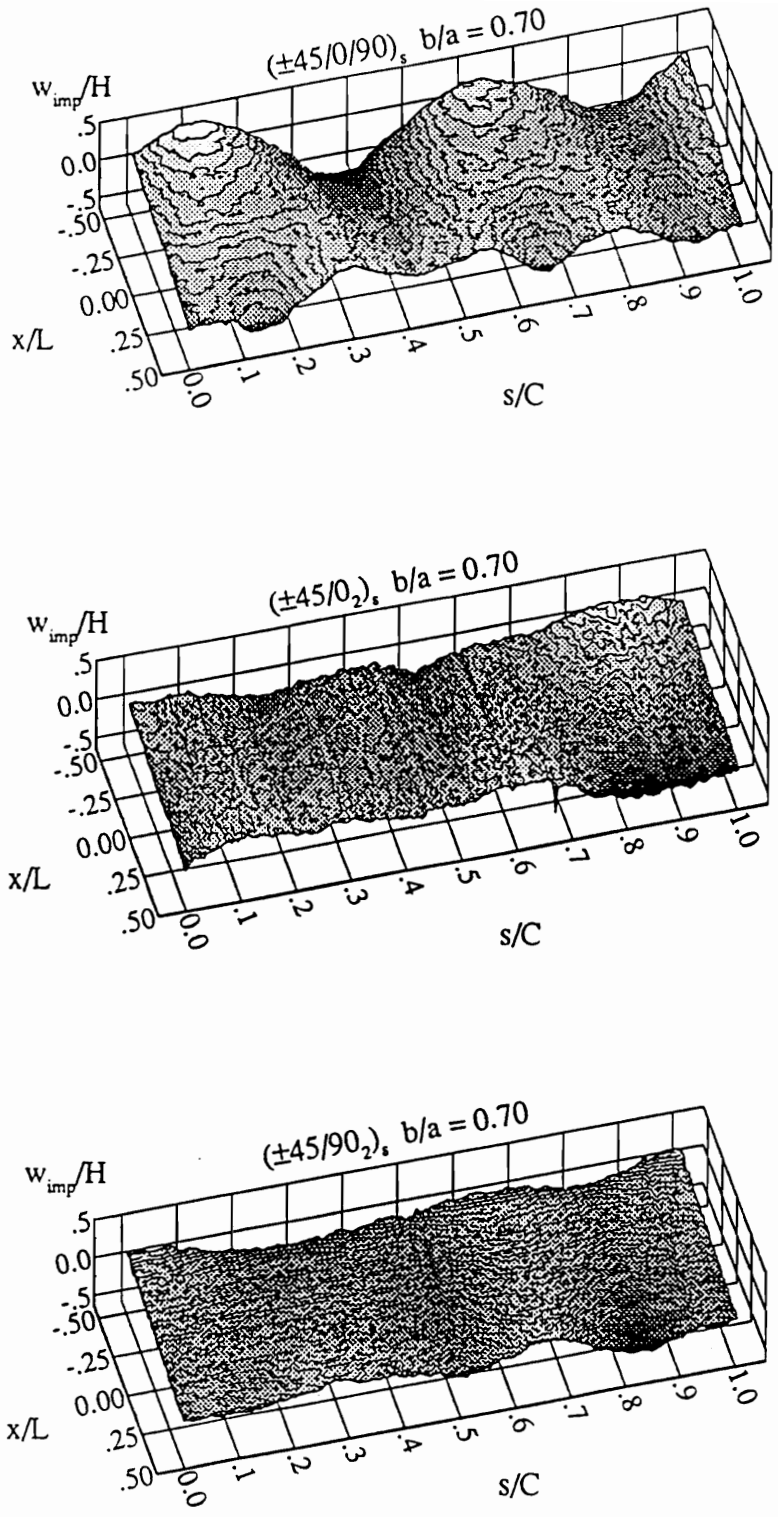

Figure A-5 Measured Geometric Imperfections for the Cylinders with b/a = 0.70.

Appendix B Specimen Fabrication and Preparation

A total of nine test specimens, three of each cross-section, were made from Hercules AS4/3501-6 graphite-epoxy prepreg tape. The specimen identification codes, lay-ups, and cross-sectional aspect ratios are given in Table B-1.

Table B-1 Experimental Specimens.

b/a	lay-up	specimen ID
1.00	$(\pm 45/0/90)_s$	EL-940330-1
	$(\pm 45/0_2)_s$	EL-940405-1
	$(\pm 45/90_2)_s$	EL-940517-1
0.85	$(\pm 45/0/90)_s$	EL-940412-1
	$(\pm 45/0_2)_s$	EL-940428-1
	$(\pm 45/90_2)_s$	EL-940426-1
0.70	$(\pm 45/0/90)_s$	EL-940503-1
	$(\pm 45/0_2)_s$	EL-940505-1
	$(\pm 45/90_2)_s$	EL-940515-1

The steps involved in fabricating the specimens and preparing them for testing are described in the following.

Cylinder Fabrication

Mandrel Preparation

Three 20.0 in. (508 mm) long mandrels with the specified cross-sectional shapes were designed and fabricated specifically for these specimens. These mandrels, which were manufactured by Iowa Machine, Inc., are shown in Figure B-1. Prior to tape lay-up, each mandrel was cleaned with acetone and then wrapped with a thin layer of nonporous teflon fabric. The nonporous teflon was firmly attached to the mandrel using 3M Super77 adhesive. After the adhesive had dried, the teflon coating was sprayed with Frekote 33 release agent and left standing for approximately 30 minutes. After each cylinder was cured and removed from the

mandrel, the nonporous teflon was stripped off and the adhesive removed with solvent. The teflon fabric was then reapplied to the mandrel in preparation for manufacturing the next specimen.

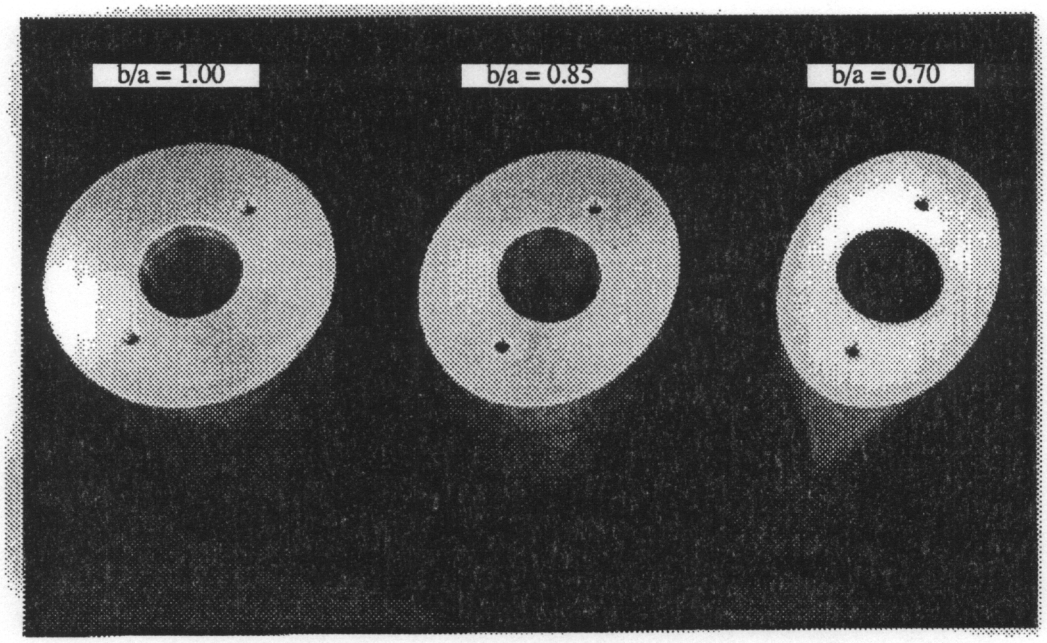

Figure B-1 Aluminum Mandrels.

Tape Lay-up

The 12-inch (305 mm) wide prepreg was cut into suitably sized segments before starting the lay-up procedure. A support fixture, similar to a barbecue spit, was constructed which allowed the mandrels to be either rotated easily about their longitudinal axis, or stopped at a particular angle in order to facilitate the tape lay-up. Each ply was wrapped around the mandrel by hand. A completed lay-up on the mandrel with b/a = 0.85 on the support fixture is shown in Figure B-2. Within a ply, every effort was made to precisely butt the pieces of prepreg together. However, some gaps and overlaps in the prepreg plies were nevertheless formed at these butt joints. These gaps and overlaps formed either axial, circumferential, or helical seams, depending on the ply orientation. The joints of adjacent plies were staggered to minimize the effects of any local stiffness discontinuities that may have occurred due to these overlaps and gaps.

Because the available facilities lacked the capability for pressurization, a decision was made to use heat shrink tape to apply pressure to the specimen during cure. Therefore, after the lay-up was completed, a sheet of nylon release cloth was wrapped tightly around the specimen. One-inch (25.4 mm) wide Airtech A5 shrink-wrap tape was then wound around the piece in such a way that the tape overlapped itself by 0.5 in.

(12.7 mm) at each turn. A heat gun was then used to shrink the tape tightly enough to the cylinder so that it would not slip when the mandrel was lifted to apply the vacuum bag. A vacuum port was then attached with teflon tape to the flattest section of the mandrel (the end of the semi-minor axis) in such a way as to minimize its footprint on the specimen. GS-43 sealant was then applied to the ends of the mandrel to form an airtight seal with the vacuum bag. After the vacuum bag was applied, the mandrel, on the fixture, was then placed

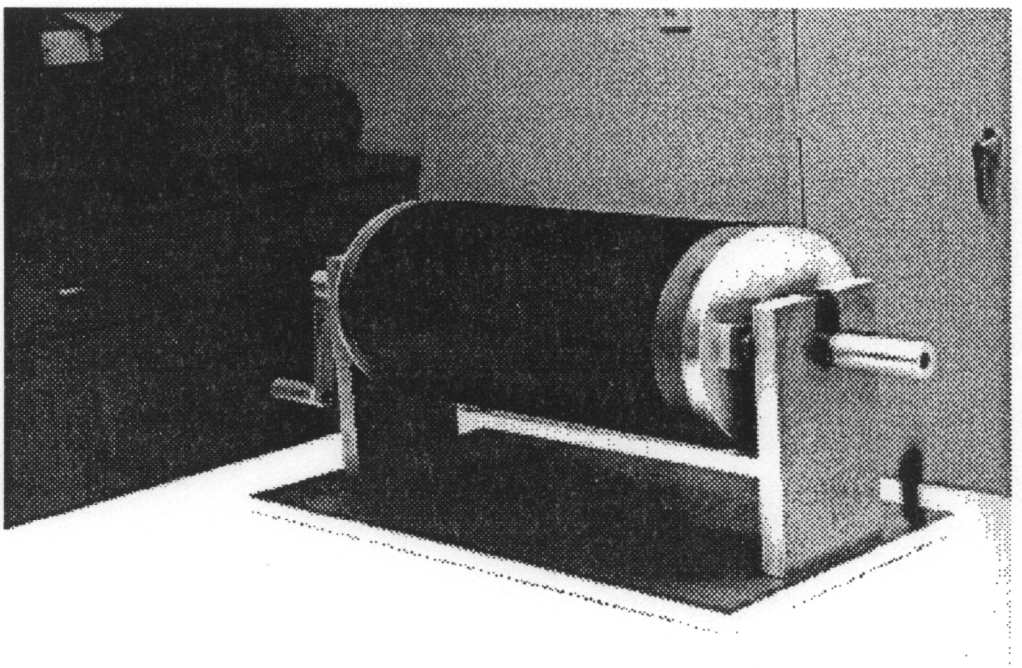

Figure B-2 Completed Lay-Up on Mandrel in Support Fixture.

in the autoclave. The piece was cured at the manufacture's recommended temperature cycle, with the heat shrink tape and the thermal expansion of the mandrel providing pressure. Once the cure was complete, the finished specimen was removed from the mandrel. The specimen could be removed from the mandrel with little difficulty.

Machining

After all nine cylinders had been cured, they were transported, along with the aluminum mandrels, to Advex Corporation of Hampton, VA for machining. In order to machine the ends flat and parallel, each cylinder was replaced on its correspondingly-shaped mandrel and clamped with wooden blocks. All cylinders were cut to a final length of 14.5 in. (368 mm).

Nondestructive Evaluation

Each cylinder was visually inspected after being removed from the mandrel. Gaps and overlaps at seams, as discussed above, were visible in some specimens. Some surface wrinkles were also observed which were believed to be due to wrinkles in the cloth wrap. An example of such visible nonuniformities is shown in Figure B-3.

Next, each cylinder was inspected ultrasonically. Due to the non-axisymmetric profile of six of the cylinders, the C-scan procedure could not be automated for the cylinders. All of the cylinders were, therefore, inspected using a hand-held two-pronged probe which carried the signal in a jet of water 'squirted' between the ends of the prongs.

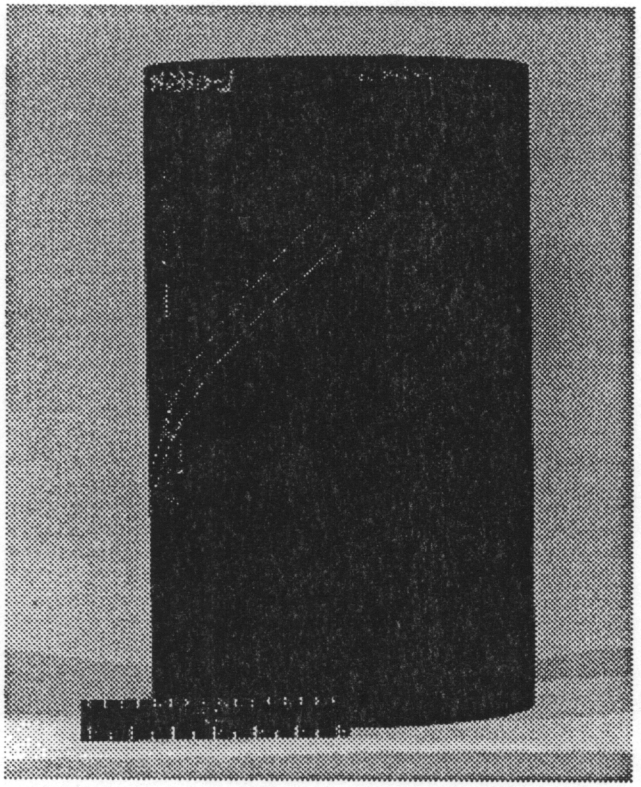

Figure B-3 Visible Seam in $(\pm 45/0/90)_s$ Circular Cylinder.

To assist in calibration and access the accuracy of this method, a cylinder section with several 1/8 - 1/4 inch (~3 - 6 mm) deliberately built-in flaws was created. The accuracy of the method was further compared with that of an automated C-scan by later taking automated C-scans of the circular cylinders and comparing the results. These comparisons indicated that the 'squirter' method was found to be reliable for detecting delaminations, inclusions, internal voids, and a variation of porosity within a given specimen. It did not provide a comparison of the average quality of the material between specimens. The automated C-scans showed that the $(\pm 45/90_2)_s$ circular cylinder was of acceptable, but slightly poorer quality (less dense), than the other two circular cylinders.

Appendix C Additional Results

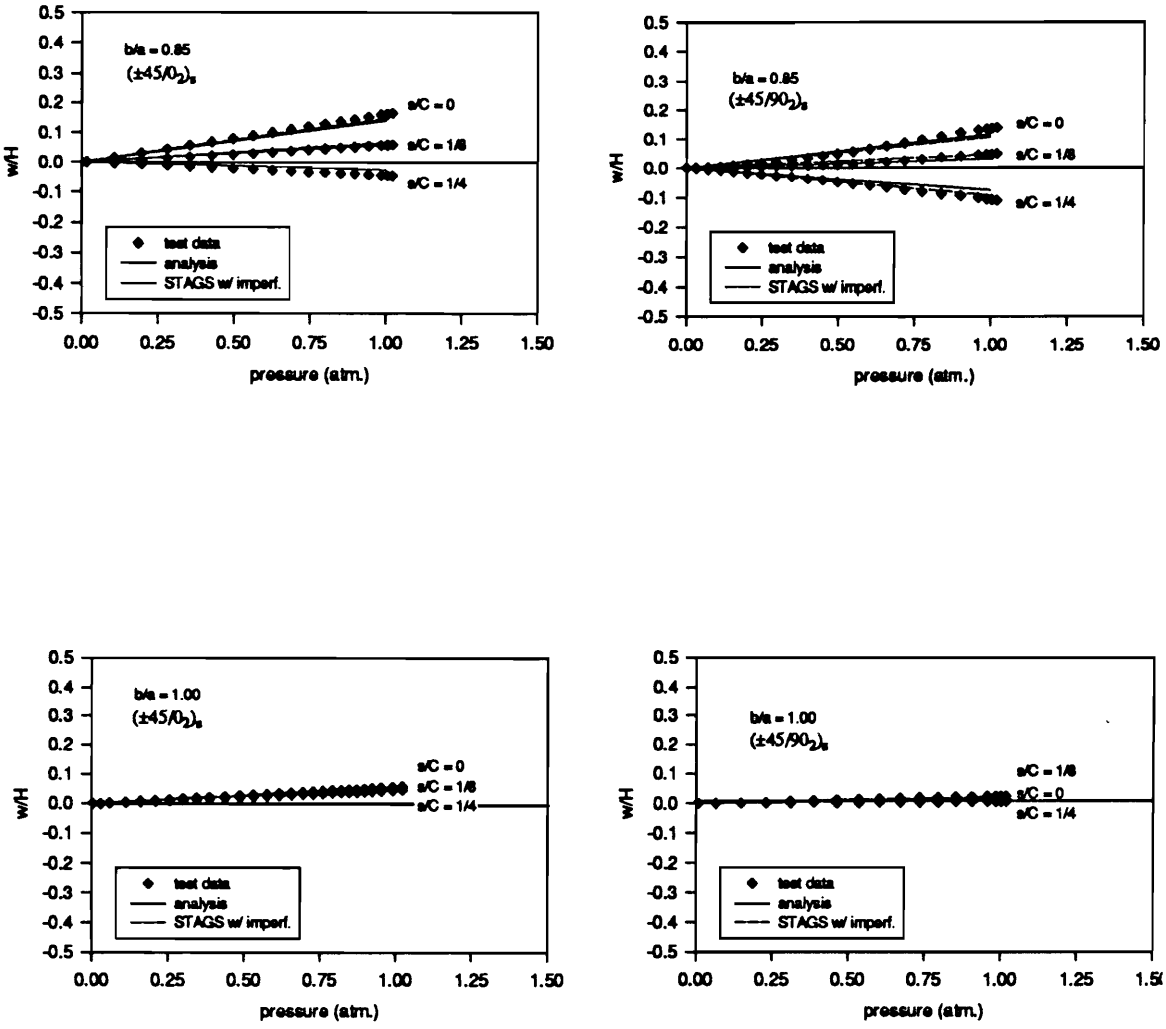

Figure C-1 Normalized Radial Displacement at Midspan for the $(\pm 45/0_2)_s$ and $(\pm 45/90_2)_s$ Cylinders, b/a = 0.85 and 1.00, Internal Pressure Loading to 1 Atm.

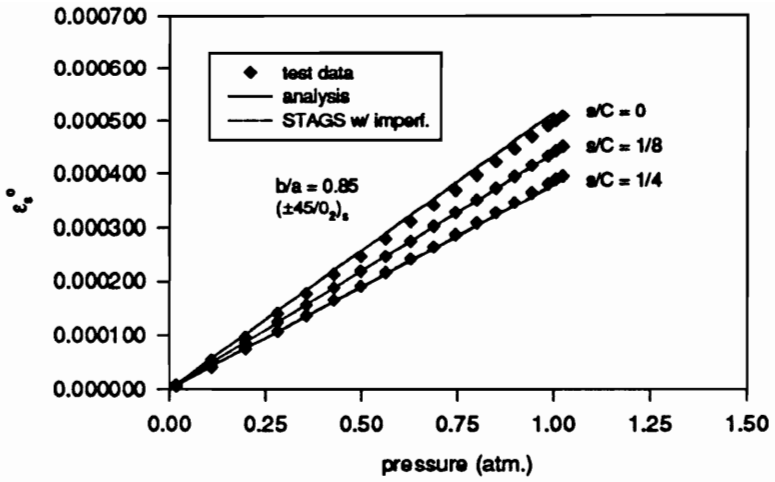

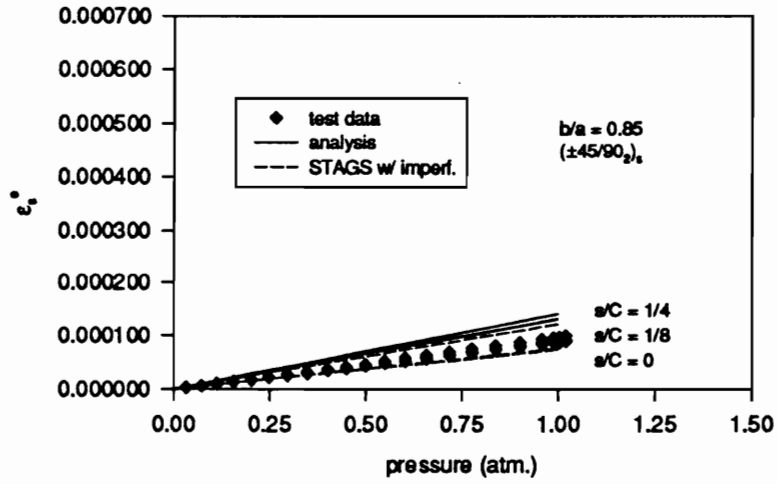

Figure C-2 Circumferential Midplane Strain at Midspan for the $(\pm 45/0_2)_s$ and $(\pm 45/90_2)_s$ Cylinders, b/a = 0.85, Internal Pressure Loading to 1 Atm.

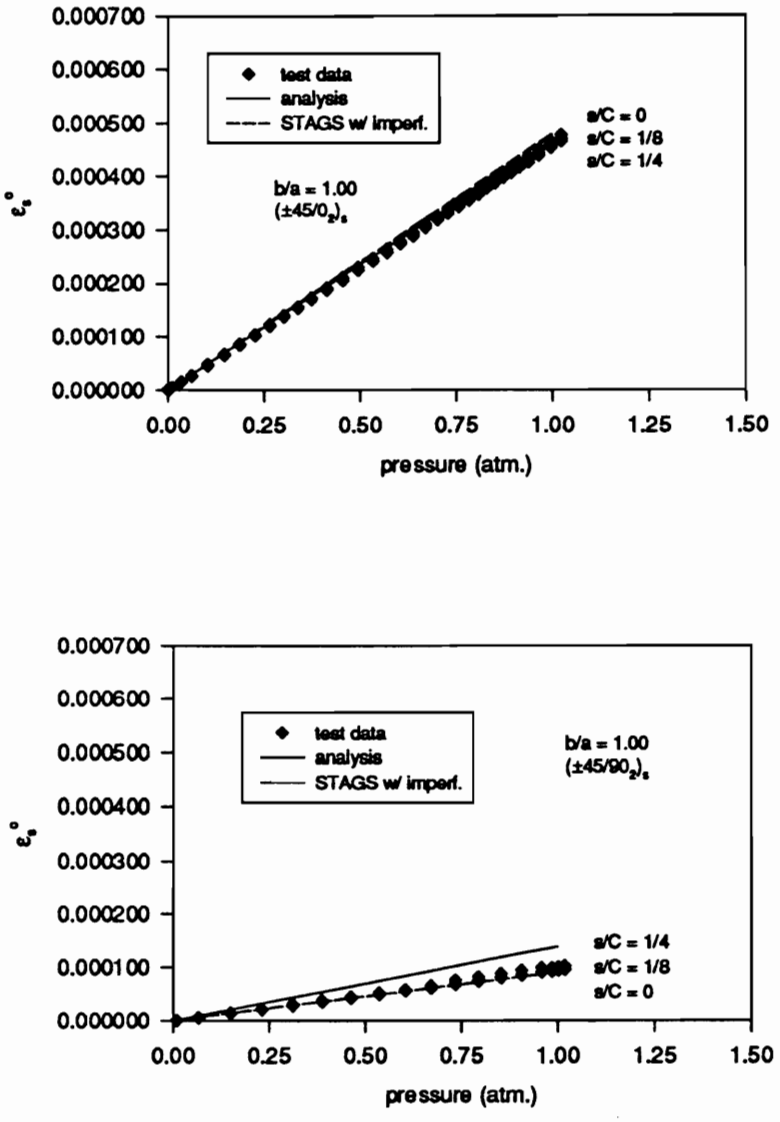

Figure C-3 Circumferential Midplane Strain at Midspan for the $(\pm 45/0_2)_s$ and $(\pm 45/90_2)_s$ Cylinders, b/a = 1.00, Internal Pressure Loading to 1 Atm.

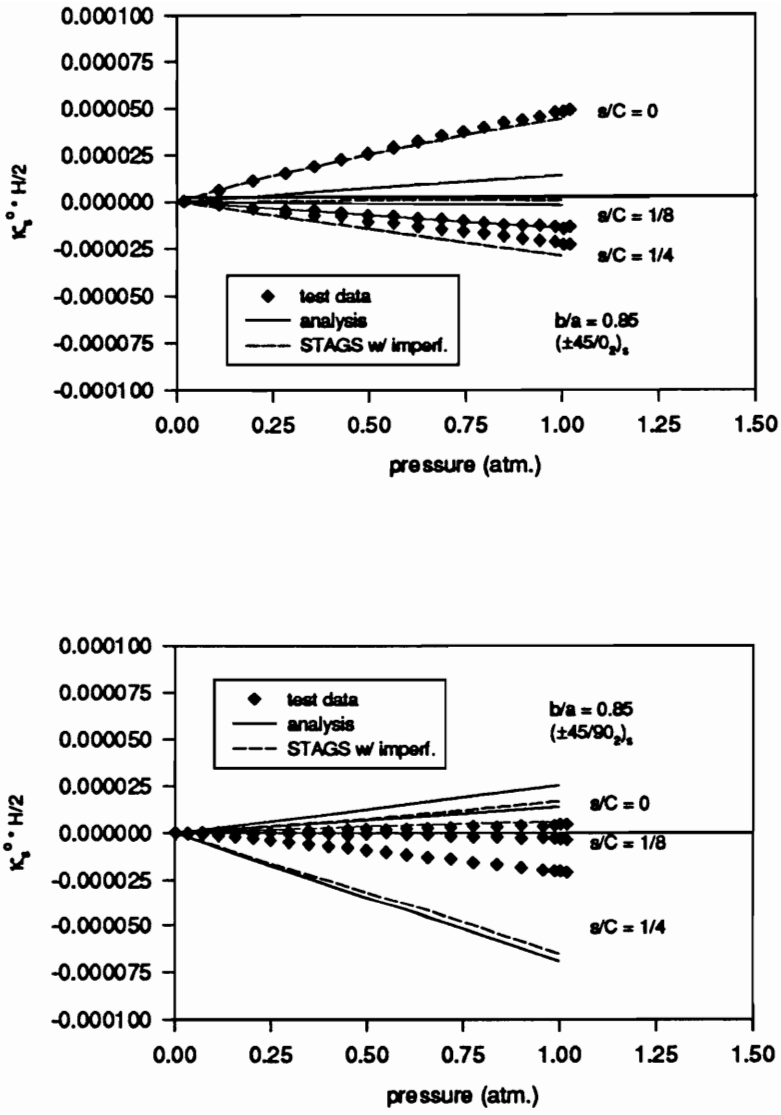

Figure C-4 Circumferential Bending Strain at Midspan for the $(\pm 45/0_2)_s$ and $(\pm 45/90_2)_s$ Cylinders, b/a = 0.85, Internal Pressure Loading to 1 Atm.

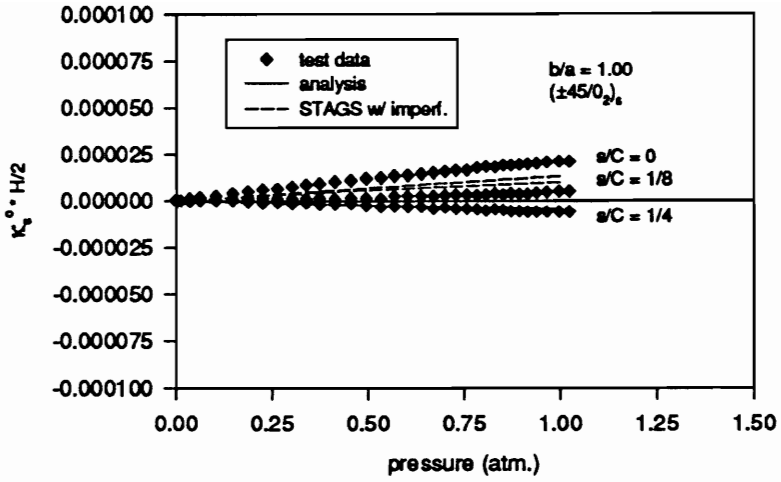

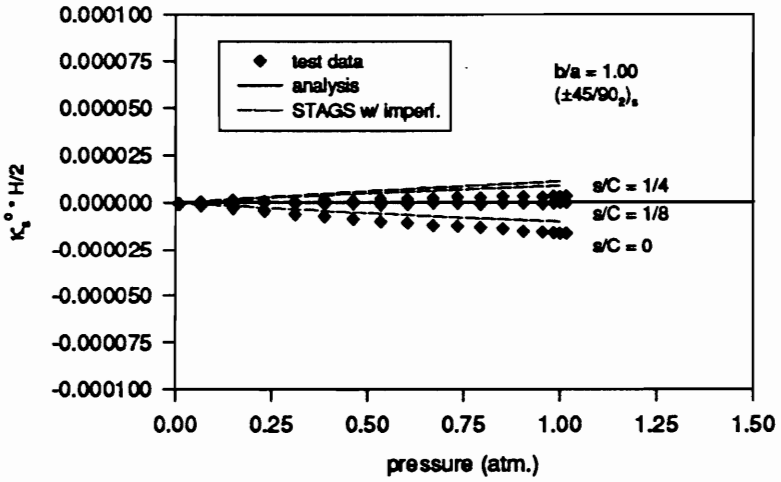

Figure C-5 Circumferential bending Strain at Midspan for the $(\pm 45/0_2)_s$ and $(\pm 45/90_2)_s$ Cylinders, b/a = 1.00, Internal Pressure Loading to 1 Atm.

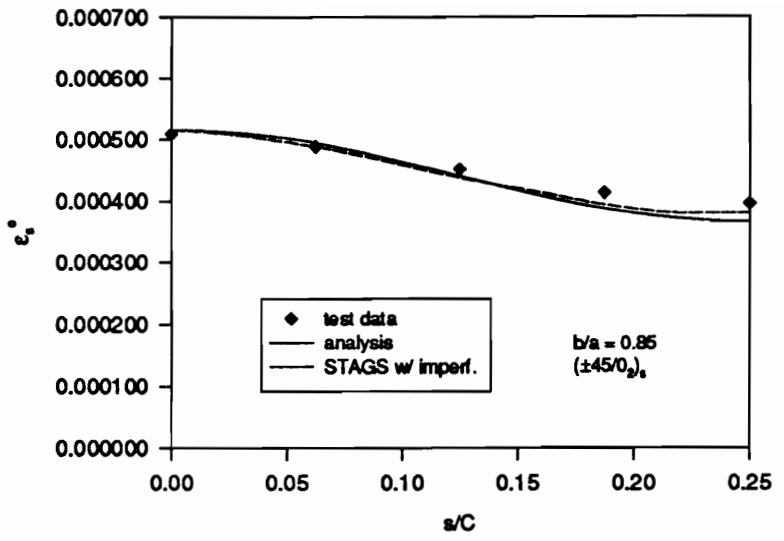

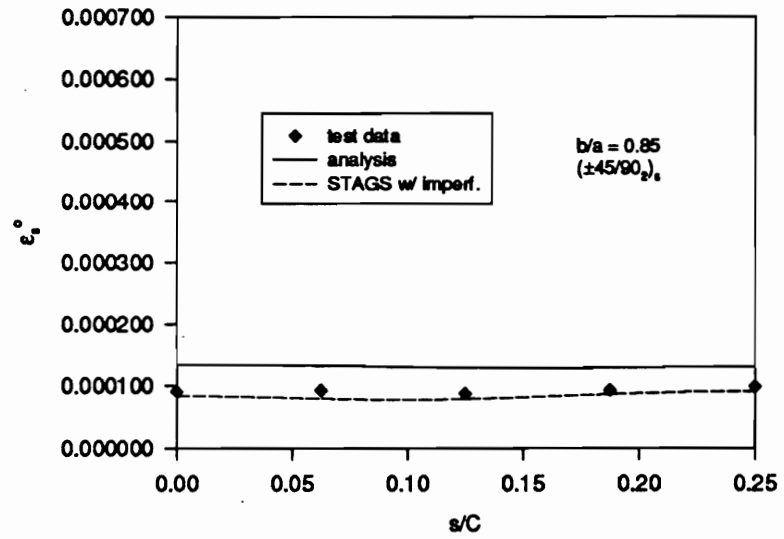

Figure C-6 Circumferential Midplane Strain vs. s/C at Midspan for the $(\pm 45/0_2)_s$ and $(\pm 45/90_2)_s$ Cylinders, b/a = 0.85, Internal Pressure Loading to 1 Atm.

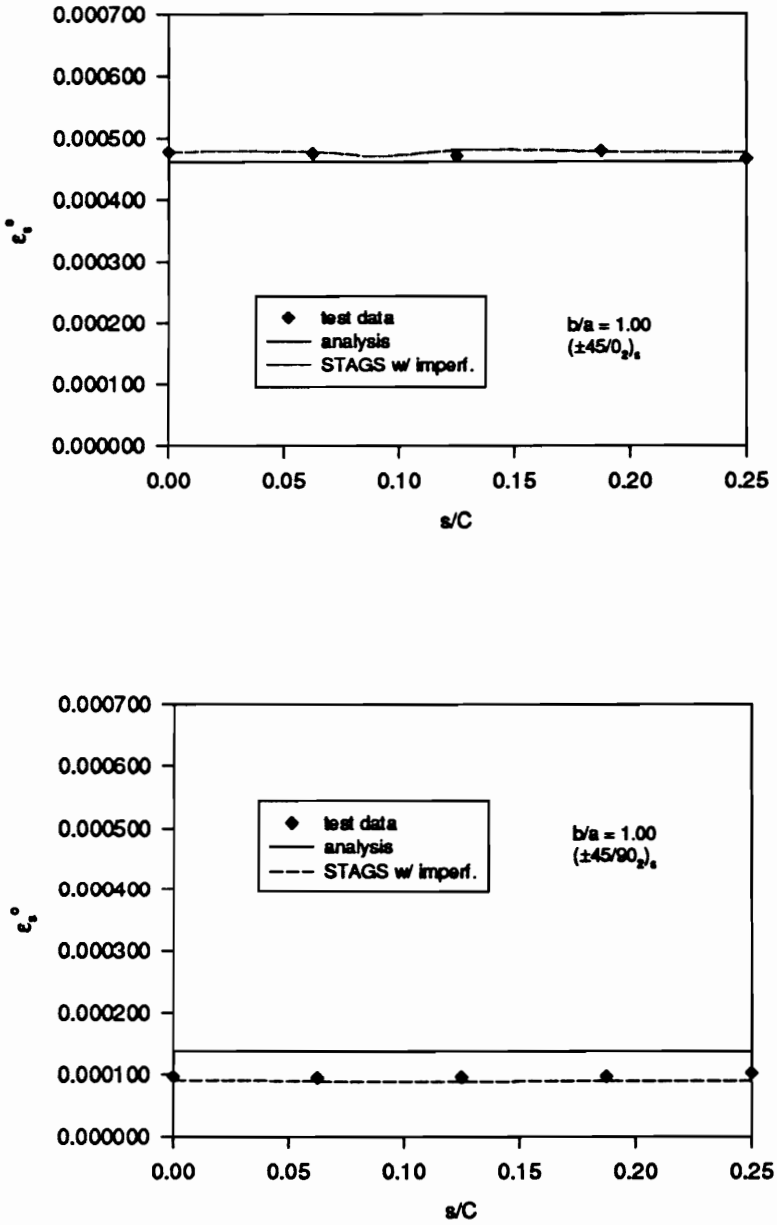

Figure C-7 Circumferential Midplane Strain vs. s/C at Midspan for the $(\pm 45/0_2)_s$ and $(\pm 45/90_2)_s$ Cylinders, b/a = 1.00, Internal Pressure Loading to 1 Atm.

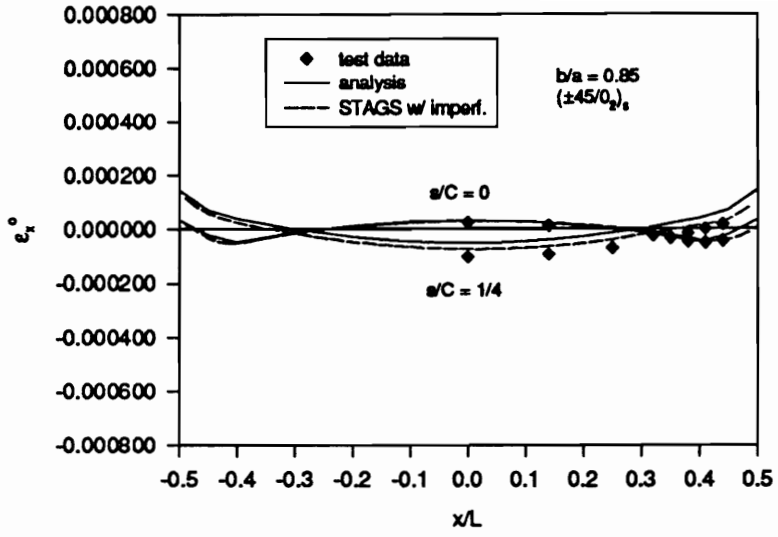

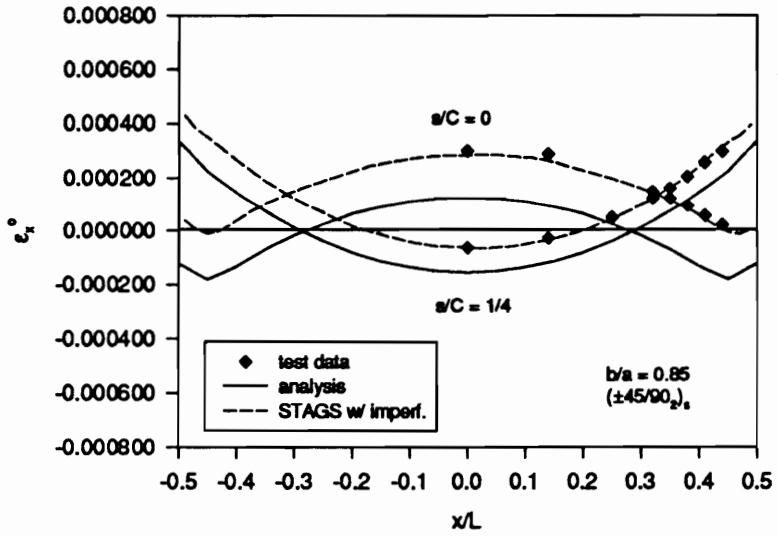

Figure C-8 Axial Midplane Strain vs. x/L for the $(\pm 45/0_2)_s$ and $(\pm 45/90_2)_s$ Cylinders, b/a = 0.85, Internal Pressure Loading to 1 Atm.

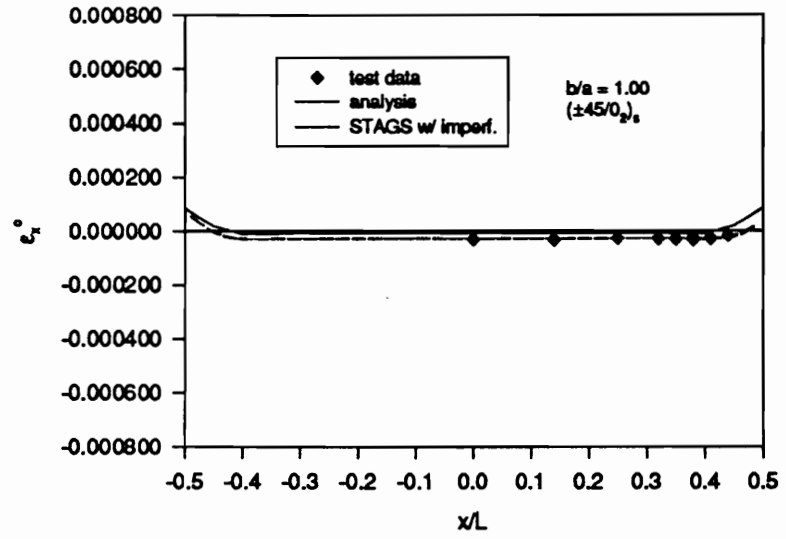

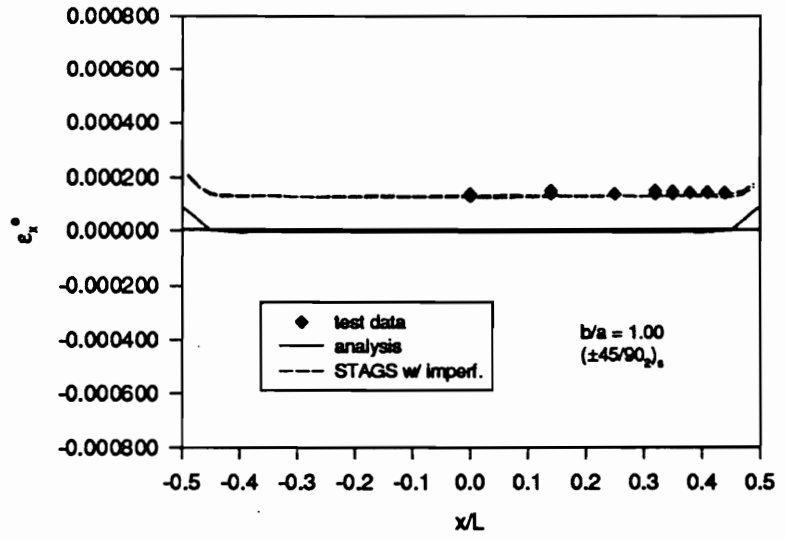

Figure C-9 Axial Midplane Strain vs. x/L for the $(\pm 45/0_2)_s$ and $(\pm 45/90_2)_s$ Cylinders, b/a = 1.00, Internal Pressure Loading to 1 Atm.

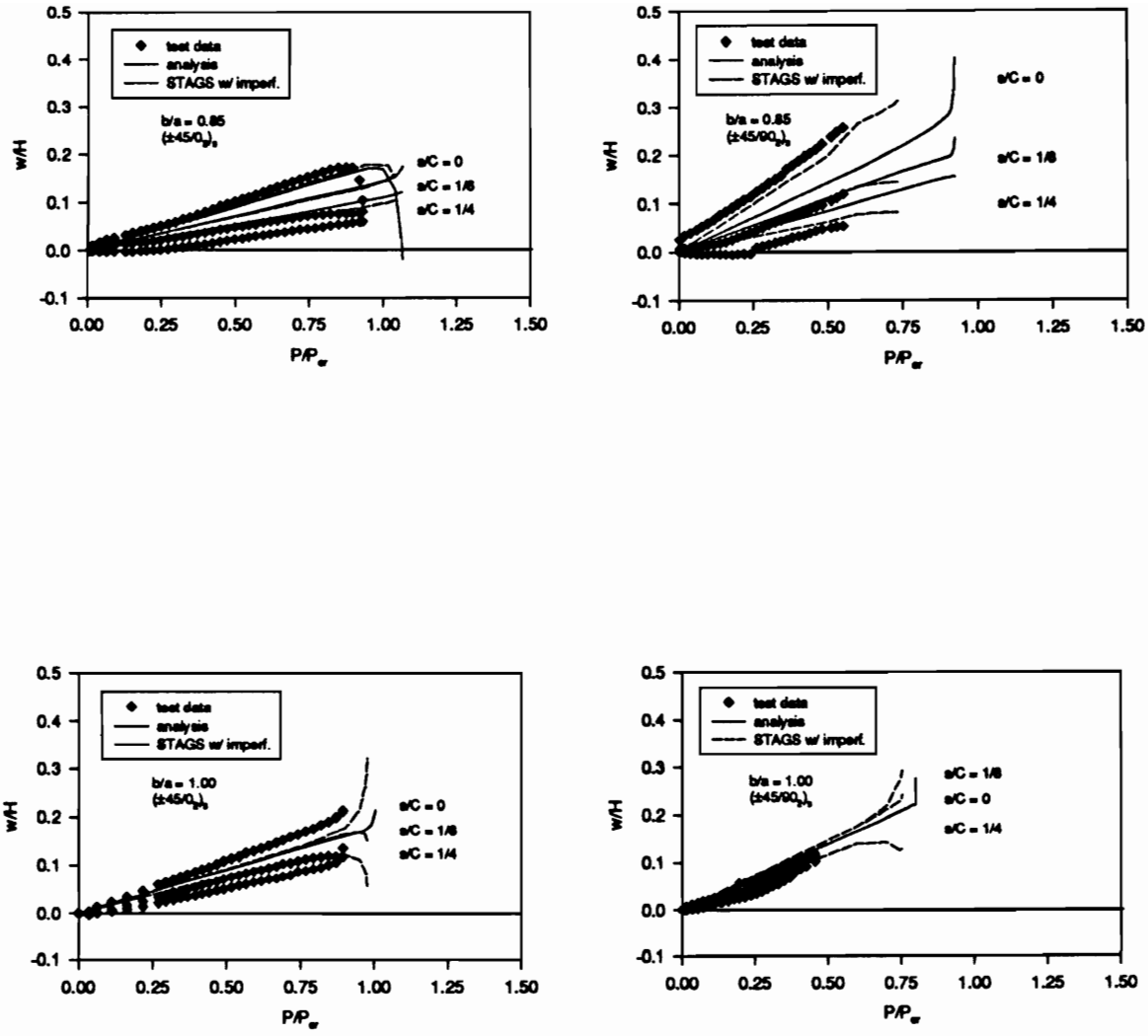

Figure C-10 Normalized Radial Displacement at Midspan vs. P/P_{cr} for the $(\pm 45/0_2)_s$ and $(\pm 45/90_2)_s$ Cylinders, b/a = 0.85 and 1.00.

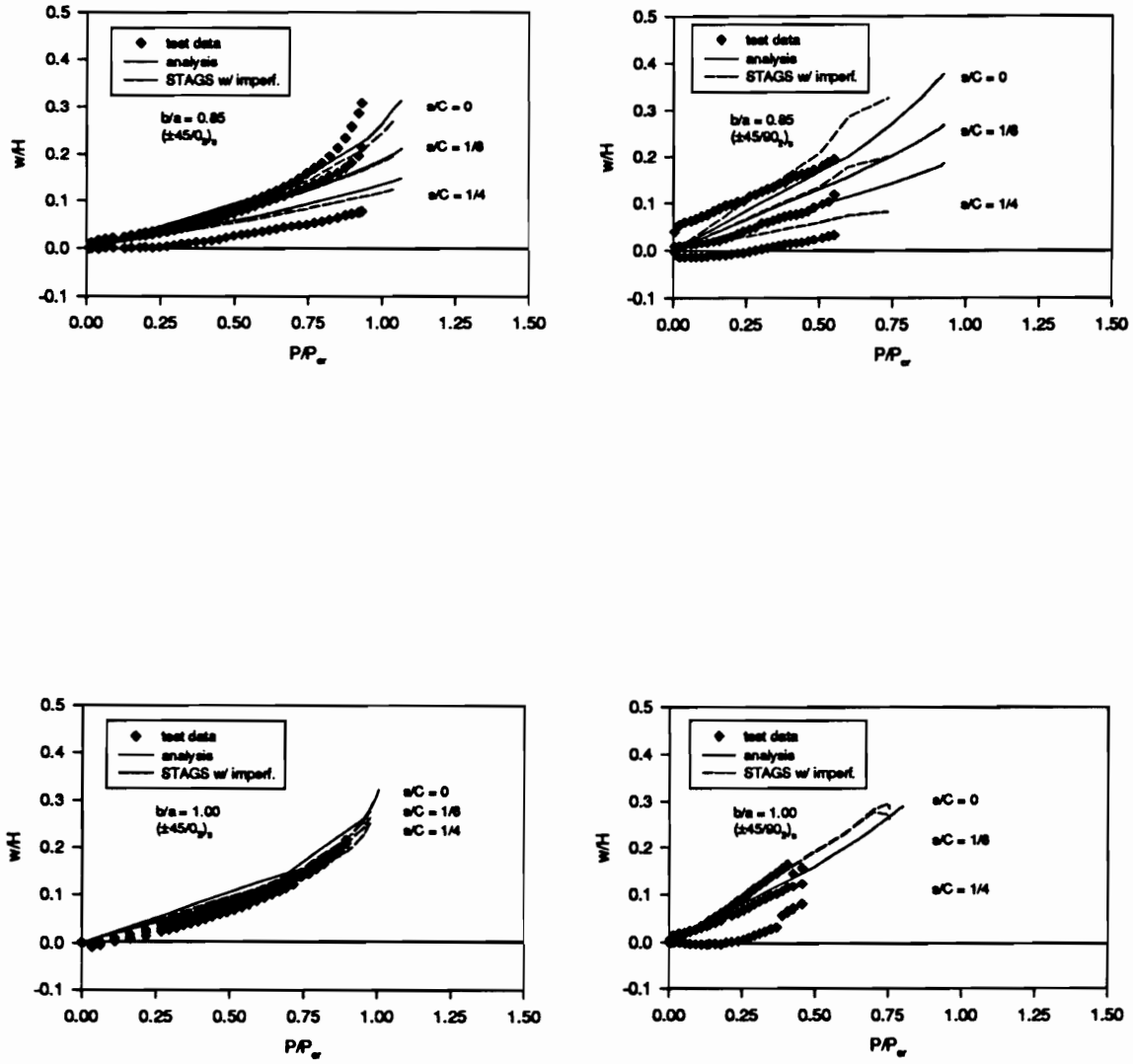

Figure C-11 Normalized Radial Displacement near the End Cap vs. P/P_{cr} for the $(\pm 45/0_2)_s$ and $(\pm 45/90_2)_s$ Cylinders, b/a = 0.85 and 1.00.

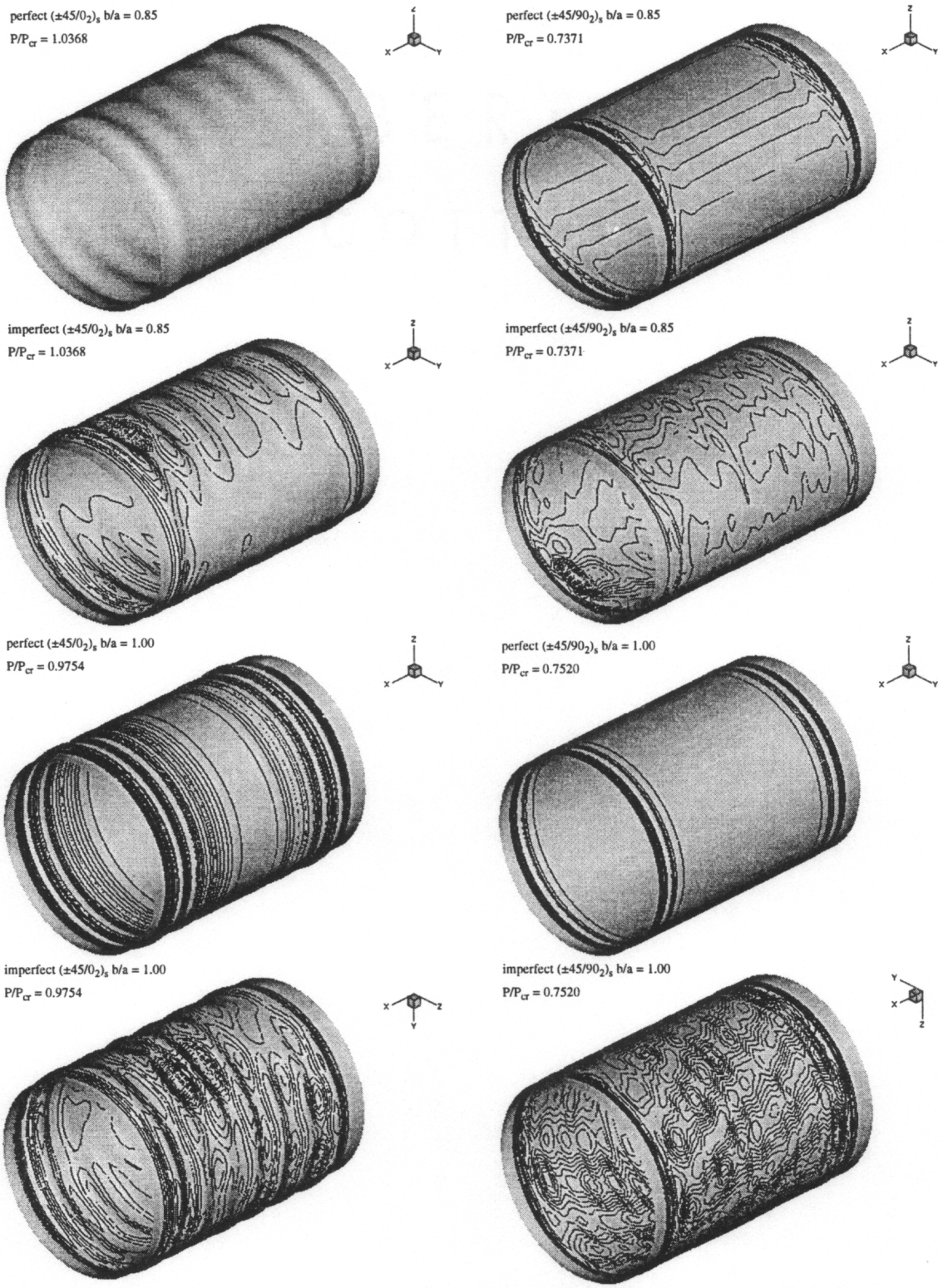

Figure C-12 Deformed Shapes of the Perfect and Imperfect $(\pm 45/0_2)_s$ and $(\pm 45/90_2)_s$ Cylinders with b/a = 0.85 and 1.00.

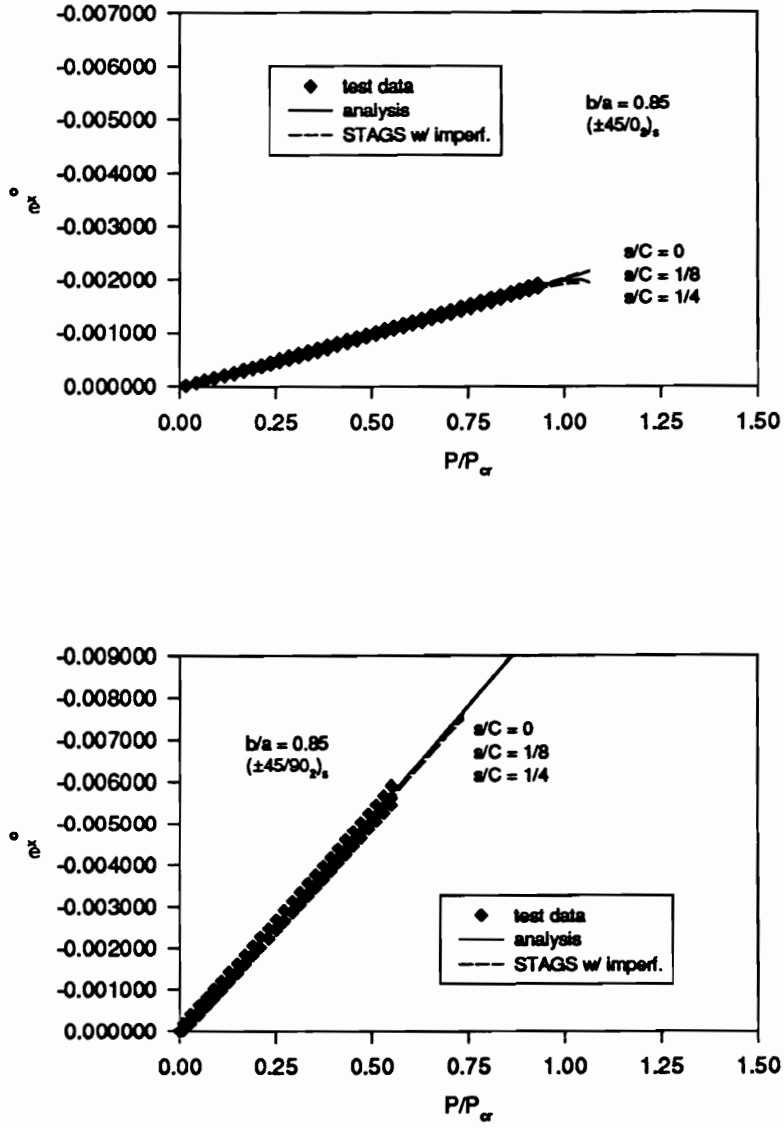

Figure C-13 Axial Midplane Strain at Midspan vs. P/P_{cr} for the $(\pm 45/0_2)_s$ and $(\pm 45/90_2)_s$ Cylinders, b/a = 0.85.

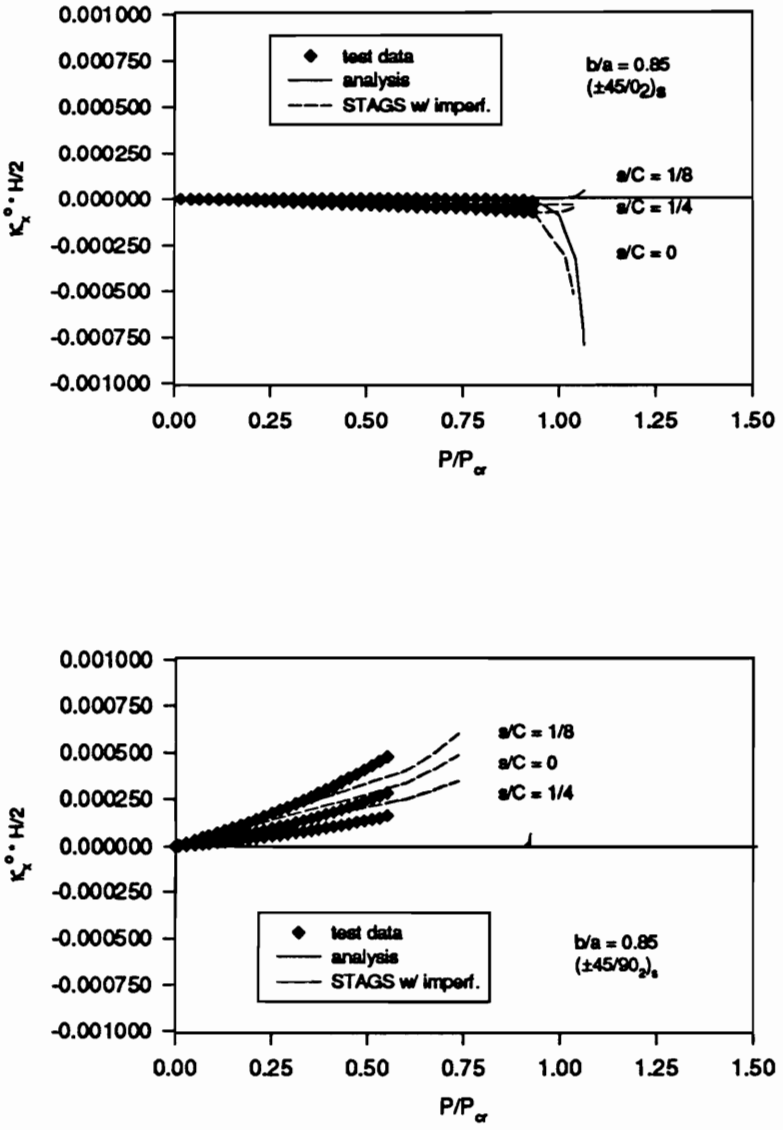

Figure C-14 Axial Bending Strain at Midspan vs. P/P_{cr} for the $(\pm 45/0_2)_s$ and $(\pm 45/90_2)_s$ Cylinders, b/a = 0.85.

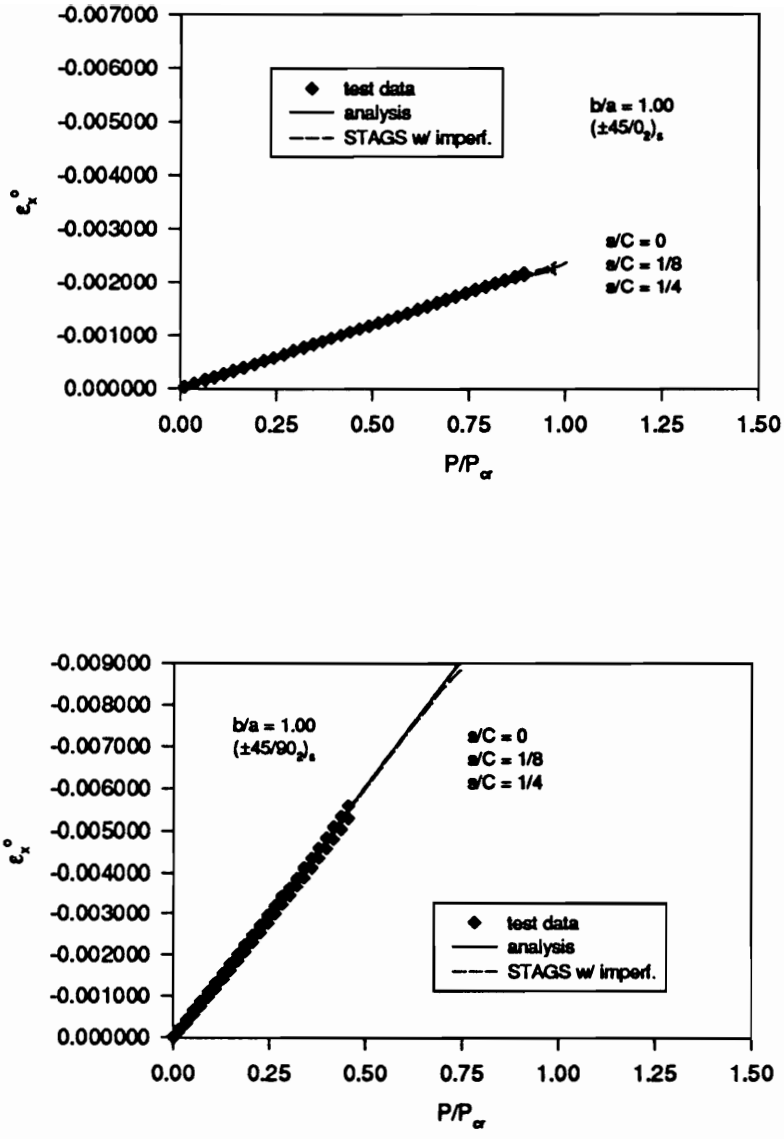

Figure C-15 Axial Midplane Strain at Midspan vs. P/P_{cr} for the $(\pm 45/0_2)_s$ and $(\pm 45/90_2)_s$ Cylinders, b/a = 1.00.

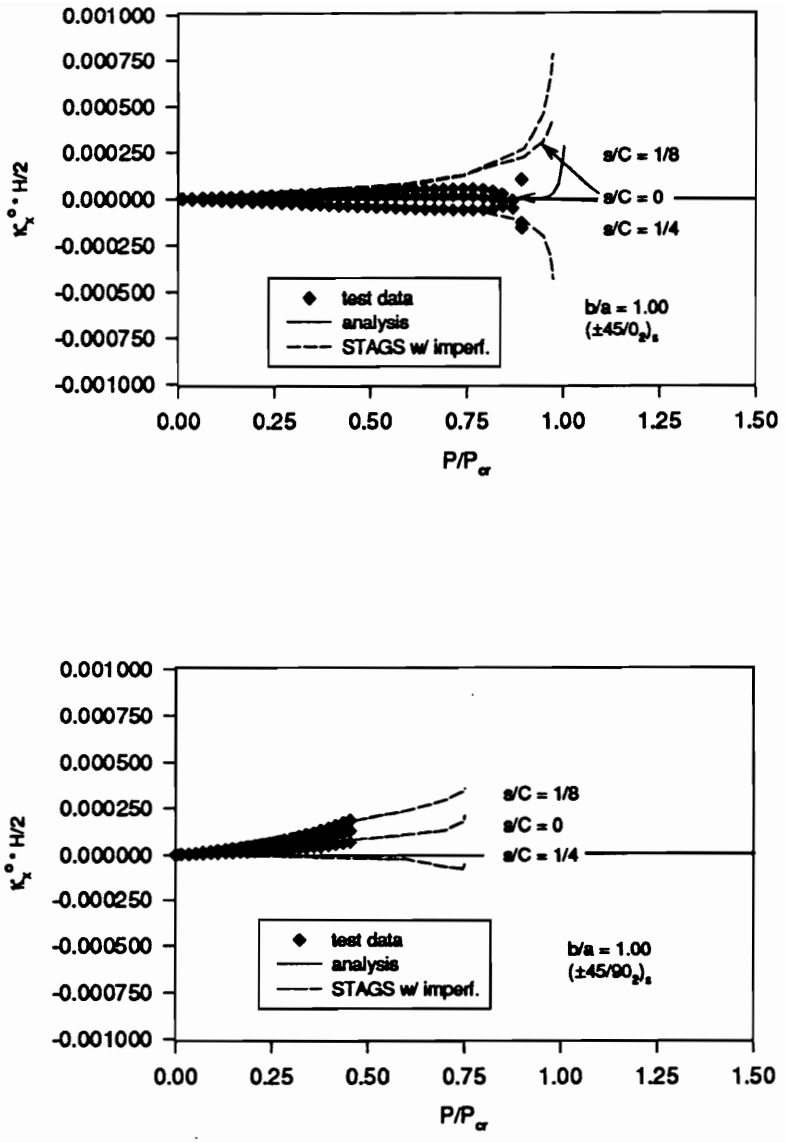

Figure C-16 Axial Bending Strain at Midspan vs. P/P_{cr} for the $(\pm 45/0_2)_s$ and $(\pm 45/90_2)_s$ Cylinders, b/a = 1.00.

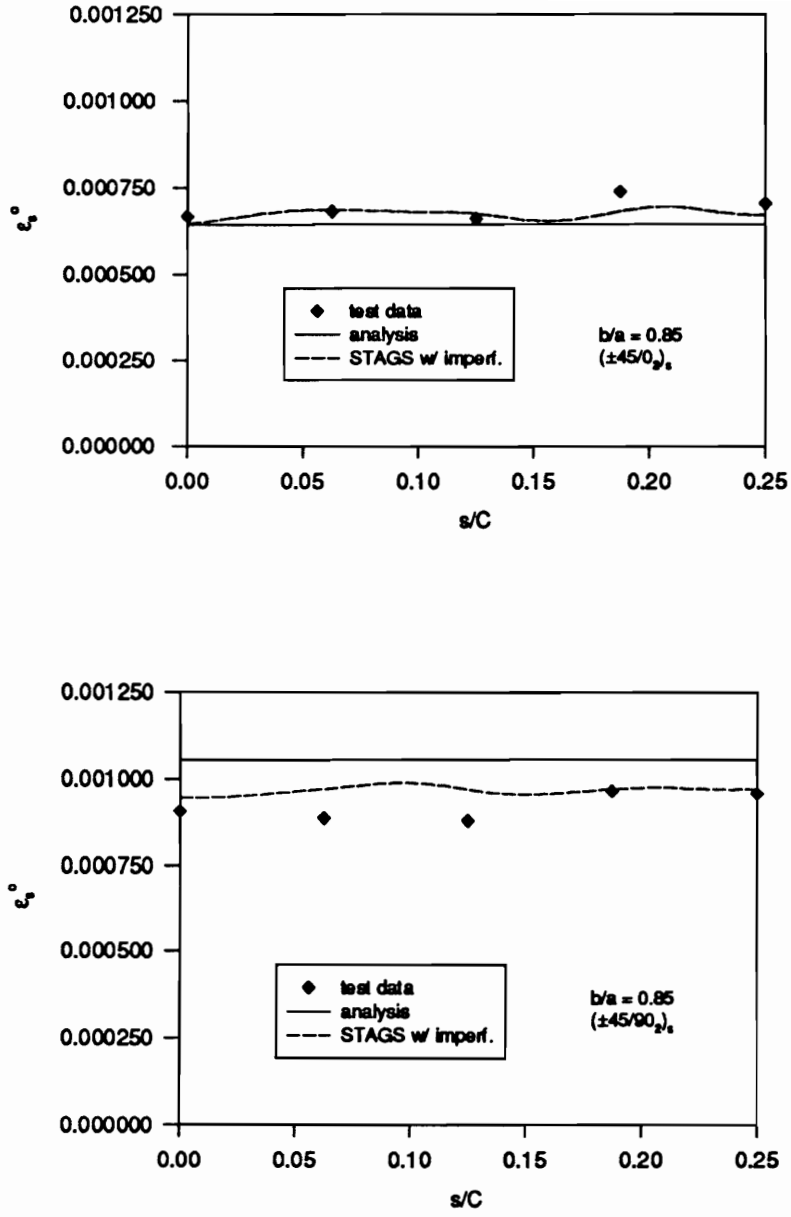

Figure C-17 Circumferential Midplane Strain vs. s/C at Midspan for the $(\pm 45/0_2)_s$ and $(\pm 45/90_2)_s$ Cylinders, b/a = 0.85, $P/P_{cr} = 0.50$.

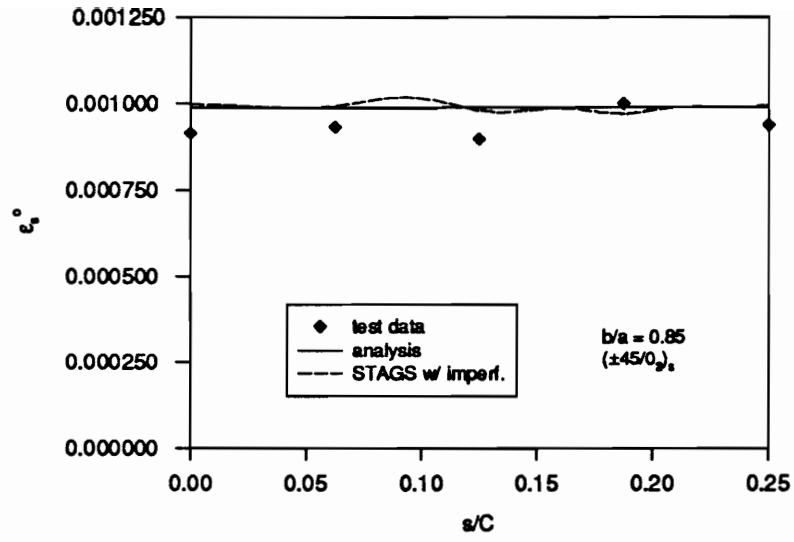

Figure C-18 Circumferential Midplane Strain vs. s/C at Midspan for the $(\pm 45/0_2)_s$ Cylinder, b/a = 0.85, $P/P_{cr} = 0.75$.

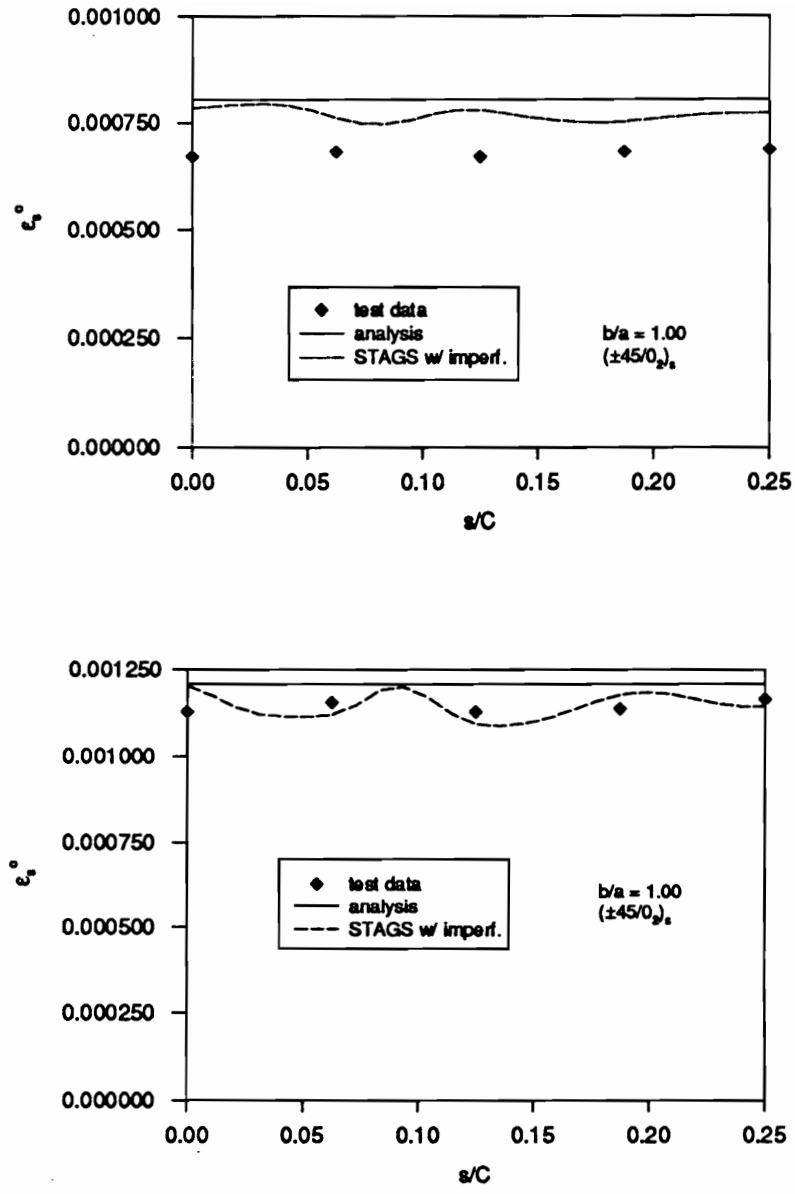

Figure C-19 Circumferential Midplane Strain vs. s/C at Midspan for the $(\pm 45/0_2)_s$ Cylinder, b/a = 1.00, P/P_{cr} = 0.50 and 0.75.

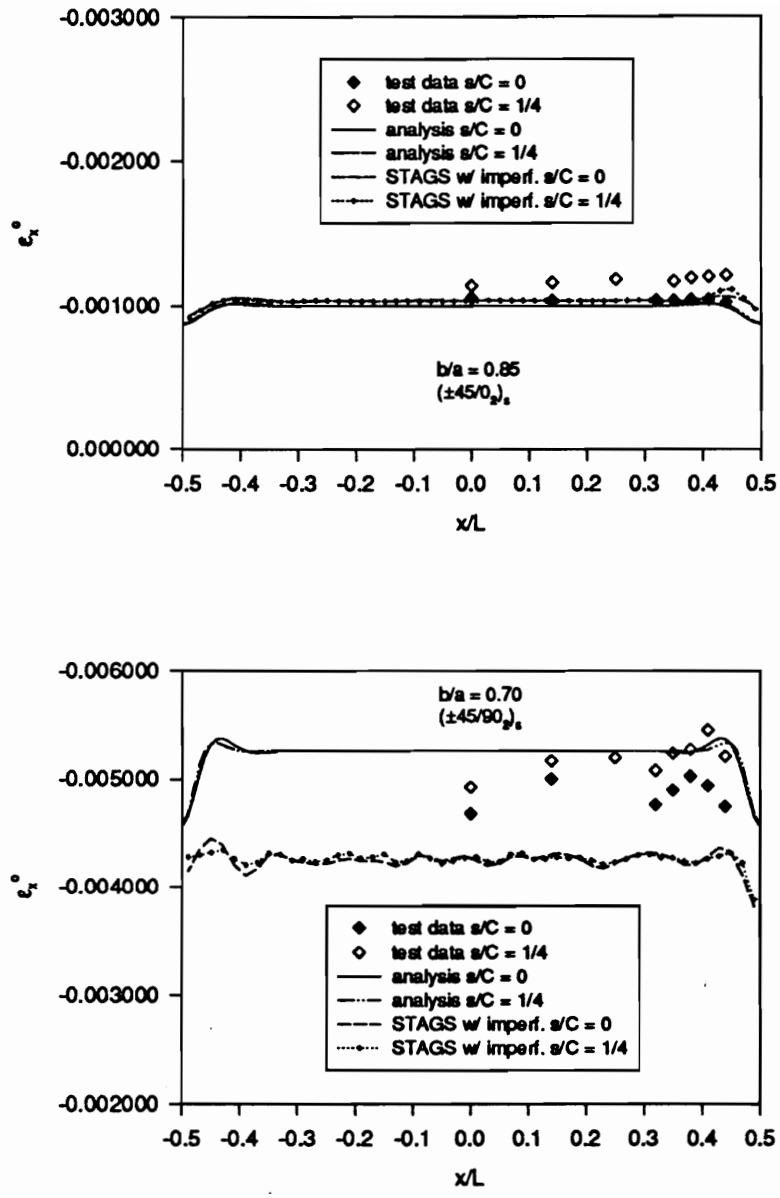

Figure C-20 Axial Midplane Strain vs. x/L for the $(\pm 45/0_2)_s$ and $(\pm 45/90_2)_s$ Cylinders , b/a = 0.85, $P/P_{cr} = 0.50$.

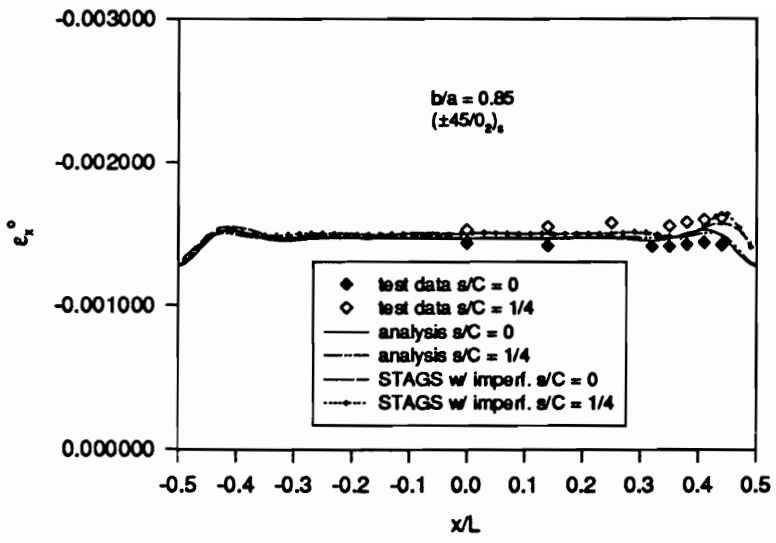

Figure C-21 Axial Midplane Strain vs. x/L for the $(\pm 45/0_2)_s$ Cylinder, b/a = 0.85, $P/P_{cr} = 0.75$.

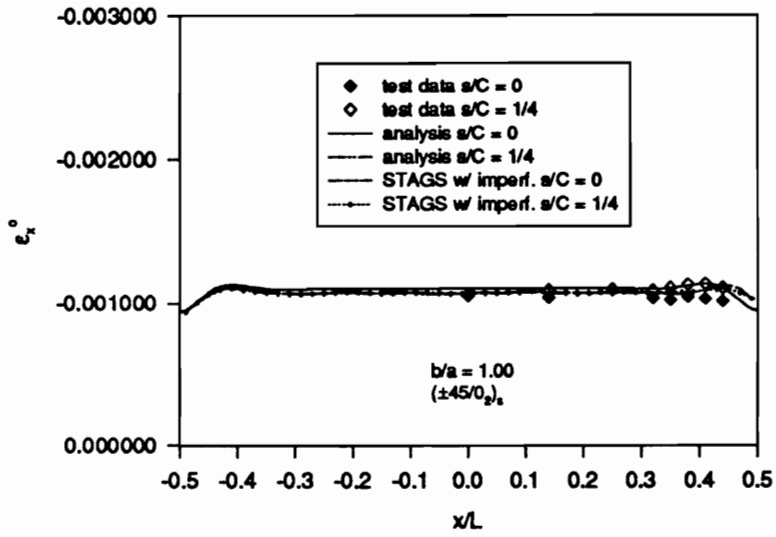

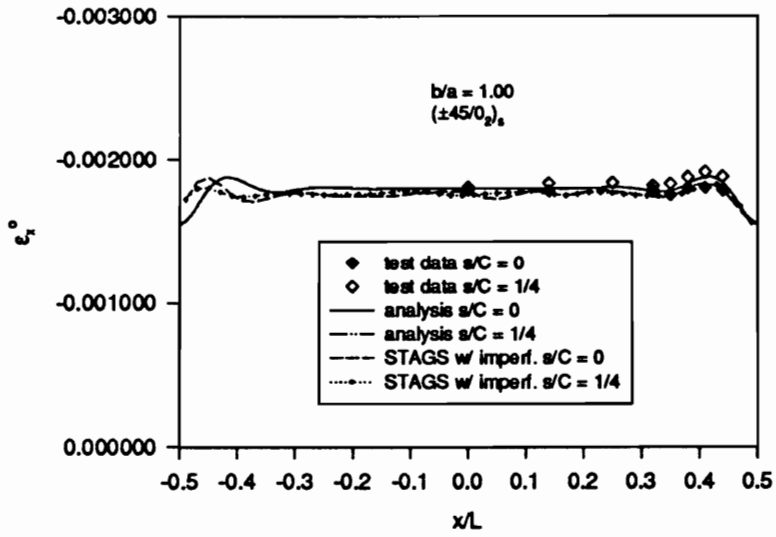

Figure C-22 Axial Midplane Strain x/L for the $(\pm 45/0_2)_s$ Cylinder, b/a = 1.00, P/P_{cr} = 0.50 and 0.75.

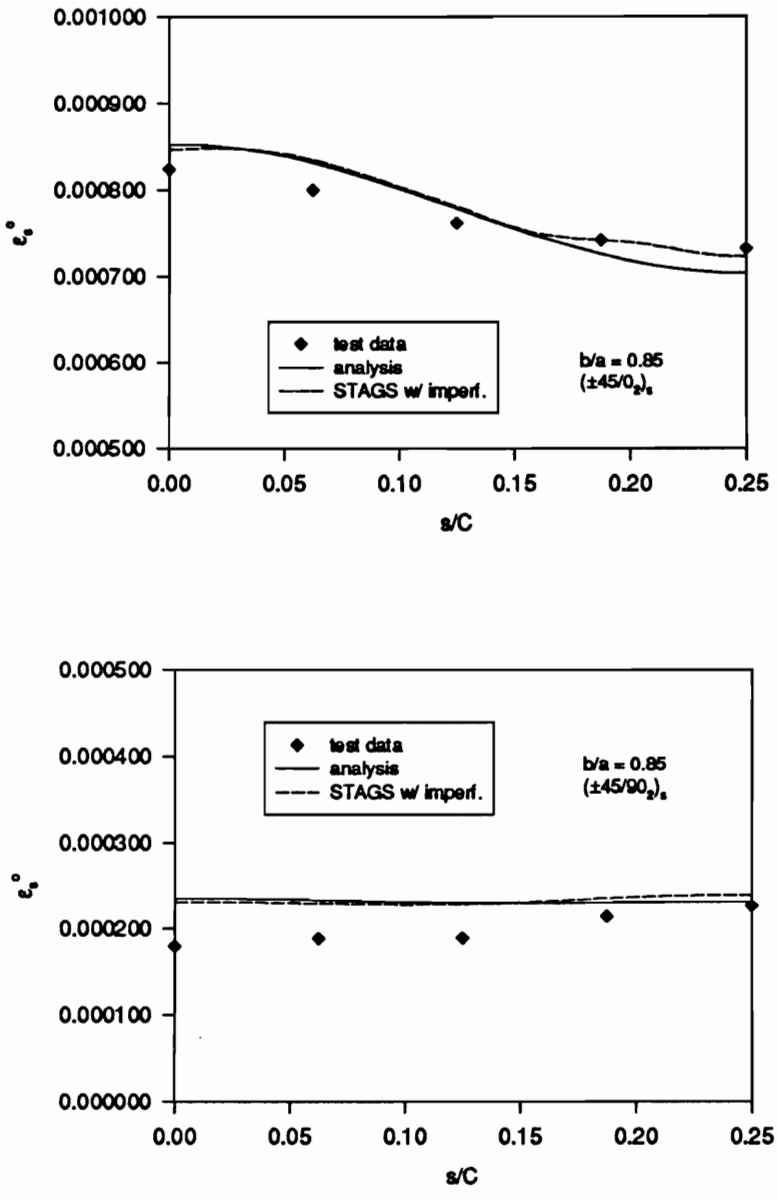

Figure C-23 Circumferential Midplane Strain vs. s/C at Midspan for the $(\pm 45/0_2)_s$ and $(\pm 45/90_2)_s$ Cylinders, b/a = 0.85, Combined Loading.

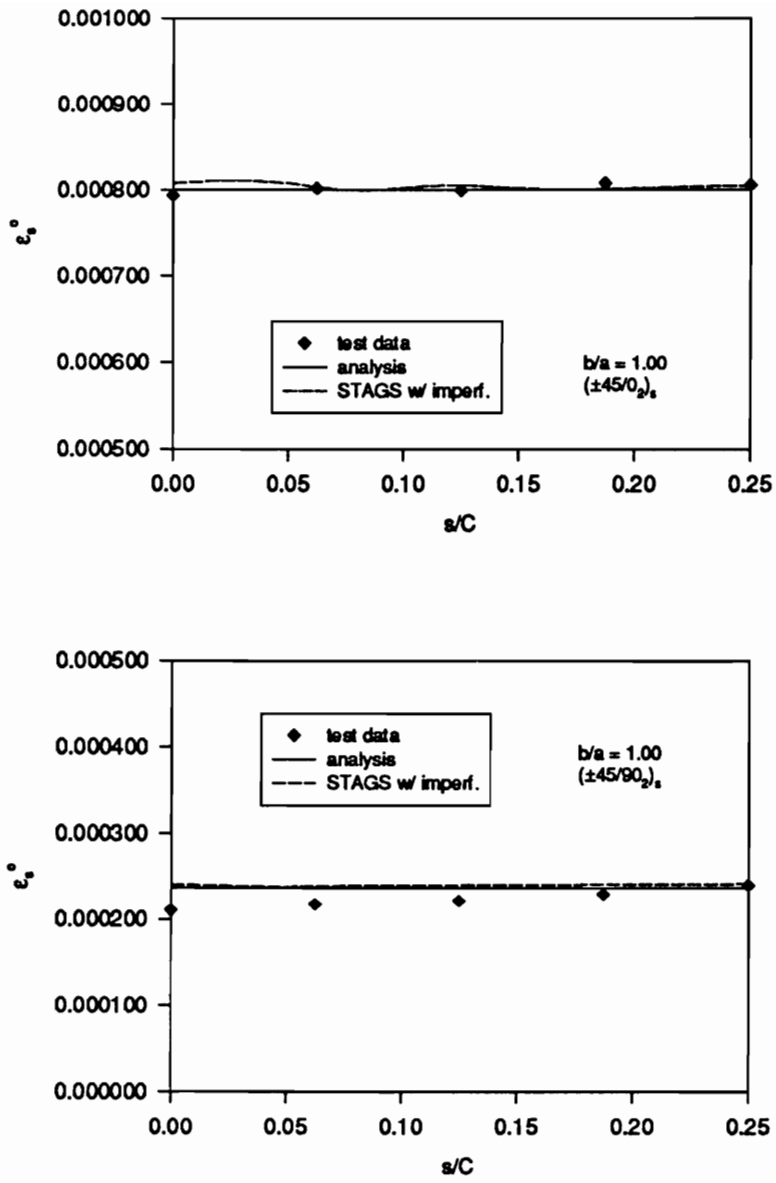

Figure C-24 Circumferential Midplane Strain vs. s/C at Midspan for the $(\pm 45/0_2)_s$ and $(\pm 45/90_2)_s$ Cylinders, b/a = 1.00, Combined Loading.

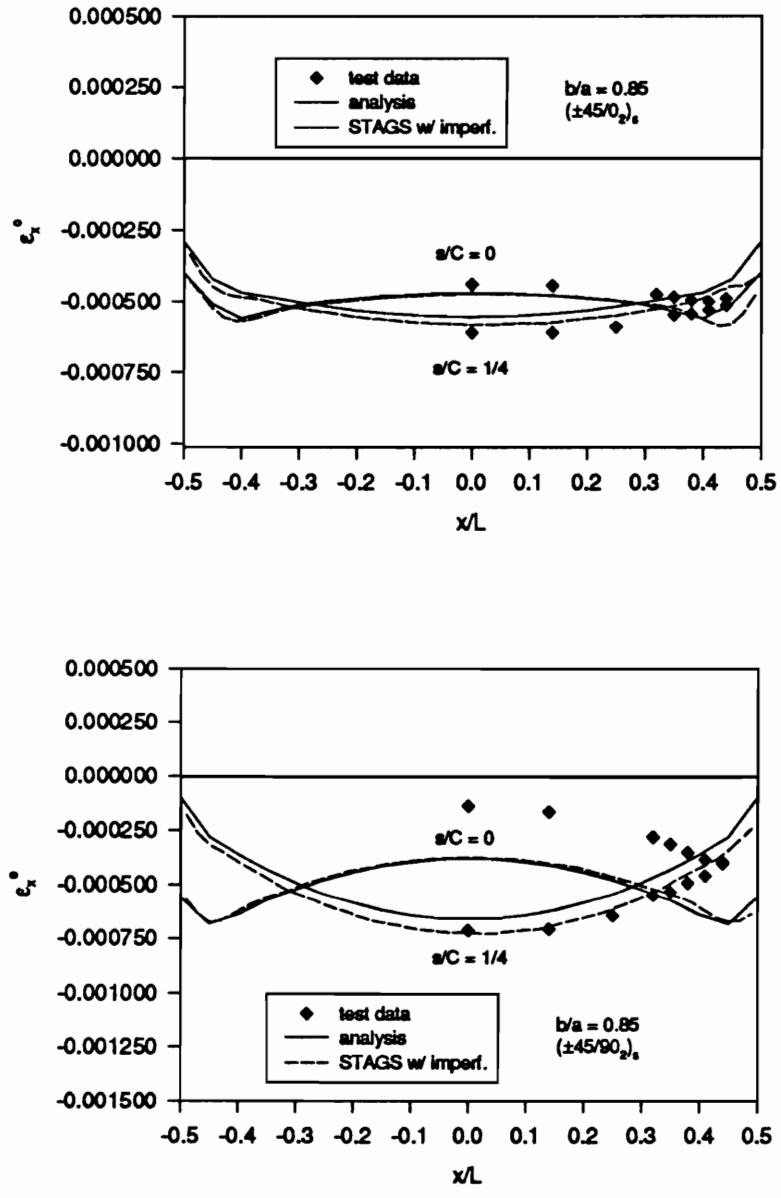

Figure C-25 Axial Midplane Strain vs. x/L for the $(\pm 45/0_2)_s$ and $(\pm 45/90_2)_s$ Cylinders, b/a = 0.85, Combined Loading.

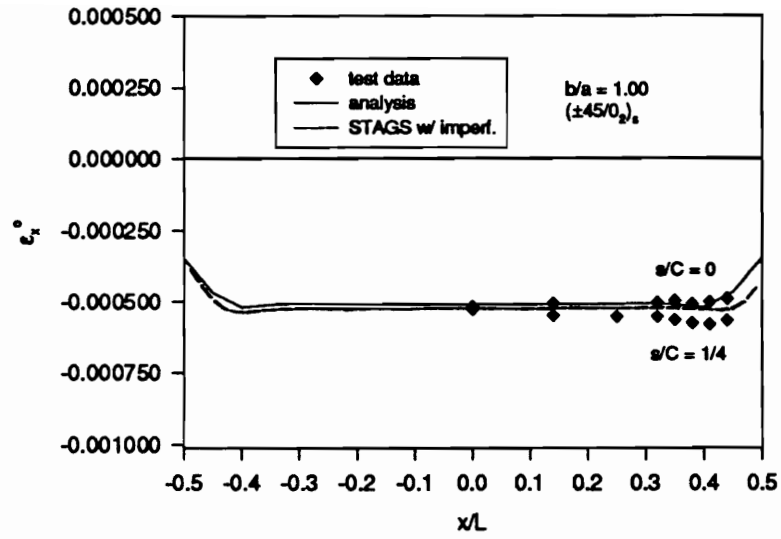

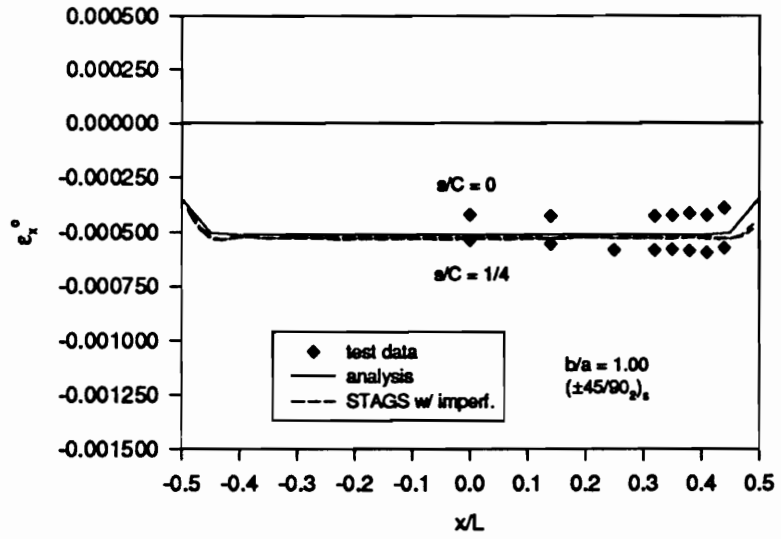

Figure C-26 Axial Midplane Strain vs. x/L for the $(\pm 45/0_2)_s$ and $(\pm 45/90_2)_s$ Cylinders, b/a = 1.00, Combined Loading.

Vita

Carol Meyers was born in Pittsburgh, Pa. on December 16, 1965. She graduated second in her class from Rutherford B. Hayes High School in 1984. She received a National Merit Scholarship and an Alumni Distinguished Scholarship to attended Michigan State University where she graduated with honors in 1988 with a dual B.S. degree in Engineering Mechanics and Mathematics. Following this, she joined the NASA-Virginia Tech Composites Program at Virginia Tech where she received a M.S. in Engineering Mechanics in 1990. At this writing, she is working in an advanced development group for Delphi Automotive Systems and lives in Birmingham, MI with her husband and her two dogs. Her other interests include reading, history, hiking, and martial arts.